

Mechanisms of Pharmacological and
Cellular Regulators of Mitophagy

A Thesis by
William Max Rosencrans

In Partial Fulfillment of the Requirements for
the degree of
Doctorate of Philosophy

The logo for the California Institute of Technology (Caltech), featuring the word "Caltech" in a bold, orange, sans-serif font.

CALIFORNIA INSTITUTE OF TECHNOLOGY
Pasadena, California

2025

(Defended June 2nd, 2025)

© 2025

William Max Rosencrans

ORCID: 0000-0003-1461-8891

ACKNOWLEDGEMENTS

“my predominant feeling is one of gratitude. I have loved and been loved; I have been given much and I have given something in return; I have read and traveled and thought and written.”

— **Oliver Sacks, *Gratitude***

Disclaimer: This work has been titled incorrectly. If I did not have to adhere to Caltech’s guidelines, this work would not be a Thesis; it would be a “Thank You!” There is much to be thankful for. Many individuals contributed to making this work possible, both through direct scientific contributions and those behind the scenes supporting my life and well-being.

I will start by dedicating this thesis to my grandmother, Marion. They say you don’t start getting old until you stop learning. By this standard, she is eternally youthful. From wildlife collection expeditions to countless museum visits, it was my grandmother who, above all, shaped and encouraged my curiosity, especially about nature. Ever inquisitive and thoughtful, she sought out experts and experiences that would fan my early interests in science. Beyond the experiences she intentionally cultivated, I have been shaped by her character. Relentlessly open-minded, resilient, and reflective—these have been the pillars I leaned on while completing a PhD characterized by uncertainty and tribulations. I am grateful to have you as a role model and guide all my life.

To my parents, Matt and Kara, if I am anything, it is thanks to you. Like master gardeners, you provided the perfect environment for growth. You did not attempt to forcefully shape me, only providing nourishment and space in which I could flourish, offering unending support to encourage growth where it was needed. From my father, I have learned agency and resourcefulness—to never back down from the formidable obstacles life throws and to proceed with lightness and humor. As I learn how difficult it is to build and maintain such a garden, my sense of awe grows. From my mother, I learned resilience, empathy, and style. You have been my number one supporter throughout my life. During these especially wonderful and difficult years, I am grateful that I could call you to celebrate and

commiserate. At the end of the day, science is the business of people (until AI takes over), and I have learned my people-skills from you.

To my siblings, Jack, Sophie, and Sam, it has been a blast doing life by your side. It was you who took that journey cross-country to drop me off at Caltech. We've had many adventures, and I look forward to sharing many more. I may be the eldest, but I have been able to lean on you all. I hope to be there for you as well.

To my partner, Romina—oh, how lucky I am! You are my confidant and inspiration. I remain in awe of your fortitude, bravery, and vision. Our discussions of science, politics, and life keep me sharp and ever-growing. My life has been enhanced in vibrant color since I met you. I look forward to painting the rest of the canvas together. جیگر تو بخورم

To my advisor, Dr. Richard Youle, when I first started my entry into mitophagy, you were the famous Youle of Youle and Narendra, a mere legend. Imagine my shock when you so nonchalantly took my meeting request and said we should work together. I admire your humble, open attitude; you have come close to creating the utopian vision of scientific exploration we all imagine the scientific endeavor should be. Talking science with you is a breath of fresh air—you grasp ideas, implications, and the path forward in an instant. Thank you for your unrelenting support. You gave me the chance to set my own direction, wherever that has led.

To my advisor, Professor Tsui-Fen Chou, from about five minutes into meeting you, you encouraged me to pursue my scientific dreams and haven't stopped since. You allowed and supported me in leading a team focused on fruitful new directions in your lab. We have been through all manner of tribulations, both in and out of the lab. Every day, you are ready to tackle the problems of both life and science. Thank you for creating and encouraging the most supportive lab I have experienced.

To my advisor, Professor David Chan, it has been an honor to work with you. I have been in awe of your incisive intellect. Your ability to cut problems down to their essential roots is unparalleled. I have become more adept at framing problems and designing compelling

experiments through your challenges and mentorship. I appreciate your expert editing of my often-verbose writing. Thank you for taking the helm of the graduate school and leading Caltech through the incessant turmoil of the last five years.

I am especially thankful to my committee chair, Professor Bruce Hays, for his unwavering enthusiasm for my work and potential, especially for supporting my highly unusual PhD track.

Thank you to my committee member Professor Rebecca Voorhees, for her critical analysis of my work. I have been especially inspired by her lab's science in recent years.

I have also been extremely fortunate to have scientific mentors well before graduate school whose support enabled me to be where I am today. Dr. Sergey Bezrukov and Dr. Tatiana Rostovtseva took a chance on an undergrad from an "unknown" college. That chance blossomed into an incredibly productive scientific collaboration and fantastic friendships. I am grateful to have found my scientific vision in your lab.

Professor Engda Hagos accepted me into his lab before I had even made a college decision, setting me up for all that unfolded at Colgate and beyond. I am forever grateful that you gave me the chance to set my own direction and learn the entire scientific process from start to finish. I have been incredibly inspired by your perseverance through unimaginable challenges and your commitment to mentorship.

To Dr. Ted Brummel, who gave me my first exposure to science and became my first scientific mentor—I will always remember those endless stories intertwining scientific and life lessons. Thank you for dedicating so much effort to local high school students; it is a testament to your vision and commitment to training the next generation of scientists. Probably unconsciously, I owe my decision to come to Caltech to your stories of the Benzer lab and my work on autophagy.

I would also like to thank my mentors Dr. Robert Gerver, Professor Kent Hatch, Professor Rebecca Metzler, and Professor Johan van der Maarel.

To my mentees Haruna Tomono, Andrew Blum, Roland Del Mundo, Nohami Elias, and Ian Horsburgh, I am especially grateful to have had the chance to work with you and watch you work toward achieving your dreams. Thank you for putting up with my unpredictable scatter and making the scientific enterprise worthwhile. This thesis is especially thanks to my incredible scientific associates, Ryan W. Lee and Jack Nguyen. You have gone above and beyond in turning ideas into real science. I am glad to have had the chance to work with you both and play a small part in your long scientific journeys.

I would also like to thank my lab members Dr. François Le Guerroué, Dr. Baiyi Quan, Dr. Ting-Yu Wang, Logan McGraw, Dr. Hsiuchen Chen, Diana Nguyen, Dr. Chunxin “Black” Wang, Dr. Yogaditya Chakrabarty, Kent Leslie, Dr. Eric Bunker, Dr. Zheng Yang, and many more. It takes a village. I am lucky to have so many people helping me make science work and having fun while doing it.

The best part of Caltech, is the sheer density of incredibly brilliant people who have become my closest friends. I am immensely appreciative of Kate Radford, who has been my scientific partner in crime these past few years and makes every day much better for everyone around her. I am lucky to learn so much from you and enjoy all the fruits of your creativity. Thank you to my friend and colleague Dr. David Nyenhuis, who has been in the trenches with me on the most difficult projects in science and bureaucracy. I appreciate our long scientific calls, your incredible tenacity, and brilliance. To my roommates Daniel Pollak, Noah Epstein, and Dr. Scott Conn—we have had a blast, and you have had my back through the best and the worst of it. Thank you for your friendship and support. Thank you to Dr. Oren Mizrahi for your clever insights, political commentary, and food and book recommendations. I am especially grateful for the espresso machine you built, which powered the writing of this thesis. Thanks to Eva Kercmer and Vera Beilenson for our tea breaks. Many more thanks including Dr. Sophie Miller, Roey Lazarovits, Linh Le, Rabii Hershey and Sheva Stolik, Professor Andres Collazo, and many others not mentioned here.

ABSTRACT

Autophagy is a highly conserved cellular process that isolates and degrades damaged or unnecessary intracellular structures. Mitochondria, well known as metabolic centers, provide ATP and critical metabolites essential for life. Unchecked mitochondrial damage impairs metabolism, releases immunogenic mitochondrial DNA, and triggers apoptosis. Mitophagy, the selective removal of mitochondria via autophagy, is vital to preventing these harmful outcomes. The PINK1/Parkin pathway detects damaged mitochondria and targets them for mitophagy. Dysfunction in this pathway underlies certain subset Parkinson's Disease (PD) cases. Efforts to understand the mechanistic basis of this pathway and its regulators provides a pathway to development of potentially disease modifying therapeutics for PD. In this thesis, I characterize the mechanism of action of a series of clinical stage mitophagy activating drugs. We find that these compounds reduce the threshold for which mitochondrial stress initiates mitophagy. However, contrary to reported literature, I demonstrate that these compounds do not directly activate PINK1 or Parkin. Rather, they act as weak mitochondrial toxins sensitizing cells to mitochondrial insult. I reveal that this phenomenon is characteristic of any weak mitochondrial toxin, revealing a potent pitfall for current drug discovery campaigns. Next, I detail a novel endogenous regulator of PINK1/Parkin mitophagy, the immune-related protein TNIP1. We show through a series of cell, biochemistry, and biophysical assays, that TNIP1 competes for autophagy machinery to slow down mitophagy. These data center TNIP1 as a important regulator of autophagic processes, and a unique negative regulator of mitophagy. Finally, I describe a biophysical analysis of the mitochondrial ion channel, VDAC2, critical in apoptosis and PINK1/Parkin pathways. Using a series of single-molecule approaches, I reveal how its structural plasticity regulates its interactions with protein partners. These finding provide a mechanistic basis for understanding its role in disparate cellular processes. I also explore the biological impact of KO of each VDAC isoform on mitochondrial and cell function. Unexpectedly, we find that the lowest expressed isoform, VDAC3, has an outsized impact on mitochondrial function.

PUBLISHED CONTENT AND CONTRIBUTIONS

Rosencrans, W. M.*, Lee, R. W.*, McGraw, L., Horsburgh, I., Wang, T.-Y., Quan, B., Huynh, D., Johnston, J. A., Chan, D. C., & Chou, T.-F. (2023). Putative PINK1/Parkin Activators Lower the Threshold for Mitophagy by Sensitizing Cells to Mitochondrial Stress. *Science Advances*, under review.

Contribution: W.M.R conceived of the project, performed or supervised most experiments, prepared the data, acquired funding, and wrote the initial manuscript.

Le Guerroué, F., Bunker, E. N., Rosencrans, W. M., Nguyen, J. T., Basar, M. A., Werner, A., Chou, T.-F., Wang, C., & Youle, R. J. (2023). TNIP1 inhibits selective autophagy via bipartite interaction with LC3/GABARAP and TAX1BP1. *Molecular Cell*, 83(6), 927–941.e8. doi:10.1016/j.molcel.2023.02.023

Contribution: W.M.R performed or supervised all in vitro biophysical experiments, prepared the data, and assisted in writing and reviewing the manuscript.

Rosencrans, W. M., Khuntia, H., Larimi, M. G., Mahalakshmi, R., Yu, T.-Y. D., Bezrukov, S. M., & Rostovtseva, T. K. (2025). Conformational plasticity of mitochondrial VDAC2 controls the kinetics of its interaction with cytosolic proteins. *Science Advances*, 11, eadv4410. doi:10.1126/sciadv.adv4410

Contribution: W.M.R helped conceive of the project, performed most experiments, prepared the data, and wrote the initial manuscript.

Rajendran, M. *, Rosencrans, W. M. *, Fitzgerald, W., Huynh, D., Beyene, B. G., Quan, B., Hwang, J., Bautista, N. A., Chou, T.-F., Bezrukov, S. M., & Rostovtseva, T. K. (2025). Unlocking the Distinct Roles of the Three Mammalian VDAC Isoforms in Mitochondrial Respiration and Cancer Cell Metabolism. *bioRxiv*. doi:10.1101/2025.02.20.639106

Contribution: W.M.R helped conceive of the project, performed or supervised proteomics and proteomics validation experiments, prepared the data, and assisted in writing and reviewing the manuscript.

* denotes equal contribution

TABLE OF CONTENTS

Acknowledgements.....	iii
Abstract	vii
Published Content and Contributions.....	viii
Table of Contents.....	ix
List of Illustrations and/or Tables.....	xi
Chapter I: Introduction to Autophagy	1
Chapter II: Putative PINK1/Parkin Activators Lower the Threshold for Mitophagy by Sensitizing Cells to Mitochondrial Stress	17
2.1 Abstract	17
2.2 Introduction	18
2.3 Results	21
2.4 Discussion	36
2.5 Methods.....	39
2.6 Acknowledgments	56
Chapter III: TNIP1 inhibits selective autophagy via interaction with LC3/GABARAP and TAX1BP1	101
3.1 Abstract	101
3.2 Introduction	102
3.3 Results	103
3.4 Discussion	117
3.5 Methods.....	120
3.6 Acknowledgments	129
Chapter IV: Conformational Plasticity of Mitochondrial VDAC2 Controls the Kinetics of its Interaction with Cytosolic Proteins	159
4.1 Abstract	159
4.2 Introduction	160
4.3 Results	164

4.4 Discussion	173
4.5 Methods.....	183
4.6 Acknowledgments	187
Chapter V: VDAC Isoforms Play Distinct Roles in Modulating Metabolism and Maintaining Mitochondrial Function	217
5.1 Abstract	217
5.2 Introduction	218
5.3 Results	221
5.4 Discussion	228
5.5 Methods.....	231
5.6 Acknowledgments	235
Conclusion	263

LIST OF ILLUSTRATIONS AND/OR TABLES

<i>Number</i>	<i>Page</i>
1.1 The major steps of Macroautophagy.....	9
1.2 Major Molecular Machinery of Macroautophagy	10
1.3 The PINK1/Parkin mitophagy pathway.....	11
2.1 PINK1/Parkin activators lower the threshold for mitophagy induction.....	58
2.2 Parkin/PINK1 activators enable potent activation of the PINK1/Parkin pathway.....	59
2.3 FB231 and MTK458 can be used to synergistically enhance mitophagy.....	61
2.4 Label free proteomics identifies the Integrated Stress Response as Off-Target effects of FB231 and MTK458	63
2.5 FB231 and MTK458 induce mitophagy independently of the integrated stress response.....	65
2.6 FB231 induces mitophagy through an iron-chelation based mechanism.....	67
2.7 FB231 and MTK458 inhibit mitochondrial function through distinct mechanisms	69
2.8 FB231 and MTK458 sensitize cells to mitochondrial stress	71
2.9 Mathematical Modeling of mitochondrial inhibitor combinations on the induction of mitophagy.....	73
S2.1 Identification of Parkin activating compounds through an in vitro ubiquitination assay	76
S2.2 Mitophagy activators do not induce mitophagy without prior mitochondrial damage	78
S2.3 Additional data related to Figure 2, Parkin/PINK1 activators enable potent activation of the PINK1/Parkin pathway	80

S2.4 FB231 cannot be utilized in a Parkin-AutoTAC strategy.....	82
S2.5 Proteomics identified pathways altered by FB231	83
S2.6 Additional blots related to Figure 4, Off-Targets of FB231 and MTK458	
S2.7 Additional blots related to Figure 4, FB231 and MTK458 induce Mitochondrial Stress upstream of PINK1/Parkin activation.....	85
S2.8 Thermal Proteome Profiling of MTK458	87
S2.9 Additional data related to Figure 8, FB231 and MTK458 sensitize cells to mitochondrial stress.....	88
S2.10 PINK1 is not required for MTK458-induced sensitization to mitochondrial stress.....	90
S2.11 Effect of a USP30i on Mitophagy and Parkin substrates	92
3.1 Ectopic localization of TNIP1 to the mitochondria induces mitophagy.....	136
3.2 LIR2 and AHD3 domain of TNIP1 are essential for its role in mitophagy.....	139
3.3 TNIP1 is a negative regulator of selective autophagy	141
3.4 The interaction between the AHD3 domain of TNIP1 and the Zinc-Finger domain of TAX1BP1 is necessary for TNIP1's mitophagy inhibition.....	143
3.5 TNIP1 binds FIP200 via its LIR motif and to the CLAW domain of FIP200.....	144
3.6 TNIP1 binds FIP200 via its FIR motif and is regulated by a phosphorylation upstream of FIR	145
S3.1 Characterization of the LIR motif of TNIP1	148
S3.2 Characterization of TNIP1's domains.....	149
S3.3 TNIP1 is not an autophagy receptor of mitophagy	152
S3.4 TNIP1 is specifically involved in selective autophagy	154
S3.5 TNIP1 recruitment of FIP200 is independent of TAX1BP1 and mATG8 proteins	156
S3.6 TNIP1 forms a complex with FIP200.....	158
4.1 VDAC2 stochastically switches between different "open" conductance substates	

4.2 VDAC2 substates are anion-selective open states.....	188
4.3 VDAC2 dynamic substates differ from each other in their interaction with cytosolic regulator α Syn	190
4.4 N-terminal extension and cysteine mutations influence but do not abolish VDAC2 substates	192
4.5 α Syn blocks the higher-conductance substates with a higher on-rate than the lower-conductance states across VDAC2 mutants	194
4.6 E84 residue of VDAC2 contributes to β -barrel stability but does not affect substates appearance.....	196
4.7 Changes in the transition state energy barrier underlie the kinetic differences in the α Syn-VDAC interaction between substates	200
S4.1 Conductance substates in VDAC2 WT are observed at low voltages.....	201
S4.2 The voltage-induced low conducting, closed state of VDAC2 is not blocked by α Syn	202
S4.3 Statistical analysis of the kinetic parameters of α Syn interaction with different VDAC2 conductance states	203
S4.4 Voltage dependences of the kinetic parameters of α Syn-VDAC2 interactions.....	204
S4.5 VDAC2 E84A mutant forms a functional voltage-gating channel with multistate behavior.....	206
S4.6 Zebrafish VDAC2 (zfVDAC2) has conductance substates that interact differently with α Syn	208
5.1 VDAC3 KO decreases metabolic activity in HeLa cells.....	236
5.2 VDAC1 KO decreases glycolysis in HeLa cells	237
5.3 VDAC3 KO decreases mitochondrial respiration in HeLa cells, resulting in the complete loss of spare respiratory capacity.....	239
5.4 Total proteomics reveals isoform-specific proteome remodeling in HeLa cells.....	241
5.5 Mitochondrial localization of HK1	

is dependent on VDAC1 isoform.....	243
5.6 VDAC isoform KO leads to distinct mitochondrial proteome remodeling.....	245
5.7 VDAC2 KO and VDAC3 KO result in widespread upregulation and downregulation of ETC components.....	247
5.8 VDAC3 KO leads to increased reliance on glutamine metabolism....	249
S5.1 Location and sequencing confirmation of VDAC isoform CRISPR target sequences	250
S5.2 VDAC1, 2, and 3 expression in HeLa cells	251
S5.3 NADH and FAD autofluorescence in HeLa WT and VDAC isoform KO cells.....	253
S5.4 ATP production rate in HeLa WT and VDAC isoform KO cells....	254
S5.5 Cell morphology and growth of HeLa WT and VDAC isoform KO cells.....	256

Chapter 1

INTRODUCTION

“The snake that cannot cast its skin perishes. So too with those minds which are prevented from changing their views: they cease to be minds.”

Nietzsche-*The Dawn of Day*,

1.1 On the importance of cleaning

At the greatest extremes, our neurons, must manage to survive upwards of 100 years or more. Those cell's persistence is the basis of our perpetuity, and in their demise, the unraveling of self. Like all things, the pieces that make up the cell fall apart. The onslaught of entropy unceasing. Across all this time, the cell must manage to fortify itself against decay and renew; taking in what it needs from the outside and managing the rot of structures within. A neuron, which replaces almost its entire set of atoms every few months, puts the *Ship of Theseus* to shame (Dorrbaum et al., 2018). Like a sacred temple, the cell is continually engaged in ritualistic cleansing. Studies in disease pathogenesis have identified breakdown of these cleaning processes in a panoply of human disease (Klionsky et al., 2021). Of the most robust findings in the field of aging, is that enhancement of these processes can, in some cases, extend lifespan (Nakamura & Yoshimori, 2018). It is therefore crucial to improve our understanding of cellular “cleaning” processes, and develop technology capable of modulating them. Pharmacologic tools targeting these pathway hold great promise in alleviating the burden of the most intractable human ailments. This thesis will investigate both the mechanisms by which existing drugs can modulate these pathways, and the endogenous mechanisms by which the cell tunes these processes.

1.2 Autophagy

Eukaryotic cells create massive molecular structures in the form of organelles and other assemblies. Much as the tearing down of a large building is often done by demolition, rather than removing brick-by-brick, the cell chooses in some case to undergo wholesale destruction of large intracellular components. Detection of this large scale cleansing process was first observed in the 1950's with the advent of Electron Microscopy (EM). Mitochondria,

organelles which by that time had been recognized as the cells' energy production hub, were observed sequestered with other material within double-membraned intracellular vesicles (Ohsumi, 2014). Stimulation with the hormone glucagon, which signals glucose depletion, or stress could induce the formation of these structures. Those double-membraned vesicles were identified to fuse with the previously identified lysosomes. Christian De Duve, discover of the lysosome, coined the term "Autophagy" for this process, greek for self-eating. As hinted by the induction of this process by glucose deprivation, autophagy is intimately linked to nutrient sensing and responses to stress. In the years that followed, more detailed exploration of the autophagic process was explored. It is now understood that the engulfment of cytoplasmic contents wholesale into double membrane autophagosomes is but one pathway to the lysosome, now identified as macroautophagy (Mizushima & Komatsu, 2011). Individual substrates can be transported directly into the lysosome, known as chaperone mediated autophagy, and material can be deposited into lysosomes and late endosomes via direct membrane invagination, known as microautophagy

Macroautophagy, referred from here after as autophagy, is carried out in a regulated step-wise manner beginning with the formation of the initial structure known a phagophore (Figure 1.1). The phagophore expands, like a cup, around cytoplasmic cargo, closing to form the canonical double-membraned autophagosome. The autophagosome then fuses with lysosomes, forming the autolysosome, that will ultimately degrade the cargo.

Despite early identification of these processes, the molecular underpinnings remained anonymous until the 1990's when Yoshinori Ohsumi's group identified a set of genes in yeast necessary for autophagy, known as Autophagy Related Genes (ATGs) for which he won the 2016 Nobel prize in Physiology and Medicine (Mizushima et al., 2011). Since the discovery of ATGs in yeast, evolutionarily conserved ATGs have been identified in humans. It is now understood that hundreds of proteins coordinate the multistep process of autophagy (Dikic & Elazar, 2018). Characterization of these proteins and how they regulate the process of autophagy is a particularly active domain of research.

1.3 Molecular Mechanisms of Autophagy

The initiation of the autophagosome is dependent on the eponymous autophagy initiation complex, also known as the ULK1-complex (Zachari & Ganley, 2017). This complex is formed from the kinase Unc-51-like kinase 1 (ULK1), ortholog of the first discovered yeast autophagy gene, ATG1. The other members include ATG13, ATG101, and FIP200. ULK1 phosphorylates downstream autophagy inducing machinery to activate the autophagy cascade (Figure 2.1 (Wold et al., 2016)). The ULK1 complex, via ATG13/101, is known to bind the only transmembrane ATG, ATG9A, which provides the initial member seed for the autophagosome (Olivas et al., 2023; Ren et al., 2023). ULK1 can be activated by the AMPK kinase, which senses cellular ATP levels, and inhibited by mTOR which integrates a variety of cellular nutrient cues (Hosokawa et al., 2009; Zachari & Ganley, 2017).

The initiation complex recruits the class 3 phosphoinositide 3-kinase (PI3K) complex, although in some cases the PI3K complex is known to recruit the initiation complex (Jaber & Zong, 2013; Nguyen et al., 2023). The PI3K complex is formed from the catalytic VPS34, VPS15, Beclin1, and ATG14. As named, the PI3K complex phosphorylates inositol headgroups, that recruit downstream factors important for expanding the autophagosome, especially WD repeat domain, phosphoinositide interacting proteins (WIPIs). WIPI proceeds to recruit the ATG8-conjugating machinery to the phagophore (Dooley et al., 2014).

ATG8-family proteins, also known as GABARAPs, are small ubiquitin-like proteins that decorate the interior and exterior of the autophagosome (Kabeya et al., 2000). Originally identified in yeast as ATG8, in humans there are six orthologs including LC3B, often used as a marker of autophagy induction. These proteins are directly conjugated to phosphoethanolamine (PE) headgroups in a multi-step process akin to ubiquitin conjugation, also known as ATG8ylation (Deretic & Lazarou, 2022). First, ATG8 proteins are activated by the E1-like ATG7, next they are transferred to the E2-like ATG3, finally they are brought to autophagosome membranes and conjugated to PE by the ATG5-12-16L1 complex. WIPI2 recruits the conjugation machinery to the membrane via ATG16L1 (Dooley et al., 2014; Rao et al., 2024; Strong et al., 2021). ATG8ylation drives the growth of the autophagosomes, helps to recruit cargo to them, and aids in final closure and fusion with the lysosomes

(Nguyen et al., 2016; Padman et al., 2019). New lipids are delivered to the growing phagophore from the ER and other sources via the bridge-like ATG2 protein family (Valverde et al., 2019). ATG2 connects these membrane sources to resident ATG9A proteins embedded within the phagophore, which scrambles the lipids across both membranes (van Vliet et al., 2022).

After engulfment of target material, the phagophore closes. The molecular basis of this process is not well characterized, however recent work implicates the ESCRT-III machinery and ATG9A as important players in this process (Javed et al., 2025; Takahashi et al., 2018). Finally, the closed autophagosome is fused with the lysosome. This process is driven by SNARE proteins, including STX17 and VAMP8, which fuse the disparate membranes together (Itakura et al., 2012; Jian et al., 2024). Catabolic enzymes in the lysosome, activated by low pH, degrade the membranes, proteins, and other structures within into their constitutive components.

An overview of these proteins and their role is detailed in Figure 1.2.

1.4 Selective autophagy

While the process of autophagy was first detected over 80 years ago, it was initially understood as a general, non-selective process, engulfing cytoplasmic milieu seemingly at random. Recent exploration in the field has revamped this conception, uncovering that intricate mechanisms exist to recognize and dispatch specific cargo to the autophagosome, known as selective autophagy (Vargas et al., 2023). Starvation, the best example of nonselective autophagy, has been shown to be regulated by the incorporation of many selective cargos (Hickey et al., 2023). It may be understood that, especially for membrane bound organelles, a cascade of selective molecular processes are required to excise pieces of organelles from their networks in order to sequester them in an autophagosome. In yeast, the ortholog of FIP200, ATG11, drives selective autophagy of mitochondria, peroxisomes, and parts of the nucleus (Suzuki, 2013).

1.5 Mitophagy

As we will discuss extensively in Chapter 2, the best studied form of selective autophagy in mammalian cells is mitophagy, the selective autophagy of mitochondria. Mitophagy can be driven by a series of orthogonal pathways which include the PINK1/Parkin pathway, BNIP3/NIX, and FUNDC1 (Li et al., 2021; Liu et al., 2012; Pickrell & Youle, 2015). Mitochondrial damage induces the stabilization of PINK1 protein, initiating the recruitment of Parkin (Figure 1.3)(D. P. Narendra et al., 2010). Parkin is an E3 ligase that deposits k63 linked-Ub chains onto proteins of mitochondrial outer membrane (OMM) (Kane et al., 2014). Of these proteins, the voltage-dependent anion channel (VDAC) and mitofusins (MFN) are robustly ubiquitinated (Ordureau et al., 2014). VDAC exists as three isoforms (VDAC1,2,3), which form the most ubiquitous protein at the OMM. VDAC is large channel protein that enables the passage of metabolites including ATP/NADH as well as ions K^+ , Cl^- , Ca^{2+} (Messina et al., 2012). The biophysical basis of VDAC's roles and cellular function will be discussed in Chapter 4. Conflicting reports suggest either a critical role of VDAC or non-essential role in PINK1/Parkin mitophagy (Geisler et al., 2010; D. Narendra et al., 2010). Recently, structural analysis has found that VDAC2 forms a complex with the mitochondrial protein import machinery, TOM complex, that enables stabilized PINK1 to dimerize and trans-autophosphorylate (Callegari et al., 2025). Ub chains on the MOM proteins recruit autophagy adaptor proteins including NDP52, OPTN, p62, NBR1, and TAX1BP1 (Lazarou et al., 2015). The adaptors bridge the substrate to the autophagosome machinery by directly recruiting FIP200 or other machinery to the cargo site (Nguyen et al., 2023; Vargas et al., 2019). The BNIP3/NIX pathway is thought to be regulated, mostly, transcriptionally in response to developmental signals, hypoxia, or other stresses (Li et al., 2021; Rosencrans et al., 2020; Sandoval et al., 2008). NIX induces mitophagy by directly recruiting WIPI2 (Bunker et al., 2023).

1.6 Autophagy in disease

Given the long lifespan of individual neurons, these cells rely on autophagy as a means of maintaining cellular function overtime. Indeed, multiple mutations in autophagy and lysosomal function are directly linked to neurodegenerative and neurodevelopmental disease (Nixon, 2013). A case study of a mutation in the gene coding for ATG7, a core protein

necessary for multiple steps in autophagy, demonstrated that loss of autophagy leads to Spinocerebellar ataxia (Collier et al., 2021). Mutations in proteins coding for autophagy receptors, such as the protein Optineurin (OPTN), as well as the autophagy related kinase TBK1 are known to cause ALS (Harding et al., 2021; Maruyama et al., 2010). The case for autophagic impairment in Alzheimer's diseases is more tenuous. Mutations that directly cause early onset Alzheimer's disease such as the Amyloid precursor protein (APP), and presenilin (PSE1 and 2) may alter endo-lysosomal function and therefore impair the later stages of autophagy (Lee et al., 2010). Consistent between many of these neurodegenerative diseases is the presence of insoluble protein aggregates found in the patients affected brain tissue. These aggregates are often ubiquitinated, but appear resistant to degradation by the proteasome (Lowe et al., 1993). The occurrence of these aggregates may therefore represent impairments of autophagy to clear them, identifying a potential therapeutic avenue for rectifying the disease state.

1.7 Mitophagy in Parkinson's disease

The role of autophagic impairments In Parkinson's disease is more clearly delineated. Two familial mutations that cause early-onset Parkinson's disease, PINK1(PARK6) and Parkin(PARK2) specifically prevent mitophagy upon mitochondrial damage (Pickrell & Youle, 2015). In patients, mutant for PINK1 or Parkin, unmitigated damage to mitochondria leads to the degeneration of vulnerable neurons within the substantia nigra. Similarly, toxins that destroy mitochondrial function including 1-methyl-4- phenyl-1,2,3,6-tetrahydropyridine (MPTP), lead to Parkinsonism (Langston, 2017). Mitochondrial damage is also characteristic of sporadic PD patients (Schapira et al., 1989). Mitochondrial damage results not only in reduced metabolic function, but release of cytotoxic factors into the cytoplasm. Damaged mitochondria release Cytochrome C, which induces programmed apoptosis(Erekat, 2018). Mitochondrial DNA is also released into the cytosol which initiates a pro-inflammatory cascade mediated by the cGAS-STING pathway (Sliter et al., 2018). Both intrinsic apoptosis and inflammation may contribute to neuronal death and PD progression (Tresse et al., 2023). Enhancing mitophagy in these patients may hold therapeutic value for delaying the onset of PD (Henrich et al., 2023). At the time of writing this proposal there are no clinically approved

drugs that can directly induce mitophagy, however there are at least two drugs ABBV1088 and MTX652 targeting the PINK1/Parkin pathway in clinical trials (Antico et al., 2025). As we will see in Chapter 2, the action of these compounds is unlikely to alleviate PD. These findings highlight the need to develop mitophagy and autophagy inducing compounds based on other strategies.

1.8 Summary

Autophagy and mitophagy represent meticulously controlled cellular processes with critical importance in disease pathogenesis. Understanding the cues and molecular machines that orchestrate these processes offers greater understanding into basic cell biology and disease mechanisms. Detailed mechanistic understanding of both pharmacologic inducers of these processes and endogenous regulators offers the possibility to develop treatments targeting neurodegenerative disease. Building on this overarching theme, this thesis delves into the detailed mechanisms of both compounds and proteins regulating mitophagy.

In Chapter 2 of this thesis, I investigate the mechanism of action of PINK1/Parkin activators MTK458, FB231, and MTX115325. Understanding the mechanism and physiological impact of clinical stage compounds is critical to assessing their potential efficacy. Using label free proteomics, I aimed to identify marker of mitophagy induction and potential off-targets, that could impact clinical use. I identify the induction of the integrated stress response by these compounds, leading to the discovery that the putative PINK1/Parkin activators are weak mitochondrial toxins. This finding has important clinical implications for these compounds, as well as future campaigns for PINK1/Parkin modulating compounds.

In Chapter 3 of this thesis, I describe a novel negative cellular regulator of mitophagy, TNIP1. TNIP1 was found to be recruited and degraded by the autophagosome. Despite having a similar structure to classical autophagy receptor protein OPTN, it was not understood what role TNIP1 played in autophagy, if any. We show that TNIP1 expression suppresses PINK1/Parkin mitophagy, but not general autophagy. I find that TNIP1 binds a series of autophagy proteins including FIP200 and the GABARAP family of proteins. We

conclude that TNIP1 inhibits mitophagy by out-competing mitochondria for both receptor and autophagy initiation complex binding.

In Chapter 4 of this thesis, I investigate the biophysical basis of the unique function of isoform VDAC2. Using single-channel electrophysiology, I discover dynamic substates of VDAC2 with different ion channel properties. I show that these substates differentially interact with alpha-synuclein, a PD associated protein and potent regulator of VDAC permeability. I find that critical structural factors such as cysteine residues and an extended n-terminus modify channel substate behavior and, thus its interaction with cytosolic regulators. These findings explain how VDAC2 can modify its structure to regulate distinct binding partners.

In Chapter 5 of this thesis, I describe the unique role of each VDAC isoform in mitochondrial function. Using CRISPR mediated KO of each VDAC isoform, I utilize label-free proteomics to identify pathways differentially altered by loss of each isoform. Contrary to expectation, I find that VDAC3 KO, the least expressed isoform, has the strongest inhibition of mitochondrial function. I confirm this effect in orthogonal metabolic assays. These findings uncover a novel role for VDAC3 in mitochondrial function.

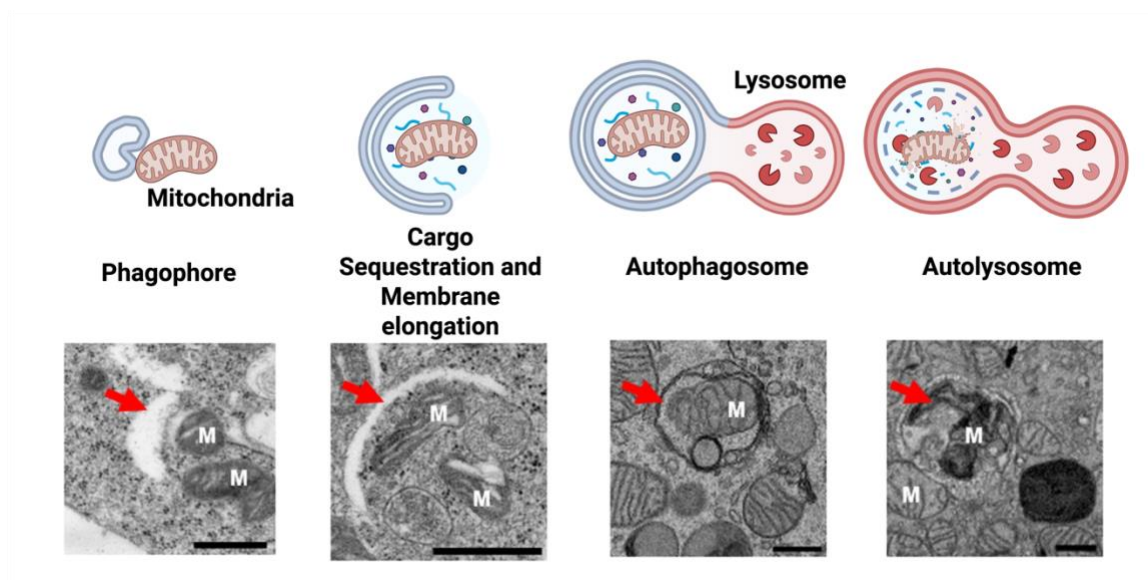


Figure 1.1: The major steps of Macroautophagy. Cartoon adapted from electron micrographs from Jung et al. (2019). Autophagy begins as a phagophore structure characterized by protein-sparse lipid vesicle. Autophagosomes form in some cases in proximity to cargo such as the mitochondria (structures labeled with a white M). The phagophore expands to a cup-like structure, apparent as a crescent in 2D micrographs. The phagophore closes to create a double-membrane structure filled with cellular material such as mitochondria. Upon lysosome fusion, digestion of enclosed organelles can be observed.

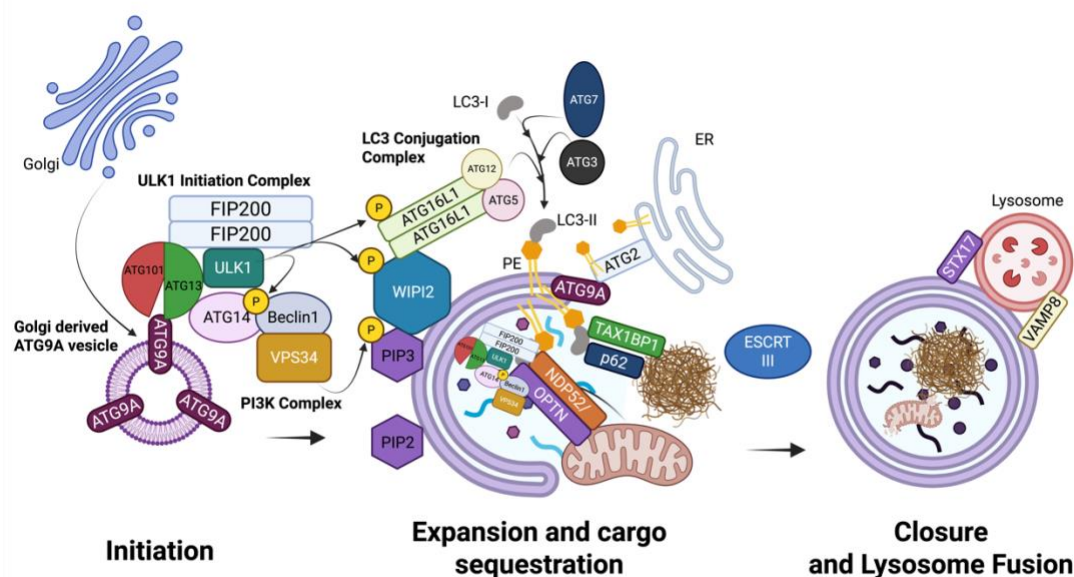


Figure 1.2: Major Molecular Machinery of Macroautophagy. Cartoon representation of a subset of the major complexes involved in autophagy. Vesicles budding from the Golgi containing ATG9A form the initial seed for the autophagosome. The ULK1 initiation complex, scaffolded by FIP200, binds directly to ATG9A via ATG13/101. The PI3K complex is recruited via ATG13 and phosphorylated by ULK1. ULK1 phosphorylates other downstream components. The PI3KC phosphorylates PIP2 to make PIP3. This recruits WIPI2 and the ATG16L1 LC3-Lipidation Complex, which conjugates active LC3 to the growing phagosome. ATG9A-ATG2 mediate lipid transfer into the phagosome from the ER. Meanwhile, often ubiquitinated cargo such as mitochondria and aggregates are linked to the phagosome via autophagy adaptors including p62, OPTN, NDP52, and TAX1BP1 which can bind Ubiquitin (Ub), LC3 or autophagy machinery simultaneously. The phagosome is sealed by the ESCRT III machinery to form the autophagosome. The autophagosome is fused to lysosomes by a series of machinery that includes STX17 and VAMP8.

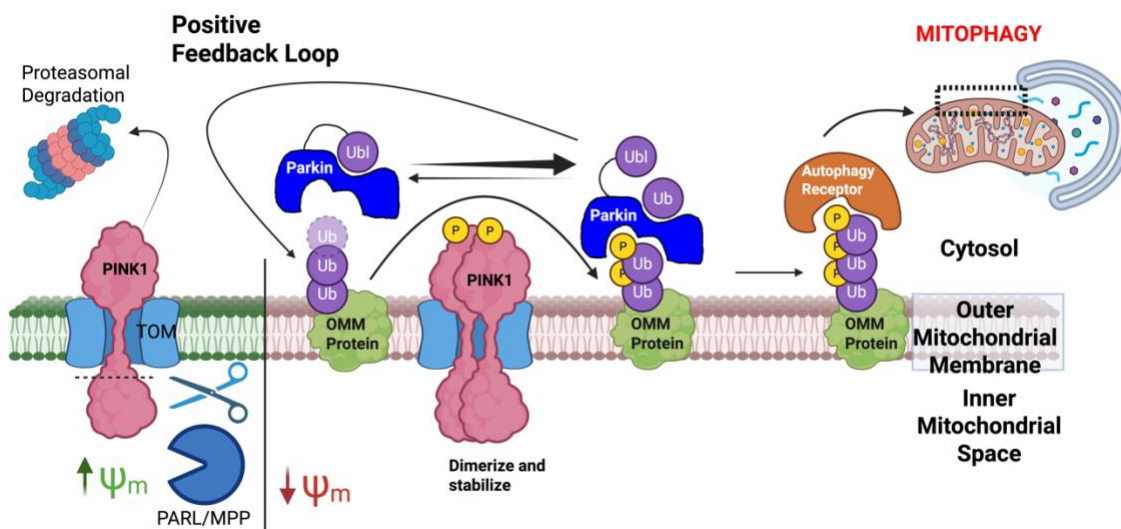


Figure 1.3: The PINK1/Parkin mitophagy pathway. Cartoon representation of the major proteins and processes driving the PINK1/Parkin mitophagy. PINK1 is continuously translated and imported into functioning mitochondria with high membrane potential (Ψ_m). Imported PINK1 is cleaved by PARL and MPP, which exposes a potent n-degron, leading to PINK1's degradation at the proteasome. In depolarized or damaged mitochondria, PINK1 is stabilized in the TOM channel where it dimerizes and autophosphorylates. PINK1 also phosphorylates Ubiquitin (pUb) on OMM proteins. pUb recruits and activates the E3-ligase Parkin enabling it to deposit further Ub chains onto OMM proteins. Phosphorylation of the Ub drives a positive feed-forward loop that decorates the mitochondria in Ub. Ub recruits autophagy receptors to drive the engulfment of the mitochondria by the autophagosome.

Works cited

- Antico, O., Thompson, P. W., Hertz, N. T., Muqit, M. M. K., & Parton, L. E. (2025). Targeting mitophagy in neurodegenerative diseases. *Nat Rev Drug Discov*, 24(4), 276-299. <https://doi.org/10.1038/s41573-024-01105-0>
- Bunker, E. N., Le Guerroue, F., Wang, C., Strub, M. P., Werner, A., Tjandra, N., & Youle, R. J. (2023). Nix interacts with WIPI2 to induce mitophagy. *EMBO J*, 42(22), e113491. <https://doi.org/10.15252/embj.2023113491>
- Callegari, S., Kirk, N. S., Gan, Z. Y., Dite, T., Cobbold, S. A., Leis, A., Dagley, L. F., Glukhova, A., & Komander, D. (2025). Structure of human PINK1 at a mitochondrial TOM-VDAC array. *Science*, 388(6744), 303-310. <https://doi.org/10.1126/science.adu6445>
- Collier, J. J., Guissart, C., Olahova, M., Sasorith, S., Piron-Prunier, F., Suomi, F., Zhang, D., Martinez-Lopez, N., Leboucq, N., Bahr, A., Azzarello-Burri, S., Reich, S., Schols, L., Polvikoski, T. M., Meyer, P., Larrieu, L., Schaefer, A. M., Alsaif, H. S., Alyamani, S., . . . Taylor, R. W. (2021). Developmental Consequences of Defective ATG7-Mediated Autophagy in Humans. *N Engl J Med*, 384(25), 2406-2417. <https://doi.org/10.1056/NEJMoa1915722>
- Deretic, V., & Lazarou, M. (2022). A guide to membrane atg8ylation and autophagy with reflections on immunity. *J Cell Biol*, 221(7). <https://doi.org/10.1083/jcb.202203083>
- Dikic, I., & Elazar, Z. (2018). Mechanism and medical implications of mammalian autophagy. *Nat Rev Mol Cell Biol*, 19(6), 349-364. <https://doi.org/10.1038/s41580-018-0003-4>
- Dooley, H. C., Razi, M., Polson, H. E., Girardin, S. E., Wilson, M. I., & Tooze, S. A. (2014). WIPI2 links LC3 conjugation with PI3P, autophagosome formation, and pathogen clearance by recruiting Atg12-5-16L1. *Mol Cell*, 55(2), 238-252. <https://doi.org/10.1016/j.molcel.2014.05.021>
- Dorrbaum, A. R., Kochen, L., Langer, J. D., & Schuman, E. M. (2018). Local and global influences on protein turnover in neurons and glia. *Elife*, 7. <https://doi.org/10.7554/eLife.34202>
- Erekat, N. S. (2018). Apoptosis and its Role in Parkinson's Disease. In T. B. Stoker & J. C. Greenland (Eds.), *Parkinson's Disease: Pathogenesis and Clinical Aspects*. <https://doi.org/10.15586/codonpublications.parkinsonsdisease.2018.ch4>
- Geisler, S., Holmstrom, K. M., Skujat, D., Fiesel, F. C., Rothfuss, O. C., Kahle, P. J., & Springer, W. (2010). PINK1/Parkin-mediated mitophagy is dependent on VDAC1 and p62/SQSTM1. *Nat Cell Biol*, 12(2), 119-131. <https://doi.org/10.1038/ncb2012>
- Harding, O., Evans, C. S., Ye, J., Cheung, J., Maniatis, T., & Holzbaur, E. L. F. (2021). ALS- and FTD-associated missense mutations in TBK1 differentially disrupt mitophagy. *Proc Natl Acad Sci U S A*, 118(24). <https://doi.org/10.1073/pnas.2025053118>
- Henrich, M. T., Oertel, W. H., Surmeier, D. J., & Geibl, F. F. (2023). Mitochondrial dysfunction in Parkinson's disease - a key disease hallmark with therapeutic

- potential. *Mol Neurodegener*, 18(1), 83. <https://doi.org/10.1186/s13024-023-00676-7>
- Hickey, K. L., Swarup, S., Smith, I. R., Paoli, J. C., Miguel Whelan, E., Paulo, J. A., & Harper, J. W. (2023). Proteome census upon nutrient stress reveals Golgiphagy membrane receptors. *Nature*, 623(7985), 167-174. <https://doi.org/10.1038/s41586-023-06657-6>
- Hosokawa, N., Hara, T., Kaizuka, T., Kishi, C., Takamura, A., Miura, Y., Iemura, S., Natsume, T., Takehana, K., Yamada, N., Guan, J. L., Oshiro, N., & Mizushima, N. (2009). Nutrient-dependent mTORC1 association with the ULK1-Atg13-FIP200 complex required for autophagy. *Mol Biol Cell*, 20(7), 1981-1991. <https://doi.org/10.1091/mbc.e08-12-1248>
- Itakura, E., Kishi-Itakura, C., & Mizushima, N. (2012). The hairpin-type tail-anchored SNARE syntaxin 17 targets to autophagosomes for fusion with endosomes/lysosomes. *Cell*, 151(6), 1256-1269. <https://doi.org/10.1016/j.cell.2012.11.001>
- Jaber, N., & Zong, W. X. (2013). Class III PI3K Vps34: essential roles in autophagy, endocytosis, and heart and liver function. *Ann N Y Acad Sci*, 1280, 48-51. <https://doi.org/10.1111/nyas.12026>
- Javed, R., Mari, M., Trosdal, E., Duque, T., Paddar, M. A., Allers, L., Mudd, M. H., Claude-Taupin, A., Akepati, P. R., Hendrix, E., He, Y., Salemi, M., Phinney, B., Uchiyama, Y., Reggiori, F., & Deretic, V. (2025). ATG9A facilitates the closure of mammalian autophagosomes. *J Cell Biol*, 224(2). <https://doi.org/10.1083/jcb.202404047>
- Jian, F., Wang, S., Tian, R., Wang, Y., Li, C., Li, Y., Wang, S., Fang, C., Ma, C., & Rong, Y. (2024). The STX17-SNAP47-VAMP7/VAMP8 complex is the default SNARE complex mediating autophagosome-lysosome fusion. *Cell Res*, 34(2), 151-168. <https://doi.org/10.1038/s41422-023-00916-x>
- Jung, M., Choi, H., & Mun, J. Y. (2019). The autophagy research in electron microscopy. *Appl Microsc*, 49(1), 11. <https://doi.org/10.1186/s42649-019-0012-6>
- Kabeya, Y., Mizushima, N., Ueno, T., Yamamoto, A., Kirisako, T., Noda, T., Kominami, E., Ohsumi, Y., & Yoshimori, T. (2000). LC3, a mammalian homologue of yeast Apg8p, is localized in autophagosome membranes after processing. *EMBO J*, 19(21), 5720-5728. <https://doi.org/10.1093/emboj/19.21.5720>
- Kane, L. A., Lazarou, M., Fogel, A. I., Li, Y., Yamano, K., Sarraf, S. A., Banerjee, S., & Youle, R. J. (2014). PINK1 phosphorylates ubiquitin to activate Parkin E3 ubiquitin ligase activity. *J Cell Biol*, 205(2), 143-153. <https://doi.org/10.1083/jcb.201402104>
- Klionsky, D. J., Petroni, G., Amaravadi, R. K., Baehrecke, E. H., Ballabio, A., Boya, P., Bravo-San Pedro, J. M., Cadwell, K., Cecconi, F., Choi, A. M. K., Choi, M. E., Chu, C. T., Codogno, P., Colombo, M. I., Cuervo, A. M., Deretic, V., Dikic, I., Elazar, Z., Eskelinen, E. L., . . . Pietrocola, F. (2021). Autophagy in major human diseases. *EMBO J*, 40(19), e108863. <https://doi.org/10.15252/emboj.2021108863>
- Lazarou, M., Sliter, D. A., Kane, L. A., Sarraf, S. A., Wang, C., Burman, J. L., Sideris, D. P., Fogel, A. I., & Youle, R. J. (2015). The ubiquitin kinase PINK1 recruits

- autophagy receptors to induce mitophagy. *Nature*, 524(7565), 309-314. <https://doi.org/10.1038/nature14893>
- Lee, J. H., Yu, W. H., Kumar, A., Lee, S., Mohan, P. S., Peterhoff, C. M., Wolfe, D. M., Martinez-Vicente, M., Massey, A. C., Sovak, G., Uchiyama, Y., Westaway, D., Cuervo, A. M., & Nixon, R. A. (2010). Lysosomal proteolysis and autophagy require presenilin 1 and are disrupted by Alzheimer-related PS1 mutations. *Cell*, 141(7), 1146-1158. <https://doi.org/10.1016/j.cell.2010.05.008>
- Li, Y., Zheng, W., Lu, Y., Zheng, Y., Pan, L., Wu, X., Yuan, Y., Shen, Z., Ma, S., Zhang, X., Wu, J., Chen, Z., & Zhang, X. (2021). BNIP3L/NIX-mediated mitophagy: molecular mechanisms and implications for human disease. *Cell Death Dis*, 13(1), 14. <https://doi.org/10.1038/s41419-021-04469-y>
- Liu, L., Feng, D., Chen, G., Chen, M., Zheng, Q., Song, P., Ma, Q., Zhu, C., Wang, R., Qi, W., Huang, L., Xue, P., Li, B., Wang, X., Jin, H., Wang, J., Yang, F., Liu, P., Zhu, Y., . . . Chen, Q. (2012). Mitochondrial outer-membrane protein FUNDC1 mediates hypoxia-induced mitophagy in mammalian cells. *Nat Cell Biol*, 14(2), 177-185. <https://doi.org/10.1038/ncb2422>
- Lowe, J., Mayer, R. J., & Landon, M. (1993). Ubiquitin in neurodegenerative diseases. *Brain Pathol*, 3(1), 55-65. <https://doi.org/10.1111/j.1750-3639.1993.tb00726.x>
- Maruyama, H., Morino, H., Ito, H., Izumi, Y., Kato, H., Watanabe, Y., Kinoshita, Y., Kamada, M., Nodera, H., Suzuki, H., Komure, O., Matsuura, S., Kobatake, K., Morimoto, N., Abe, K., Suzuki, N., Aoki, M., Kawata, A., Hirai, T., . . . Kawakami, H. (2010). Mutations of optineurin in amyotrophic lateral sclerosis. *Nature*, 465(7295), 223-226. <https://doi.org/10.1038/nature08971>
- Messina, A., Reina, S., Guarino, F., & De Pinto, V. (2012). VDAC isoforms in mammals. *Biochim Biophys Acta*, 1818(6), 1466-1476. <https://doi.org/10.1016/j.bbamem.2011.10.005>
- Mizushima, N., & Komatsu, M. (2011). Autophagy: renovation of cells and tissues. *Cell*, 147(4), 728-741. <https://doi.org/10.1016/j.cell.2011.10.026>
- Mizushima, N., Yoshimori, T., & Ohsumi, Y. (2011). The role of Atg proteins in autophagosome formation. *Annu Rev Cell Dev Biol*, 27, 107-132. <https://doi.org/10.1146/annurev-cellbio-092910-154005>
- Nakamura, S., & Yoshimori, T. (2018). Autophagy and Longevity. *Mol Cells*, 41(1), 65-72. <https://doi.org/10.14348/molcells.2018.2333>
- Narendra, D., Kane, L. A., Hauser, D. N., Fearnley, I. M., & Youle, R. J. (2010). p62/SQSTM1 is required for Parkin-induced mitochondrial clustering but not mitophagy; VDAC1 is dispensable for both. *Autophagy*, 6(8), 1090-1106. <https://doi.org/10.4161/auto.6.8.13426>
- Narendra, D. P., Jin, S. M., Tanaka, A., Suen, D. F., Gautier, C. A., Shen, J., Cookson, M. R., & Youle, R. J. (2010). PINK1 is selectively stabilized on impaired mitochondria to activate Parkin. *PLoS Biol*, 8(1), e1000298. <https://doi.org/10.1371/journal.pbio.1000298>
- Nguyen, T. N., Padman, B. S., Usher, J., Oorschot, V., Ramm, G., & Lazarou, M. (2016). Atg8 family LC3/GABARAP proteins are crucial for autophagosome-lysosome fusion but not autophagosome formation during PINK1/Parkin mitophagy and starvation. *J Cell Biol*, 215(6), 857-874. <https://doi.org/10.1083/jcb.201607039>

- Nguyen, T. N., Sawa-Makarska, J., Khuu, G., Lam, W. K., Adriaenssens, E., Fracchiolla, D., Shoebridge, S., Bernklau, D., Padman, B. S., Skulsuppaisarn, M., Lindblom, R. S. J., Martens, S., & Lazarou, M. (2023). Unconventional initiation of PINK1/Parkin mitophagy by Optineurin. *Mol Cell*, 83(10), 1693-1709 e1699. <https://doi.org/10.1016/j.molcel.2023.04.021>
- Nixon, R. A. (2013). The role of autophagy in neurodegenerative disease. *Nat Med*, 19(8), 983-997. <https://doi.org/10.1038/nm.3232>
- Ohsumi, Y. (2014). Historical landmarks of autophagy research. *Cell Res*, 24(1), 9-23. <https://doi.org/10.1038/cr.2013.169>
- Olivas, T. J., Wu, Y., Yu, S., Luan, L., Choi, P., Guinn, E. D., Nag, S., De Camilli, P. V., Gupta, K., & Melia, T. J. (2023). ATG9 vesicles comprise the seed membrane of mammalian autophagosomes. *J Cell Biol*, 222(7). <https://doi.org/10.1083/jcb.202208088>
- Ordureau, A., Sarraf, S. A., Duda, D. M., Heo, J. M., Jedrychowski, M. P., Sviderskiy, V. O., Olszewski, J. L., Koerber, J. T., Xie, T., Beausoleil, S. A., Wells, J. A., Gygi, S. P., Schulman, B. A., & Harper, J. W. (2014). Quantitative proteomics reveal a feedforward mechanism for mitochondrial PARKIN translocation and ubiquitin chain synthesis. *Mol Cell*, 56(3), 360-375. <https://doi.org/10.1016/j.molcel.2014.09.007>
- Padman, B. S., Nguyen, T. N., Uoselis, L., Skulsuppaisarn, M., Nguyen, L. K., & Lazarou, M. (2019). LC3/GABARAPs drive ubiquitin-independent recruitment of Optineurin and NDP52 to amplify mitophagy. *Nat Commun*, 10(1), 408. <https://doi.org/10.1038/s41467-019-08335-6>
- Pickrell, A. M., & Youle, R. J. (2015). The roles of PINK1, parkin, and mitochondrial fidelity in Parkinson's disease. *Neuron*, 85(2), 257-273. <https://doi.org/10.1016/j.neuron.2014.12.007>
- Rao, S., Skulsuppaisarn, M., Strong, L. M., Ren, X., Lazarou, M., Hurley, J. H., & Hummer, G. (2024). Three-step docking by WIPI2, ATG16L1, and ATG3 delivers LC3 to the phagophore. *Sci Adv*, 10(6), eadj8027. <https://doi.org/10.1126/sciadv.adj8027>
- Ren, X., Nguyen, T. N., Lam, W. K., Buffalo, C. Z., Lazarou, M., Yokom, A. L., & Hurley, J. H. (2023). Structural basis for ATG9A recruitment to the ULK1 complex in mitophagy initiation. *Sci Adv*, 9(7), eadg2997. <https://doi.org/10.1126/sciadv.adg2997>
- Rosencrans, W. M., Walsh, Z. H., Huerbi, N., Blum, A., Belew, M., Liu, C., Chernak, B., Brauer, P. R., Trazo, A., Olson, A., & Hagos, E. (2020). Cells deficient for Kruppel-like factor 4 exhibit mitochondrial dysfunction and impaired mitophagy. *Eur J Cell Biol*, 99(1), 151061. <https://doi.org/10.1016/j.ejcb.2019.151061>
- Sandoval, H., Thiagarajan, P., Dasgupta, S. K., Schumacher, A., Prchal, J. T., Chen, M., & Wang, J. (2008). Essential role for Nix in autophagic maturation of erythroid cells. *Nature*, 454(7201), 232-235. <https://doi.org/10.1038/nature07006>
- Sliter, D. A., Martinez, J., Hao, L., Chen, X., Sun, N., Fischer, T. D., Burman, J. L., Li, Y., Zhang, Z., Narendra, D. P., Cai, H., Borsche, M., Klein, C., & Youle, R. J. (2018). Parkin and PINK1 mitigate STING-induced inflammation. *Nature*, 561(7722), 258-262. <https://doi.org/10.1038/s41586-018-0448-9>

- Strong, L. M., Chang, C., Riley, J. F., Boecker, C. A., Flower, T. G., Buffalo, C. Z., Ren, X., Stavoe, A. K., Holzbaur, E. L., & Hurley, J. H. (2021). Structural basis for membrane recruitment of ATG16L1 by WIPI2 in autophagy. *Elife*, 10. <https://doi.org/10.7554/eLife.70372>
- Suzuki, K. (2013). Selective autophagy in budding yeast. *Cell Death Differ*, 20(1), 43-48. <https://doi.org/10.1038/cdd.2012.73>
- Takahashi, Y., He, H., Tang, Z., Hattori, T., Liu, Y., Young, M. M., Serfass, J. M., Chen, L., Gebru, M., Chen, C., Wills, C. A., Atkinson, J. M., Chen, H., Abraham, T., & Wang, H. G. (2018). An autophagy assay reveals the ESCRT-III component CHMP2A as a regulator of phagophore closure. *Nat Commun*, 9(1), 2855. <https://doi.org/10.1038/s41467-018-05254-w>
- Tresse, E., Marturia-Navarro, J., Sew, W. Q. G., Cisquella-Serra, M., Jaber, E., Riera-Ponsati, L., Fauerby, N., Hu, E., Kretz, O., Aznar, S., & Issazadeh-Navikas, S. (2023). Mitochondrial DNA damage triggers spread of Parkinson's disease-like pathology. *Mol Psychiatry*, 28(11), 4902-4914. <https://doi.org/10.1038/s41380-023-02251-4>
- Valverde, D. P., Yu, S., Boggavarapu, V., Kumar, N., Lees, J. A., Walz, T., Reinisch, K. M., & Melia, T. J. (2019). ATG2 transports lipids to promote autophagosome biogenesis. *J Cell Biol*, 218(6), 1787-1798. <https://doi.org/10.1083/jcb.201811139>
- van Vliet, A. R., Chiduzza, G. N., Maslen, S. L., Pye, V. E., Joshi, D., De Tito, S., Jefferies, H. B. J., Christodoulou, E., Roustan, C., Punch, E., Hervas, J. H., O'Reilly, N., Skehel, J. M., Cherepanov, P., & Tooze, S. A. (2022). ATG9A and ATG2A form a heteromeric complex essential for autophagosome formation. *Mol Cell*, 82(22), 4324-4339 e4328. <https://doi.org/10.1016/j.molcel.2022.10.017>
- Vargas, J. N. S., Hamasaki, M., Kawabata, T., Youle, R. J., & Yoshimori, T. (2023). The mechanisms and roles of selective autophagy in mammals. *Nat Rev Mol Cell Biol*, 24(3), 167-185. <https://doi.org/10.1038/s41580-022-00542-2>
- Vargas, J. N. S., Wang, C., Bunker, E., Hao, L., Maric, D., Schiavo, G., Randow, F., & Youle, R. J. (2019). Spatiotemporal Control of ULK1 Activation by NDP52 and TBK1 during Selective Autophagy. *Mol Cell*, 74(2), 347-362 e346. <https://doi.org/10.1016/j.molcel.2019.02.010>
- Wold, M. S., Lim, J., Lachance, V., Deng, Z., & Yue, Z. (2016). ULK1-mediated phosphorylation of ATG14 promotes autophagy and is impaired in Huntington's disease models. *Mol Neurodegener*, 11(1), 76. <https://doi.org/10.1186/s13024-016-0141-0>
- Zachari, M., & Ganley, I. G. (2017). The mammalian ULK1 complex and autophagy initiation. *Essays Biochem*, 61(6), 585-596. <https://doi.org/10.1042/EBC20170021>

*Chapter 2****PUTATIVE PINK1/PARKIN ACTIVATORS LOWER THE THRESHOLD FOR MITOPHAGY BY SENSITIZING CELLS TO MITOCHONDRIAL STRESS***

The following chapter is adapted from Rosencrans and Lee et al., 2025 and modified according to the Caltech thesis format.

William M. Rosencrans*, Ryan W. Lee*, Logan McGraw, Ian Horsburgh, Ting-Yu Wang, Baiyi Quan, Diana Huynh, Jennifer A. Johnston, David C. Chan, Tsui-Fen Chou (2023). Putative PINK1/Parkin Activators Lower the Threshold for Mitophagy by Sensitizing Cells to Mitochondrial Stress, in press Science Advances.

* denotes equal contribution

2.1 Abstract

The PINK1/Parkin pathway is responsible for targeting damaged mitochondria for degradation via mitophagy. Because genetic evidence strongly implicates impaired mitophagy in Parkinson's disease, pharmacologic enhancement of mitophagy represents a promising disease-modifying strategy. Here, we characterize two pharmacological mitophagy activators: a new Parkin activator, FB231, described here and the reported PINK1 activator MTK458. We demonstrate that both compounds indeed lower the threshold for mitochondrial stressors to induce PINK1/Parkin-mediated mitophagy. Using global proteomics, however, we find that both FB231 and MTK458 exert mild mitochondrial stress that leads to cleavage of OPA1 and activation of the integrated stress response. These effects are PINK1/Parkin-independent and therefore represent off-target effects. Furthermore, we show that FB231 and MTK458 impair mitochondria by distinct mechanisms and can synergize to reduce mitochondrial function and cell viability. We provide a model that rationalizes the properties of these two mitophagy activators, whereby normally weak or "silent" mitochondrial toxins can potentiate the ability of other mitochondrial stressors to induce PINK1/Parkin-mediated mitophagy.

2.2 Introduction

Parkinson's disease (PD) is the second most common neurodegenerative disease. Affecting over 10 million people worldwide, there exists no treatment that corrects the underlying mechanism (Ben-Shlomo et al., 2024). The disease is predominantly characterized by loss of neurons in the dopamine-producing substantia nigra (Dickson, 2012). PD is characterized at the molecular level by accumulation of protein aggregates known as Lewy Bodies as well as mitochondrial dysfunction (Dickson, 2012). Multiple lines of evidence implicate mitochondrial defects in the initial pathogenesis of the disease. (Moon et al., 2013) Mitochondrial toxins such as rotenone, paraquat, and MPTP are associated with development of PD. (Tanner et al., 2011) Moreover, post-mortem samples of idiopathic PD patients demonstrate defects in mitochondrial function. (Flones et al., 2024)

The strongest tie between mitochondrial dysfunction and PD is genetic evidence demonstrating that the loss of mitochondrial quality control pathways cause familial forms of PD. Mutations in the Parkin and PINK1 proteins are the most common form of autosomal recessive PD. (Pickrell & Youle, 2015) Parkin is an E3 ligase that functions together with the ubiquitin kinase PINK1 to flag damaged mitochondria for removal via a selective form of autophagy known as mitophagy. Under healthy conditions, PINK1 is continually degraded and kept at very low levels. PINK1 is translated in the cytosol and imported into the mitochondria via the translocase of the outer mitochondrial membrane (TOM) and the translocase of the inner membrane (TIM). It is then cleaved by the proteases MPP and PARL and released back into the cytosol. (Sekine, 2020) Cleavage reveals a potent n-degron, resulting in rapid proteasomal degradation of PINK1. (Yamano & Youle, 2013) In conditions of mitochondrial stress, including mitochondrial membrane potential loss or protein aggregation, PINK1 fails to import and instead remains stabilized on the TOM complex leading to its accumulation, dimerization, and activation. (Burman et al., 2017; Jin et al., 2010; Narendra et al., 2010; Raimi et al., 2024; Rasool et al., 2022) Active PINK1 phosphorylates freely monomeric as well as outer mitochondrial membrane (OMM) protein conjugated ubiquitin on Serine 65 (pUb). (Kazlauskaite et al., 2014; Koyano et al., 2014) Accumulation of the unique pUb signal recruits cytosolic Parkin to the mitochondria where

it is also phosphorylated by PINK1.(Kazlauskaite et al., 2015; Koyano et al., 2014; Narendra et al., 2008) Binding of the pUb partially activates Parkin from its auto-inhibited state by allosterically releasing the inhibiting Ubiquitin-like domain (Ubl) from RING1.(Gladkova et al., 2018; Sauve et al., 2015; Trempe et al., 2013; Wauer & Komander, 2013; Wauer et al., 2015) PINK1 can then phosphorylate Parkin at the Ubl, freeing Parkin's catalytic cysteine 431 to bind ubiquitin on E2-ubiquitin conjugating enzymes.(Riley et al., 2013)

Parkin generates ubiquitin chains including, notably K63-linked Ub, on the OMM, which in turn can be phosphorylated by PINK1, leading to further Parkin recruitment in a feed-forward mechanism.(Narendra et al., 2010) This process can be opposed by deubiquitinases such as USP30, which remove ubiquitin from the OMM.(Bingol et al., 2014) Accumulation of the K63-Ub chains recruits a series of autophagy adaptor proteins including NDP52 and OPTN that initiate the formation of the autophagosome at the damaged mitochondria via recruitment of the autophagy initiation complex.(Lazarou et al., 2015; Nguyen et al., 2023; Vargas et al., 2019) This feed-forward mechanism leads to a strong switch-like behavior that can rapidly clear damaged mitochondria upon PINK1 accumulation.(Ordureau et al., 2014; Waters et al., 2023)

Beyond the subset of familial PD patients with PINK1/Parkin mutations, there is evidence suggesting that the pathway may be impaired in the idiopathic PD population. Increased levels of pUb are found in the brains and plasma of PD patients, suggesting an impairment in mitophagy completion downstream of PINK1.(Chin et al., 2023; Hou et al., 2018) Moreover, mitochondrial toxins have been used as potent pharmacological models of PD for the last 30 years, since the discovery that mitochondrial toxin MPTP could directly cause Parkinsonism in humans.(Langston, 2017) Enhancement of PINK1/Parkin mitophagy represents a strategy towards improving mitochondrial quality control and enabling a disease-modifying strategy in PD.(Miller & Muqit, 2019)

Multiple small-molecule compounds have been developed with the reported ability to enhance PINK1/Parkin mitophagy.(Antico et al., 2025) These include USP30 inhibitors that have shown promise in enhancing mitophagy and protecting cells in Parkinson’s disease models.(Fang et al., 2023) A PINK1 activating compound, MTK458, was recently reported by the companies Mitokinin and Abbvie.(Chin et al., 2023) A potential derivative of MTK458, ABBV1088, is in Phase I clinical trials toward eventual treatment of PD.(Antico et al., 2025) MTK458 was shown to enhance mitophagy in contexts of mitochondrial stress, but no direct measurement of PINK1 binding has been shown. PINK1 inhibiting compounds have also been described.(Rasool et al., 2024) Parkin targeting compounds have remained hitherto unsuccessful in inducing mitophagy in WT cell models. Biogen reported a direct Parkin activating compound that showed potent in vitro Parkin activation but failed to enhance mitophagy in vivo.(Shlevkov et al., 2022) Recent work on the Biogen compounds suggests they act as “molecular glues” between Parkin and pUb and can restore activity to two rare point mutants of Parkin in cells.(Sauve et al., 2024) These results demonstrate the potential for small-molecule-based Parkin activators but highlight that potent in vitro activation does not necessarily translate to in vivo augmentation of the PINK1/Parkin pathway.

In this work, we describe the compound FB231 that enhances Parkin activity in vitro. Developing a high-throughput assay for mitophagy induction, we quantitatively compare FB231 and the recently reported PINK1 activator MTK458 and show that both compounds reduce the threshold for mitophagy induction via the PINK1/Parkin pathway across cell types. We demonstrate that these activators can be used in combination to synergistically enhance mitophagy. Using label-free proteomics and biochemistry, we show that FB231 causes activation of the integrated stress response and perturbation to iron-dependent pathways. We unexpectedly find that these compounds act as weak mitochondrial toxins that sensitize mitochondria to damage by classical mitochondrial stressors and lead to activation of the mitochondrial integrated stress response (mitoISR) and PINK1 accumulation. By limiting mitochondrial function, these compounds ultimately impair cell growth and sensitize cells to death from mitochondrial toxins. These data suggest a hitherto unknown common

pitfall for current pharmacological screens, whereby weak mitochondrial toxins can act as potent PINK1/Parkin activators.

2.3 Results

Identification of a putative Parkin activating compound through in vitro activity assays

We had previously identified small molecules capable of activating Parkin.(Regnström et al., 2013) The compound used in this study, FB231, was subsequently identified in a high throughput assay for Parkin activators based on Parkin ubiquitylation activity. In our scheme, we utilized a His₆-tagged full-length Parkin construct (FL-Parkin) and a derivatized Ubiquitin suicide probe [vinyl-sulfone modified ubiquitin (Ub-VS)] as described in Riley et al (2013).(Riley et al., 2013) Because the Ub-VS probe selectively reacts with the activated conformation to form a covalent bond, we used this assay to screen small-molecules capable of activating Parkin. Binding of the probe to Parkin was measured by a FRET readout. We utilized the sensitive Europium-Cryptate (Eu) + d2 FRET pair, by using Europium tagged anti-HA antibody that binds the Ub-VS probe and a d2-tagged anti-His₆ antibody that binds to the tagged Parkin.(Lopez-Crapez et al., 2001; Sauve et al., 2024) (Figure S2.1A).

A potent compound identified in this screen, CMPD001, had already been flagged as a potential activator of Parkin in a previous screen (compound X) and patented.(Jennifer Johnston, 2017; Regnström et al., 2013) CMPD001 has an EC₃₀ of 3.9 μ M in the UB-VS assay (Figure S2.1C) and was therefore used as an internal control for assessing the activity of subsequent compounds. We also utilized a second assay, TR-FRET, that measured Parkin autoubiquitination by the covalent attachment of Europium tagged Ub. CMPD001 showed similar potency in this autoubiquitination assay (Figure S2.1D).

We pursued derivatives of CMPD001 that could improve its pharmacokinetic properties. FB231 is a derivative of CMPD001 with two methyl substitutions at the ortho position of both benzamides (Fig. S2.1B). It showed improved drug metabolism and pharmacokinetic properties across a range of in vitro and in vivo assays, especially a longer half-life (Figure S2.1B, Table S1). FB231 had slightly less potency than CMPD001 in the UB-VS assay, and

no activity in the autoubiquitination assay (Figure S2.1D). Despite unclear activity in vitro, preliminary work in cell models suggested FB231 could accentuate PINK1/Parkin mitophagy in cells exposed to low levels of mitochondrial toxins (Jennifer Johnston, 2017). These results were similar to data reported for the clinically relevant reported PINK1 activator, MTK458 (Chin et al., 2023). Given the improved pharmacology profile, preliminary cellular activity, and potential for clinical relevance we next sought to rigorously determine if these compounds had the ability to alter mitophagy in a cellular context.

Putative Parkin and PINK1 activators reduce the threshold for mitophagy activation by antimycin/oligomycin

In the context of mitochondrial stress, the PINK1/Parkin pathway becomes activated by stabilization and retention of PINK1 at the outer mitochondrial membrane through its interaction with the TOM complex (Narendra et al., 2010). This complex can be stabilized by membrane depolarization and mitochondrial protein aggregation (Burman et al., 2017; Narendra et al., 2010). In cell culture models, membrane depolarization is readily accomplished through chemical manipulation. Ionophores including CCCP and FCCP permit protons to directly pass through the inner mitochondrial membrane. Alternatively, toxins targeting complexes of the electron transport chain are also commonly employed to activate PINK1. These include complex III inhibitor antimycin A, and complex V inhibitor oligomycin A. Although having no activity on its own, FB231 was shown to accelerate mitophagy in cells exposed to CCCP (Jennifer Johnston, 2017). The reported PINK1 activator MTK458 was screened in the presence of FCCP and oligomycin (Chin et al., 2023). MTK458 is hypothesized to stabilize the active form of PINK1, leading to enhanced mitophagy in the presence of stress (Figure 2.1A). We therefore compared FB231 to MTK458 as two compounds that sensitize cells to mitophagy in the presence of additional mitochondrial stress.

We first sought to establish a consistent regimen for testing mitophagy activating compounds. We chose to use a cocktail of equimolar oligomycin/antimycin (O/A) widely used in mitophagy studies rather than ionophores CCCP/FCCP which have been reported to

have more pleiotropic effects.(Lazarou et al., 2015; Padman et al., 2013) O/A is usually used at micromolar-level doses to maximally induce PINK1/Parkin mitophagy. Because wildtype HeLa cells are devoid of Parkin, we employed HeLa cells expressing YFP-Parkin and the mitophagy reporter mt-Keima. Mt-Keima is a mitochondrial-targeted, pH-sensitive fluorescent protein used to monitor mitophagy by distinguishing mitochondria in acidic autolysosomes from those in the neutral cytoplasm. It shifts its fluorescence excitation when exposed to different pH levels, enabling ratiometric quantification of mitophagy.(Sun et al., 2017)

We utilized high-content confocal microscopy to determine the extent of mitophagy with varying combinatorial doses of O/A with the experimental compounds MTK458 and FB231. Pan-caspase inhibitor quinolyl-valyl-O-methylaspartyl-[-2,6-difluorophenoxy]-methyl ketone (QVD) was also added to cells to prevent apoptosis. Mitolysosomes could be observed as puncta expressing high 555 nm fluorescence with low 470 nm fluorescence (Figures 2.1B and S2.2).(Lazarou et al., 2015)

In the absence of PINK1/Parkin activators, 6 hours of O/A treatment showed a threshold of 15 nM for inducing mitophagy and quickly approached saturation by 31.25 nM (Figures 2.1C and 2.1D). We monitored mitophagy with varying concentrations of O/A in the presence of either FB231 or MTK458. We found that both FB231 and MTK458 lowered the O/A threshold for induction of mitophagy (Figures 2.1C–E). However, in the absence of O/A, both compounds fail to induce mitophagy at any dose tested, up to 20 μ M. For varying doses of the activators, we calculated the half-max effective concentration (EC_{50}) of O/A, referred to hereafter as the mitophagy induction threshold (Figure 2.1F). FB231 reduced the mitophagy induction threshold of O/A from \sim 16.6 nM to 7.6 nM at 1.25 μ M of the compound, plateauing the threshold to \sim 5 nM O/A at 5 μ M FB231. Increasing doses of FB231 has no effect on the maximum mitophagy level. MTK458 was able to lower the threshold to a greater extent, dropping mitophagy induction threshold to 1.7 nM at 20 μ M.

FB231 and MTK458 potently activate the PINK1/Parkin pathway in combination with mitochondrial toxins

Next, we sought to directly compare FB231 and MTK458 at a constant dose of O/A. We chose 10 nM O/A, which failed to induce mitophagy alone, but showed robust mitophagy when co-treated with the activators. We measured YFP-Parkin cells at 6, 12, and 24 hours after treatment with O/A and pan-caspase inhibitor QVD. We found that both compounds induced mitophagy in a dose-dependent and time-dependent manner (Figures 2.2A and 2.2B). FB231 demonstrated higher potency than MTK458, with an EC₅₀ of 0.67 μ M compared to 2.7 μ M in MTK458 after 24 hours of co-treatment with 10 nM O/A (Figure 2C). Both compounds showed similar time-dependent mitophagy activation. At the highest doses tested (10 μ M and 20 μ M), FB231 appeared to deviate from the expected response and reduce mitophagy at 20 μ M. These results suggest a potential off-target effect not seen in MTK458.

To confirm that MTK458 and FB231 act through the PINK1/Parkin pathway, we tested whether both compounds would induce mitophagy in YFP-Parkin-expressing PINK1 KO cells. We found that PINK1 KO abolished MTK458/FB231-induced mitophagy, indicating that the mitophagy inducing effects of both compounds are strictly dependent on the PINK1/Parkin pathway (Figure 2.2D).

To biochemically confirm PINK1/Parkin activation, we performed a western blot for phospho-S65-Ubiquitin (pUb). pUb is a readout of both PINK1 and Parkin activation and has been reported to be a potential biomarker of Parkinson's disease. (Chin et al., 2023) We treated cells with and without 10 nM O/A and/or in combination with varying doses of FB231 and MTK458 and blotted for pUb. 10 nM O/A alone and either activator compound alone demonstrated no pUb signal at any dose tested, whereas co-treatment of O/A with FB231 or MTK458 induced robust pUb accumulation (Figure 2.2E). We also blotted for Parkin, which is both auto-ubiquitinated and degraded during the process of mitophagy. We observed increases in a higher molecular weight Parkin band and loss of Parkin signal upon MTK458/FB231 co-treatment with O/A. Additionally, we observed loss of the inner

mitochondrial complex IV subunit 4 isoform 2 (COX4I2) upon co-treatment with MTK458/FB231 and O/A in a dose-dependent manner (Figures 2.2E and 2.2F).

These blots independently confirm the activation of PINK1/Parkin as the source of mitophagy in the mt-Keima assay. Loss of COX4I2 could be partially prevented by the addition of the V-ATPase inhibitor bafilomycin A, which inhibits degradation by the lysosome in the final step of autophagy (Figures S2.3A and S2.3B). Having shown that FB231 and MTK458 could induce mitophagy in the YFP-Parkin-expressing HeLa cell line, we sought to determine if this effect was conserved in a cell line expressing endogenous levels of Parkin. SH-SY5Y is a neuroblastoma cell line often used as a Parkinson's disease model, since they display some neuronal phenotypes and can be induced to produce Tyrosine Hydrolase, a marker of dopaminergic neurons.(Xicoy et al., 2017) Importantly, they naturally express Parkin and undergo PINK1/Parkin-dependent mitophagy in response to mitochondrial damage.(Geisler et al., 2010) We first tested whether FB231 or MTK458 could induce mitophagy in these cells upon co-treatment with O/A. We measured mitophagy using mt-Keima analyzed by flow cytometry. We treated cells with 1.25 μ M FB231 or 2.5 μ M MTK458 with or without 10 nM O/A for 24 hours; we also tested 100 nM O/A as a positive mitophagy control. As in YFP-Parkin-expressing HeLa cells, FB231 alone had no effect on mitophagy. We observe a slight induction of mitophagy upon MTK458 alone, or 10 nM O/A alone, compared to DMSO treated samples (Figures 2.2G). Combination of either drug with 10 nM O/A led to a robust mitophagy signal. Next, we treated SH-SY5Y cells with 10 μ M FB231 or 5 μ M MTK458 with or without 10 nM O/A for 16 hours. Blotting for pUb we found that FB231, MTK458, and 10 nM O/A alone had no signal, whereas combination of O/A with either FB231 or MTK458 resulted in a strong pUb signal as well as loss of the inner mitochondrial membrane protein COX4I2 (Figure 2.2H and 2.2I).

FB231 and MTK458 can synergistically enhance mitophagy

PINK1/Parkin modulating compounds have been developed with the goal of creating disease-modifying treatments for Parkinson's disease. A critical aspect of moving these compounds to the clinic is the ability to selectively target these pathways without inducing

off-target effects. Minimizing the effective therapeutic dose of such compounds minimizes the chance that these compounds induce side-effects due to lower-affinity interactions with off-target proteins. Both MTK458 and FB231 were designed to target the PINK1/Parkin pathway at distinct steps. We hypothesized that co-treatment could achieve an additive or potentially synergistic effect. To test this hypothesis, we performed a dose combination screen of FB231 and MTK458 to identify potential synergistic regimes in the mt-Keima assay at 10 nM O/A. We found that certain combinations FB231 and MTK458 produced exceptionally strong mitophagy induction (Figure 2.3A). We performed a synergy analysis using the SynergyFinder tool with the Zero-Interaction Potential (ZIP) model of synergy. The ZIP model fits a 4-point logistic equation to the dose response data for each compound alone. The synergy score readout describes the percentage of activity that cannot be attributed to a linear combination of each compound at a measured dose. We observed an area of positive synergy between 0.625–1.25 μM FB231 and around 2.5 μM MTK231, with a max synergy score of 40, indicating 40% of the effect size was beyond a linear combination of either drug's effect (Figure 2.3B). Concentrations of FB231 above 5 μM in combination with MTK458 above 5 μM were found to be anti-synergistic. These results indicate that both compounds can be used in parallel to synergistically enhance mitophagy but suggest caution in the limits of this approach.

We subsequently measured levels of pUb at the synergistic regime via western blot. (Figure 2.3C). We found that, as in the mt-Keima assay, combinations of MTK458 and FB231 enhanced the pUb signal. To estimate synergy, the observed pUb signal was compared to the expected output if the individual pUb signals at the corresponding activator concentrations were added. Synergy in the pUb signature was observed at 0.625 μM FB231 and 1.25 μM MTK458, slightly lower in dosage than the regime observed in the mt-Keima assay (Figure 2.3D). These data provide additional evidence for synergy between FB231 and MTK458, and suggest that they enhance mitophagy through distinct mechanisms.

FB231 alone does not activate mitophagy upon artificial recruitment of Parkin to the mitochondria

One possibility to consider is that FB231 fails to induce mitophagy on its own, since active Parkin is not intrinsically localized to the mitochondria where it can ubiquitinate substrates to trigger mitophagy. To assess this possibility, we sought to reroute Parkin to the mitochondria and check if addition of FB231 could induce mitophagy. We utilized the FKBP-FRB chemically induced dimerization system to recruit FKBP-GFP-tagged Parkin to FRB-tagged mitochondria in combination with either a dose titration of FB231, or O/A (Figure S2.4A). FKBP-FRB dimerization has been previously used to induce mitophagy through recruitment of various autophagic factors (Vargas et al., 2019). We treated cells with the dimerizing drug rapalog or an ethanol control to induce FKBP-Parkin recruitment to the mitochondria. The success of this system was confirmed by observing colocalization of GFP with the mt-Keima reporter (Figure S2.4B). FB231 failed to induce significant increases in mitophagy with or without rapalog at any dose, though a slight positive trend in mitophagy was observed at doses above 5 μ M (Figure S2.4C). Rapalog-induced Parkin recruitment to the mitochondrial surface failed to reduce the threshold for O/A-induced mitophagy in the dosing regime tested in this assay, as it did not alter the levels of mitophagy observed at any dose of O/A (Figure S2.4D). These data indicate that FB231 is not capable of inducing mitophagy on its own, without the accumulation of PINK1 on the outer mitochondrial membrane.

Proteomic analysis identifies induction of the integrated stress response by FB231 and MTK458.

Reduction of mitophagy at high doses of FB231 suggests potential detrimental effects in cells (Figure 2.2A). Moreover, slight mitophagy observed in SH-SY5Y cells treated with MTK458 alone suggested subtle effects on mitophagy (Figure 2.2G). We performed whole-cell label free proteomics to explore possible off-target effects in YFP-Parkin-expressing HeLa cells treated with 20 μ M MTK458 or 10 μ M FB231 (Figure 2.4A and 2.4B). The effects of MTK458 appeared widespread with no clear altered pathway evidence by the lack of significant Gene Ontology terms (GO). However, perturbations in mitochondrial proteins including loss of COA5, HIGD1A and upregulation of fatty acid metabolism genes ACADS (Figure 2.4A). FB231 alone induced a stress-response-like signature that included the

upregulation of ATF3, IFRD1, and VLDLR (Figure 2.4B).(Quiros et al., 2017) Moreover, there was upregulated iron response element binding protein 2 (IREB2) and downregulated iron-related mitochondrial protein ferrochelatase (FECH), suggesting a potential off-target effect on iron related pathways based on GO molecular function term analysis (Figure S2.5).(Anderson et al., 2012; Crooks et al., 2010; Shetty et al., 2020)

We validated a subset of these hits in an orthogonal manner using western blotting. We treated both YFP-Parkin-expressing cells and the background WT HeLa cells (which do not express any endogenous Parkin) with 10 μ M FB231, 5 μ M MTK458, with or without 10 nM O/A. We found that FB231 alone led to induction of ATF3 and its activator in the ISR, ATF4, as well as IFRD1 (Figures S2.1A-D). FB231 treatment alone also led to loss of FECH in WT and YFP-parkin cells. These results confirm that FB231 indeed activated the ISR and perturbed an iron-dependent pathway. Addition of O/A alone also induced the induction of ISR and loss of FECH in YFP-Parkin HeLa cells. This effect was enhanced by co-treatment with either mitophagy activator.

Given the lack of Parkin in WT HeLa cells, these data indicate that the effects of FB231 on the ISR and iron-related pathway response are independent of Parkin modulation. We therefore blotted for PINK1 in WT HeLa cells, and found that in combination with 10 nM O/A, both FB231 and MTK458 led to the stabilization of full length PINK1 (Figure 2.1C). Even though Parkin is the intended target of FB231, these data suggest that HeLa cells experience mitochondrial stress (as reflected by PINK1 stabilization) upon FB231 treatment, regardless of whether Parkin is present or not.

To determine if the effect of MTK458 and FB231 on the ISR was independent of PINK1 activation, and if there is a therapeutic window in which mitophagy could be enhanced while minimizing the ISR, we tested both FB231 and MTK458 in a 6-point dosing curve alone or in the presence of O/A. We performed this experiment in YFP-Parkin-expressing HeLa, WT HeLa, and YFP-Parkin/PINK1 KO HeLa. In YFP-Parkin-expressing WT cells, co-treatment of O/A with FB231/MTK458 resulted in depletion of ATP5A, a biochemical readout for

mitochondrial mass (Figures 2.5A and 2.5C). Loss of ATP5A was blocked by loss of Parkin or PINK1 (Figures 2.5A–D, S2.7A, and S2.7B), indicating that mitophagy is dependent on the PINK1/Parkin pathway. Notably, FB231 induced pUb accumulation in WT HeLa cells that lack Parkin, indicating that FB231 is activating PINK1 (Figure 2.4E). Consistent with the idea that PINK1 is the only known Ub kinase, both compounds failed to induce pUb signal in PINK1 KO cells (Figures 2.4H and S2.7A).

We found other evidence of cellular stress upon treatment with these compounds. Both FB231 and MTK458 greatly enhanced the cleavage of the stress-sensitive mitochondrial fusion protein, OPA1, into lower molecular weight isoforms in the presence of 10 nM O/A (Figures 2.4D–H, S2.7A–B). These effects were found in all tested HeLa cell lines, regardless of PINK1 or Parkin expression. OPA1 cleavage is indicative of mitochondrial stress and can be induced by a wide range of mitochondrial toxins. (Baker et al., 2014) At this same dosing regime, we observe induction of the ISR protein ATF4 and its downstream target ATF3 (Figure 2.4F and 2.4I). We observed induction of the ISR proteins within 6 hours of treatment with activators and 10 nM O/A (Figure S2.6E and S2.6F). Notably the induction of ATF3/4 appeared enhanced in the YFP-Parkin HeLa cells. We wondered if this observation could indicate that PINK1 activation by MTK458 could explain at least part of the ISR induction. We tested this by using higher doses of O/A in YFP-Parkin-expressing HeLa, WT HeLa, and YFP-Parkin/PINK1 KO HeLa (Figure S2.7C). We found loss of PINK1 or Parkin attenuated the ISR response as measured by ATF3 accumulation after 16 hrs (Figure S2.7D). These data indicate that the PINK1/Parkin pathway can enhance the ISR response induced by mitochondrial toxins, and this effect was not unique to FB231 or MTK458.

We also sought to confirm whether the effects on the ISR and iron-related pathways were conserved in the endogenous Parkin-expressing SH-SY5Y cells. Blotting for ATF3, ATF4, and IFRD1, we found that all three proteins were upregulated upon FB231 treatment alone (Figures 2.4I and 2.4K). O/A treatment enhanced the expression of these stress markers. As in WT HeLa, MTK458 in combination with O/A enhanced the expression of ISR markers ATF4 and IFRD1 compared to O/A treatment alone (Figures 2.4I and 2.4K). This confirms

the finding that MTK458 may enhance the ISR response upon co-treatment with low doses of O/A. Treatment with FB231 alone reduced expression of FECH, but this was partially mitigated upon co-treatment with O/A (Figure 2.4I). This may be due to stimulation of FECH expression upon O/A treatment in this cell type.

Together these markers indicate the induction of a potent mitochondrial stress, leading to the activation of the ISR at or below the doses of the compounds that we and other groups have observed to induce mitophagy. These data indicate that FB231 and MTK458 both may act as weak mitochondrial toxins independently of Parkin or PINK1.

Mitophagy activators trigger the DELE1/HRI dependent ISR independent of PINK1/Parkin

It is now known that mitochondrial stress can be relayed to the cytosol by the recently described DELE1-HRI pathway, converging on activation of EIF2a.(Fessler et al., 2020; Guo et al., 2020) In this pathway, the short lived mitochondrial protein DELE1 can be activated either by cleavage by OMA1, allowing it to be released into the cytosol, or by iron loss, which stabilizes the full length form of DELE1 at the OMM, analogous to PINK1 stabilization.(Sekine et al., 2023) In both cases, DELE1 can activate HRI in the cytosol to phosphorylate EIF2a, thereby turning on the ISR through global translational repression and selective translation of ATF4 (2.5A). We sought to determine if ISR activation by FB231 and MTK458 is mediated by the DELE1-HRI pathway. We first blotted for endogenous DELE1 in a previously developed 293T line containing endogenous HA tagged DELE1 with combinations of MTK458 and FB231 with and without 10 nM OA (Figure S2.7E). We observed the presence of cleaved, lower-molecular weight form of DELE1 upon cotreatment with MTK458/FB231 and 10 nM O/A. Given the low signal-to-noise of these endogenous DELE1 blots, we next transiently expressed DELE1-HA in WT HeLa cells and treated cells with MTK458/FB231/10 nM OA combinations for 16 hrs. We now observed the presence of multiple DELE1-HA bands (Figure 2.5B). FB231 alone predominantly lead to the accumulation of full length DELE1 previously associated with iron depletion (Figure 2.5B, inset i). Upon co-treatment of MTK458 or FB231 with 10 nM O/A, we observed the

additional accumulation of the lower molecular weight, presumably OMA1 cleaved, DELE1 species and ATF3/4 accumulation (Figure 2.5D). We next performed this experiment in the YFP-Parkin/ PINK1 KO HeLa cells and observed identical results, confirming independence of this phenomenon from the PINK1/Parkin pathway (Figure 2.5C and 2.5E). Our work, and recent pre-prints have suggested that the DELE1-HRI pathway may in some cases reduce PINK1 driven mitophagy and enhance other forms of mitophagy(Chakrabarty et al., 2024; Singh, 2023; Yang et al., 2024). We knocked down HRI to confirm this pathway was responsible for ISR induction and whether it had any effect the mitophagy observed (Figure 5F). We found that KD of HRI attenuated ATF4/ATF3 induction by FB231 alone and by FB231/MTK458 in combination with 10 nM O/A (Figures 2.5G and 2.5H). We found that mitophagy induction by FB231 and MTK458 was unaffected by HRI KD, indicating that ISR induction is discrete from mitophagy induction in this context (Figures 2.5I and 2.5J). However we observed some increases in basal levels of mitophagy upon HRI KD.

FB231 induces mitophagy through an iron-chelation based mechanism

Having determined that FB231 and MTK458 induce mitochondrial damage leading to the ISR and independent of PINK1, we sought to determine the direct target of these molecules using thermal proteome profiling (TPP). This technique uses mass-spectrometry based proteomics in cell lysate treated with high doses of a compound and subjected to a heat gradient. Proteins whose heat-stability are altered by the compound directly or a change in binding partners can be detected by altered abundance, enabling unbiased proteome wide discovery of potential drug targets. We performed TPP for FB231 and MTK458 in YFP-Parkin expressing HeLa lysate. Parkin and PINK1 were not detected in any samples and therefore no determination about direct binding could be made. MTK458 had no clear hits that could directly explain its effects on mitochondria (Figure S2.8). Top hits for FB231 stabilization included phosphoribosyl pyrophosphate amidotransferase (PPAT), and the HECT-domain containing E3 ligase, HERC4 (Figure 2.6A). The stabilization of HERC4 could indicate a general interaction of FB231 with HECT domain ligases, which like Parkin form a transient thioester intermediate with Ub.(Lazarou et al., 2013) FB231 also lead to the

destabilization of the iron responsive protein IREB2, which we had also found upregulated upon FB231 treatment (Figure 2.6). IREB2, also known as IRP2 is known to bind iron as a molecular glue that links it to E3 ligase FBXL5.(Wang et al., 2020) IREB2 can also be activated by iron loss independent of FBXL5 by an unknown mechanism.(Terzi et al., 2021) Confirming the mass-spectrometry results, we found treatment with FB231 lead to upregulation of IREB2 in a dose dependent manner (Figure 2.6B and 2.6C). 10 nM O/A was found to slightly reduce IREB2 accumulation. Thus, several observations suggested that FB231 may be acting as an iron chelator: The TPP and total proteome showing changes in IREB2, the loss of FECH, and the stabilization of full length DELE1. We confirmed FB231 could chelate Fe^{2+} ions using a ferrozine-based colorimetric assay (Figure 2.6D). FB231 showed comparable chelation ability to the widely used chelator, deferiprone (DFP).(Devos et al., 2022) To test if ferrous iron had any effect on FB231's mitophagy induction, we cotreated 2.5 μ M FB231 with or without 10 nM O/A and with the addition of 25 μ M $FeSO_4$. Mitophagy induction by FB231 + 10 nM O/A was completely blocked by iron supplementation (Figure 2.6E). In contrast, iron had no effect on mitophagy induced by 100 nM O/A. These experiments strongly suggest that FB231's mechanism of action is via chelation of iron. To test if this was a general feature of iron chelators, we tested whether the stronger chelator DFP could alter the O/A induced mitophagy threshold. High doses of DFP alone induces a distinct PINK1/Parkin independent mitophagy (Figure 2.6F). We found that 500 μ M DFP induced moderate mitophagy which could be enhanced by O/A. Co-treatment of 500 μ M DFP with O/A led to increased mt-Keima signal beyond what was observed in O/A or DFP mitophagy alone, indicating an additive contribution from both mitophagy pathways (Figure 2.6F). Upon treatment with O/A, we observe potent mitophagy induction at doses above 15 nM. Co-treatment of DFP with O/A significantly reduced the mitophagy induction threshold of O/A starting at 100 μ M DFP (Figure 2.6G). These findings demonstrate that an iron loss can potentiate the PINK1/Parkin pathway.

FB231 and MTK458 inhibit mitochondrial function through distinct mechanisms

To explore the effect of MTK458 and FB231 on mitochondrial function, we used Seahorse extracellular flux assays to evaluate mitochondrial oxidative phosphorylation activity. With

6 hours of treatment, MTK458 caused strong reductions in the oxygen consumption rate (OCR), whereas the extracellular acidification rate (ECAR) was largely unaffected and resulted in a lowered OCR/ECAR ratio (Figure 2.7A-C). MTK458 reduced sensitivity to oligomycin, but cells were still affected by decoupler FCCP and ETC inhibitors rotenone and antimycin A. In contrast, after treatment with FB231, OCR was elevated, showed less sensitivity to oligomycin, and no sensitivity to FCCP (Figure 2.7A-C). We hypothesized that this may be explained by FB231 causing electron leak across the inner membrane.

The data for MTK458 was particularly surprising, since other groups have found MTK458 to have little to no effect on OCR, except at 25 μ M MTK458.(Chin et al., 2023) In those experiments, OCR was measured immediately after drug injection. Interestingly, we found that MTK458 induced only a slight reduction in basal OCR within the 20 minute observation period after drug injection (Figure 2.7D). Trends in MTK458 and FB231 appeared to approach data measurements observed in the 6-hour pretreatments (Figure 2.7A). When we extended the measurements to two hours, we observed 20 μ M MTK458 to slowly and progressively reduce the basal OCR rate compared to the untreated control, which remained stable (Figure 2.7E). These results explain the apparent incongruity between our pretreatment regimen and the injection experiments performed by another group.(Chin et al., 2023)

We next measured mitochondrial membrane potential (MMP) using the potentiometric dye TMRE via flow cytometry. Cells were treated for between one and two hours with varying combinations of the experimental drugs and 10 nM O/A, as well as depolarizer CCCP and oligomycin as minimum and maximum controls. We found that MTK458 led to significant hyperpolarization of MMP at 20 μ M, which was partially dissipated by 10 nM O/A (Figure 2.7F). FB231 had more subtle effects. We observed a slight, but insignificant, reduction of MMP. The striking result of MTK458 on MMP taken together with Seahorse data indicates that it may act complex V inhibitor. The slow kinetics of OCR reduction suggests it is either a weak inhibitor or acts through an indirect mechanism.

FB231 and MTK458 reduce cell viability in the presence of mitochondrial stress

Our evidence suggests that both compounds act independently of PINK1/Parkin to enhance O/A-induced mitophagy by acting as weak mitochondrial toxins. We next asked if FB231 and MTK458 would enhance toxicity or protect cells from the effects of O/A. To assess this question, we co-treated various doses of FB231 or MTK458 with O/A for 24 hours and measured cell viability through the CellTiter-Glo assay in WT HeLa cells. Both FB231 and MTK458 alone caused loss of viability at high doses. FB231 was more toxic, resulting in ~50% viability at 10 μ M and above (Figure 2.8A). Significant toxicity in MTK458 alone was only observed at 20 μ M, with a reduction to ~70% viability. Increasing doses of O/A led to 50% reduction in viability with an IC_{50} of 48 nM. Combinations of either FB231 or MTK458 with O/A enhanced viability loss, suggesting a potential synergistic interaction (Figures 2.6A–D). Using the ZIP synergy model, we found that both FB231 and MTK458 showed dosage regimes exhibiting positive synergy with O/A (Figures 2.8E and 2.8F). FB231 had a narrow synergistic regime between 25 and 100 nM O/A and centered at 1.25 μ M FB231. At higher doses of FB231, negative synergy was observed. MTK458 demonstrated higher levels of synergy across a wide range of doses with peak synergy observed at 12.5 nM O/A and 5 μ M MTK458. As another way to visualize the synergistic effect of these compounds on O/A's potency in the context of cell viability, we calculated the O/A IC_{50} at each dose of either activator (Figure 2.8G). Increasing the dose of FB231 or MTK458 corresponded to a lower O/A IC_{50} . At the highest doses of FB231, this trend diverged as O/A was anti-synergistic in this regime. Because CellTiter-Glo relies on cellular ATP levels to quantify viability, we also imaged cells treated with FB231/MTK458 and O/A combinations with Propidium Iodide staining, observing similar synergistic regimes of cell killing (Figure S2.9A and S2.9B). These results indicate that rather than protect cells from mitochondrial stress, both activators enhanced susceptibility to mitochondrial toxins.

It is well known that in conditions of high glucose used in normal cell culture media, cells can use glycolysis to provide most of their ATP needs, rendering them insensitive to mitochondrial defects. This is known as the Crabtree-effect.(Marroquin et al., 2007) Replacing glucose with galactose forces cells to rely on mitochondrial oxidative phosphorylation for ATP, effectively sensitizing them to mitochondrial damage. This effect

was apparent upon O/A treatment, where a significant loss of viability and a reduced O/A IC_{50} was apparent in galactose media (Figure 2.8H). MTK458 had been previously been tested in the glucose/galactose assay in SK-OV-3 cells where enhanced susceptibility in galactose over glucose at high doses had been observed. (Chin et al., 2023) In WT HeLa cells, we found that galactose significantly enhanced susceptibility to MTK458, resulting in ~40% viability in galactose compared to over ~70% in glucose media at 20 μ M. FB231 viability-dose response was virtually unchanged in galactose vs glucose media, suggesting that FB231's cell killing function was not necessarily due to an inhibition of mitochondrial function. This result was similar to that seen for DFP (Figure S2.9C). We also performed the Glucose/Galactose assay in SY-SY5Y cells and found they were more sensitive to MTK458 (Figure 2.8I). To determine if MTK458's mitochondrial toxicity was related to a direct interaction with PINK1, we repeated the O/A dose-combination and glucose/galactose viability assays in the YFP-Parkin PINK1KO HeLa cell line. MTK458 showed potent synergy with O/A and reduced cell viability was observed in galactose vs glucose (Figures S2.10A–E). Taken together, these data suggest that both MTK458 and FB231 acts as weak mitochondrial toxins, whose enhancement of mitophagy is due to a synergistic interaction with mitochondrial toxins such as O/A, independent of PINK1. Synergistic inhibition of mitochondrial function in combination with mitochondrial toxins leads to mitophagy through PINK1 stabilization, and induction of the mitoISR through DELE1 cleavage and HRI activation (Figure 2.8J).

MTX115325 (USP30i) is another small molecule targeting mitophagy entering clinical trials for PD. MTX115325 was designed to inhibit USP30, a OMM deubiquinase that can counteract Parkin ubiquitination. (Antico et al., 2025) Mission therapeutics suggested that USP30i could enhance mitophagy in response to mitochondrial damage, similar to the compounds tested here. (Fang et al., 2023) We aimed to test this compound using the O/A threshold assay developed here. We found no effect of the USP30i on mitophagy induction or the O/A threshold (Figure S2.11A). We also tested whether we could observe accumulation of Parkin ubiquitinated substrates TOMM20 and MFN2. We performed the same experiment in the original USP30i paper using 1 μ M O/A with either various doses of

USP30i or MG132 (Fang et al., 2023). We observed ubiquitinated MFN2 substrate which appeared slightly stabilized by the addition of 1 μ M USP30i, however the level of non-ubiquitinated MFN2 was also increased (Figure S2.11B). No effect on TOMM20 or pUb was observed.

2.4 Discussion

Cellular screens for mitophagy activators are plagued by hits that damage the mitochondria to induce mitophagy.(Tjahjono et al., 2021; Tufi et al., 2023) Identifying lead compounds based on in vitro assays directly targeting PINK1 or Parkin promises to alleviate this problem. However, our work cautions that compounds with mild mitochondrial toxicity can arise from such screens and appear to activate mitophagy.

We believe that this challenge arises from the unique dynamics of the PINK1/Parkin pathway. The PINK1/Parkin pathway displays potent switch-like behavior, which at its root is caused by the input threshold being dependent on PINK1 accumulation and a feed-forward step dependent on Parkin activation. The system avoids activation of mitophagy in response to minor fluctuations of mitochondrial function, but potently clears mitochondria in conditions of sustained damage. The PINK1 accumulation threshold and feed-forward dynamics mean that the pathway is exquisitely sensitive to combinations of mitochondrial inhibitors. FB231 and MTK458 at their maximum doses do not inhibit mitochondrial function beyond the threshold of PINK1 accumulation needed to induce mitophagy, and therefore neither drug in isolation behaves as a mitophagy inducing agent.

We can use a simplified mathematical model to further rationalize how these sub-threshold toxins can enhance mitophagy in the presence of a classical toxin or stressor (Figure 2.9A). Each toxin inhibits a parameter we denote as “mitochondrial function”. Inhibition of mitochondrial function will not manifest as mitophagy until the level of PINK1 accumulation sufficient to recruit Parkin is breached; this occurs at the "mitophagy threshold". At doses beyond the mitophagy threshold, mitophagy levels will be inversely proportional to the mitochondrial function, but quickly saturate. In the model, the weak inhibitor causes limited

damage to the mitochondria but never induces mitophagy (Figures 9B–C). A classical, or “Strong Inhibitor” potentially inhibits mitochondrial function and results in mitophagy at a sufficient dose (Figure 2.9B). When combined, there is an enhanced inhibition of mitochondria, and the dose of the Strong Inhibitor needed to induce mitophagy is reduced as a function of the Weak inhibitor concentration (Figure 2.9C). Despite the mild effects of the Weak Inhibitor alone, weak inhibitors can drastically alter the mitophagy induction threshold, or EC_{50} , of the strong inhibitor (Figure 2.9D). This model can reproduce the general features of the threshold data observed for FB231 and MTK458 (Figures 2.1C–E).

The totality of our results suggests that the ability of FB231 and MTK458 to enhance O/A-induced mitophagy is not due to direct activation of Parkin or stabilization of PINK1, respectively. FB231 induces mitochondrial disruption that is independent of Parkin expression, as evidenced by pUb accumulation, DELE1 accumulation, OPA1 cleavage, and COX4I2 loss in WT HeLa cells, which lack Parkin expression (Figures 2.4E and 2.8A). Moreover, these effects occur at doses around 1 μ M, six times lower than the observed EC_{50} of FB231 on purified Parkin (Figures 2.7A, B, S2.7A, and S2.1C). MTK458 similarly induces mitochondrial stress independently of PINK1, evidenced by enhancement of OPA1 cleavage and COX4I2 loss in PINK1 KO cells (Figures 2.4C and 2.4D). MTK458 has an inhibitory effect on oxygen consumption and sensitizes cells to both galactose and O/A, indicating clear mitochondrial toxicity (Figures 2.7 and 2.8). The precursor to MTK458, kinetin, was initially thought to act as a potent substrate for PINK1, replacing ATP in the ATP binding site and enhancing PINK1 activity.(Hertz et al., 2013) A recent study indicated that kinetin does not bind to *Pediculus humanus corporis* PINK1 or human PINK1 due to a steric clash, suggesting that kinetin does not enhance PINK1 kinase activity through the originally proposed mechanism.(Gan et al., 2024) No effect on PINK1 phosphorylation activity was seen in a second study on isolated mitochondria.(Rasool et al., 2024) MTK458 alone has minimal effect on cell line growth, and slow inhibition of mitochondrial function in the Seahorse assay, explaining why MTK458 evaded detection as a mitochondrial toxin.

Our study highlights an important challenge towards identifying activators of the PINK1/Parkin mitophagy pathway. We show that two putative activators have sufficient mitochondrial toxicity to plausibly explain their mitophagy inducing properties when administered in conjunction with classical mitochondrial toxins. Our results suggest that development of more sensitive methods to detect subtle mitochondrial stress may be a potentially effective strategy for counter-screening mitotoxic compounds in future drug discovery campaigns. Both MTK458 and FB231 generate mitochondrial damage that stabilizes PINK1 and activates the more sensitive DELE1-HRI pathway. Moreover, ATF4 induction by MTK458 and FB231 was observed at doses below induction of mitophagy. High-throughput and sensitive ATF4-reporters have long been in use and represent another appealing strategy to identify subtle mitochondrial toxins.(Sidrauski et al., 2013)

A major question given our results clarifying the mechanism of action of MTK458 and FB231 is whether they may be clinically useful in PD. Given that mitochondrial toxins have been shown to directly cause and are associated with the development of PD, a weak toxin such as MTK458 or FB231 would be expected to have no benefit at best, or at worst, promote PD progression. DFP is another weak mitochondrial toxin that behaves similarly to FB231 and was previously shown to enhance the progression of Parkinson's disease in a large phase 2 clinical trial.(Devos et al., 2022) However the unique action of FB231 to induce an iron stress response at low doses suggests it may be useful in other indications such as oncology. Given Parkin's role as a cytoplasmic stress response sensor, it may be that mitochondrial damaging compounds can bind directly to Parkin as part of an activation sensing mechanism. In this case, many compounds that activate Parkin may also function as weak mitochondrial toxins, as we have seen in multiple screens that yielded diverse chemotypes.

An ideal mitophagy activator would enhance cell viability in response to mitochondrial toxins or genetic defects in mitochondrial function. A recent preprint demonstrates that a HIF1 α stabilizing drug, which induces mitophagy through the BNIP3/NIX receptor pathway, could protect neurons from mitochondrial toxins in PINK1/Parkin null cells.(Lam, 2024)

These results provide hope that alternative mitophagy inducers may yet demonstrate clinically relevant protection in PD.

Ultimately, this study demonstrates the ability of weak mitochondrial toxins to lower the mitophagy induction threshold by sensitizing the cell to mitochondrial stress. These data indicate the need for caution in screening for mitophagy activators in the presence of mitochondrial stressors, because seemingly “silent” mitochondrial toxins may appear as promising pharmacological mitophagy potentiators, even if the initial compound hits were obtained using in vitro purified enzyme targets in the absence of cells.

2.5 Methods

Reagents

The following chemicals were used in this study: antimycin A (1397-94-0, USB Corporation), oligomycin A (HY-100558, MedChemExpress), Q-VD-OPh (HY-12305, MedChemExpress), FB231 (This paper), MTK458 (HY-152943, MedChemExpress), Bafilomycin A (HY-100558, MedChemExpress), FuGENE® 6 Transfection Reagent (E2691, Promega), Rapalog A/C Heterodimerizer (635056, Takara Bio), and DFP ([379409](#), Sigma-Aldrich). FB231 was synthesized by Wuxi App Therapeutics, detailed synthesis schema can be found in Supplementary Document S2

Cell lines

All cell lines were cultured at 37 °C and 5% CO₂. HeLa (RRID:CVCL_0058), SH-SY5Y (RRID:CVCL_0019), and HEK293T (RRID:CVCL_0063) cells were obtained from the American Type Culture Collection (ATCC). YFP-Parkin/mt-Keima, YFP-Parkin/mt-Keima/PINK1KO, and FRB-Fis1/mt-Keima HeLa cells were supplied by the Youle Lab. FKBP-GFP-Parkin/FRB-Fis1/mt-Keima HeLa and Mt-Keima SH-SY5Y cells were generated from this study. All cells were cultured in DMEM (D6429, Sigma-Aldrich) supplemented with 10% (v/v) fetal bovine serum (F0926, Sigma-Aldrich) and 1% (v/v) penicillin/streptomycin (15140-122, Thermo Fisher). All cell lines were routinely tested for mycoplasma contamination.

Transient transfection of plasmids

Transient transfection was achieved by using polyethylenimine Max 40K (PEI, KyforaBio) A 3:1 ratio of PEI to DNA (w/w) was used to transfect cells with the plasmid of interest. The transfection media is then replaced with fresh media 16 h post-transfection, at which point downstream experiments are performed. The following plasmid vectors were used for transfections in this study: pLVX-puro-DELE1-HA.

Generation of stable cell lines

Stable cell lines were generated using lentiviral expression systems. For lentiviral transductions, HEK293T cells (RRID:CVCL_0063) were transfected with HGPM2, REV-1b, Tat-1b, VSV-G, and pHAGE constructs containing our gene of interest using FuGENE® 6 Transfection Reagent (E2691, Promega). For retroviral transfection, HEK293T cells were transfected with pUMVC and VSV-G. The day after transfection, the culture medium was replaced with fresh media. Viruses were harvested 48 h post-transfection and filtered through 0.45 μ m syringe filters (WHA9914-2504, Cytiva) to avoid contamination of cultures with HEK293T cells. Cells were seeded into 12-well plates at 50,000 cells/well and infected via centrifugation by the virus-containing media supplemented with 8 mg/ml polybrene (Sigma-Aldrich). Cells having undergone successful infection were selected for by puromycin or neomycin, when the selection marker is present on the vector. Cells were then expanded and sorted by FACS to additionally select for infected cells and normalize protein expressions across individual cells.

The following vectors were used in this study: pHAGE-FKBP-GFP-Parkin and pHAGE-mtKeima. For RNA interference, retroviral transduction was used to express shRNAs from the H1 promoter. The target sequences were: HRI, 5' GCATGAACCAAAC CCACTTCG 3'.

qPCR

Total RNA was extracted from 800,000 cells using Direct-zol RNA MicroPrep kit (R2062, Zymo Research). 1 μ g of total RNA was used for cDNA synthesis via High Capacity cDNA Reverse Transcription Kit (4368814, Thermo Fisher Scientific) for RT-PCR as per the manufacturer protocol. Quantitative PCR was done with primers for HRI (Forward: 5'-ACACCAACACATACGTCCAG-3', Reverse: 5'-GCTCCATTTCTGTTCCAAACG-3'), and β -actin (Forward: 5'-TCATCACCATTGGCAATGAG-3', Reverse: 5'-

ACTTCATGATGGAGTTGAAG-3'), using Power SYBR® Green PCR Master Mix (4368577, Thermo Fisher Scientific). Fold changes in RNA expression were calculated using the $\Delta\Delta C_t$ method.

Mitophagy experiments

Cells were treated with 10 nM each oligomycin A (HY-100558, MedChemExpress) and antimycin A (1397-94-0, USB Corporation) to induce mitochondrial damage. To induce mitophagy, varying doses of PINK1 activator MTK458 (HY-152943, MedChemExpress) and/or Parkin activator FB231 was added. In some experiments, as noted, we additionally added 20 μ M Q-VD-OPh (HY-12305, MedChemExpress) to inhibit apoptosis. Samples were then analyzed by SDS-PAGE and western blot or mt-Keima assay.

Imaging-based mt-Keima assay

HeLa cells stably expressing YFP-Parkin and mt-Keima (YPMK) were previously generated and used to measure induction of mitophagy. A HeLa cell line expressing mt-Keima and YFP-Parkin with PINK1 knocked out was used as a negative control. Both cell lines were plated at 15,000 cells/well in 96-well plates (655086, Greiner) and incubated overnight. The following day, compound dilutions were performed in a separate 96-well plate. To investigate the mitophagy induction threshold, compounds were serially diluted two-fold to generate a six-dose titration, with final concentrations ranging from 0-20 μ M for FB231 and MTK458, and 0-500 μ M for DFP. A serial two-fold dilution of an equimolar combination of oligomycin A and antimycin A was performed to generation a ten-dose titration, with final concentrations ranging from 0-500 nM. In each well, 190 μ L of serum-free DMEM (Sigma-Aldrich) containing 50 μ M Q-VD-OPh was added to 10 μ L of compound dilutions in DMSO. Then, 12 μ L of solutions from both the O/A and activator plate were added to the plated cells. Cells were incubated at 37 °C/5% CO₂, then imaged at 6 h via an ImageXpress Micro Confocal Plate Reader (Molecular Devices). The two channels used for imaging were excitation at 470 nm or 555 nm, with emission detected by a 610/20 filter. The average fluorescence intensity for each channel was calculated in the MetaXpress software of Version 6.7.1.157 (Molecular Devices). Five images were taken and averaged for each well, and three

separate plates, each representing independent experiments, were imaged to ensure reproducibility of data.

To experimentally obtain the EC₅₀ of the mitophagy activators at 10 nM O/A, compounds were serially diluted two-fold to generate a ten-dose titration (final concentration 0-20 μM). In each well, 190 μL of serum-free DMEM (Sigma-Aldrich) containing 50 nM oligomycin A, 50 nM antimycin A, and 50 μM Q-VD-OPh was added to 10 μL of compound dilutions in DMSO. Then, 25 μL of these solutions were added to the plated cells, resulting in a final concentration of 10 nM oligomycin A, 10 nM antimycin A, and 10 μM Q-VD-OPh. Cells were imaged as described above at 6 h, 12 h, and 24 h. Each dose was performed with six technical replicates. For the quantification of mt-Keima emission signals, the MetaXpress software (RRID:SCR_016654) was utilized. These values were plotted and subjected to statistical testing via GraphPad Prism.

mt-Keima assay cells via flow cytometry

Stable cell lines expressing mt-Keima were seeded in 12-well plates at 200,000 cells per well and treated the following day with DMSO, 10 nM O/A, 1.25 μM FB231 alone or with 10 nM O/A, 2.5 μM MTK458 alone or with 10 nM O/A, and 100 nM O/A for 24 h. Cells were then trypsinized and resuspended in sorting buffer (145 mM NaCl, 5 mM KCL, 1.8 mM CaCl₂, 10 mM HEPES, 10 mM glucose, 0.1% BSA). The cells were then filtered through 35 μm strainer caps into 5 mL polystyrene FACS tubes (FSC-9005, Stellar Scientific) to eliminate large clumps of cells. Analysis was performed using CytExpert software Version 2.6 on a Beckman Coulter CytoFLEX flow cytometer. Measurements of lysosomal mt-Keima were taken by calculating the ratio of mt-Keima emission at 610 nm after excitation by a 555 nm (pH 4) laser over mt-Keima emission at 610 nm after excitation by a 470 nm (pH 7) laser. For each sample, at least 30,000 events were collected and subsequently gated for live, single cells expressing mt-Keima. Flow cytometry data was analyzed using FlowJo Version 10.10.0 (BD Biosciences).

Animal Experiments

Experiments with Sprague Dawley rats were done at BioDuro-Sundia (Shanghai, China). All animal experiments were reviewed and approved by IACUC (BD-201609126 Rats were obtained from Zhejiang Vital River Laboratory Animal Technology Co.,Ltd, caged in Static Caging System fashion (3 rat/cage), and fed experimental rat maintenance feed (Shanghai Protein Bio-Technology Limited, Shanghai, China) diet. During the study, the care and use of animals was conducted in accordance with the regulations of the Association for Assessment and Accreditation of Laboratory Animal Care (AAALAC, accreditation number is 001516).

Western blotting

Cells were plated in 6-well plates at a density of 400,000 cells/well and incubated overnight. Cells were harvested by trypsinization (12604-013, Thermo Fisher) and centrifugation. Cell pellets were washed with PBS and lysed in RIPA buffer (50 mM Tris, 150 mM NaCl, 0.1% SDS, 0.5% sodium deoxycholate, 1% Triton X-100) supplemented by EDTA-free broad-spectrum protease inhibitors (Thermo Fisher). After incubating for 15 min on ice, samples were spun down by centrifugation and soluble fractions were collected. Protein concentrations were normalized for equal loading. 5-10 µg of protein for each sample was resolved on 4-20% Mini-PROTEAN TGX gels (Bio-Rad), then transferred to nitrocellulose membranes using the Trans-Blot Turbo Transfer System (Bio-Rad). Membranes were stained with Ponceau S for 5 min at rt, washed with DI water, then imaged using a ChemiDoc MP Imaging System (Bio-Rad). Membranes were washed in TBS-T (TBS + 0.1% Tween 20), then blocked at rt for 1 hour in TBS-T with 5% non-fat milk powder. Membranes were incubated overnight at 4 °C with primary antibodies diluted in TBS-T with 5% milk. Membranes were washed three times with TBS-T, then incubated for 1 hour at rt with goat anti-mouse or goat anti-rabbit HRP-conjugated antibodies (1706515 & 1706516, Bio-Rad) diluted in TBS-T with 5% non-fat milk powder. Membranes were washed three times with TBS-T, then imaged using Immobilon ECL Ultra Western HRP Substrate (WBULS0500, MilliporeSigma) and a ChemiDoc MP Imaging System (Bio-Rad). For the quantification of immunoblots, we performed densitometry analysis using ImageLab Version 6.1 (RRID:SCR_014210).

Label-free proteomics

HeLa YFP-Parkin/mt-Keima cells were plated onto 6-well plates at 750,000 cells/well and incubated overnight. Cells were then treated with 100 nM oligomycin/antimycin, 5 μ M MTK458, and 10 μ M FB231 for 12 h. Cells were harvested following treatment, then prepared using the EasyPep Mini MS Sample Prep Kit (A4006, Thermo) according to the manufacturer's instructions. Peptide concentration was measured via the Pierce Quantitative Fluorometric Peptide Assay (Cat #23290, Thermo).

The LC-MS/MS experiments were performed using an EASY-nLC 1000 (ThermoFisher Scientific, San Jose, CA) connected to a QExactive HF mass spectrometer. The sample (1 μ g) in 0.1% FA solution was loaded onto an Aurora UHPLC Column (25 cm x 75 mm, 1.6 mm C18, AUR225075C18A, Ion Opticks) and separated over 136 min at a flow rate of 0.35 mL/min with the following gradient: 2-6% Solvent B (7.5 min), 6-25% B (82.5 min), 25-40% B (30 min), 40-98% B (1 min), and 98% B (15 min). Solvent A consisted of 97.9% H₂O, 2% ACN, and 0.1% formic acid, and solvent B consisted of 19.9% H₂O, 80% ACN, and 0.1% formic acid. An MS1 scan was acquired in the Orbitrap at 120,000 resolution with a scan range of 350-1500 m/z. The AGC target was 4×10^5 , and the maximum injection time was 50 min. Dynamic exclusion was set to exclude features after 1 time for 60 s with a 10-ppm mass tolerance. Higher-energy collisional dissociation (HCD) fragmentation was performed with 35% collision energy after quadrupole isolation of features using a 1.6 m/z isolation window, 5×10^4 AGC target, and 35 ms maximum injection time. MS2 scans were then also acquired by the Orbitrap with 50,000 resolution. Ion source settings were as follows: ion source type, NSI; spray voltage, 2400 V; ion transfer tube temperature, 275 °C. System control and data collection were performed by Xcalibur software. The mass spectrometry proteomics data have been deposited to the ProteomeXchange Consortium via the PRIDE partner repository with the dataset identifier PXD058150.(Perez-Riverol et al., 2022)

Thermal Proteome Profiling

TPP was performed following methods from the literature.(Cabrera et al., 2020; McDowell et al., 2013; Quan et al., 2023) Detailed methods and analysis of the TPP experiments can be found in the supplementary document S2.

Rapalog-induced chemical dimerization experiments

Chemically induced dimerization experiments were conducted using the Fis1-FRB and Parkin-FKBP system. Lentiviral transduction of FKBP-GFP-Parkin was performed on Fis1-FRB/mt-Keima HeLa cells procured from the Youle Lab. The resulting stable cell line was then treated with A/C heterodimerizer (635056, Takara) for 24 h. Cells were then analyzed by mt-Keima as described above.

Cell viability assay

HeLa cells or SH-SY5Y were seeded at 400 cells/well in each well of a white 384-well plate (Greiner 781080). 30 μ L of DMEM supplemented with 4.5 mg/ml Glucose, 10% FBS, and 1% penicillin/streptomycin was used as the culture medium. In the galactose condition 10 mM galactose replaced glucose in the medium. Following a 24-hour incubation at 37 °C and 5% CO₂, cells were treated with the designated compound cocktail with DMSO concentration no more than 0.5%, 4 biological replicates per condition. Cells were incubated with compounds for 24 hours, then cell viability was assessed either by the addition of 30 μ L of CellTiter Glo reagent (G7572, Promega) or Propidium Iodide (1 μ M). Cells were incubated for 10 min at room temperature, and luminescence/fluorescence was measured using a BioTek Synergy Neo Microplate Reader or high throughput confocal. Cell viability for each well was calculated by comparing the percentage of viable treated cells to the DMSO control (i.e., 0 μ M compound). IC₅₀ values were then calculated from 8 replicates collected in at least two separate experiments via non-linear regression in GraphPad Prism 10.

Mitochondrial Membrane Potential measurements

WT HeLa cells were trypsinized and resuspended in complete media (DMEM supplemented with 10% FBS, 1% Pen/Strep) containing 20 nM Tetramethylrhodamine, Ethyl Ester, Perchlorate (TMRE, #T669, Thermofisher). The cells were then filtered through 35 μ m

strainer caps into 96-well plates containing drug treatments dissolved in DMSO. Cells were kept shaking on an orbital shaker for 5 minutes before being allowed to incubate for one hour in the dark at room temperature. Analysis was performed using CytExpert software Version 2.6 on a Beckman Coulter CytoFLEX flow cytometer. Measurements of membrane potential were taken using FL3. Three biological replicates were measured for each condition, for each experiment. For each sample, at least 12,000 events were collected and subsequently gated for live, single cells. Flow cytometry data was analyzed using Floread.io online analysis tool (<https://floreada.io>).

In vitro Iron Chelation assay

Ferrous iron chelating assays using Ferrous Iron Chelating (FIC) Assay Kit (#AOX-15, AMSbio) according to manufacturers protocol. EDTA (from kit), DFP ([379409](#), Sigma-Aldrich), and FB231 stocks were diluted in assay buffer to make a 9-point 3x dilution dose series, with final volume of 100 uL. Controls with Assay Solution (no drug) and distilled water were used to determine maximum signal and background signal. 100 uL of working ferrozine solution was added, mixed on an orbital shaker for 10 minutes. Absorbances were read at 562 nm using a BioTek Synergy Neo2 plate reader (Agilent). Ferrous ion chelating was calculated as a % of the max signal observed in EDTA 200 uM condition: (%) = $100 \times (\text{Abs}_{\text{max}} - \text{Abs}_{\text{test}}) / \text{Abs}_{\text{max}}$. Three replicate wells were measured for each condition.

Seahorse Extracellular Flux measurements

20,000 WT HeLa cells were plated onto a 96-well plate 24 hr before the Seahorse experiment in complete media (DMEM supplemented with 10% FBS, 1% Pen/Strep). Six hours before the experiment, cells were washed into Seahorse media (Sigma-Aldrich; #D5030 supplemented with glutamine, sodium pyruvate, Pen/Strep, and 25 mM glucose). For pretreatment experiments, cells were treated with compound doses diluted in Seahorse media. One hour prior to analysis, cells were transferred to a 37° C incubator with ambient CO₂. The Mitochondrial Stress Test was performed using a Seahorse Biosciences Extracellular Flux Analyzer (model XF96). 5 μM oligomycin was added to inhibit complex

V; 1 μ M FCCP was added to uncouple the proton gradient; and 5 μ M Rotenone/Antimycin A was added to inhibit complex I/III. For drug injection experiments, either DMSO or the experimental drug was injected prior to the mitochondrial stress test. For extended observation of drug treatments, either DMSO or the experimental drug was injected and measurements were recorded every 7 minutes for two hours.

Synergy Score

Synergy scores were calculated using the SynergyFinder web server.(Ianevski et al., 2022) Mitophagy scores such that the DMSO treated condition was set to 0 and the max mitoKeima 555/488 nm value was set to 1 in each experiment. Viability data was normalized to the untreated condition in each experiment. Curves were fitted with the LL4 method and outliers were not excluded. The ZIP model of synergy was utilized.

Autoubiquitination

Parkin autoubiquitination was assayed using a pre-incubation of 196nM FL-Parkin, 196nM pUb, 196nM Ub, and compound or DMSO control (to a maximum of 1% DMSO) for 15 minutes in reaction buffer (50mM HEPES, 50mM NaCl, 800mM KF, 0.005% Tween20, 0.1% PF-127, pH8.5), followed by the addition of a master mix of 5nM E1 (Boston Biochem E-305), 50nM UbcH7 E2 (Boston Biochem E2-640), 8.8nM Ubiquitin-Europium (CisBio 61UBIKLA) in reaction buffer and incubation for an additional 120 minutes at 23°C, in a total reaction volume of 10 μ l. Anti-6His-d2 (CisBio 61HISDLA) was added in Detection buffer (Reaction buffer plus 5mM EDTA) for 120 minutes at room temperature, followed by reading plates on Perkin Elmer Envision with top mirror: LANCE/DELFI A Duel/Bias, emission Filter APC665 EM, and 2nd emission filter Europium 615 EM, reading 655 (channel 1) and 615nm (channel 2) wavelengths on Envision, with HTRF ratio = (Channel 1/Channel 2) * 10000; % Activation = (HTRF – BKGD/Max) * 100. Percent activation of compound titration was used to find activation EC50, where fit = (A + ((B-A)/1+((C/x)^D)))) and A = Bottom; B = Top, C = Relative EC50, D = Hill Slope where bottom = 0 and Top = 100 of control compound CMPD001. 100% activation signal = pUb activated Parkin plus 40 μ M control activator CMPD001; 0% activation signal = pUb activated Parkin + DMSO,

Parkin activator compounds can be identified by an increase in activation signal from the 0% activation signal TR-FRET.

Probe Assay

Probe binding to Parkin protein was determined by incubation of 40nM heat-activated Parkin, 70nM Ha-Ub-VS probe (Boston Biochem U-212), 2x activator/2% DMSO (Sigma-Aldrich, D4540-100ML) for 60 minutes at 22°C with reaction buffer (50mM HEPES (pH 8.5), 150mM NaCl, 0.01% Tween 20, 0.1% BSA) to total 10µL reaction, followed by the addition of 2.6nM Anti-6His-Eu cryptate (CisBio 61HISKLA) and 40nM Anti-HA-XL665 (CisBio 610HAXLA) in detection buffer (50mM HEPES (pH 8.5), 150mM NaCl, 0.01% Tween 20, 0.1% BSA, 800mM KF). Plates were incubated for 60 minutes at room temperature, and read on a Perkin Elmer Envision in White 384 well plate (Corning 3572) with top mirror: LANCE/DELTA Duel/Bias, emission Filter APC665 EM, and 2nd emission filter Europium 615 EM, reading 655 (channel 1) and 615nm (channel 2) wavelengths on Envision, with HTRF ratio = (Channel 1/Channel 2) * 10000; % Activation = (HTRF – BKGD/Max) * 100. Percent activation of compound titration was used to find activation EC50, where fit = $(A + ((B-A)/(1 + ((C/x)^D))))$ and A = Bottom; B = Top, C = Relative EC50, D = Hill Slope.

Statistical analysis

All statistical data were calculated and graphed using GraphPad Prism Version 10.2.3 (RRID:SCR_002798). To show statistical significance, we employed either a one-way or two-way ANOVA test with appropriate multiple comparison tests. Statistical significance is denoted as *p < 0.05; **p < 0.01; ***p < 0.001; ****p < 0.0001; ns, not significant. Error bars are reported as mean ± SD. To ensure reproducibility of experiments, we showed one representative replicate in the paper out of at least two replicates, as indicated in figure legends.

SUMMARY TABLES

Antibodies

The primary antibodies used in this study for western blotting are:

anti-ATP5A (1:1000, Abcam Cat# ab176569, RRID:AB_2801536)

anti-ATF3 (1:1000, Cell Signaling Cat# 33593, RRID:AB_2799039)

anti-Parkin (1:1000, Cell Signaling Cat# 4211, RRID:AB_2159920)

anti-phospho-Ubiquitin S65 (1:1000, Cell Signaling Cat# 62802, RRID:AB_2799632)

anti-IFRD1 (1:1000, Novus Cat# NBP1-87327, RRID:AB_11052376)

anti-COX4I2 (1:1000, Proteintech Cat# 11463-1-AP, RRID:AB_2085287)

anti-FECH (1:1000, Proteintech Cat# 14466-1-AP, RRID:AB_2231579)

anti-OPA1 (1:1000, Proteintech Cat#27733-1-AP, RRID:AB_2810292)

anti-ATF4 (1:500, Santa Cruz Cat# sc-390063, RRID:AB_2058752)

anti-HRI (1:1000, Proteintech Cat# 20499-1-AP; RRID:AB_10697665)

anti-IREB2 (1:1000, Cell Signaling Cat#37135; RRID:AB_2799110)

The secondary antibodies used in this study for western blotting are:

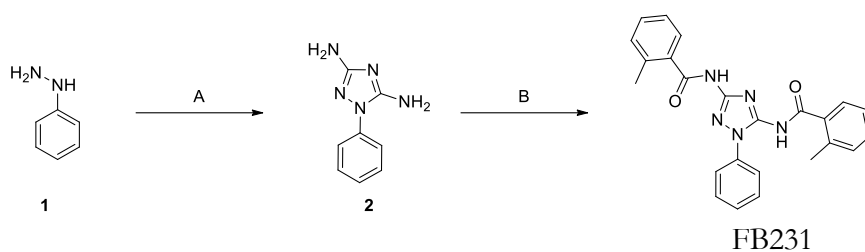
Goat anti-Rabbit (H+L)-HRP Conjugate (Bio-Rad Laboratories Cat# 1706515, RRID:AB_11125142)

Goat anti-Mouse (H+L)-HRP Conjugate (Bio-Rad Laboratories Cat# 1706516, RRID:AB_2921252)

Cell lines

All parental cell lines, including HeLa (RRID:CVCL_0058), HEK293T (RRID:CVCL_0063), and SH-SY5Y (RRID:CVCL_0019) were acquired from the American Type Culture Collection (ATCC). YFP-Parkin/mt-Keima, YFP-Parkin/PINK1KO/mt-Keima, and FRB-Fis1/mt-Keima HeLa cells were acquired from the Youle Lab. KI DELE1-HA 293T line was obtained from the Lucas Jae lab. FRB-Fis1/FKBP-GFP-Parkin/mt-Keima HeLa and mt-Keima SH-SY5Y cells were generated from this study by stable lentiviral transduction.

Chemistry.



Reagents and conditions: (A) dicyandiamide, 2M *aq.* HCl, reflux, 16 h; B) 2-methylbenzoyl chloride, pyridine, MeCN, 80 °C, 20 min.

Chemistry. Mass spectra were acquired on LC-MS systems using electrospray, chemical and electron impact ionization methods from a range of instruments of the following configurations: SHIMADZU LCMS-2020, Agilent 1200 LC/G1956A MSD and Agilent 1200\G6110A, Agilent 1200 LC & Agilent 6110 MSD Mass Spectrometer $[M+H]^+$ refers to protonated molecular ion of the chemical species. NMR spectra were run on Bruker 400MHz spectrometers using ICON-NMR, under TopSpin program control. Spectra were measured at 298K, unless indicated otherwise, and were referenced relative to the solvent resonance.

Prepared HPLC condition:

column: Phenomenex luna C18 250 × 50 mm × 10 μm; mobile phase: [water (0.05%HCl)-ACN].

Instrumentation:

LC-MS Methods: Using SHIMADZU LCMS-2020, Agilent 1200 LC/G1956A MSD and Agilent 1200\G6110A, Agilent 1200 LC & Agilent 6110 MSD

Method 1: 0-60CD_2MIN_220&254

Column	XBridge C18 2.1×50mm, 5μm
Column Temperature	40 °C
Eluents	A: 0.025% NH ₃ •H ₂ O in water (v/v) , B: Acetonitrile (v/v)
Flow Rate	1 ml/min
Gradient	1.2 min, 0% to 60% B; 0.4 min, 60% B, 60% to 0% B in 0.01 min, 0.39 min 0% B
Ionization source	ESI
Drying Gas	N ₂

Drying Gas Flow	10(L/min)
Nebulizer Pressure	35 (psig)
Drying Gas Temp	350(°C)
Capillary Voltage	2500(V)
MS Polarity	Positive
MS Mode	Scan
Mass range	100-1000

1-phenyl-1*H*-1,2,4-triazole-3,5-diamine (2)

The mixture of phenylhydrazine (128.6 g, 1.19 mol, 1 eq) and 1-cyanoguanidine (100 g, 1.19 mol, 1 eq) in hydrochloric acid (500 mL) (2 M) at reflux for 16 h. After being cooled to room temperature, the mixture was basified with aq. NaOH (40 wt%) to pH=8. The solvent was concentrated under reduced pressure. The residue was triturated with hexane (800 mL) for 1 h. The crude product was collected by filtration which was further triturated with DCM (1 L) for 16 h. The crude product was collected by filtration which was further triturated with DCM/MeOH (1 L/50 mL) for 16 h. The solid was collected by filtration and dried *in vacuo* to afford 1-phenyl-1*H*-1,2,4-triazole-3,5-diamine (140 g, crude) as a brown solid.

LC-MS (ESI): m/z (M+H) 176.0

***N,N'*-(1-phenyl-1*H*-1,2,4-triazole-3,5-diyl)bis(2-methylbenzamide) (FB231)**

To a solution of 1-phenyl-1*H*-1,2,4-triazole-3,5-diamine (60 g crude, 342 mmol, 1 eq) and pyridine (235 g, 2.97 mol, 240 mL, 8.68 eq) in ACN (400 mL) was added 2-methylbenzoyl chloride (225 g crude, 1.46 mol, 189 mL, 4.25 eq) at 80 °C. The mixture was stirred at 80 °C for 20 min. After being cooled to 15 °C, LiOH (62.8 g, 2.62 mol, 7.66 eq) in 100 mL H₂O was added to and the mixture was stirred at 15 °C for 16 h. The mixture was concentrated under reduced pressure. The mixture was extracted with CH₂Cl₂ (500 mL) and washed with H₂O (300 mL). The organic layer was separated and concentrated under reduced pressure. The residue was purified by reverse phase column (ACN/0.1% FA as additive) to give 24 g of crude product, which was purified by silica gel chromatography (petroleum ether / ethyl acetate =5/1 to 1/1) to afford *N,N'*-(1-phenyl-1*H*-1,2,4-triazole-3,5-diyl)bis(2-methylbenzamide) (20 g TFA salt, 93%purity) as an off-white solid. This TFA salt was dissolved in EtOAc (200 mL) and the solution was washed with aqueous NaHCO₃ (20%,

200 mL). The organic layer was separated and concentrated under reduced pressure to give 18 g freebase as a white solid. The residue (that was combined with 27 g of freebase, EW4062-260-P1) was dissolved in MeOH (150 mL) and hydrochloric acid (2 M, 150 mL). The solution was concentrated under vacuum to give 46.8 g of *N,N'*-(1-phenyl-1*H*-1,2,4-triazole-3,5-diyl)bis(2-methylbenzamide) HCl salt (99% purity) as a yellow solid. This batch of HCl salt was combined with 10.2 g of EW4062-262-P1 with 98% purity to give a single batch, which was registered as AH00231.01.06.

LC-MS (ESI): m/z (M+H) 412.2; ^1H NMR (400MHz, DMSO-*d*₆) δ = 11.25- 11.02 (m, 1H), 10.92 (s, 1H), 7.63-7.61 (m, 2H), 7.58-7.55 (m, 2H), 7.52-7.45 (m, 3H), 7.43-7.39 (m, 2H), 7.33-7.27 (m, 4H), 2.43 (s, 3H), 2.22 (s, 3H); ^{13}C NMR (75 MHz, DMSO-*d*₆) δ = 168.5, 167.6, 154.5, 145.3, 136.8, 136.2, 135.6, 134.1, 130.9, 130.6, 129.3, 128.5, 127.4, 125.7, 125.6, 123.5, 19.4, 19.2.

One-pot TPP experiment

The one-pot TPP protocol was adopted from literature with minor adjustment.(69,70) The cells are lysed by freeze-thaw in phosphate-buffered saline (PBS) using liquid nitrogen for 5 cycles. Cell debris was removed by centrifugation at 20000g for 15min. Protein concentration was determined using Bradford assay, and was adjusted to ~5 mg/ml. The lysate was subsequently aliquoted into 12 aliquots, and each aliquot was incubated with MTK or FB231 under different concentration for 1 hr under room temperature. The 12 samples were grouped into 3 sample groups, with 3 aliquots treated with each of the following drug concentration: 100 μM MTK, 40 μM FB231. The rest 6 samples were treated with only DMSO, and the DMSO concentration in each sample was adjusted to ~0.5% (v/v). Each of the 12 aliquots was further aliquoted into 12 aliquots, and each of the small aliquots was heated under each of the following temperatures (43.0C, 43.5C, 44.7C, 46.6C, 49.2C, 51.8C, 54.2C, 56.8C, 59.4C, 61.3C, 62.5C, and 63.0C). The aliquots were heated under corresponding temperature for 3 min, followed by 3 min equilibration under room temperature, before sitting back on ice. 12 aliquots for the same sample were pooled together, and the precipitation is removed by ultracentrifugation under 100000g for 20 min. The supernatant is collected and subjected to an isobaric-labeled filter-aided sample preparation (iFASP) protocol with minor changes.(71) Briefly, supernatant from each sample was

loaded onto a 10kDa Amicon filter (Pierce), and washed with 8M Urea in 100mM HEPES (Urea buffer) for 3 times. Without further notice, each washing step includes adding 200 ul of the corresponding solution followed by 14000 g centrifugation for 15 min. After 3 washes with Urea buffer, 200 ul of Urea buffer containing 5 mM tris(2-carboxyethyl)phosphine (TCEP) was added into each filter to break disulfide bonds. The reaction was allowed for 1hr under room temperature, and 200 ul of Urea buffer containing 20 mM of chloroacetamide (CAA) was added into each filter to alkylate free thiols. The alkylation reaction was allowed for 15 min under room temperature, and the filters were centrifuged for 14000 g for 15 min. The filters were further washed by 150 ul of 100 mM of triethylamine bicarbonate (TEAB) in water for 3 times. After TEAB washes, 120 ul of 100 mM TEAB containing 1 ug of Trypsin (Pierce) was added into each filter. Enzyme to substrate ratio should be around 1:50 to 1:100. The trypsinization step was allowing under 37C for 16 hr. After trypsinization, 41 ul of acetonitrile containing 0.5 mg of TMTpro reagent (Thermo) was added into each filter, and the labeling was allowed for 1 hr. 4 ul of 5% hydroxylamine was added into each filter to quench the TMT labeling, and samples were eluted from the filters by 14000g centrifugation for 15 min. The filters were further washed by 50 ul of 0.5 M NaCl in water for 3 times, and all elutes were pooled together. The pooled sample was dried using a CentriVap concentrator (LabConco), and was desalted with a monospin C18 column (GL Science) according to manufacturer's instruction. The desalted sample was dried again using a CentriVap concentrator, and was further fractionated into 8 fractions using the Pierce High pH Reversed-Phase Peptide Fractionation Kit (Pierce) according to manufacturer's protocol. The fractionated samples were dried again using CentriVap concentrator (LabConco) and stored under -80C until LC-MS/MS analysis.

LC-MS/MS analysis for TMT labeled samples

The samples were reconstituted in 20 ul of 2% acetonitrile and 0.2% formic acid in water. Peptide concentration was determined using the Pierce Colorimetric Quantitative Peptide Assay, and an aliquot of 500 ug of the peptide was used for LC-MS/MS analysis. The sample is separated on an Aurora UHPLC Column (25 cm × 75 μm, 1.6 μm C18, AUR2-25075C18A, Ion Opticks) using an Thermo Vanquish Neo liquid chromatography system. The gradient settings follows **Table 1**.

Time	Duration	Flow (nl/min)	%B
0:00	0:00	300	2
7:30	7:30	300	6
90:00	72:00	300	25
120:00	30:00	300	40
121:00	1:00	300	98
130:00	9:00	300	98

Table 1. LC gradient for TMT samples

Mobile Phase A contains 0.2% formic acid, 2% acetonitrile, and 97.8% water, and mobile Phase B contains 0.2% formic acid, 80% acetonitrile, and 19.8% water.

The samples were analyzed on a Thermo Eclipse Tribrid mass spectrometer using a data-dependent acquisition method. Detailed parameters of the scans are listed in **Table 2**.

Global settings	
Ion source type	NSI
Spray voltage	1500 V
Ion transfer tube temperature	275 C
Polarity	Positive
MS1 scan settings	
Resolution	120000
Normalized AGC target	250
Maximum IT	50 ms
Scan range	375-1600 m/z
MS2 scan settings	
Resolution	50000
Normalized AGC target	Standard
Maximum IT	Dynamic
Loop time	3 sec
Isolation window	0.7 m/z
NCE	35

Spectrum data type	Centroid
Fixed first mass	110z

Table 2. MS settings for TMT samples

Data analysis for TMT-labeled proteomic samples

The raw data generated by mass spectrometer is analyzed using Proteome Discoverer 2.5. The data is searched using the mouse proteome achieved from UniprotKB on 10/26/2022. The parameters for PD search are listed below in **Table 3**. All the parameters that are not mentioned are left defaulted.

SequestHT settings	
Enzyme name	Trypsin (Full)
Max. missed cleavage	2
Min. peptide length	6
Max. peptide length	144
Precursor mass tolerance	10 ppm
Fragment mass tolerance	0.02 Da
Max. equal modification	3
Dynamic modification	Oxidation/ +15.995 Da (M)
Dynamic modification (protein terminus)	Acetyl/ + 42.011 Da (N-Terminal)
Dynamic modification (protein terminus)	Met-loss/ - 131.040 Da (M)
Dynamic modification (protein terminus)	Met-loss+Acetyl/ - 89.030 Da (M)
Static modification (peptide terminus)	TMTpro/ + 304.027 Da (N-Terminal)
Static modification	TMTpro/ + 304.027 Da (N-Terminal)
Static modification	Carbamidomethyl/ + 57.021 Da (C)
Percolator	
Target/Decoy selection	Concatenated
Validation based on	q-Value

Target FDR (Strict)	0.01
Target FDR (Relaxed)	0.05

Table 3. Parameters for PD searching

The resulting data was exported as excel file and processed by in-house python scripts. Briefly speaking, the protein abundances were median normalized across samples, and Welch's t-test was used to test if the drug treated samples were significantly different from DMSO treated samples.

Software and code

1. Prism software (Version 10.2.3; GraphPad Software, Boston, MA, USA) for statistical analysis and graph generation (RRID:SCR_002798)
2. Image Lab software (Version 6.1; Bio-Rad Laboratories, Hercules, CA, USA) for densitometry analysis of western blots (RRID:SCR_014210)
3. ImageJ software (Schindelin et al. 2015) (Version 1.54j) for confocal microscopy image processing (RRID:SCR_003070)
4. MetaXpress software (Version 6.7.1.157; Molecular Devices, San Jose, CA, USA) for analysis of mt-Keima imaging (RRID:SCR_016654)
5. CytExpert software (Version 2.6; Beckman Coulter, Brea, CA, USA) for live analysis of flow cytometry data (RRID:SCR_017217)
6. FlowJo software (Version 10.10.0; BD Biosciences, Ashland, OR, USA) for analysis of flow cytometry data (RRID:SCR_008520)
7. Custom Python Scripts

2.6 Acknowledgments.

We thank the Youle lab for the YFP-Parkin Mitokeima and PINK1 KO cell lines as well as various plasmids. We thank Dr. Richard Youle for helpful discussions and critical review of the manuscript. We thank Dr. Chunxin Wang for his critical review. We thank Dr. Yogaditya Chakrabarty for help with analysis of mtKeima data, ISR shRNA's, and critical review. We thank Dr. Shiori Sekine and Dr. Lucas Jae for the KI DELE1-HA 293T line, and insight into the ISR/DELE1 pathway. We thank members of the Chou and Chan lab for helpful discussions. We thank Dr. Paul Fatheree and Dr. Albert W. Garofalo for their work on the development of FB231 and critical feedback, and Sarah Finley for compound management.

W.M.R was supported by the NINDS Intramural program and the Center for Alzheimer's and Related Dementia, NIA/NINDS NIH. This research was supported (in part) by the Intramural Research Program of the NIH, NINDS. This work was funded in part by the Merkin Institute for Translational Research at Caltech, NIH grant R35GM127147 (D.C.C.), and the Michael J. Fox Foundation (J.A.J.).

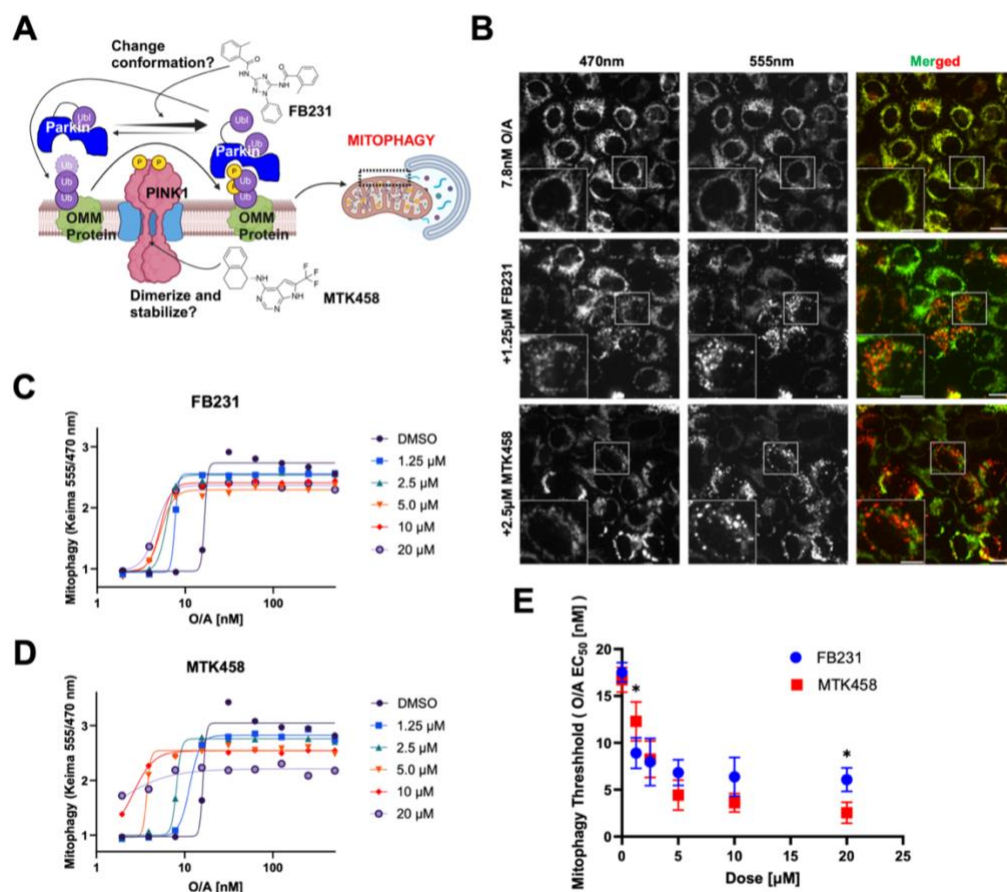


Figure 2.1: PINK1/Parkin activators lower the threshold for mitophagy induction. (A) Diagram detailing the proposed mechanism of FB231 and MTK458 in the PINK1/Parkin pathway's activation. **(B)** Confocal imaging of mt-Keima-expressing HeLa cells after treatment with 7.8 nM O/A alone, 7.8 nM O/A and 1.25 µM FB231, or 7.8 nM O/A and 2.5 µM MTK458 for 6 h. Scale bars, overviews, 20 µm; insets, 10 µm. **(C)** mt-Keima assay of YFP-Parkin mt-Keima HeLa cells treated with varying doses of O/A and different doses of the Parkin activator FB231 for 6 h each colored uniquely. Data is normalized to DMSO alone at 6 h. Solid lines are fits to the Hill equation to determine the EC₅₀. **(D)** As in (C), with the compound MTK458. **(E)** Mitophagy induction threshold, or the O/A EC₅₀, is calculated for each dose of FB231 (blue)

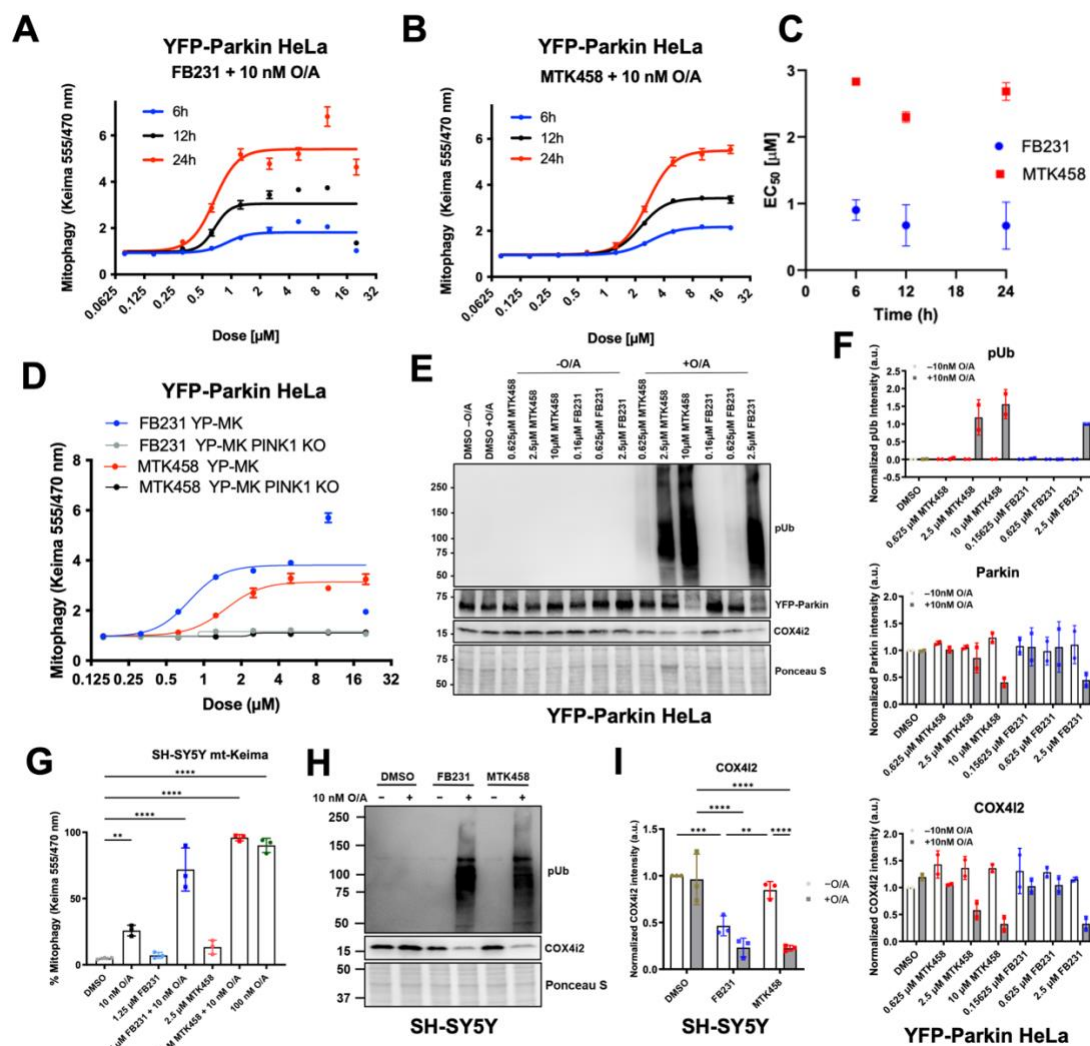


Figure 2.2: Parkin/PINK1 activators enable potent activation of the PINK1/Parkin pathway. (A) YFP-Parkin/mt-Keima-expressing HeLa cells were treated with O/A and varying doses of FB231, the mt-Keima signal measured at 6, 12, and 24 h after treatment (N=3). Solid lines represent fits to the Hill equation to determine EC₅₀. (B) As in (A) with MTK458. (C) EC₅₀ of FB231 and MTK458 are calculated for each time point (N=3). Error represents the standard deviation of residuals of each point from fits to the Hill equation. (D) As in (A) with YFP-Parkin/ mt-Keima-expressing WT and PINK1 KO HeLa cells. (E) Immunoblots of mitophagy biomarkers pUb, YFP-Parkin, and COX4I2 in YFP-Parkin/mt-Keima-expressing HeLa cells treated with varying doses of FB231 or MTK458 with or

without 10 nM O/A for 6 h. **(F)** Normalized densitometry analysis of (E), (N=2). **(G)** Flow cytometry analysis of mt-Keima-expressing SH-SY5Y cells treated with different combinations of O/A, FB231, and MTK458 for 24 h (N=3). Data represents the proportion of cells undergoing mitophagy as indicated by the ratio of mt-Keima 555/470 nM emission for at least 15K cells. **(H)** Immunoblot of COX4I2 in SH-SY5Y cells treated with or without 10 nM O/A for 16 h alone or in combination with 10 μ M FB231 or 5 μ M MTK458. **(I)** Normalized densitometry analysis of COX4I2 in (H), (N=3). All cells were administered with 20 μ M Q-VD-Oph to prevent cell death. Ponceau S stain was used as total protein loading control. Data are presented as mean \pm SD; **P \leq 0.01, ***P \leq 0.001, ****P \leq 0.0001 (G: One-way ANOVA; I: Two-way ANOVA).

and MTK458 (red). Symbols are mean \pm SD from three independent experiments; *p \leq 0.05, two-way ANOVA.

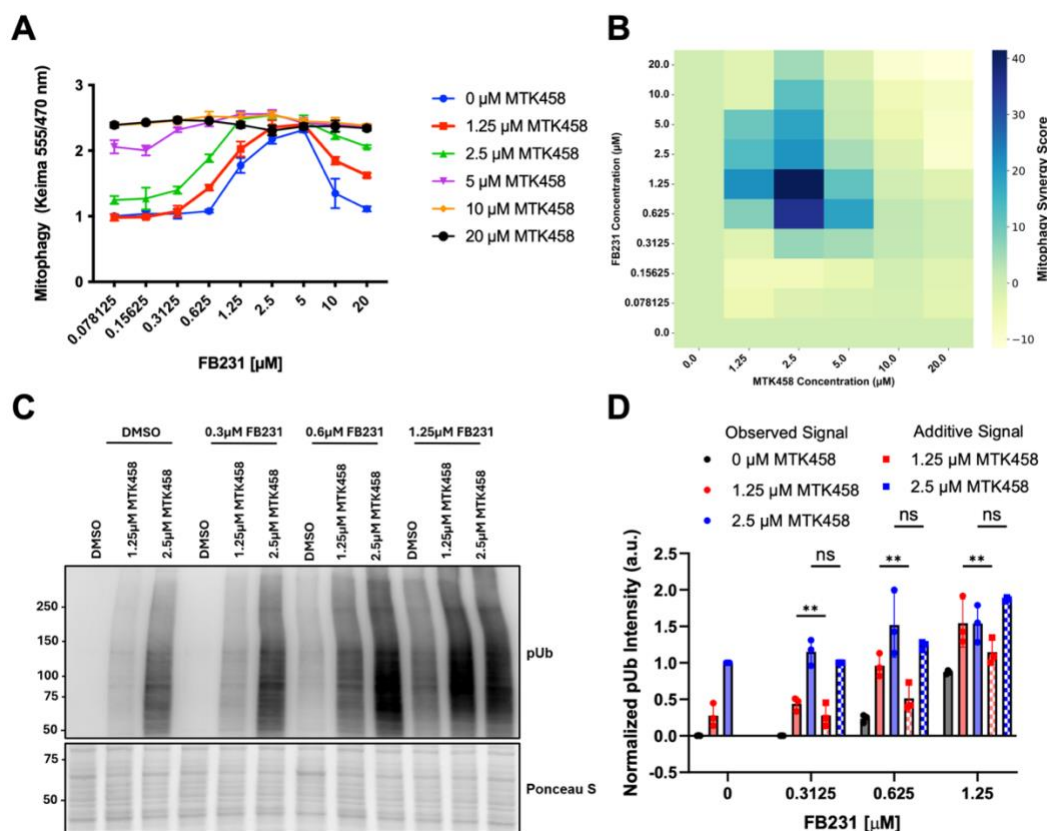


Figure 2.3: FB231 and MTK458 can be used to synergistically enhance mitophagy. (A) YFP-Parkin/mt-Keima-expressing HeLa cells were treated with 10 nM O/A and varying combinatorial doses of FB231 and MTK458 for 6 h whereupon mt-Keima signal was measured. Each combinatorial dose is represented as colored points connected with solid lines. Three cell wells are measured for each point. (B) ZIP Synergy score calculated for each dose of FB231 and MTK458 from (A). Positive synergy (blue) peak is observed in the region around 1.25 μM FB231 and 2.5 μM MTK458. Negative synergy (yellow) is observed at the highest doses of FB231. (C) YFP-Parkin/mt-Keima HeLa cells were treated with combinatorial doses identified in (B) to induce synergy for 6 h and analyzed via western blot. Western blotting detected pUb for cells treated with varying doses of FB231 or MTK458 and with or without 10 nM O/A. Ponceau stain is used as a total protein loading control. (D) Normalized densitometry analysis of (C). Solid colors represent measured pUb signal compared to the additive signal expected if the combination of the compounds were purely

additive (checkered). Data in (D) are mean \pm SD from three independent experiments; **p \leq 0.01 (Two-way ANOVA).

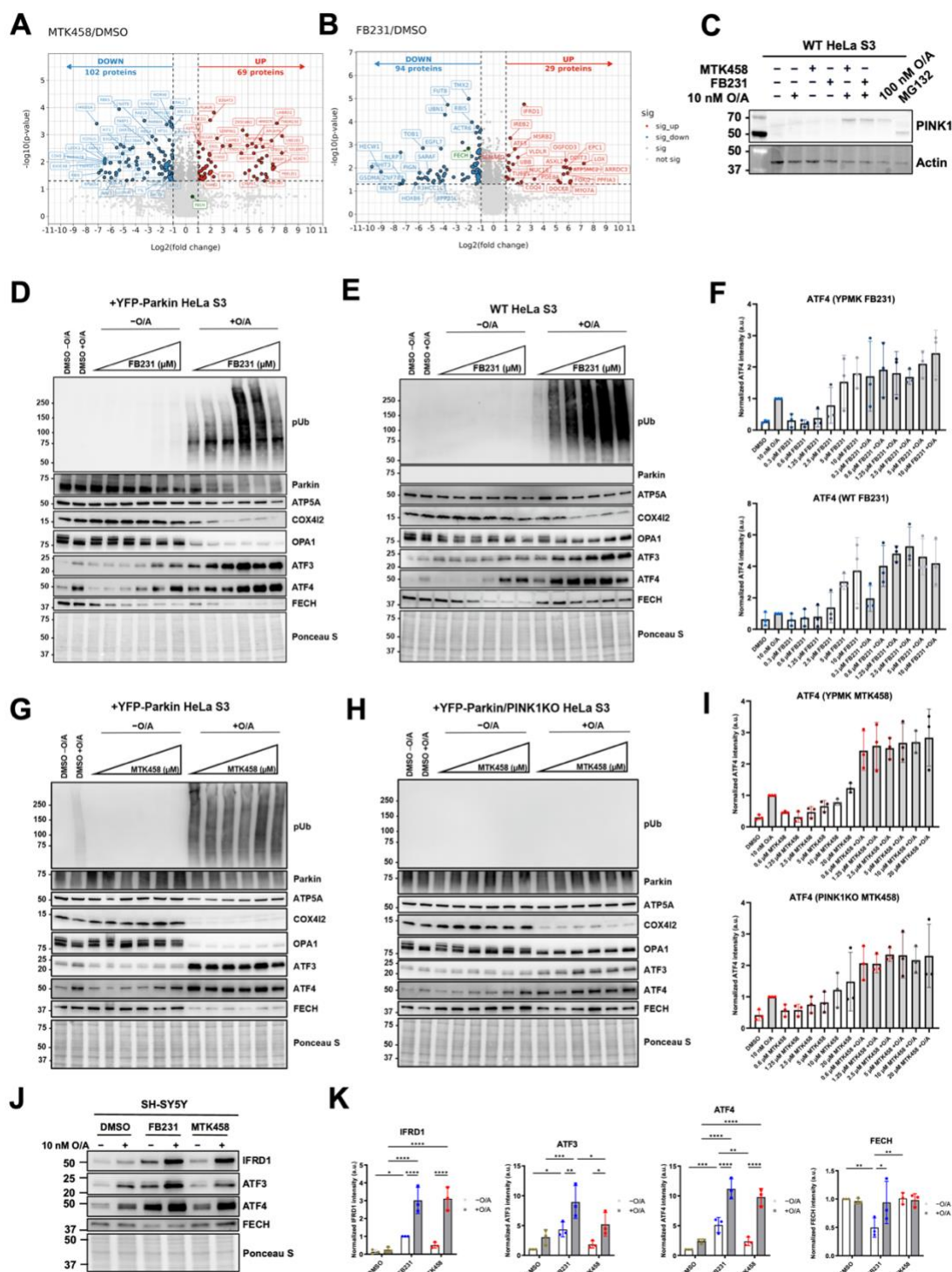


Figure 2.4. Label free proteomics identifies the Integrated Stress Response as Off-Target effects of FB231 and MTK458. (A and B) Volcano plots of label-free proteomics

of YFP-Parkin-expressing HeLa cells treated for 12 h with DMSO, (A) 20 μ M MTK458, or (B) 10 μ M FB231. Proteins with lower expression levels compared to DMSO (\log_2 -fold-change < -1 , $P < 0.05$) in blue; proteins with higher expression compared to DMSO (\log_2 -fold-change > 1 , $P < 0.05$) in red. (C) Immunoblot of PINK1 in WT HeLa cells treated with various combinations of O/A, FB231, MTK458, and MG132 proteasome inhibitor for 16 h. β -actin was used as protein loading control. (D) Immunoblots of proteins involved in mitophagy, mitochondrial stress, and integrated stress response in YFP-Parkin-expressing HeLa cells treated with 10 nM O/A and 0.3–10 μ M FB231 for 16 h. (E) As in (D) with WT HeLa cells. (F) Normalized densitometry analysis of ATF4 integrated stress response biomarker in (D) and (E), (N=3). (G) As in (D) with 0.6–20 μ M MTK458 (H) As in (G) for YFP-Parkin/PINK1KO HeLa cells. (I) Normalized densitometry analysis of ATF4 in (G) and (H), (N=3). (J) Immunoblots of IFRD1, ATF3, ATF4, and FECH in WT SH-SY5Y cells treated with 10 nM O/A, 10 μ M FB231, and 5 μ M MTK458 for 16 h. (K) Normalized densitometry analysis of (J), (N=3). All cells were administered with 20 μ M Q-VD-OPh to prevent cell death. Ponceau S stain was used as a total protein loading control, unless stated otherwise. Data are presented as mean \pm SD; * $P \leq 0.05$, ** $P \leq 0.01$, *** $P \leq 0.001$, **** $P \leq 0.0001$ (Two-way ANOVA).

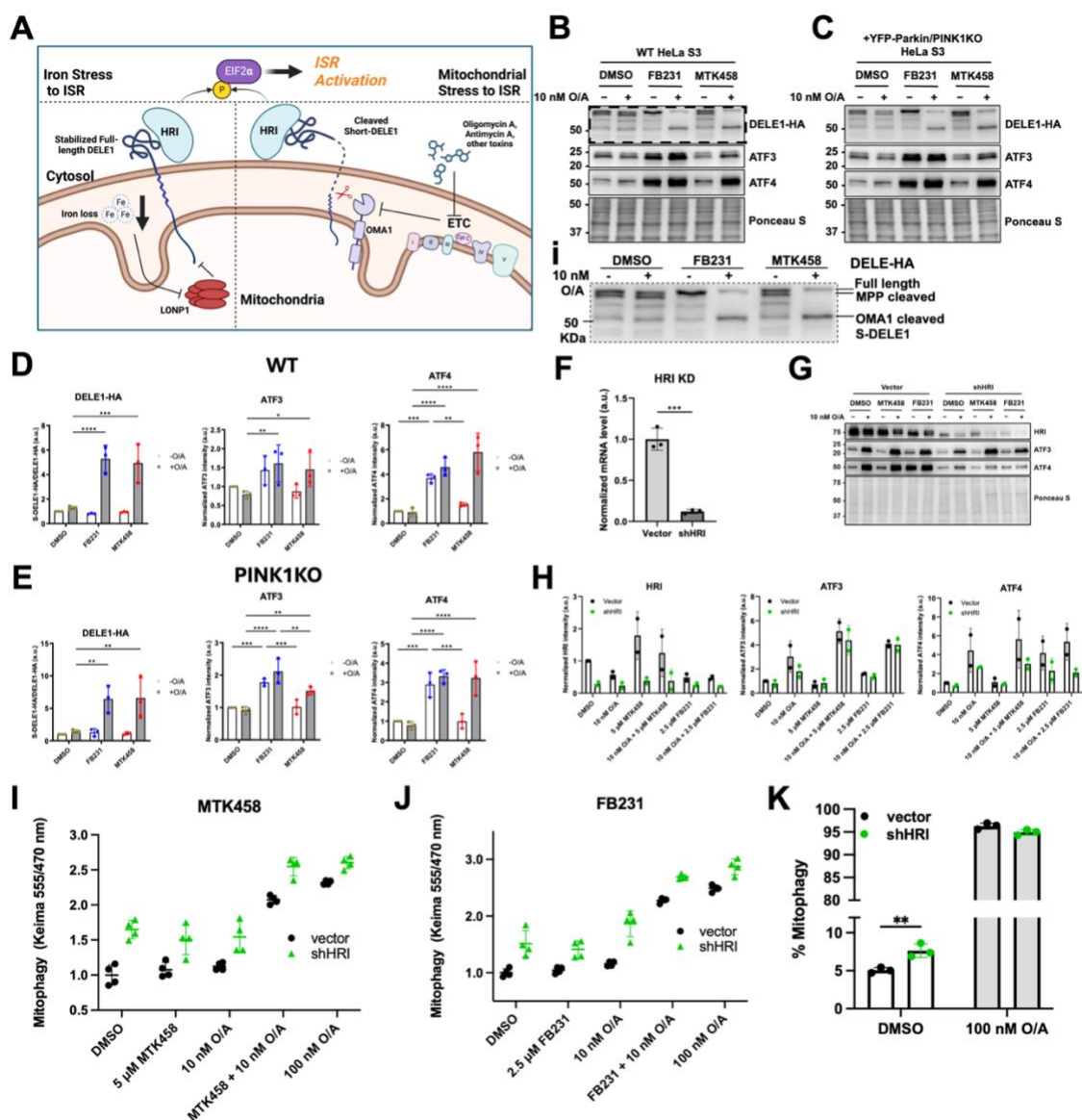


Figure 2.5: FB231 and MTK458 induce mitophagy independently of the integrated stress response. (A) Diagram detailing the activation of the integrated stress response upon exposure to mitochondrial toxins. (B and C) Immunoblots of integrated stress response biomarkers in (B) WT or (C) YFP-Parkin/PINK1KO HeLa cells treated with 10 nM O/A, 10 μM FB231, and 10 μM MTK458. Inset i depicts full-length, MPP-cleaved, and OMA1-cleaved DELE1-HA in (B). (D and E) Normalized densitometry analysis for (B) and (C), respectively (N=3). (F) Effectiveness of shRNA knockdown of HRI by qPCR analysis. (N=3). (G) Immunoblots of integrated stress response biomarkers in YFP-Parkin-expressing

HeLa cells expressing an HRI-targeting shRNA or the same plasmid vector lacking the shRNA-producing region treated with 10 nM O/A, 2.5 μ M FB231 or 5 μ M MTK458 with and without O/A for 16 h. **(H)** Normalized densitometry analysis of integrative stress response biomarkers in (G), (N=2). **(I and J)** mt-Keima assay of HRI knockdown YFP-Parkin/mt-Keima-expressing HeLa cell lines treated with O/A and (I) MTK458 or (J) FB231 for 6 h (N=4). **(K)** Flow cytometry analysis of mt-Keima-expressing HeLa cells treated with DMSO or O/A for 24 h (N=3). Data represents the proportion of cells undergoing mitophagy as indicated by the ratio of mt-Keima 555/470 nM emission for at least 30K cells. All cells, except in (C), were administered with 20 μ M Q-VD-Oph to prevent cell death. Ponceau S stain was used as a total protein loading control. Data are presented as mean \pm SD; *P \leq 0.05, **P \leq 0.01, ***P \leq 0.001, ****P \leq 0.0001 (D, E, K: Two-way ANOVA; F: Student's t-test).

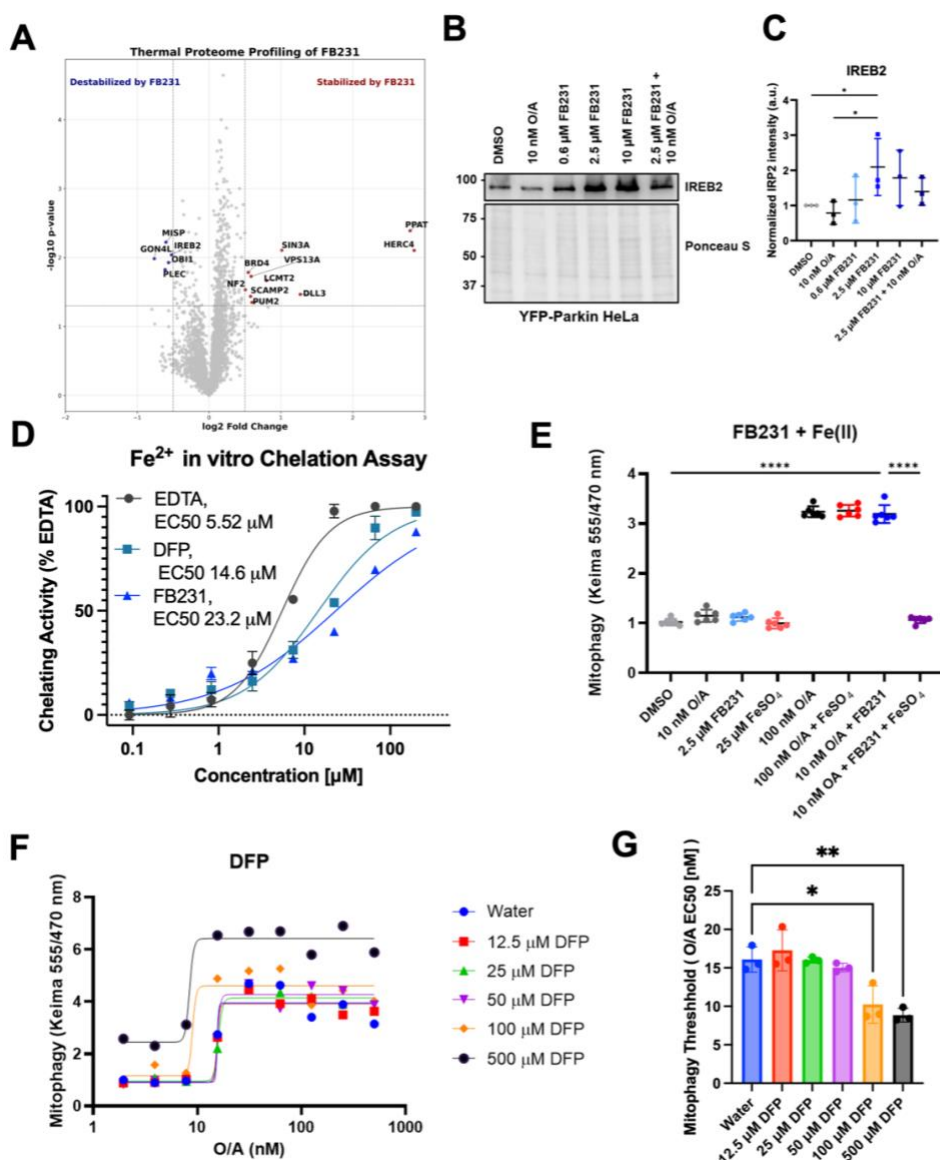


Figure 2.6: FB231 induces mitophagy through an iron-chelation based mechanism. (A) Volcano plot of thermal proteome profiling of YFP-Parkin-expressing HeLa cell lysate treated with 40 μM FB231 compared to equivalent DMSO-treated lysate. Significantly destabilized proteins compared to DMSO, with fold-change < -1 and P < 0.05 indicated in blue. Proteins significantly stabilized compared to DMSO, fold-change > 1 and P < 0.05 indicated in red. Gene names of significantly altered proteins are labelled. (B) Immunoblots of iron-sensitive protein IREB2 in YFP-Parkin-expressing HeLa cells treated with various doses of FB231 or in combination with 10 nM O/A. (C) Normalized densitometry analysis

of (B), (N=3). **(D)** In vitro ferrous ion (Fe^{2+}) chelation assay using colorimetric analysis of ferrozine. EDTA, DFP, and FB231 chelation ability is normalized to the maximum chelating activity observed for EDTA. Points represent mean and standard deviation (N=3) for individual well measurements, solid lines represent corresponding fits of the data to a 4-parameter Hill equation used to determine the EC_{50} . **(E)** mt-Keima-based mitophagy assays for YFP-Parkin HeLa cells treated alone or in combinations of FB231, 10 nM O/A, 25 μM FeSO_4 , and 100 nM O/A for 24 h (N=6). **(F)** mt-Keima-based mitophagy assay of YFP-Parkin/mt-Keima-expressing HeLa cells treated with varying doses of O/A and previously reported mitochondrial toxin DFP for 24 h. **(G)** Mitophagy induction threshold, the EC_{50} of O/A for mitophagy, is calculated for each dose of DFP (N=3). All cells were administered with 20 μM Q-VD-OPh to prevent cell death. Data are presented as mean \pm SD; * $P \leq 0.05$, ** $P \leq 0.01$, *** $P \leq 0.0001$ (One-way ANOVA).

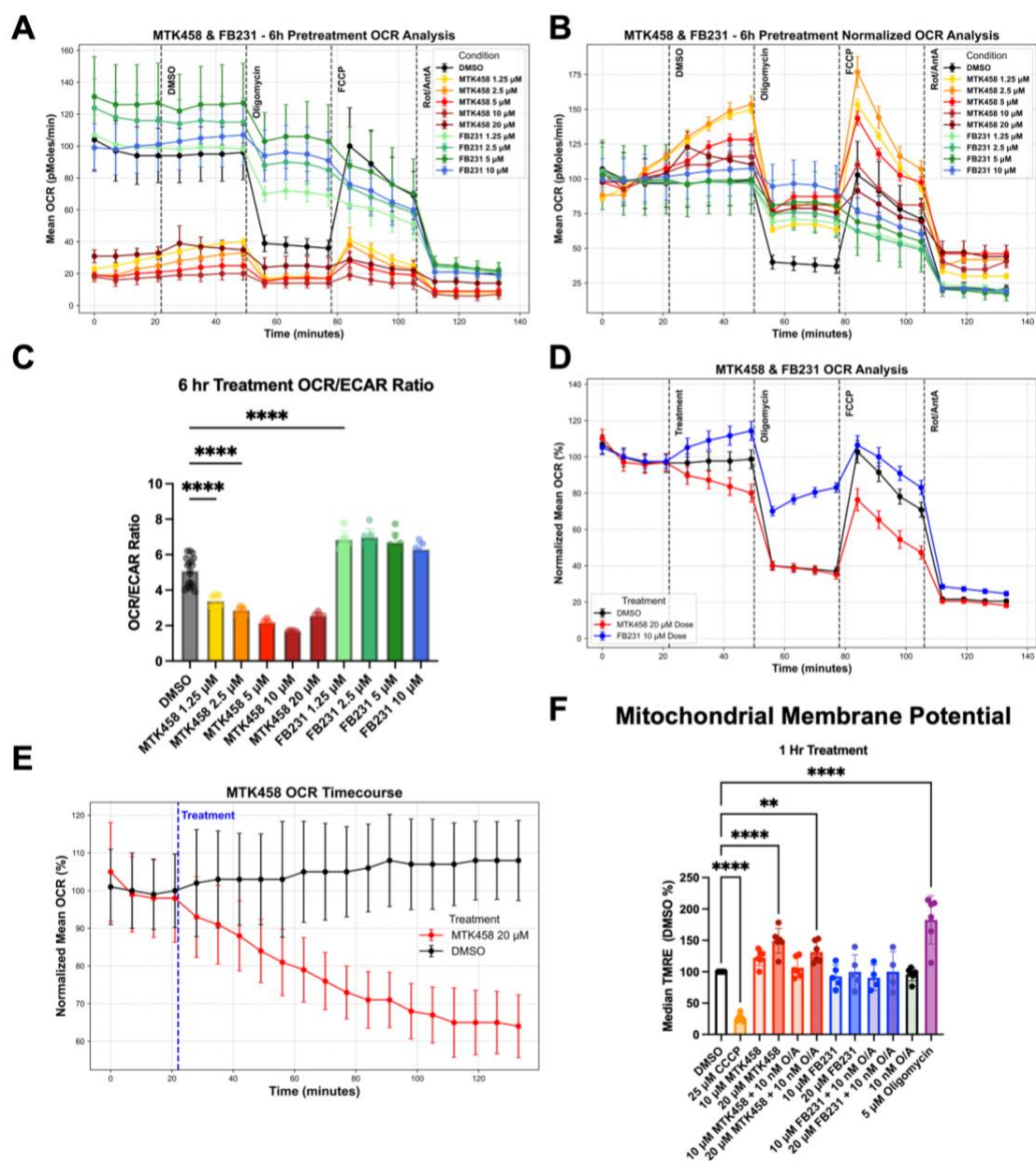


Figure 2.7: FB231 and MTK458 inhibit mitochondrial function through distinct mechanisms. (A) Raw Seahorse XF OCR plots for WT HeLa cells treated for 6 h with increasing concentrations of MTK458 (yellow-orange-red), FB231 (green-blue), or DMSO control (black). Cells were treated with inhibitors at the time indicated by the vertical dotted line. (B) OCR plots in (A) normalized to the average of the first 4 time points for each treatment condition. Data is given as the % of the initial average. (C) Initial OCR/ECAR ratio for cells treated for 6 h with varying doses of MTK458, FB231, or DMSO control. (D)

Normalized OCR plot of WT HeLa cells treated in real time with MTK458, FB231, and DMSO followed by mitochondrial inhibitors at the indicated times (N=4). **(E)** Normalized OCR plot of WT HeLa cells treated with either 20 uM MTK458 or DMSO and measured every 7-min for ~2 h. **(F)** Flow-cytometry analysis of mitochondrial membrane potential measured by TMRE median fluorescence in cells treated with indicated compound cocktails for 1-2 h prior to analysis. Each colored dot represents the average of three cell-well replicates from at least 4 separate experiments. Dotted bars represent the addition of 10 nM O/A. All data from seahorse experiments represents the mean of at least four separate wells. Data are presented as means \pm SD; *P \leq 0.05, **P \leq 0.01, ****P \leq 0.0001 (One-way ANOVA).

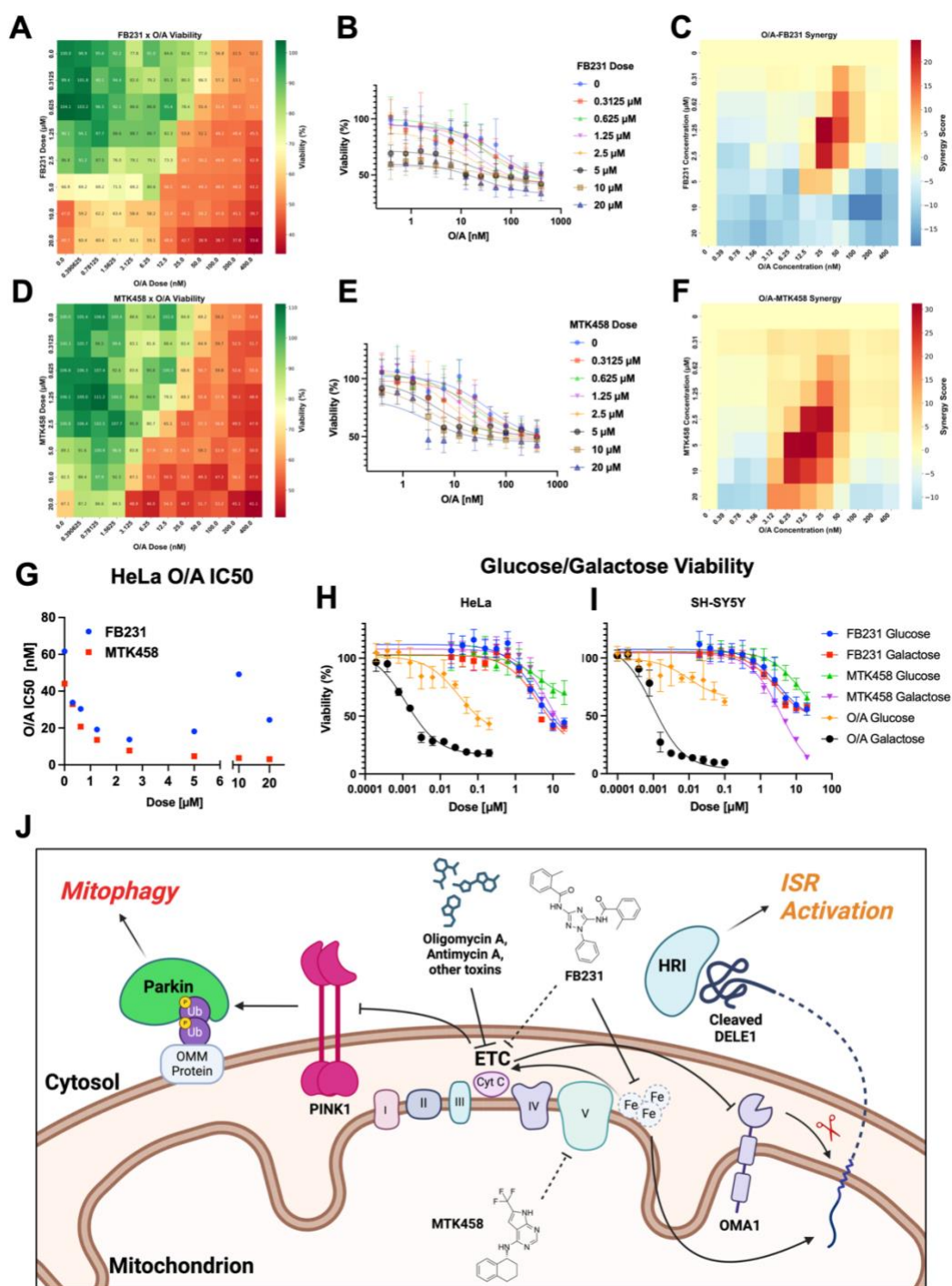


Figure 2.8: FB231 and MTK458 sensitize cells to mitochondrial stress. (A) Heatmap showing cell viability in WT HeLa cells treated with combinatorial doses of FB231 and O/A for 24 h (N=8). **(B)** WT HeLa viability dose response curves for O/A at increasing doses of

FB231 (N=8). Solid lines are fits to a Hill equation to determine the IC_{50} . **(C)** Synergy score heat map of O/A and FB231 combinations on cell viability. **(D)** As in (A) for cells treated with MTK458 and O/A. **(E)** As in (B) for MTK458 (N=8). **(F)** As in (C) for MTK458. **(G)** Plot of calculated O/A viability IC_{50} at different doses of FB231 (blue) or MTK458 (red). **(H)** Dose-viability plot of WT HeLa cells in glucose-containing media or galactose-containing media treated with increasing doses of O/A, FB231, or MTK458 for 24 h (N=8). Solid lines represent fits the Hill equation. **(I)** As in (H) for WT SH-SY5Y cells (N=8). **(J)** Diagram detailing the activation of PINK1/Parkin-mediated mitophagy and integrated stress response upon exposure to various mitochondrial toxins. Data are presented as means \pm SD.

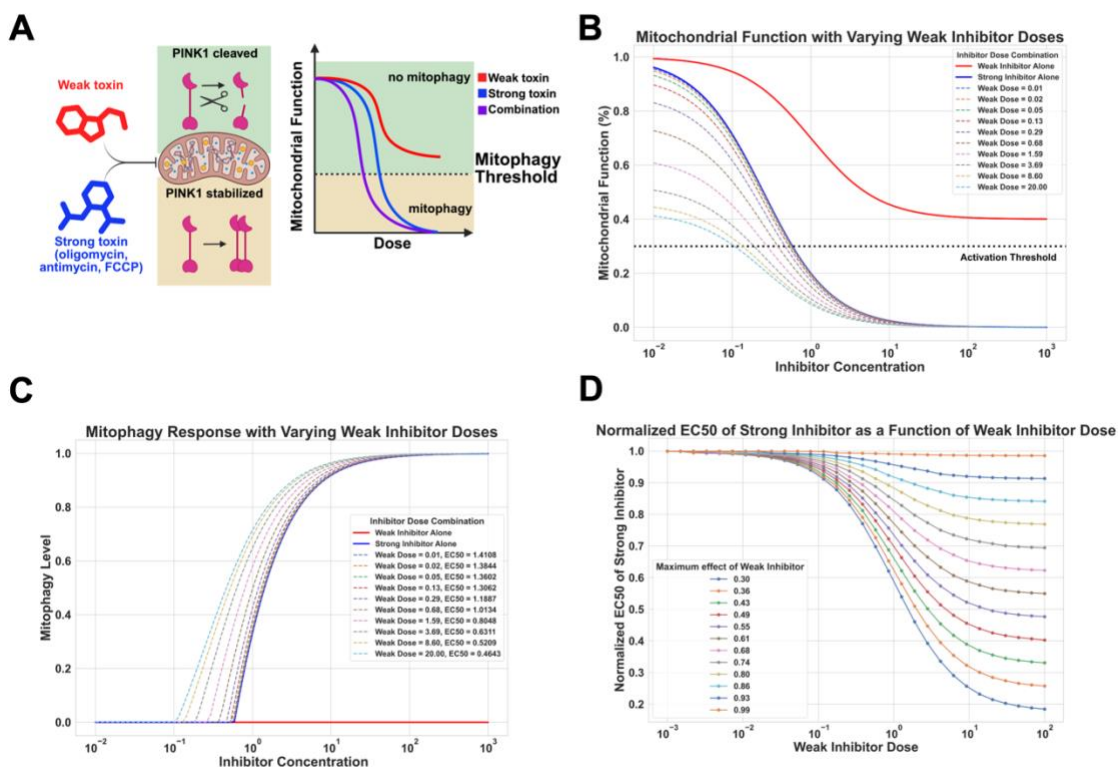


Figure 2.9: Mathematical Modeling of mitochondrial inhibitors combinations on the induction of mitophagy. (A) Simplified model of mitochondrial toxin combinations altering mitochondrial function and mitophagy levels via PINK1 accumulation. (B) Mitochondrial function parameter as function of a Weak Inhibitor (red) with subthreshold mitochondrial toxicity, and a Strong Inhibitor (blue). The effect of the inhibitor is modeled as a Hill curve, with the response of combinations of inhibitors being multiplied together. Colored dashed curves represent the inhibition of mitochondrial function observed at a range of doses of the Strong Inhibitor, when co-treated with a constant dose of the Weak Inhibitor. (C) Apparent mitophagy as a function of inhibitor dose. Mitophagy is modeled as piecewise function dependent on the induction threshold. When mitochondrial function is above the threshold, mitophagy is set at 0. At, or below the threshold, mitophagy is modeled as a power-law of the proportion of mitochondrial function below the threshold. The effect of the Weak Inhibitor is shown in red; the Strong Inhibitor in blue. Dashed curves represent the Mitophagy dose response for the Strong Inhibitor at varying doses of Weak Inhibitor. The 50% mitophagy threshold (EC₅₀) is reduced at increasing doses of the Weak Inhibitor. (D)

The relative mitophagy induction threshold of the Strong Inhibitor, (EC_{50}), is calculated as a function of the Weak Inhibitor dose. EC_{50} is normalized to that of the Strong Inhibitor alone. Each color represents the EC_{50} of the Strong Inhibitor calculated for the Weak Inhibitor's maximum inhibitory effect on mitochondrial function.

Supplementary Tables and Figure Legends:

Table S2.1: In vitro and in vivo comparison of CMPD001 properties and DMPK.

	In Vitro DMPK							
	MDCK P _{app} (10 ⁻⁶ cm/s) A to B	Kin. Sol. (μ M)	HLM t1/2 (min)	RLM t1/2 (min)	cLogP			
CMPD001	20	157	151	21	3.7			
FB231	16	166	578	630	4.4			
	In Vivo DMPK - Rat							
	IV (1 mg/kg)		PO (5 mg/kg)		IP 3 mg/kg			
	Cl (mL/min/kg)	V _{ss} (L/kg)	%F	AUC (0-t) (ng.hr/mL)	AUC (0-t) (ng.hr/mL)	C _{max} (ng/mL)	t1/2 (hr)	%F
CMPD001	15.7	0.4	7%	0.4K				
FB231	4	0.4	24%	5.2K	10K	1.5K	3.2h	75%

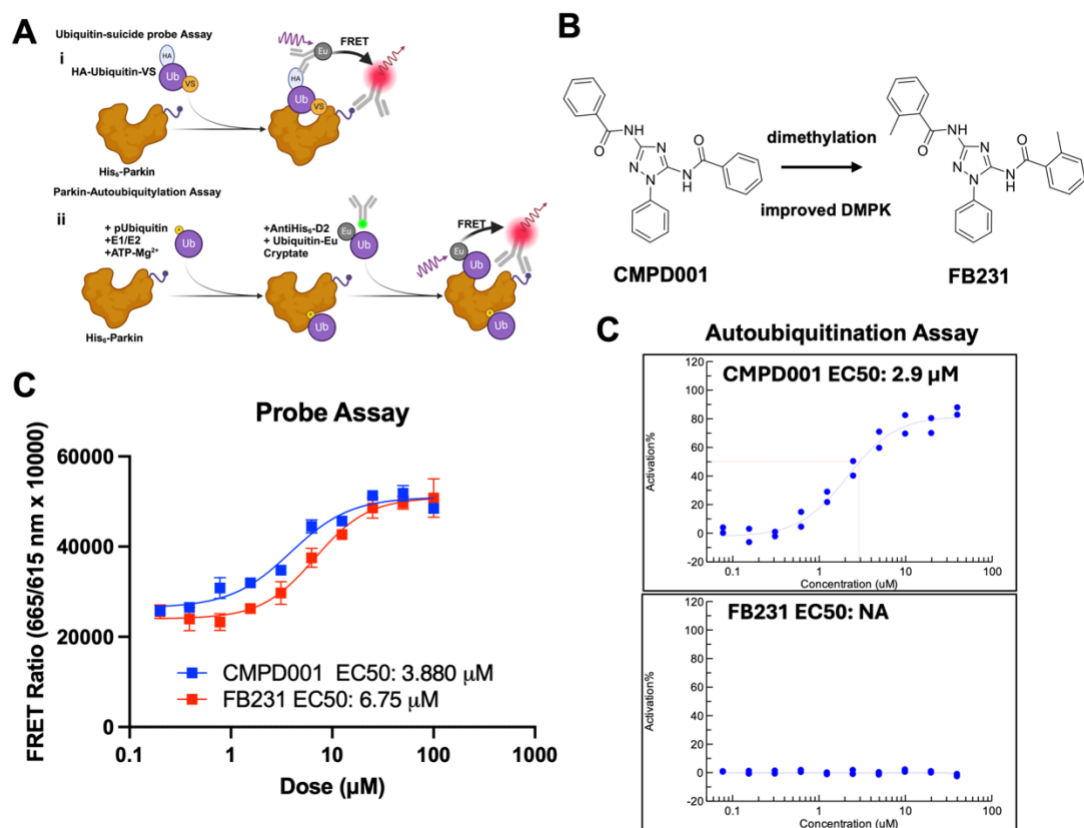


Figure S2.1: Identification of Parkin activating compounds through an in vitro ubiquitination assay. (A) Cartoons representing the scheme for the Ubiquitin-suicide probe assay. **(B)** Chemical structures of CMPD001 and FB231. **(C)** A representative assay readout of the Ubiquitin Probe assay for CMPD001 (Red) and FB231 (Blue), (N=2). Lines represent fits Hill Equation fits to the data to calculate the EC₅₀.

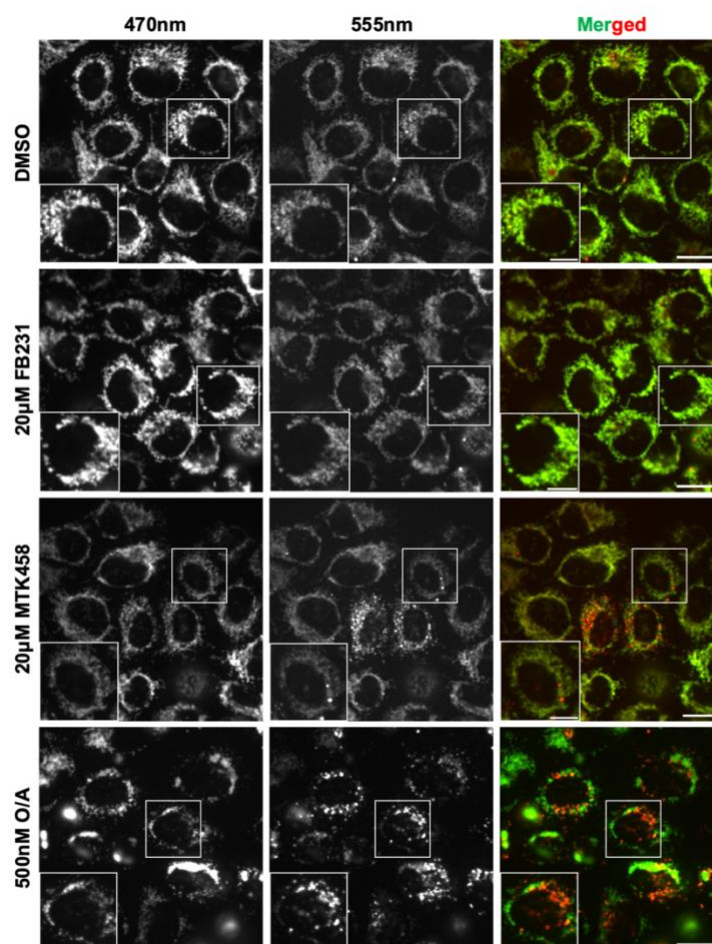


Figure S2. Mitophagy activators do not induce mitophagy without prior mitochondrial damage. Representative confocal images of YFP-Parkin/mt-Keima-expressing cells treated with FB231 or MTK458 alone. No 555 nm puncta induction are observed in the activators alone, whereas 500 nM O/A induces clear mitolysosomal puncta. Scale bars: overviews, 20 μm; insets, 10 μm.

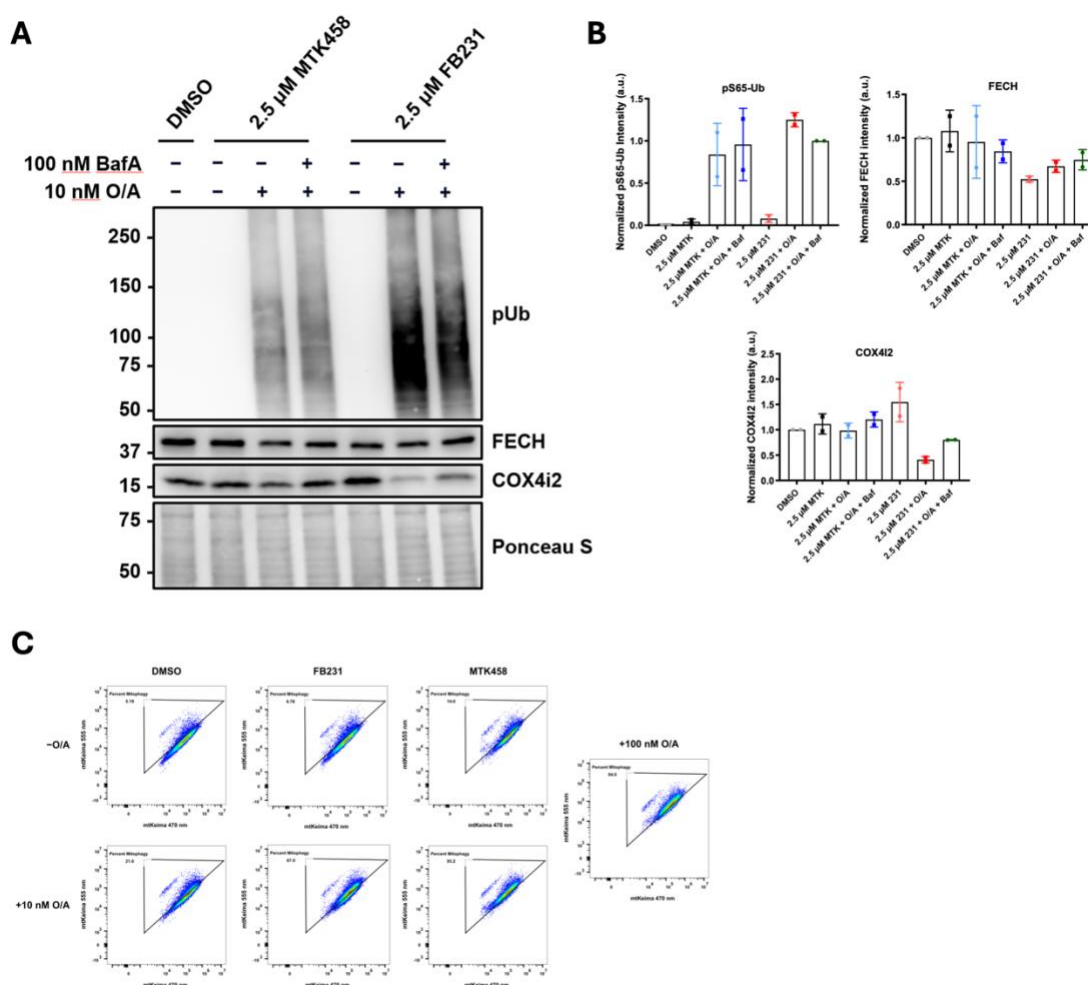


Figure S2.3. Additional data related to Figure 2, Parkin/PINK1 activators enable potent activation of the PINK1/Parkin pathway. (A) Immunoblots of YFP-Parkin-expressing HeLa cells treated with or without 10 nM O/A and 2.5 μ M MTK458/FB231 and 100 nM BafA for 6 h. (B) Normalized densitometry measurements for (A), (N=2). (C) Representative flow cytometry plots of mt-Keima-expressing SH-SY5Y cells treated with DMSO, 10 nM O/A, 1.25 μ M FB231, 2.5 μ M MTK458, a combination of 10 nM O/A and FB231/MTK458 at the same doses, or 100 nM O/A for 24 h. For each sample, at least 30,000 events were collected and subsequently gated for live, single cells expressing mt-Keima. Data represents the percentage of cells undergoing mitophagy as indicated by the ratio of mt-Keima 555/470 nm emission.

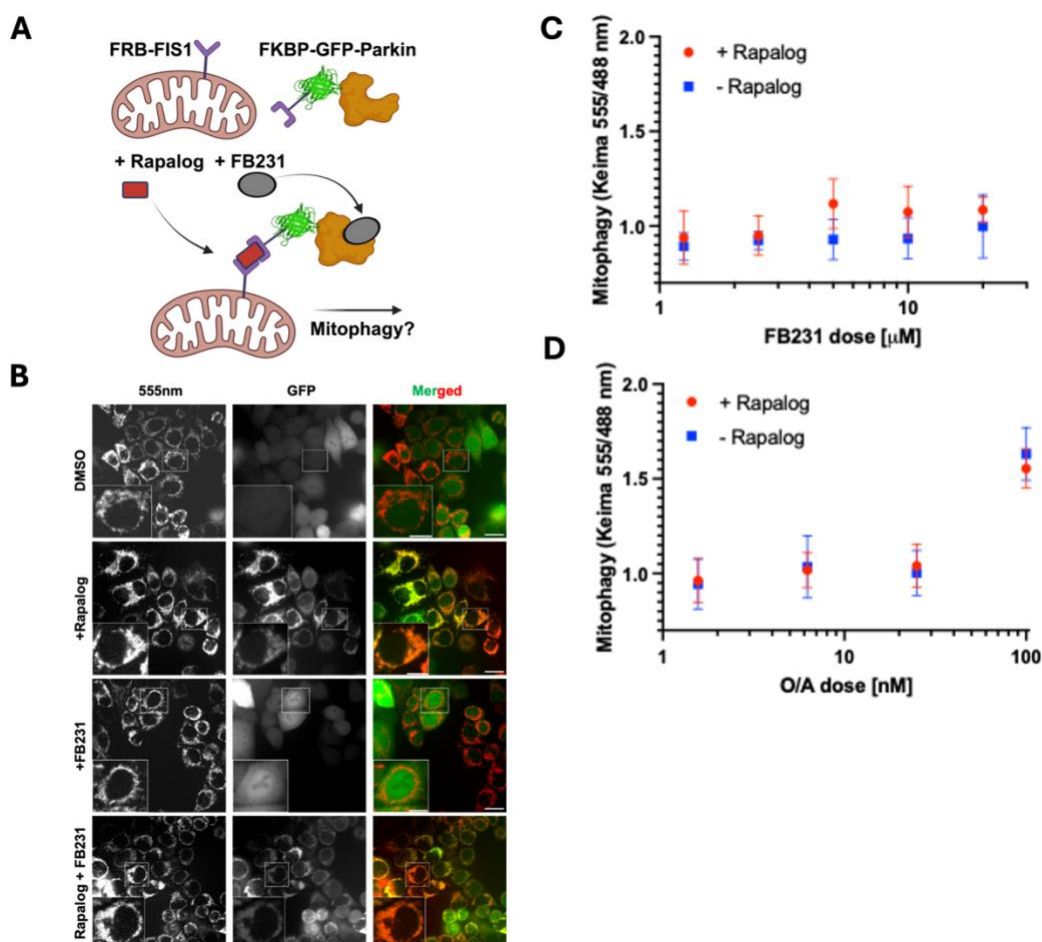


Figure S2.4. FB231 cannot be utilized in a Parkin-AutoTAC strategy. (A) Cartoon scheme of the CID Parkin recruitment assay to test the potential of FB231 in a Parkin-PROTAC. Parkin is tagged with FKBP-GFP while mt-Keima-expressing mitochondria are tagged with FRB-FIS1. Upon addition of a rapalog, Parkin is forced to the surface of the mitochondria. Varying doses of FB231 are added. (B) Representative confocal images of cytosolic FKBP-GFP-Parkin (Green) being recruited to the mitochondria (mt-Keima 555 nm) upon rapalog addition (200 nM). Scale bars: overviews, 20 μm ; insets, 10 μm . (C) mt-Keima measurement of the Parkin recruitment assay with (red) or without (blue) rapalog upon increasing doses of FB231 after 24 h. (D) As in (C) with O/A.

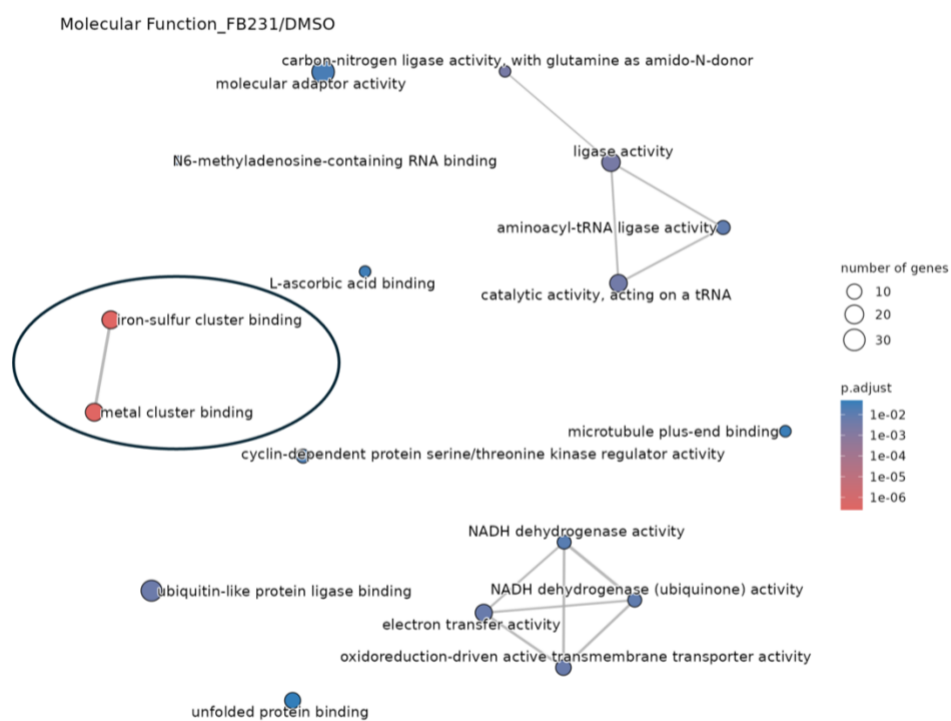


Figure S2.5: Proteomics identified pathways altered by FB231. GO enrichment analysis of molecular functions shows significant alterations of a cluster of proteins related to iron-sulfur/metal cluster binding in YFP-Parkin-expressing HeLa cells upon treatment with 10 μ M FB231.

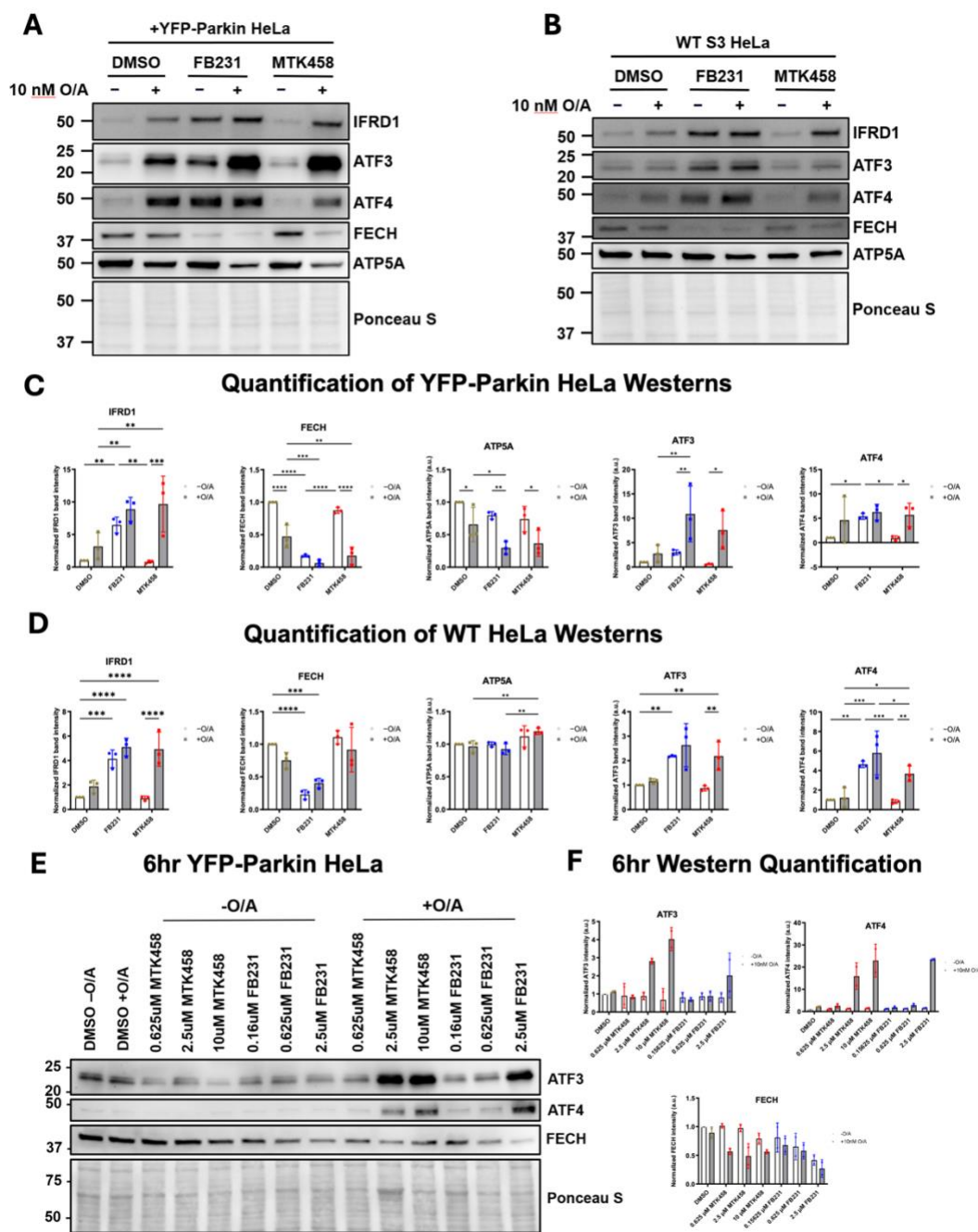


Figure S2.6: Additional blots related to Figure 4, Off-Targets of FB231 and MTK458. (A and B) Immunoblots of markers identified in the proteomic data sets. (A) YFP-Parkin-expressing and (B) WT HeLa cells were treated with DMSO, 10 nM O/A and/or 10 uM FB231 or 5 uM MTK458 for 16 h. (C and D) Normalized densitometry analysis for

immunoblots in (A) and (B), respectively (N=3). **(E)** Immunoblots of ATF3, ATF4, and FECH in YFP-Parkin-expressing HeLa cells treated with various doses of MTK458/FB231 for 6 h with or without 10 nM O/A. **(F)** Normalized densitometry analysis for immunoblots in (E), (N=2). Data are presented as mean \pm SD; *P \leq 0.05, **P \leq 0.01, ***P \leq 0.001, ****P \leq 0.0001 (Two-way ANOVA).

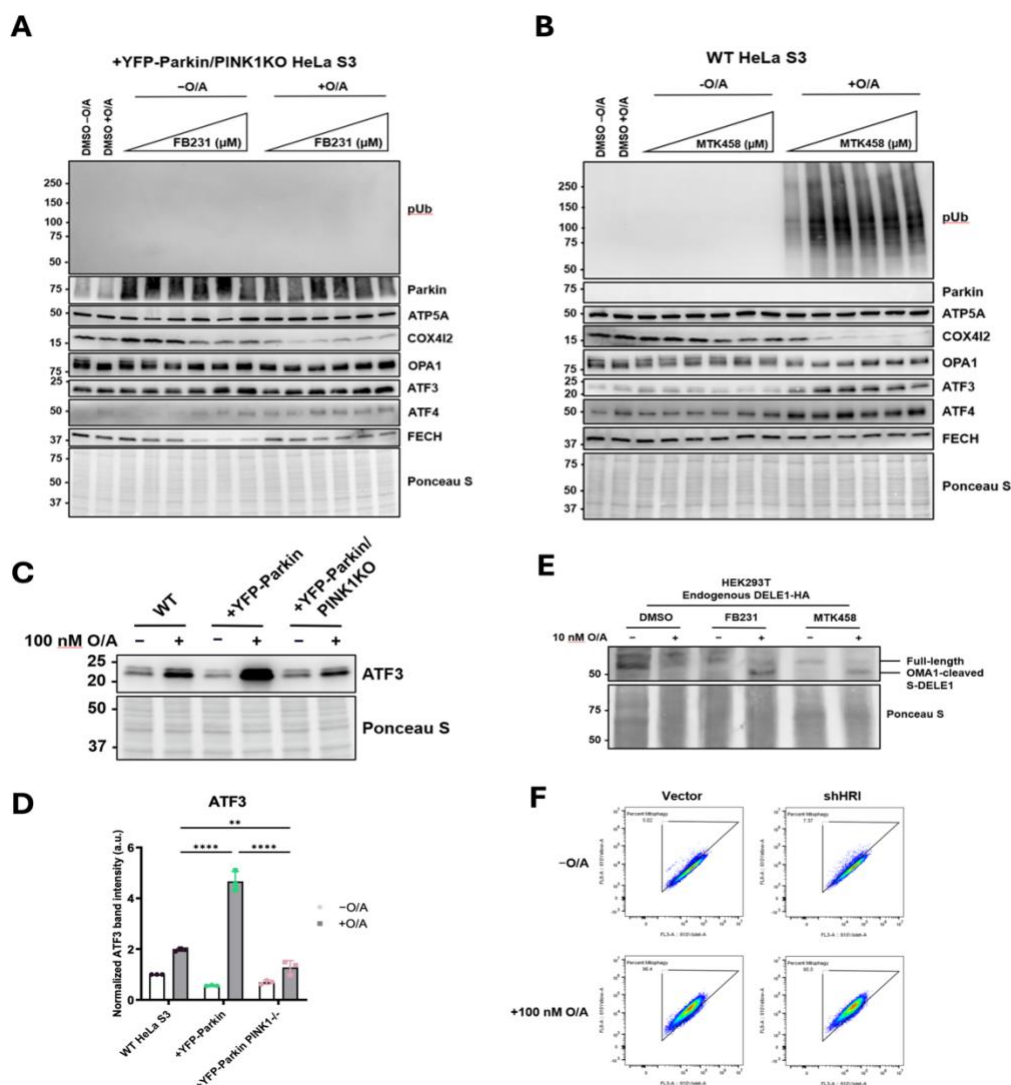


Figure S2.7: Additional blots related to Figure 4, FB231 and MTK458 induce Mitochondrial Stress upstream of PINK1/Parkin activation. (A) Immunoblots of mitophagy, mitochondrial stress, and integrated stress response biomarkers in YFP-Parkin/PINK1 KO HeLa cells treated with DMSO, 10 nM O/A, 0.3–10 μM FB231, and the same doses of FB231 with 10 nM O/A for 16 h. (B) As in (A) with 0.6–20 μM MTK458. (C) Immunoblot of ATF3, an integrated stress response biomarker, in WT, YFP-Parkin-expressing, and YFP-Parkin/PINK1KO HeLa cells treated with DMSO or 100 nM O/A. (D) Normalized densitometry analysis of (C), (N=3). (E) Immunoblots of DELE1-HA in endogenous DELE1-HA knock-in HEK293T cells treated with or without 10 nM O/A for 16

h alone or in combination with 10 μ M FB231 or 10 μ M MTK458. **(F)** Representative flow cytometry plots of mt-Keima-expressing HeLa cells treated with DMSO or 100 nM O/A for 6 h. For each sample, at least 30,000 events were collected and subsequently gated for live, single cells expressing mt-Keima. Data represents the percentage of cells undergoing mitophagy as indicated by the ratio of mt-Keima 555/470 nM emission. All cells, except those in (C), were administered with 20 μ M Q-VD-OPh to prevent cell death. Ponceau S stain was used as total protein loading control.

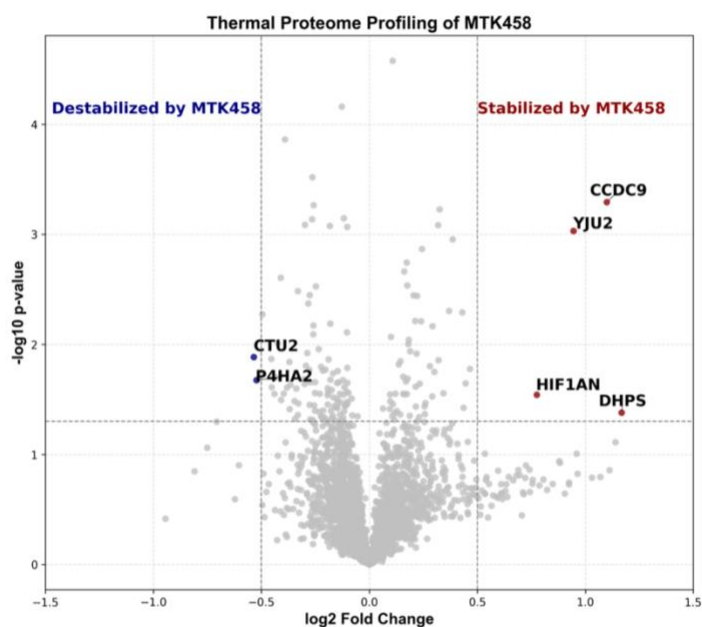


Figure S2.8: Thermal Proteome Profiling of MTK458.

Volcano plot of thermal proteome profiling of YFP-Parkin-expressing HeLa lysate treated with 50 μ M MTK458 compared to equivalent DMSO-treated lysate. Significantly destabilized proteins compared to DMSO, with fold-change < -1 and $P < 0.05$ indicated in blue. Proteins significantly stabilized compared to DMSO, fold-change > 1 and $P < 0.05$ indicated in red. Gene names of significantly altered proteins are labelled.

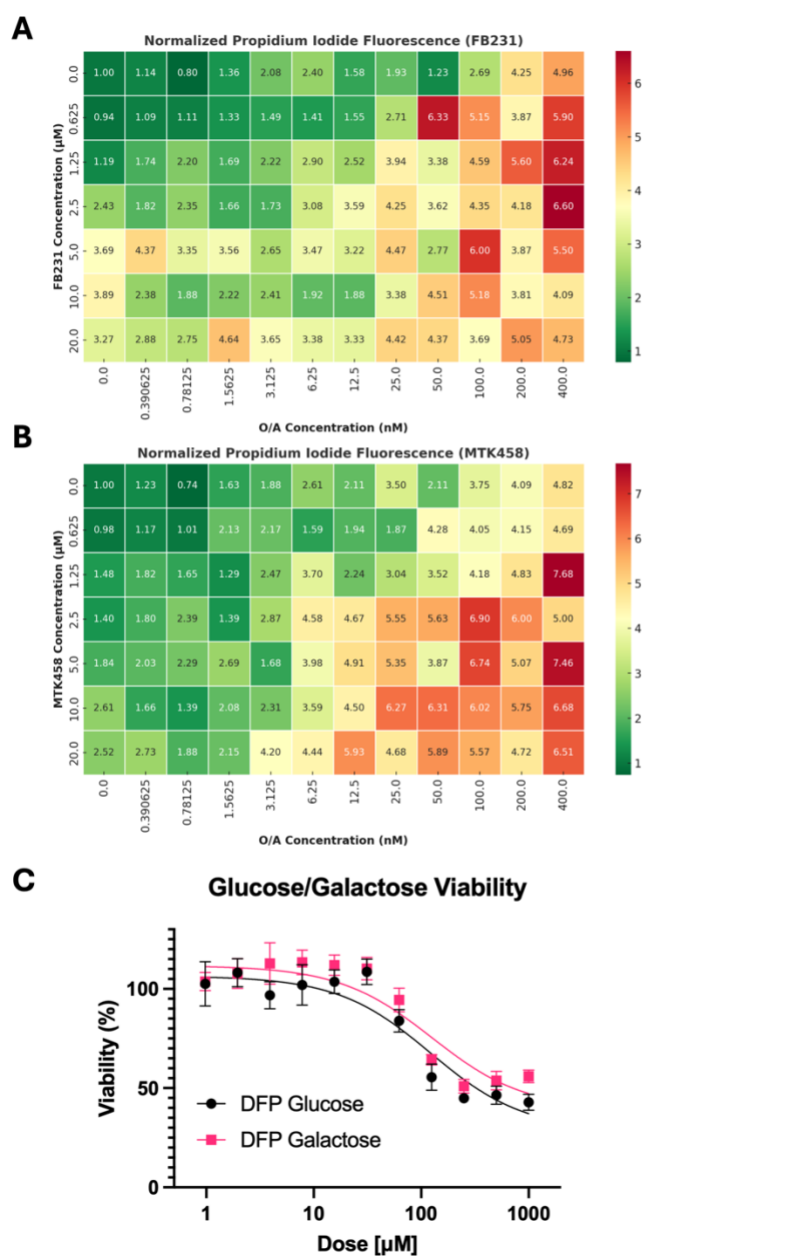


Figure S2.9: Additional data related to Figure 8, FB231 and MTK458 sensitize cells to mitochondrial stress

(A) Heatmap showing normalized propidium iodide (PI) fluorescence intensity, a marker of dead cells, for cells treated for 24 h with various dose combinations of FB231 and O/A. Each block represents the average intensity of N=4 wells. Fluorescence is normalized to the

average of the DMSO-only condition. **(B)** as in (A) for various doses combinations of MTK458 and O/A. **(C)** Dose-viability plot of WT HeLa cells in glucose-containing media (black) or galactose-containing media (pink) treated with increasing doses of 24 h (N=8). Data are presented as means \pm SD.

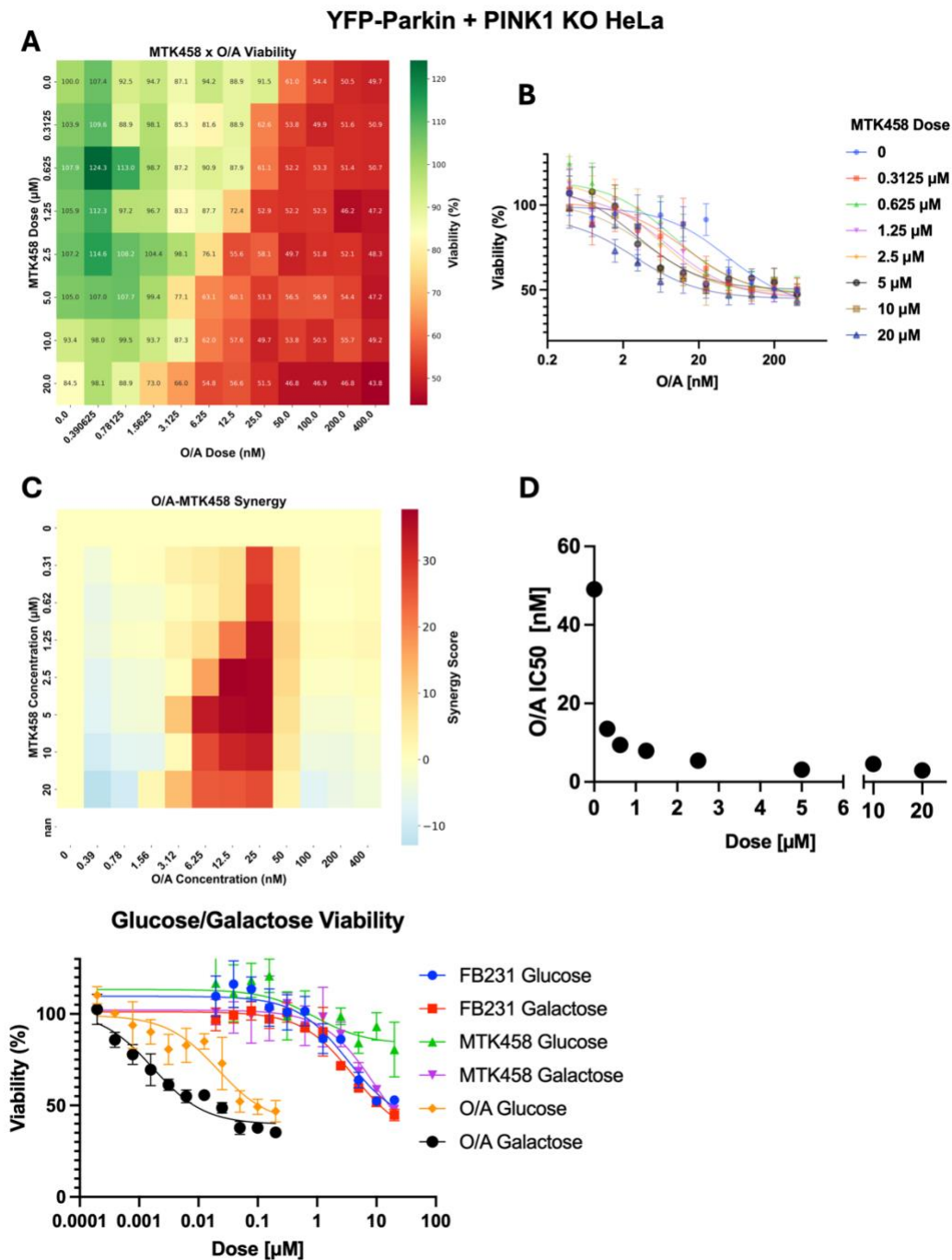


Figure S2.10: PINK1 is not required for MTK458-induced sensitization to mitochondrial stress.

(A) Heatmap showing cell viability as in YFP-Parkin/PINK1 KO HeLa cells treated with combination doses of MTK458 and O/A for 24 h. (B) YFP-Parkin/PINK1 KO HeLa cells

viability dose response curves for O/A at increasing doses of MTK458. Points represent the mean and standard deviation of 8 replicates. Solid lines are fits to a Hill equation to determine the IC_{50} . **(C)** Synergy score heat map of O/A and MTK458 combinations on cell viability. **(D)** Plot of calculated O/A viability IC_{50} at different doses of MTK458 in YFP-Parkin/PINK1 KO HeLa cells. **(E)** Dose-viability plot of YFP-Parkin/PINK1 KO HeLa cells in glucose media or galactose-containing media treated with increasing doses of O/A, FB231, or MTK458 for 24 h. Points and error bars represent the mean and standard deviation from 8 replicates. Solid lines represent fits the Hill equation.

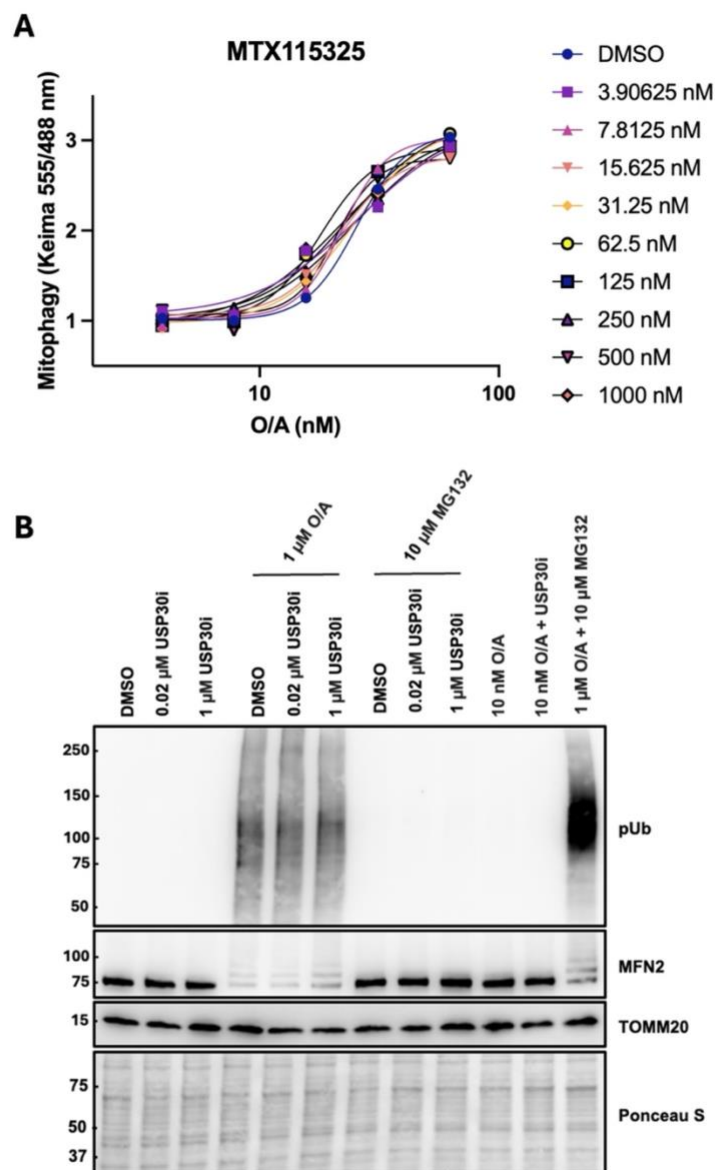


Figure S2.11: Effect of a USP30 inhibitor on Mitophagy and Parkin substrates. (A) YFP-Parkin mt-Keima HeLa Cells were treated with various doses of USP30i (MTX115325)

and O/A. Mitophagy was measured 6 hours later. Data is representative of N=2 independent experiments. **(B)** Western blot of YFP-Parkin expressing HeLa cells treated with various compound combinations for 16 hours.

Works Cited

- Anderson, C. P., Shen, M., Eisenstein, R. S., & Leibold, E. A. (2012). Mammalian iron metabolism and its control by iron regulatory proteins. *Biochim Biophys Acta*, 1823(9), 1468-1483. <https://doi.org/10.1016/j.bbamcr.2012.05.010>
- Antico, O., Thompson, P. W., Hertz, N. T., Muqit, M. M. K., & Parton, L. E. (2025). Targeting mitophagy in neurodegenerative diseases. *Nat Rev Drug Discov*, 24(4), 276-299. <https://doi.org/10.1038/s41573-024-01105-0>
- Baker, M. J., Lampe, P. A., Stojanovski, D., Korwitz, A., Anand, R., Tatsuta, T., & Langer, T. (2014). Stress-induced OMA1 activation and autocatalytic turnover regulate OPA1-dependent mitochondrial dynamics. *EMBO J*, 33(6), 578-593. <https://doi.org/10.1002/emboj.201386474>
- Ben-Shlomo, Y., Darweesh, S., Llibre-Guerra, J., Marras, C., San Luciano, M., & Tanner, C. (2024). The epidemiology of Parkinson's disease. *Lancet*, 403(10423), 283-292. [https://doi.org/10.1016/S0140-6736\(23\)01419-8](https://doi.org/10.1016/S0140-6736(23)01419-8)
- Bingol, B., Tea, J. S., Phu, L., Reichelt, M., Bakalarski, C. E., Song, Q., Foreman, O., Kirkpatrick, D. S., & Sheng, M. (2014). The mitochondrial deubiquitinase USP30 opposes parkin-mediated mitophagy. *Nature*, 510(7505), 370-375. <https://doi.org/10.1038/nature13418>
- Burman, J. L., Pickles, S., Wang, C., Sekine, S., Vargas, J. N. S., Zhang, Z., Youle, A. M., Nezich, C. L., Wu, X., Hammer, J. A., & Youle, R. J. (2017). Mitochondrial fission facilitates the selective mitophagy of protein aggregates. *J Cell Biol*, 216(10), 3231-3247. <https://doi.org/10.1083/jcb.201612106>
- Cabrera, A., Wiebelhaus, N., Quan, B., Ma, R., Meng, H., & Fitzgerald, M. C. (2020). Comparative Analysis of Mass-Spectrometry-Based Proteomic Methods for Protein Target Discovery Using a One-Pot Approach. *J Am Soc Mass Spectrom*, 31(2), 217-226. <https://doi.org/10.1021/jasms.9b00041>
- Chakrabarty, Y., Yang, Z., Chen, H. C., & Chan, D. C. (2024). The HRI branch of the integrated stress response selectively triggers mitophagy. *Molecular Cell*, 84(6). <https://doi.org/10.1016/j.molcel.2024.01.016>
- Chin, R. M., Rakhit, R., Ditsworth, D., Wang, C., Bartholomeus, J., Liu, S., Mody, A., Laishu, A., Eastes, A., Tai, C., Kim, R. Y., Li, J., Hansberry, S., Khasnavis, S., Rafalski, V., Herendeen, D., Garda, V., Phung, J., de Roulet, D., . . . Hertz, N. T. (2023). Pharmacological PINK1 activation ameliorates Pathology in Parkinson's Disease models. *bioRxiv*. <https://doi.org/10.1101/2023.02.14.528378>
- Crooks, D. R., Ghosh, M. C., Haller, R. G., Tong, W. H., & Rouault, T. A. (2010). Posttranslational stability of the heme biosynthetic enzyme ferrochelatase is dependent on iron availability and intact iron-sulfur cluster assembly machinery. *Blood*, 115(4), 860-869. <https://doi.org/10.1182/blood-2009-09-243105>
- Devos, D., Labreuche, J., Rascol, O., Corvol, J. C., Duhamel, A., Guyon Delannoy, P., Poewe, W., Compta, Y., Pavese, N., Ruzicka, E., Dusek, P., Post, B., Bloem, B. R., Berg, D., Maetzler, W., Otto, M., Habert, M. O., Lehericy, S., Ferreira, J., . . . Group, F.-I. S. (2022). Trial of Deferiprone in Parkinson's Disease. *N Engl J Med*, 387(22), 2045-2055. <https://doi.org/10.1056/NEJMoa2209254>

- Dickson, D. W. (2012). Parkinson's disease and parkinsonism: neuropathology. *Cold Spring Harb Perspect Med*, 2(8). <https://doi.org/10.1101/cshperspect.a009258>
- Fang, T. Z., Sun, Y., Pearce, A. C., Eleuteri, S., Kemp, M., Luckhurst, C. A., Williams, R., Mills, R., Almond, S., Burzynski, L., Markus, N. M., Lelliott, C. J., Karp, N. A., Adams, D. J., Jackson, S. P., Zhao, J. F., Ganley, I. G., Thompson, P. W., Balmus, G., & Simon, D. K. (2023). Knockout or inhibition of USP30 protects dopaminergic neurons in a Parkinson's disease mouse model. *Nat Commun*, 14(1), 7295. <https://doi.org/10.1038/s41467-023-42876-1>
- Fessler, E., Eckl, E. M., Schmitt, S., Mancilla, I. A., Meyer-Bender, M. F., Hanf, M., Philippou-Massier, J., Krebs, S., Zischka, H., & Jae, L. T. (2020). A pathway coordinated by DELE1 relays mitochondrial stress to the cytosol. *Nature*, 579(7799), 433-437. <https://doi.org/10.1038/s41586-020-2076-4>
- Flones, I. H., Toker, L., Sandnes, D. A., Castelli, M., Mostafavi, S., Lura, N., Shadad, O., Fernandez-Vizarra, E., Painous, C., Perez-Soriano, A., Compta, Y., Molina-Porcel, L., Alves, G., Tysnes, O. B., Dolle, C., Nido, G. S., & Tzoulis, C. (2024). Mitochondrial complex I deficiency stratifies idiopathic Parkinson's disease. *Nat Commun*, 15(1), 3631. <https://doi.org/10.1038/s41467-024-47867-4>
- Gan, Z. Y., Callegari, S., Nguyen, T. N., Kirk, N. S., Leis, A., Lazarou, M., Dewson, G., & Komander, D. (2024). Interaction of PINK1 with nucleotides and kinetin. *Sci Adv*, 10(3), ead7408. <https://doi.org/10.1126/sciadv.adj7408>
- Geisler, S., Holmstrom, K. M., Skujat, D., Fiesel, F. C., Rothfuss, O. C., Kahle, P. J., & Springer, W. (2010). PINK1/Parkin-mediated mitophagy is dependent on VDAC1 and p62/SQSTM1. *Nat Cell Biol*, 12(2), 119-131. <https://doi.org/10.1038/ncb2012>
- Gladkova, C., Maslen, S. L., Skehel, J. M., & Komander, D. (2018). Mechanism of parkin activation by PINK1. *Nature*, 559(7714), 410-414. <https://doi.org/10.1038/s41586-018-0224-x>
- Guo, X., Aviles, G., Liu, Y., Tian, R., Unger, B. A., Lin, Y. T., Wiita, A. P., Xu, K., Correia, M. A., & Kampmann, M. (2020). Mitochondrial stress is relayed to the cytosol by an OMA1-DELE1-HRI pathway. *Nature*, 579(7799), 427-432. <https://doi.org/10.1038/s41586-020-2078-2>
- Hertz, N. T., Berthet, A., Sos, M. L., Thorn, K. S., Burlingame, A. L., Nakamura, K., & Shokat, K. M. (2013). A neo-substrate that amplifies catalytic activity of parkinson's-disease-related kinase PINK1. *Cell*, 154(4), 737-747. <https://doi.org/10.1016/j.cell.2013.07.030>
- Hou, X., Fiesel, F. C., Truban, D., Castanedes Casey, M., Lin, W. L., Soto, A. I., Tacik, P., Rousseau, L. G., Diehl, N. N., Heckman, M. G., Lorenzo-Betancor, O., Ferrer, I., Arbelo, J. M., Steele, J. C., Farrer, M. J., Cornejo-Olivas, M., Torres, L., Mata, I. F., Graff-Radford, N. R., . . . Springer, W. (2018). Age- and disease-dependent increase of the mitophagy marker phospho-ubiquitin in normal aging and Lewy body disease. *Autophagy*, 14(8), 1404-1418. <https://doi.org/10.1080/15548627.2018.1461294>
- Ianevski, A., Giri, A. K., & Aittokallio, T. (2022). SynergyFinder 3.0: an interactive analysis and consensus interpretation of multi-drug synergies across multiple samples. *Nucleic Acids Res*, 50(W1), W739-W743. <https://doi.org/10.1093/nar/gkac382>

- Jennifer Johnston, A. W. G., Paul Ross Fatheree (2017). *Triazole benzamide derivatives and the compositions and methods of treatment regarding the same* (United States Patent No. U. S. P. Office.
- Jin, S. M., Lazarou, M., Wang, C., Kane, L. A., Narendra, D. P., & Youle, R. J. (2010). Mitochondrial membrane potential regulates PINK1 import and proteolytic destabilization by PARL. *J Cell Biol*, *191*(5), 933-942. <https://doi.org/10.1083/jcb.201008084>
- Kazlauskaitė, A., Kondapalli, C., Gourlay, R., Campbell, D. G., Ritorto, M. S., Hofmann, K., Alessi, D. R., Knebel, A., Trost, M., & Muqit, M. M. (2014). Parkin is activated by PINK1-dependent phosphorylation of ubiquitin at Ser65. *Biochem J*, *460*(1), 127-139. <https://doi.org/10.1042/BJ20140334>
- Kazlauskaitė, A., Martinez-Torres, R. J., Wilkie, S., Kumar, A., Peltier, J., Gonzalez, A., Johnson, C., Zhang, J., Hope, A. G., Pegg, M., Trost, M., van Aalten, D. M., Alessi, D. R., Prescott, A. R., Knebel, A., Walden, H., & Muqit, M. M. (2015). Binding to serine 65-phosphorylated ubiquitin primes Parkin for optimal PINK1-dependent phosphorylation and activation. *EMBO Rep*, *16*(8), 939-954. <https://doi.org/10.15252/embr.201540352>
- Koyano, F., Okatsu, K., Kosako, H., Tamura, Y., Go, E., Kimura, M., Kimura, Y., Tsuchiya, H., Yoshihara, H., Hirokawa, T., Endo, T., Fon, E. A., Trempe, J. F., Saeki, Y., Tanaka, K., & Matsuda, N. (2014). Ubiquitin is phosphorylated by PINK1 to activate parkin. *Nature*, *510*(7503), 162-+.
<https://doi.org/10.1038/nature13392>
- Lam, W. K., Runa S. J. Lindblom, Bridget Milky, Paris Mazzachi, Marjan Hadian-Jazi, Catharina Küng, Grace Khuu, Louise Uoselis, Thanh Ngoc Nguyen, Marvin Skulsuppaisarn, Tahnee L. Saunders, Marlene F. Schmidt, Grant Dewson, Adam I. Fogel, Cedric Bardy, Michael Lazarou. (2024). Presynapses are mitophagy pit stops that prevent axon degeneration. *bioRxiv*, 2024.09.09.611943. <https://doi.org/10.1101/2024.09.09.611943>
- Langston, J. W. (2017). The MPTP Story. *J Parkinsons Dis*, *7*(s1), S11-S19. <https://doi.org/10.3233/JPD-179006>
- Lazarou, M., Narendra, D. P., Jin, S. M., Tekle, E., Banerjee, S., & Youle, R. J. (2013). PINK1 drives Parkin self-association and HECT-like E3 activity upstream of mitochondrial binding. *J Cell Biol*, *200*(2), 163-172. <https://doi.org/10.1083/jcb.201210111>
- Lazarou, M., Sliter, D. A., Kane, L. A., Sarraf, S. A., Wang, C., Burman, J. L., Sideris, D. P., Fogel, A. I., & Youle, R. J. (2015). The ubiquitin kinase PINK1 recruits autophagy receptors to induce mitophagy. *Nature*, *524*(7565), 309-314. <https://doi.org/10.1038/nature14893>
- Lopez-Crapez, E., Bazin, H., Andre, E., Noletti, J., Grenier, J., & Mathis, G. (2001). A homogeneous europium cryptate-based assay for the diagnosis of mutations by time-resolved fluorescence resonance energy transfer. *Nucleic Acids Res*, *29*(14), E70. <https://doi.org/10.1093/nar/29.14.e70>
- Marroquin, L. D., Hynes, J., Dykens, J. A., Jamieson, J. D., & Will, Y. (2007). Circumventing the Crabtree effect: replacing media glucose with galactose

- increases susceptibility of HepG2 cells to mitochondrial toxicants. *Toxicol Sci*, 97(2), 539-547. <https://doi.org/10.1093/toxsci/kfm052>
- McDowell, G. S., Gaun, A., & Steen, H. (2013). iFASP: combining isobaric mass tagging with filter-aided sample preparation. *J Proteome Res*, 12(8), 3809-3812. <https://doi.org/10.1021/pr400032m>
- Miller, S., & Muqit, M. M. K. (2019). Therapeutic approaches to enhance PINK1/Parkin mediated mitophagy for the treatment of Parkinson's disease. *Neurosci Lett*, 705, 7-13. <https://doi.org/10.1016/j.neulet.2019.04.029>
- Moon, H. E., Yoon, S. H., Hur, Y. S., Park, H. W., Ha, J. Y., Kim, K. H., Shim, J. H., Yoo, S. H., Son, J. H., Paek, S. L., Kim, I. K., Hwang, J. H., Kim, D. G., Kim, H. J., Jeon, B. S., Park, S. S., & Paek, S. H. (2013). Mitochondrial dysfunction of immortalized human adipose tissue-derived mesenchymal stromal cells from patients with Parkinson's disease. *Exp Neurobiol*, 22(4), 283-300. <https://doi.org/10.5607/en.2013.22.4.283>
- Narendra, D., Tanaka, A., Suen, D. F., & Youle, R. J. (2008). Parkin is recruited selectively to impaired mitochondria and promotes their autophagy. *J Cell Biol*, 183(5), 795-803. <https://doi.org/10.1083/jcb.200809125>
- Narendra, D. P., Jin, S. M., Tanaka, A., Suen, D. F., Gautier, C. A., Shen, J., Cookson, M. R., & Youle, R. J. (2010). PINK1 is selectively stabilized on impaired mitochondria to activate Parkin. *PLoS Biol*, 8(1), e1000298. <https://doi.org/10.1371/journal.pbio.1000298>
- Nguyen, T. N., Sawa-Makarska, J., Khuu, G., Lam, W. K., Adriaenssens, E., Fracchiolla, D., Shoebridge, S., Bernklau, D., Padman, B. S., Skulsuppaisarn, M., Lindblom, R. S. J., Martens, S., & Lazarou, M. (2023). Unconventional initiation of PINK1/Parkin mitophagy by Optineurin. *Mol Cell*, 83(10), 1693-1709 e1699. <https://doi.org/10.1016/j.molcel.2023.04.021>
- Ordureau, A., Sarraf, S. A., Duda, D. M., Heo, J. M., Jedrychowski, M. P., Sviderskiy, V. O., Olszewski, J. L., Koerber, J. T., Xie, T., Beausoleil, S. A., Wells, J. A., Gygi, S. P., Schulman, B. A., & Harper, J. W. (2014). Quantitative proteomics reveal a feedforward mechanism for mitochondrial PARKIN translocation and ubiquitin chain synthesis. *Mol Cell*, 56(3), 360-375. <https://doi.org/10.1016/j.molcel.2014.09.007>
- Padman, B. S., Bach, M., Lucarelli, G., Prescott, M., & Ramm, G. (2013). The protonophore CCCP interferes with lysosomal degradation of autophagic cargo in yeast and mammalian cells. *Autophagy*, 9(11), 1862-1875. <https://doi.org/10.4161/auto.26557>
- Perez-Riverol, Y., Bai, J., Bandla, C., Garcia-Seisdedos, D., Hewapathirana, S., Kamatchinathan, S., Kundu, D. J., Prakash, A., Frericks-Zipper, A., Eisenacher, M., Walzer, M., Wang, S., Brazma, A., & Vizcaino, J. A. (2022). The PRIDE database resources in 2022: a hub for mass spectrometry-based proteomics evidences. *Nucleic Acids Res*, 50(D1), D543-D552. <https://doi.org/10.1093/nar/gkab1038>
- Pickrell, A. M., & Youle, R. J. (2015). The roles of PINK1, parkin, and mitochondrial fidelity in Parkinson's disease. *Neuron*, 85(2), 257-273. <https://doi.org/10.1016/j.neuron.2014.12.007>

- Quan, B., Bailey, M. A., Mantyh, J., Hsu, D. S., & Fitzgerald, M. C. (2023). Protein Folding Stability Profiling of Colorectal Cancer Chemoresistance Identifies Functionally Relevant Biomarkers. *J Proteome Res*, 22(6), 1923-1935. <https://doi.org/10.1021/acs.jproteome.3c00045>
- Quiros, P. M., Prado, M. A., Zamboni, N., D'Amico, D., Williams, R. W., Finley, D., Gygi, S. P., & Auwerx, J. (2017). Multi-omics analysis identifies ATF4 as a key regulator of the mitochondrial stress response in mammals. *J Cell Biol*, 216(7), 2027-2045. <https://doi.org/10.1083/jcb.201702058>
- Raimi, O. G., Ojha, H., Ehses, K., Dederer, V., Lange, S. M., Rivera, C. P., Deegan, T. D., Chen, Y., Wightman, M., Toth, R., Labib, K. P. M., Mathea, S., Ranson, N., Fernandez-Busnadiego, R., & Muqit, M. M. K. (2024). Mechanism of human PINK1 activation at the TOM complex in a reconstituted system. *Sci Adv*, 10(23), eadn7191. <https://doi.org/10.1126/sciadv.adn7191>
- Rasool, S., Shomali, T., Truong, L., Croteau, N., Veyron, S., Bustillos, B. A., Springer, W., Fiesel, F. C., & Trempe, J. F. (2024). Identification and structural characterization of small molecule inhibitors of PINK1. *Scientific Reports*, 14(1). <https://doi.org/ARTN 7739>
10.1038/s41598-024-58285-3
- Rasool, S., Veyron, S., Soya, N., Eldeeb, M. A., Lukacs, G. L., Fon, E. A., & Trempe, J. F. (2022). Mechanism of PINK1 activation by autophosphorylation and insights into assembly on the TOM complex. *Mol Cell*, 82(1), 44-59 e46. <https://doi.org/10.1016/j.molcel.2021.11.012>
- Regnström, K., Yan, J. L., Nguyen, L., Callaway, K., Yang, Y. L., Diep, L., Xing, W. M., Adhikari, A., Beroza, P., Hom, R. K., Riley, B., Rudolph, D., Jobling, M. F., Baker, J., Johnston, J., Konradi, A., Bova, M. P., & Artis, R. D. (2013). Label Free Fragment Screening Using Surface Plasmon Resonance as a Tool for Fragment Finding - Analyzing Parkin, a Difficult CNS Target. *PLoS One*, 8(7). <https://doi.org/ARTN e66879>
10.1371/journal.pone.0066879
- Riley, B. E., Loughheed, J. C., Callaway, K., Velasquez, M., Brecht, E., Nguyen, L., Shaler, T., Walker, D., Yang, Y., Regnstrom, K., Diep, L., Zhang, Z., Chiou, S., Bova, M., Artis, D. R., Yao, N., Baker, J., Yednock, T., & Johnston, J. A. (2013). Structure and function of Parkin E3 ubiquitin ligase reveals aspects of RING and HECT ligases. *Nat Commun*, 4, 1982. <https://doi.org/10.1038/ncomms2982>
- Sauve, V., Lilov, A., Seirafi, M., Vranas, M., Rasool, S., Kozlov, G., Sprules, T., Wang, J., Trempe, J. F., & Gehring, K. (2015). A Ubl/ubiquitin switch in the activation of Parkin. *EMBO J*, 34(20), 2492-2505. <https://doi.org/10.15252/embj.201592237>
- Sauve, V., Stefan, E., Croteau, N., Goiran, T., Fakih, R., Bansal, N., Hadzipasic, A., Fang, J., Murugan, P., Chen, S., Fon, E. A., Hirst, W. D., Silvian, L. F., Trempe, J. F., & Gehring, K. (2024). Activation of parkin by a molecular glue. *Nat Commun*, 15(1), 7707. <https://doi.org/10.1038/s41467-024-51889-3>
- Sekine, S. (2020). PINK1 import regulation at a crossroad of mitochondrial fate: the molecular mechanisms of PINK1 import. *J Biochem*, 167(3), 217-224. <https://doi.org/10.1093/jb/mvz069>

- Sekine, Y., Houston, R., Eckl, E. M., Fessler, E., Narendra, D. P., Jae, L. T., & Sekine, S. (2023). A mitochondrial iron-responsive pathway regulated by DELE1. *Mol Cell*, 83(12), 2059-2076 e2056. <https://doi.org/10.1016/j.molcel.2023.05.031>
- Shetty, T., Sishtla, K., Park, B., Repass, M. J., & Corson, T. W. (2020). Heme Synthesis Inhibition Blocks Angiogenesis via Mitochondrial Dysfunction. *iScience*, 23(8), 101391. <https://doi.org/10.1016/j.isci.2020.101391>
- Shlevkov, E., Murugan, P., Montagna, D., Stefan, E., Hadzipasic, A., Harvey, J. S., Kumar, P. R., Entova, S., Bansal, N., Bickford, S., Wong, L. Y., Hirst, W. D., Weihofen, A., & Silvian, L. F. (2022). Discovery of small-molecule positive allosteric modulators of Parkin E3 ligase. *iScience*, 25(1), 103650. <https://doi.org/10.1016/j.isci.2021.103650>
- Sidrauski, C., Acosta-Alvear, D., Khoutorsky, A., Vedantham, P., Hearn, B. R., Li, H., Gamache, K., Gallagher, C. M., Ang, K. K., Wilson, C., Okreglak, V., Ashkenazi, A., Hann, B., Nader, K., Arkin, M. R., Renslo, A. R., Sonenberg, N., & Walter, P. (2013). Pharmacological brake-release of mRNA translation enhances cognitive memory. *Elife*, 2, e00498. <https://doi.org/10.7554/eLife.00498>
- Singh, P. K., Shalini Agarwal, Ilaria Volpi, Léa P. Wilhelm, Giada Becchi, Andrew Keenlyside, Thomas Macartney, Rachel Toth, Adrien Rousseau, Glenn R. Masson, Ian G. Ganley, Miratul M. K. Muqit. (2023). Kinome screening identifies integrated stress response kinase EIF2AK1 / HRI as a negative regulator of PINK1 mitophagy signaling. *bioRxiv 2023.03.20.533516*. <https://doi.org/https://doi.org/10.1101/2023.03.20.533516>
- Sun, N., Malide, D., Liu, J., Rovira, II, Combs, C. A., & Finkel, T. (2017). A fluorescence-based imaging method to measure in vitro and in vivo mitophagy using mt-Keima. *Nat Protoc*, 12(8), 1576-1587. <https://doi.org/10.1038/nprot.2017.060>
- Tanner, C. M., Kamel, F., Ross, G. W., Hoppin, J. A., Goldman, S. M., Korell, M., Marras, C., Bhudhikanok, G. S., Kasten, M., Chade, A. R., Comyns, K., Richards, M. B., Meng, C., Priestley, B., Fernandez, H. H., Cambi, F., Umbach, D. M., Blair, A., Sandler, D. P., & Langston, J. W. (2011). Rotenone, paraquat, and Parkinson's disease. *Environ Health Perspect*, 119(6), 866-872. <https://doi.org/10.1289/ehp.1002839>
- Terzi, E. M., Sviderskiy, V. O., Alvarez, S. W., Whiten, G. C., & Possemato, R. (2021). Iron-sulfur cluster deficiency can be sensed by IRP2 and regulates iron homeostasis and sensitivity to ferroptosis independent of IRP1 and FBXL5. *Sci Adv*, 7(22). <https://doi.org/10.1126/sciadv.abg4302>
- Tjahjono, E., Pei, J., Revtovich, A. V., Liu, T. E., Swadi, A., Hancu, M. C., Tolar, J. G., & Kirienko, N. V. (2021). Mitochondria-affecting small molecules ameliorate proteostasis defects associated with neurodegenerative diseases. *Sci Rep*, 11(1), 17733. <https://doi.org/10.1038/s41598-021-97148-z>
- Trempe, J. F., Sauve, V., Grenier, K., Seirafi, M., Tang, M. Y., Menade, M., Al-Abdul-Wahid, S., Krett, J., Wong, K., Kozlov, G., Nagar, B., Fon, E. A., & Gehring, K. (2013). Structure of parkin reveals mechanisms for ubiquitin ligase activation. *Science*, 340(6139), 1451-1455. <https://doi.org/10.1126/science.1237908>

- Tufi, R., Clark, E. H., Hoshikawa, T., Tsagkaraki, C., Stanley, J., Takeda, K., Staddon, J. M., & Briston, T. (2023). High-content phenotypic screen to identify small molecule enhancers of Parkin-dependent ubiquitination and mitophagy. *SLAS Discov*, 28(3), 73-87. <https://doi.org/10.1016/j.slasd.2022.12.004>
- Vargas, J. N. S., Wang, C., Bunker, E., Hao, L., Maric, D., Schiavo, G., Randow, F., & Youle, R. J. (2019). Spatiotemporal Control of ULK1 Activation by NDP52 and TBK1 during Selective Autophagy. *Mol Cell*, 74(2), 347-362 e346. <https://doi.org/10.1016/j.molcel.2019.02.010>
- Wang, H., Shi, H., Rajan, M., Canarie, E. R., Hong, S., Simoneschi, D., Pagano, M., Bush, M. F., Stoll, S., Leibold, E. A., & Zheng, N. (2020). FBXL5 Regulates IRP2 Stability in Iron Homeostasis via an Oxygen-Responsive [2Fe2S] Cluster. *Mol Cell*, 78(1), 31-41 e35. <https://doi.org/10.1016/j.molcel.2020.02.011>
- Waters, C. S., Angenent, S. B., Altschuler, S. J., & Wu, L. F. (2023). A PINK1 input threshold arises from positive feedback in the PINK1/Parkin mitophagy decision circuit. *Cell Rep*, 42(10), 113260. <https://doi.org/10.1016/j.celrep.2023.113260>
- Wauer, T., & Komander, D. (2013). Structure of the human Parkin ligase domain in an autoinhibited state. *EMBO J*, 32(15), 2099-2112. <https://doi.org/10.1038/emboj.2013.125>
- Wauer, T., Simicek, M., Schubert, A., & Komander, D. (2015). Mechanism of phospho-ubiquitin-induced PARKIN activation. *Nature*, 524(7565), 370-374. <https://doi.org/10.1038/nature14879>
- Xicoy, H., Wieringa, B., & Martens, G. J. (2017). The SH-SY5Y cell line in Parkinson's disease research: a systematic review. *Mol Neurodegener*, 12(1), 10. <https://doi.org/10.1186/s13024-017-0149-0>
- Yamano, K., & Youle, R. J. (2013). PINK1 is degraded through the N-end rule pathway. *Autophagy*, 9(11), 1758-1769. <https://doi.org/10.4161/autophagy.24633>
- Yang, M., Mo, Z., Walsh, K., Liu, W., & Guo, X. (2024). The Integrated Stress Response Suppresses PINK1-dependent Mitophagy by Preserving Mitochondrial Import Efficiency. *bioRxiv*. <https://doi.org/10.1101/2024.10.16.617214>

Chapter 3

TNIP1 inhibits selective autophagy via interaction with LC3/GABARAP and TAX1BP1

The following chapter is adapted from Le Guerroué et al 2023 according to Caltech's thesis requirements. All biophysical experiments were performed or supervised by myself.

François Le Guerroué, Eric N. Bunker, William M. Rosencrans, Jack T. Nguyen, Mohammed A. Basar, Achim Werner, Tsui-Fen Chou, Chunxin Wang, and Richard J. Youle. *Molecular Cell*. 2023 Mar 16;83(6):927-941.e8. doi: 10.1016/j.molcel.2023.02.023.

3. 1 Abstract

Mitophagy is a form of selective autophagy that disposes of superfluous and potentially damage-inducing organelles in a tightly controlled manner. While the machinery involved in mitophagy induction is well known, the regulation of the components is less clear. Here, using Chemically Inducible Dimerization (CID) and mitophagy assays with the fluorescent probe mt-Keima, we reveal that the ubiquitin binding domain-containing protein TNIP1 is able to induce mitophagy when ectopically targeted to mitochondria. We further demonstrate that TNIP1 knock out accelerates mitophagy rates, and that ectopic TNIP1 negatively regulates the rate of mitophagy. These functions of TNIP1 depend on an evolutionarily conserved LIR motif as well as an AHD3 domain, which are required for binding to the LC3/GABARAP family of proteins and the autophagy receptor TAX1BP1, respectively. We further show that phosphorylation appears to regulate its association with the ULK1 complex member FIP200, allowing TNIP1 to compete with autophagy receptors, providing a molecular rationale for its inhibitory function during mitophagy. Taken together, our findings identify a novel negative regulator of mitophagy that acts at the early steps of autophagosome biogenesis.

3. 2 Introduction

Macroautophagy, one of the main cellular degradation pathways, sequesters cytosolic components inside a double membrane structure called an autophagosome, before catabolizing its content by fusing to lysosomes. The molecular mechanisms of the formation and maturation processes are well described and revolve around a set of proteins called the ATG conjugation system¹. Initially described as a non-selective degradation process triggered when cells face starvation, more recent work shows autophagy can selectively eliminate certain proteins, protein aggregates and organelles^{2,3}. Selective autophagy specifically sequesters cytosolic structures via autophagy receptors. The main feature of these autophagy receptors is their capacity to bind to mATG8 (mammalian ATG8 proteins) as well as FIP200 and to ubiquitin in most cases⁴. One of the best characterized selective autophagy processes is the degradation of mitochondria via mitophagy⁵. The PINK1/Parkin axis of mitophagy participates in a feed-back loop involving stabilization of the kinase PINK1, phosphorylation of resident ubiquitinated proteins at the surface of the mitochondria prior to recruitment of the E3 ligase Parkin, followed by activation of Parkin via its phosphorylation by PINK1. Autophagy receptors such as NDP52 or OPTN are subsequently recruited to ubiquitinated mitochondria via their ubiquitin-binding domains, allowing the autophagy machinery to assemble and degrade the mitochondria in a wholesale fashion^{6,7}.

TNIP1 (TNFAIP3-interacting protein 1), also called ABIN1 (A20-binding inhibitor of NF- κ B activation 1) participates in the NF- κ B pathway, where it negatively regulates NF- κ B activation, maintaining immune homeostasis^{8,9}. Structurally, TNIP1 possesses a Ub-binding domain (UBAN domain – Ubiquitin binding of ABIN and NEMO) common among ABIN proteins, 3 Abin homology domains (AHD) and a NEMO binding domain (NBD)^{8,10}. Although the AHD3 domain function is currently not described, AHD1 mediates binding with the ubiquitin editing enzyme Tumor necrosis factor alpha-induced protein 3 (TNFAIP3, A20) and AHD4 mediates the interaction with OPTN¹¹. TNIP1 also interacts with TAX1BP1, together with A20 to restrict antiviral signaling¹². Being involved in immune responses, dysregulation of TNIP1 was shown to be implicated in various human diseases in a number of genome-wide associated studies (GWAS)¹³. TNIP1 single nucleotide polymorphisms (SNP) have been strongly associated with autoimmune diseases¹⁴ and cross

ethnic genetic studies identified the *GPX3-TNIP1* locus to associate with amyotrophic lateral sclerosis (ALS)¹⁵. However, a later study concluded that this locus was less likely to contribute to ALS risk¹⁶. In addition, a recent GWAS study identified TNIP1 as the locus of a newly identified risk allele for Alzheimer's disease (AD)¹⁷.

Here we describe a role of TNIP1 as a LC3/GABARAP-interacting protein, that is able to trigger mitophagy when synthetically targeted to mitochondria, and that normally negatively inhibits early stages of mitophagy. Furthermore, we show that physical interaction of TNIP1 with LC3/GABARAP proteins and with TAX1BP1, drives mitophagy inhibition. This inhibition appears regulated by phosphorylation of TNIP1, promoting binding with FIP200 and resulting in a counteracting effect on inhibition. Our study suggests that TNIP1 thus acts as a security check to fine tune the rate of mitophagy.

3.3 Results

Ectopic localization of TNIP1 to the mitochondria induces mitophagy.

TNIP1 possesses a UBAN domain similar to that in OPTN^{18,19} and was suggested to be an autophagy substrate²⁰. Most autophagy receptors are defined by a ubiquitin-binding domain and an LC3 interacting region (LIR). We thus investigated if TNIP1 contained an LIR motif. In silico searches of LIR²¹ motif using the bioinformatic tool iLIR²² website revealed two potential canonical LIR domains in TNIP1 (**Figure 3.1A**). A Blast alignment with 4 other higher eukaryote TNIP1 proteins showed that LIR2 is conserved but not LIR1 (**Supp Figure 3.1A**). In order to determine whether TNIP1 LIR1 and LIR2 are functional LIR domains, we mutated LIR1 F83 and L86 to alanine and LIR2 F125 and V128 to alanine (**Supp Figure 3.1B**). We also made a LIR1 and LIR2 double mutant construct that carries all 4 mutations. Lysates of HeLa cells transfected with TNIP1 wild type (WT), LIR1 mutant, LIR2 mutant and LIR1+LIR2 mutant were subjected to GST pull down experiments, an assay previously used to assess binding to mATG8 proteins (i.e. MAP1LC3A, MAP1LC3B, MAP1LC3C, GABARAP, GABARAPL1 and GABARAPL2)^{23,24}. As a positive control, SQSTM1/p62 was demonstrated to bind strongly to all mATG8 proteins (**Supp Figure 3.1C**). Conversely,

as a negative control we employed the TNIP family member TNIP3 where no LIR motif was detected when using iLIR search and accordingly where no LC3/GABARAP binding was observed (**Supp Figure 3.1D**). TNIP1, on the other hand, was able to bind to all mATG8 proteins, with an apparent preference for LC3C and GABARAP, and a weaker binding to LC3A, LC3B and GABARAPL2 (**Figure 3.1B**). LIR1 mutations diminished LC3C binding while LIR2 mutations diminished GABARAP binding. LC3A and LC3B binding was lost with both constructs. However, the double LIR1+LIR2 mutations resulted in a total loss of all 6 mATG8 binding indicating that TNIP1 is a *bona fide* mATG8 binding protein, where LIR1 seems to preferentially bind LC3C and LIR2 GABARAP, although both LIR seem to be able to compensate for each other's loss of function. In addition, TNIP1 was previously shown to form a complex with TAX1BP1 in a non-autophagy context¹². Consequently, we investigated whether TNIP1 is involved in mitophagy by interaction with TAX1BP1. Knockout of all five mitophagy receptors (OPTN, p62, TAX1BP1, NBR1 and NDP52) was reported to completely block mitophagy²⁵, indicating that TNIP1 is unlikely to act alone in mitophagy induction. Therefore, we took advantage of the chemically induced dimerization (CID) assay in cells expressing mitochondrial-targeted mKeima (mt-Keima)²⁵ (**Figure 3.1C**). We fused the protein FRB to the C-terminus tail of the outer mitochondrial protein FIS1 and TNIP1 to the soluble protein FKBP. Adding the small molecule RAPALOG induces dimerization of FRB and FKBP, conditionally localizing TNIP1 to the mitochondria. The A/C heterodimerizer RAPALOG is an analog of the autophagy-induction drug Rapamycin, however, key mutations makes RAPALOG unable to inhibit mTor and thus is incapable of inducing autophagy²⁶. We then gauge mitophagy using Fluorescent Activated Cell Sorting (FACS) by measuring the ratio of mt-Keima under neutral and acidic pH conditions. Because cells are gated to the same intensity levels for the mKeima and GFP channels, we ultimately measure cells with the same level of overexpressed protein²⁷. Interestingly, localizing TNIP1 to mitochondria for 24 Hrs induced robust mitophagy, and the UBA1 loss of function mutation (D472N) was able to trigger mitophagy to levels similar to WT TNIP1, indicating that the ubiquitin binding domain of TNIP1 is not necessary for inducing mitophagy when TNIP1 is artificially targeted to mitochondria (**Figure 3.1D**). We next investigated whether the LIR motifs have any role in the ability of TNIP1 to trigger

mitophagy. While LIR1 mutations had a relatively minor effect and retained an ability to substantially trigger mitophagy, CID with LIR2 mutant was also able to trigger mitophagy, but with an approximately 55% defect compared to WT TNIP1, indicating the importance of the LIR2 domain of TNIP1 in carrying out mitophagy (**Figure 3.1E**). No additional effect was observed when using the LIR1+LIR2 double mutant construct, indicating that the effect seen is due only to the LIR2 modifications. Immunocytochemistry recapitulated the GST pull down data, with LIR1 and LIR2 mutant constructs showing a defect but still retained the ability to recruit LC3B and GABARAP to the mitochondria. LIR1+LIR2 double mutant, however, showed a significant defect in LC3B recruitment. Interestingly, recruitment of GABARAP was not impaired with any of the LIR mutants (**Supp Figure 3.1E&F**). Based on these results we hypothesize that TNIP1's function on mitochondria does not depend only on binding with mATG8 proteins, but probably also interacts with other autophagy machinery proteins as the LIR2 mutant construct is still able to trigger mitophagy. These IF data also support the GST-pull down data, where we showed that TNIP1 binds more strongly to GABARAP than to LC3B. An interesting observation is the clumping of the mitochondria upon RAPALOG treatment as is typically observed upon mitochondrial depolarization in Parkin-expressing cells, due to the clustering of p62/SQSTM1²⁸. A similar mechanism thus might occur when ectopically expressing TNIP1 to the mitochondria.

Mammalian cells possess 3 TNIP homologs, TNIP1, TNIP2 and TNIP3, sharing certain ABIN homology domains (AHDs) that characterize them (**Figure 3.1F**). CID and FACS analysis with TNIP2 and TNIP3 revealed that they were not able to induce mitophagy as substantially as TNIP1, indicating the singular capacity of TNIP1 in mitophagy. To further characterize the important domains of TNIP1 other than LIR2, we carried out CID with versions of TNIP1 missing individual AHD domains (**Figure 3.2A and Supp Figure 3.2A**). Looking at their localization, all constructs displayed an even, cytosolic distribution in puncta, like the full-length construct. The construct lacking AHD3 however seemed to have a bigger propensity to aggregate. (**Supp Figure 3.2B**). The AHD1 domain has been shown to be essential for interacting with A20/TNFAIP3, a central gatekeeper in inflammation and immunity. AHD1 deletion had no effect on mitophagy, suggesting that binding to A20 is not

necessary for its capacity in mitophagy. TNIP1 with the AHD3 deletion showed a strong reduction in its ability to induce mitophagy, while deletion of AHD4 domain in TNIP1 showed moderate inhibitory effect on mitophagy (**Figure 3.2B**). Since we discovered that the LIR2 mutant and AHD3 deletion mutant TNIP1 displayed the strongest deficiency in mitophagy, we combined both and made an AHD3 deletion and LIR2 mutant construct and observed that this construct completely abolished TNIP1's ability to induce mitophagy (**Figure 3.2C**). We conclude that the LIR2 motif and AHD3 domain of TNIP1 are both involved and possibly have distinct roles in mitophagy. Both N-terminal and C-terminal fragments of TNIP1 (**Figure 3.2D**) proved incapable of inducing mitophagy, indicating that more than just LIR and AHD3 domains are required for mitophagy, and a fully folded protein is necessary.

To determine the molecular mechanisms of TNIP1 in mitophagy, we performed CID-induced mitophagy in different cellular backgrounds: FIP200 KO, WIPI2 KO, A20 KO and pentaKO²⁵ cells (5KO: NDP52, OPTN, TAX1BP1, SQSTM1 and NBR1). 5KO cells were previously described to be deficient in mitophagy, owing to the dependence on recruitment of autophagy receptors to recruit the autophagy machinery. To our surprise, TNIP1 was able to mediate mitophagy in 5KO cells at a level similar to that in WT cells (**Figure 3.2E and Supp Figure 3.2C**). This implies that TNIP1 is able to recruit an essential effector of the autophagy machinery on its own and does not depend on further recruitment of autophagy receptors previously deemed critical for mitophagy responses. In FIP200 KO and WIPI2 KO cells, no mitophagy was observed (**Figure 3.2E and Supp Figure 3.2C**), consistent with their essential roles as general autophagy machineries. Because of the tight role TNIP1 plays with A20 in the NF- κ B pathway, we explored mitophagy activation in an A20 KO background (**Figure 3.2E and Supp Figure 3.2C**). Consistent with the results seen with the AHD1 deletion mutant, A20 KO did not alter the mitophagy response, supporting the idea that TNIP1's role in CID induced mitophagy does not depend on A20, and revealing a new activity of TNIP1 distinct from prior work on its role in inflammation. Mitophagy independent of autophagy receptors (5KO) indicates that TNIP1 likely acts downstream of or in parallel with autophagy receptor recruitment and can recruit mATG8 and the autophagy

machinery independent of the autophagy receptors, including TAX1BP1 previously reported to bind TNIP1.

To clarify the role of TNIP1 requirement in mitophagy, we conducted different CID experiments in TNIP1 KO cells. Unfortunately, due to the size of FIP200, we could not produce a functioning FKBP-GFP-FIP200 construct. Consequently, we assessed whether other autophagy machinery proteins (i.e. WIPI2 and ATG16L1), as well as A20 were able to trigger mitophagy when placed on mitochondria in WT or TNIP1 KO cells. As previously reported, CID with ATG16L1 showed a strong mitophagy response in control cells⁷. TNIP1 KO did not impair that response, and even slightly enhanced it, although not significantly (**Figure 3.2F and Supp Figure 3.2D**). Similarly, CID with WIPI2 displayed a robust mitophagy response and this response was significantly stronger in TNIP1 KO cells (**Figure 3.2F and Supp Figure 3.2D**). Finally, CID with A20 displayed a weak mitophagy response that was abolished in TNIP1 KO cells (**Figure 3.2F and Supp Figure 3.2D**). This could be explained by a weak recruitment of TNIP1 mediated by A20 to the mitochondria, and the subsequent recruitment of the autophagy machinery. In light of these results, we conclude that TNIP1 can induce mitophagy independently of autophagy receptors but is dependent on early autophagy machinery and is dispensable for these autophagy machinery proteins to induce mitophagy.

TNIP1 is a negative regulator of mitophagy

The CID results showed that TNIP1 has the potential to trigger mitophagy and allowed us to identify the domains of TNIP1 required for this function. Since TNIP1 possesses a ubiquitin-binding domain as well as a LIR motif, we speculated that it could act as an autophagy receptor. To test this hypothesis, we compared TNIP1 to known autophagy receptors in mitophagy flux assays. When subjected to mitophagy induced by mitochondrial depolarization, receptors are degraded in an autophagy-specific manner, together with their cargo. Blocking autophagosomal degradation with the V-ATPase inhibitor Bafilomycin A1 (BafA1) is a common way to estimate substrates specifically degraded in lysosomes. Combining the mitochondrial ATP synthase and complex III inhibitors Oligomycin A and

AntimycinA1 (OA), respectively, is an established treatment for triggering mitophagy. Autophagy receptors are selectively degraded during mitophagy, as can be seen with TAX1BP1, NDP52 and OPTN (**Supp Figure 3.3A**). Double treatment of cells with BafA1 and OA promotes mitophagy but prevents lysosomal degradation of the encapsulated proteins (**Supp Figure 3.3A**). However, similar to the ULK1 complex protein FIP200, TNIP1 levels were not influenced by Bafilomycin or OA treatment. Interestingly, TNIP1 was recently found to be an autophagy substrate in an autophagosome profiling content screening²⁰, and thus would appear to be an autophagy substrate. Consequently, its apparent lack of degradation upon mitophagy or absence of accumulation upon Bafilomycin A1 treatment may be due to a fast turnover rate. Therefore, we performed OA treatments combined with cycloheximide (CHX) to investigate TNIP1 degradation (**Supp Figure 3.3B**). Remarkably, TNIP1 seems to be a long-lived protein, as no degradation of TNIP1 was seen after 4 hours of CHX treatment, indicating that TNIP1 does not seem to be rapidly turned over. Interestingly, under steady state conditions, FIP200 is degraded rapidly but counterintuitively is slightly stabilized during mitophagy induction. Consequently, TNIP1 is very likely not degraded *en masse* via mitophagy, as is also the case for FIP200. Immunocytochemistry allowed observation of TNIP1 localization under steady state condition as well as upon mitophagy. To trigger mitophagy, HeLa cells stably expressing HA-Parkin were treated for 4 Hrs with OA (**Supp Figure 3.3C**). Under steady state conditions, endogenous TNIP1 appeared as puncta, in the vicinity of the mitochondria, with some colocalization events at the periphery of mitochondria, in a manner reminiscent of autophagy receptors. However, upon OA treatment, TNIP1 was found to coalesce in the perinuclear region and not to substantially relocate to mitochondria, as can be seen with FIP200, contrary to what is seen with the autophagy receptor TAX1BP1, prompting us to reconsider the role of TNIP1 as an autophagy receptor.

Because TNIP1 was able to induce mitophagy when artificially placed onto mitochondria, we next asked if TNIP1 KO cells and such cells rescued with FKBP-GFP-TNIP1 (**Figure 3.3A**) show any alteration in PINK1/Parkin mediated mitophagy. HeLa cells expressing mt-Keima and HA-Parkin were treated for 6 Hrs with OA and analyzed by FACS. This treatment

induced a strong mitophagy response in WT cells and showed the same response in TNIP1 KO cells (**Figure 3.3B**). In contrast, re-expression of TNIP1 in TNIP1 KO cells showed a substantial defect in mitophagy. These results indicate that TNIP1 may be a negative regulator of mitophagy and prompted us to investigate earlier time points in mitophagy. Indeed, at 2 Hrs of OA treatment, when mitophagy was lower in WT cells, we saw a stronger mitophagy induction in TNIP1 KO cells, a response that could be reversed by re-expression of TNIP1 (**Figure 3.3C**). To further validate TNIP1's role in inhibiting mitophagy, we overexpressed TNIP1 in HeLa cells instead of rescuing in TNIP1 KO cells and monitored mitophagy using mt-Keima and FACS. Similar to results seen with rescue experiments in the TNIP1 KO background, over-expression of TNIP1 in WT HeLa cells induced a robust inhibition of mitophagy (**Figure 3.3D**). Overexpression of AHD domain deletion mutants in WT cells was then used to compare to the full length TNIP1 and assess the deletion mutant abilities to inhibit mitophagy. While the Δ AHD1 construct showed a mitophagy response similar to WT TNIP1, in accordance with a lack of function in previous CID experiments, Δ AHD3 displayed higher mitophagy, while Δ AHD4 showed an intermediate response compared to Δ AHD3 and WT TNIP1.

We next carried out rescue experiments in TNIP1 KO cells with the LIR mutant construct in PINK1-Parkin dependent mitophagy. Similarly to the observations with the AHD3 deletion construct, the inhibition of mitophagy was drastically reduced with the LIR mutant construct, but not as much as seen with the AHD3 deletion construct (**Figure 3.3E**). Therefore, we conclude that the LIR motif and the AHD3 domain of TNIP1 are both contributing to its role in inhibiting mitophagy. These results are consistent with the results obtained with CID, where we identified the AHD3 domain and LIR motif as being important for TNIP1 function.

To further confirm the specificity of TNIP1 in inhibiting mitophagy, we performed the same over-expression experiments with TNIP2 and TNIP3 (**Supp Figure 3.3D**). While TNIP2 overexpression had no effect, TNIP3 overexpression showed a mild inhibition of mitophagy,

but much less than seen with TNIP1 over-expression. This may be explained by the presence of an AHD3 domain in TNIP3 but not in TNIP2.

We next performed a complementary mitophagy assay by monitoring the degradation of the mitochondrial matrix protein MTCO2 (COXII) and outer membrane protein MFN2 upon longer OA treatment. In WT cells expressing BFP-Parkin, the outer mitochondrial protein MFN2 is rapidly degraded via the proteasome, while the mitochondrial electron transport chain COXII is degraded at later time points in the lysosome. A robust degradation of COXII was observed after 15 Hrs, progressing further after 21Hrs or 24Hrs of mitochondrial depolarization (**Figure 3.3F**). When GFP-TNIP1 is overexpressed in cells expressing BFP-Parkin, the steady state level of COXII is higher than in non-overexpressing cells. 15 Hrs after mitophagy induction, COXII degradation is impaired in GFP-TNIP1 overexpressing cells. 24 Hrs after mitophagy induction, however, COXII levels are similar in non-overexpressing and overexpressing cells, reflecting the observation with the FACS data where TNIP1 reduces the rate of mitophagy but does not abolish it. As we wondered whether TNIP1's function was specific for mitophagy, we next decided to investigate non-selective autophagy. Ectopic expression of TNIP1 did not influence starvation-mediated autophagy as degradation of p62/SQSTM1 was not blocked when GFP-TNIP1 was overexpressed (**Supp Figure 3.3E**). To further explore the involvement of TNIP1 in non-selective autophagy, we took advantage of a modified version of the autophagic flux probe YFP-LC3B_RFP-LC3B Δ G reporter²⁹. This probe utilizes the nature of the YFP marker, that is quenched when localized in an acidic environment. An ATG4 cleaving site is present between LC3B and RFP, resulting in cleavage of the reporter and conjugation of YFP-LC3B to phosphatidylethanolamine (PE) upon autophagy induction. Since the RFP-LC3B Δ G reporter is not able to conjugate to PE, it serves here as an internal control as it cannot be degraded. Autophagic flux can thus be estimated by measuring the YFP/RFP signal ratio. Because we use the YFP and RFP channels for our imaging experiments, we overexpress TNIP1 with a BFP tag (**Supp Figure 3.4A**). In agreement with the results reported above, overexpression of BFP-TNIP1 had no effect on the autophagic flux upon starvation (**Supp Figure 3.4B**). We next investigated whether TNIP1 was also involved in inhibition of other selective

autophagy pathways by monitoring aggregate clearance using puromycin treatment³⁰. In cells that ectopically express GFP-TNIP1, we observed a defect in aggregate clearance when puromycin was washed out compared to non-overexpressing cells (**Supp Figure 3.4C**). Additionally, we explored an alternative mitophagy pathway triggered by iron depletion³¹. We treated cells with the iron chelator Phenanthroline (Phen) for 16 Hrs and observed the mitophagy response by FACS in WT and TNIP1 KO cells expressing the mt-Keima reporter. To our surprise and contrary to results seen with mitophagy triggered by membrane depolarization, TNIP1 KO cells displayed a small defect in mitophagy response compared to WT cells (**Supp Figure 3.4D**). The lack of inhibition of Phen-mediated mitophagy may relate to the lack of ubiquitination in this pathway, in contrast to Parkin-mediated mitophagy and aggrephagy. Together, these data indicate that TNIP1 inhibits some forms of selective autophagy but not non-selective autophagy.

Binding of TAX1BP1 to the AHD3 domain is required for TNIP1's inhibition of mitophagy

To obtain mechanistic insights into the function of TNIP1 as a negative regulator of selective autophagy, we performed an unbiased mass spectrometry (MS) screen to identify specific interactors of the AHD3 domain. We immuno-precipitated (IP) HA-TNIP1 full length, TNIP1 Δ AHD3 and TNIP1 Δ AHD4 and determined high confidence interaction partners (HCIPs) by MS followed by Comparative Proteomics Analysis Software Suite (compPASS) analysis as previously described^{32,33} (**Figure 3.4A, Supplementary Table**). While TNIP1 co-immunoprecipitated with many cell surface receptors and secreted proteins, Gene Ontology (GO) analysis revealed autophagy components as the only significantly enriched class of proteins. In particular, RAB11FIP5, the autophagy receptors TAX1BP1, OPTN and to a smaller extent CALCOCO2 (NDP52) as well as the ULK1 complex component RB1CC1 (FIP200) were the most abundant HCIPs.

Consistent with previous reports¹¹, we observed that the TNIP1-OPTN interaction occurs via the Δ AHD4 domain by IP/MS and validated this by IP/immunoblotting (**Figure 3.4A and 3.4B**). As a control, we used TNIP3, that also possesses an AHD3 domain and observed

binding to TAX1BP1 but not to OPTN. We also confirmed binding of TNIP1 to TAX1BP1¹², which we found to require the AHD3 domain, suggesting that TNIP1's function in mitophagy might depend on TAX1BP1 binding. To test this possibility, we further characterized the interaction between TNIP1 and TAX1BP1. We overexpressed HA-tagged TAX1BP1 full length, coiled-coil (CC), Δ SKICH or Δ zinc-finger (ZF) constructs in 293T cells stably expressing GFP-TNIP1 followed by anti-GFP IPs (**Figure 3.4C**). these experiments revealed that TNIP1 is able to interact with full length TAX1BP1 and Δ SKICH TAX1BP1, but not with TAX1BP1 CC and Δ ZF constructs. These results indicate that TNIP1 binds via the TAX1BP1 ubiquitin binding domain ZF. We next performed FACS experiments to assess the involvement of TAX1BP1 in TNIP1's role in mitophagy inhibition (**Figure 3.4D**). No reduction in mitophagy was observed in TAX1BP1 KO cells compared to WT cells, in accordance to previously published data²⁵. Furthermore, when we overexpressed TNIP1 in TAX1BP1 KO cells, we observed that TNIP1 did not inhibit mitophagy to levels similar to those in WT cells. These results indicate that TAX1BP1 is involved in TNIP1 inhibition of mitophagy. Overall, TNIP1 binds the ZF domain of TAX1BP1 via its AHD3 domain, and this binding is critical for its inhibitory action.

Binding of FIP200 to an evolutionarily conserved LIR motif is required for TNIP1's inhibition of mitophagy

The paradigm for selective autophagy initiation recently shifted from the previous models that autophagy receptors role was to recruit mATG8 proteins, which in turn recruit the autophagy machinery, with the recent discovery that autophagy receptors can directly recruit the ULK1 complex for autophagosome formation^{7,34,35}. Other high confidence IPs in our MS data were FIP200 and other members of the ULK1 complex (ATG13 and ATG101). We confirmed binding with FIP200 by IP/Immunoblotting (**Figure 3.4B**) and observed binding with the Δ AHD3 and Δ AHD4 mutants of TNIP1 but not with TNIP3. FIP200 binding to TNIP1 potentially explains how CID with TNIP1 induced mitophagy, as it was previously demonstrated that CID with a FIP200-binding peptide was sufficient to induce mitophagy⁷.

Reflecting the MS data that showed the Δ AHD4 mutant seemed to bind more strongly to FIP200 (**Figure 3.4A**), the Δ AHD4 mutant displayed a much stronger IP interaction with FIP200. We next performed IP/Immunoblotting in TAX1BP1 KO cells and confirmed that TNIP1 was also able to pull down FIP200 (**Figure 3.4E**), implying that TNIP1 binding to FIP200 is independent to TAX1BP1 binding. Surprisingly, the increase of FIP200 binding seen with constructs Δ AHD3 and Δ AHD4 was not observed in TAX1BP1 KO cells, suggesting that TAX1BP1 may mediate this stronger binding. However, while the data in Figure 4B was obtained using 293T cells, Figure 4E was obtained using HeLa cells, thus we cannot exclude that this observation could be cell type specific.

SQSTM1/p62 was recently demonstrated to bind to FIP200 through its LIR motif³⁴. We therefore examined whether the TNIP1 LIR2 mutant construct was able to retain binding with FIP200 (**Figure 3.5A**). Interestingly, we could not detect any FIP200 binding with the LIR2 mutant TNIP1. Reflecting the MS data where we did not detect a co-immunoprecipitation of TNIP1 with WIPI2, binding with WIPI2 was not detected. Similar to observations made with CID, where N-Terminal and C-terminal deletion constructs were nonfunctional (**Supp Figure 3.2C**), neither of these truncation constructs was able to bind FIP200 (**Supp Figure 3.5A**). This is somewhat surprising as we expected the N-terminal construct to still bind FIP200 as it retains the LIR motif. We suspect that truncating TNIP1 disturbs its folding and thus its ability to bind FIP200. In order to exclude the possibility that TNIP1 could pull down FIP200 via a secondary interaction with mATG8 binding, we performed CID experiments coupled with immunocytochemistry in a hATG8 6KO or TAX1BP1 KO background (**Figure 3.5B and Supp Figure 3.5B**). In WT cells, TNIP1 was able to recruit FIP200 upon RAPALOG treatment. The LIR2 mutant TNIP1, however, was not able to recruit FIP200, confirming that this region is necessary for FIP200 binding. Recruitment of FIP200 to mitochondria in hATG8 6KO cells appeared stronger than in WT cells, but the LIR mutant construct failed to recruit FIP200. In TAX1BP1 KO cells, however, we could observe events of recruitment of FIP200 with TNIP1 WT construct but to a much lesser extent than in WT cells. As expected, no recruitment was observed when using the LIR mutant construct. These results attest of an apparent synergy between TAX1BP1 and

FIP200 for FIP200 recruitment. To further characterize the interaction between TNIP1 and FIP200, we sought to identify the binding region of TNIP1 within FIP200 (**Figure 3.5C**). While TNIP1 was able to bind full length and the C-terminal region of FIP200, it was not able to bind the N-terminal part of FIP200 (**Figure 3.5C**), prompting us to further map the C-terminal region for the interaction with FIP200. NDP52 was previously shown to interact with the leucine zipper domain of FIP200, while the CLAW domain of FIP200 was recently identified as responsible for binding with p62/SQSTM1³⁴. Consequently, we investigated which of these two domains bind to TNIP1. TNIP1 was able to pull-down only the Claw domain of FIP200, indicating that the CLAW domain is the minimal necessary region for binding to TNIP1 (**Figure 3.5C**).

Phosphorylation of the FIR motif regulates TNIP1's binding to FIP200 CLAW domain

A consensus FIP200 Interacting Region (FIR) core motif present in several autophagy receptors was recently reported, showing that this FIR motif overlapped with their LIR motif³⁶. It was further demonstrated that phosphorylation of a residue immediately preceding the FIR core motif increases binding to the CLAW domain of FIP200. Careful examination of the LIR motif of TNIP1 showed one threonine and two serine are immediately preceding the LIR motif (**Supp Figure 3.1A**). Furthermore, phosphorylation was predicted by the NetPhos 3.1 server³⁷, and these serine proximal to the LIR domain were recently found to be phosphorylated, resulting in an increased binding to LC3s³⁸. We thus hypothesized that TNIP1 interacts with FIP200 in a phospho-FIR-dependent manner and that allows it to compete with autophagy receptors for interaction with FIP200. To test this, we generated FITC-labeled peptides unmodified or with either a phosphorylated S122 (pS122) or phosphorylated S123 (pS123) and monitored their ability to bind recombinant CLAW domain using fluorescence polarization (FP) as previously demonstrated for the FIR of ER-phagy receptor protein CCPG1. Confirming our hypothesis, phosphorylation at either site on TNIP1 displayed a stronger binding to the CLAW domain, with a KD of 46 μ M for unmodified TNIP1 versus a KD of 9.7 μ M for the pS122 peptide and 3.27 μ M for the pS123 peptide (**Figure 3.6A**). Of note, as previously reported, a phosphorylated CCPG1 displayed

a much stronger binding to the CLAW domain with a K_D of $0.75\mu\text{M}$ vs $8.7\mu\text{M}$ for the unphosphorylated version. Using unlabeled TNIP1 peptides, we performed a competition assay with the FITC-labeled pCCPG1 FIR peptide for the binding to the CLAW domain. TNIP1 pS123 peptide was able to compete with CCPG1 for the binding with the CLAW domain, with an absolute IC_{50} of $70.16\mu\text{M}$ (**Figure 3.6B**). This suggests that TNIP1 acts as a competitive inhibitor and provides an explanation of how TNIP1 inhibits mitophagy, by competing with autophagy receptors for the binding with the CLAW domain. Of note, the mitophagy receptor OPTN was previously measured with a K_D of $306\mu\text{M}$ for unmodified and $11.5\mu\text{M}$ when phosphorylated³⁶, indicating a lower affinity for the CLAW domain than TNIP1, suggesting that TNIP1 would outcompete OPTN for binding with the CLAW domain. To our knowledge, TAX1BP1 binding to the CLAW domain of FIP200 has not been estimated. To validate that full length TNIP1 binds the CLAW domain of FIP200, we purified recombinant TNIP1 protein and performed dynamic light scattering (DLS) analysis. When TNIP1 and CLAW were measured alone, peaks around 2.5nm were observed, with a broader distribution for purified TNIP1 alone. Mixing CLAW and TNIP1 at equal mass-ratios lead to the observation of a second larger peak at 5.5nm (purple), indicating that TNIP1 and CLAW bind together. Adding the pFIR of CCPG1 in excess ($100\mu\text{M}$) prevented TNIP1 to bind to the CLAW domain, reducing the formation of the 5.5nm complex, shifting the apparent peak to 3.1nm (Green) (**Supp Figure 3.6A**). We noticed the formation of a precipitate upon mixing TNIP1 and the CLAW domain, suggesting larger particle formation than is typically measured by DLS. We thus assessed the turbidity, allowing us to characterize the formation of larger particles when TNIP1 and CLAW were mixed, confirming the formation of an insoluble complex. Adding excess of pFIR CCPG1 peptide resulted in perturbation of this complex by competition binding and partially prevented this precipitation (**Supp Figure 3.6B**).

We next performed FACS experiments to assess the contribution of the phosphorylation to the function of TNIP1 by using a phospho-dead mutant, where Thr and Ser residues were replaced by Ala. Overexpressing TNIP1 WT displayed a reduction in mitophagy, while an TSS_121-123_AAA mutant displayed an even stronger inhibition indicating that TNIP1

binding with FIP200 counteracts the inhibition (**Figure 3.6C**). Additionally, IP/immunoblotting with the AAA mutant showed a weaker binding to FIP200 compared to WT TNIP1, confirming that phosphorylation of TNIP1 promotes FIP200 binding (**Figure 3.6D**). We additionally performed GST pull-down of TNIP1 AAA mutant and observed that, while LC3B binding seemed lost, no such loss to binding with GABARAP was observed compared to the LIR2 mutant (**Figure 3.1B**), indicating that AAA mutant likely impairs binding to FIP200 but not to GABARAP. In an attempt to mimic phosphorylated TNIP1, we mutated residues TSS_121-123_EDD and performed IP/immunoblotting. Unfortunately, the mutations did not seem to be effective as the phospho-mutant construct did not recapitulate the FP data and no stronger binding to FIP200 was observed (**Supp Figure 3.6C**). We also tried using single mutations, but neither S122E nor S123E displayed phospho-mimicking abilities (**Supp Figure 3.6D**). TANK-Binding Kinase 1 (TBK1) regulates several autophagy receptors in the autophagy pathway⁷. Furthermore, TBK1 was previously shown to be recruited to the TNIP1-TAX1BP1 complex¹². We thus investigated whether TBK1 was involved in phosphorylating TNIP1. Similarly to results seen with the AAA mutant, cells treated with the TBK1 inhibitor displayed a weaker binding to FIP200, implying that TBK1 is likely the kinase responsible for phosphorylating TNIP1 (**Figure 3.6F**). Lastly, in order to compare the affinity of TNIP1's FIR peptide for FIP200-CLAW and mATG8 proteins, we performed FP using purified mATG8 proteins (**Figure 3.6G and Supp Figure 3.6E**). As seen with FIP200-CLAW, phosphorylated FIR displayed a stronger binding with all 6 mATG8 proteins than unmodified TNIP1, with the strongest binding observed with LC3C and GABARAP, as observed using GST pulldowns. Crucially, the K_d of the binding with all 6 mATG8 is smaller than measured with FIP200-CLAW domain, implying that the binding of the phosphorylated TNIP1 is stronger with mATG8 proteins than with FIP200, although we only used the CLAW domain of FIP200 and not the full length protein like we did with mATG8 proteins. From these results we thus hypothesize that a competition between TNIP1, mATG8 and FIP200 takes place, conditioning the mitophagy status. When TNIP1 is in complex with TAX1BP1, mitophagy is reduced because TNIP1 prevents TAX1BP1 from performing its function by recognizing ubiquitinated substrates by allosteric binding with the Zinc-Finger domain. When the FIR motif of TNIP1 is phosphorylated,

TAX1BP1 binding is released, binding to FIP200 instead, allowing TAX1BP1 to proceed with mitophagy. However, the correct interpretation of the data is made difficult by the fact that phosphorylated TNIP1 also binds strongly to mATG8 proteins. We therefore cannot conclude with certainty that phosphorylation of TNIP1 displaces binding with mATG8 toward FIP200, although our pull down experiments show that AAA mutant loses binding to FIP200 but not to GABARAP, indicating that the phosphorylation more likely has an effect on FIP200 than on GABARAP *in vivo*.

Overall, we here show that TNIP1 is a negative regulator of selective mitophagy, by interacting with autophagy receptors and competing with them for binding with FIP200 via a FIR domain. We therefore speculate that FIR phosphorylation by TBK1 modulates the affinity of TNIP1 by increasing binding to FIP200, displacing the complex FIP200-autophagy receptor to a complex comprised of FIP200 and TNIP1 (**Supp Figure 3.6F**).

3.4 Discussion

Here, we investigated the involvement of the NF- κ B pathway-associated protein TNIP1 in autophagy and identify it as a novel inhibitor of mitophagy. TNIP1-mediated mitophagy inhibition relies on binding to both TAX1BP1 (via its AHD3 domain) and LC3/GABARAPs (via a previously unrecognized LIR motif). Binding with FIP200, via phosphorylation of a FIR motif, on the other hand, counteracts this inhibition. Our findings have important implications for our understanding of the regulation of early events of mitophagy induction, ULK1 complex recycling at the forming autophagosome, and the development of neurodegenerative diseases.

One of the key findings of this report is the identification of a LIR motif in TNIP1. However, similar to a recent publication describing the FIP200 binding region of SQSTM1/p62 encompassing the LIR motif³⁴, it is very likely that a longer sequence than the LIR is responsible for binding to FIP200. In this instance, TNIP1 could be driven to the forming autophagosomes by binding to the LC3/GABARAP proteins, and at the same time, binding TAX1BP1 via the zinc finger domain of TAX1BP1, preventing it from binding to

ubiquitinated cargos, ultimately acting as a security check to regulate the rate of the formation of the autophagosome (**Supp Figure 3.6F**). Upon mitophagy activation, FIP200 is driven to the forming autophagosome and binds TAX1BP1 (and other receptors like NDP52). Phosphorylation of TNIP1 at its FIR motif increases its affinity for interaction with FIP200, resulting in a competition with TAX1BP1 for FIP200 binding, displacing TNIP1 from LC3/GABARAP binding. TAX1BP1 would then be free to bind ubiquitinated cargos, allowing mitophagy to carry on. We also hypothesize that releasing FIP200 from binding with autophagy receptors then allows FIP200 to be available at another place on the growing phagophore and thus promoting phagophore elongation. The MS data with the Δ AHD3 and Δ AHD4 mutants showing a stronger binding to FIP200 could reflect this binding competition between TNIP1, TAX1BP1 (or OPTN) and FIP200, as it seems that losing the domains responsible for binding to the autophagy receptors enhances FIP200 binding. Furthermore, an apparent synergy seems to be taking place between TNIP1, TAX1BP1 and FIP200, as an absence of TAX1BP1 does not prevent FIP200 binding (**Figure 3.4E**), but it impairs recruitment of FIP200 to cargo (**Figure 3.5B and S3.5B**). Additionally, the FIR-binding deficient mutant (AAA mutant) seems to bind more strongly to TAX1BP1 than the WT construct (**Supp Figure 3.6C**), exemplifying the binding competition between FIP200 and TAX1BP1. Although the AAA mutant seems to be working, we unfortunately could not test a phospho-mimicking mutant as this did not seem to bind better to FIP200 as true TNIP1 phosphopeptides do. This is not uncommon for phosphomimicking mutants to not always mimic phosphates, and this was already seen with previous LIR motifs³⁹. It is interesting to note that NDP52 was also identified by MS as an interacting partner via the AHD3 domain of TNIP1. Although we haven't investigated its role, we hypothesize that the role of TAX1BP1 discovered here would be similar for NDP52.

We also show that the role of TNIP1 in inhibition is not solely observed in mitophagy, but in aggrephagy as well, albeit with a smaller effect. These results are important as clearance of aggregates was shown to mainly rely on TAX1BP1³⁰, one of the important factors for the inhibition of mitophagy mediated by TNIP1. These results are potentially very interesting considering the importance of aggregate clearance in neurodegenerative diseases and the

recent discoveries that implicate TNIP1 in ALS and AD. Interestingly TNIP1 seems to be involved in the non-conventional mitophagy induced by iron chelation, as loss of TNIP1 display lower mitophagy rates. This would be an opposite effect compared to the conventional mitophagy induced by membrane depolarization where loss of TNIP1 promotes mitophagy. This may reflect the absence of ubiquitination during iron chelation mitophagy⁴⁰ in contrast to Parkin-mediated mitophagy and aggrephagy.

Interestingly, this inhibition of mitophagy mediated by TNIP1 is reminiscent of its role in the negative regulation of the NF- κ B pathway or interferon response as well as apoptosis^{8,12,19,41}. To date, very few proteins have been characterized as inhibitors of autophagy. The deubiquitinating enzyme (DUB) USP30 was shown to oppose Parkin by removing ubiquitin moieties from mitochondria⁴². Most other proteins have been identified to negatively regulate bulk autophagy and not selective autophagy. This is exemplified by the negative regulation via the production of PI3P, where several proteins have been shown to act. The antiapoptotic protein Bcl-2 was shown to interact with and inhibit Beclin-1's function in autophagy⁴³. The PI3P phosphatase Jumpy was shown to control autophagy initiation by acting at the autophagic isolation membrane stage⁴⁴. Autophagy is also inhibited at the LC3 level, with FLIP altering the interaction between ATG3 and LC3⁴⁵. Also acting at the LC3 level, UBA6-BIRC6 was shown to ubiquitinate LC3, regulating it's availability for autophagy and resulting in an inhibition⁴⁶. Finally, further down the pathway, the Beclin-1 interacting protein Rubicon was shown to negatively regulate autophagosome maturation^{47,48}. TNIP1 thus is an addition to these handful of described negative regulators of autophagy, albeit TNIP1, like Usp30, seems to downregulate selective autophagy and not bulk autophagy.

Although to our knowledge this is the first time that a negative function of mitophagy is described for TNIP1, it was previously found in proteomics studies as being an autophagy substrate^{20,49}. It should be noted that we do not see TNIP1 degradation by the autophagy-lysosomal pathway upon mitophagy induction, so its turn-over during autophagy is likely negligible. Furthermore, although we confirmed that A20 was not involved in the negative

regulation of mitophagy, A20 was previously shown to interact with ATG16L1, together controlling intestinal homeostasis⁵⁰. However, TNIP1 was not investigated in that study, thus its involvement there is unknown. TNIP1 was recently shown to be a signal-induced autophagy receptor in the context of inflammation, using pro-inflammatory signaling that is phosphorylated at a serine upstream of a LIR motif⁵¹. Additionally, phosphorylation of serine residues upstream of the LIR motif by TBK1, resulting in an increased binding to LC3 proteins was recently described³⁸. Another study implicated TNIP1 as a modulator of mitophagy⁵², where its loss resulted in a relative lower mitophagy. However, the apparent discrepancy between this study and our present results can be explained by the fact that the authors looked at a late stage of mitophagy where not much change can be observed, as we observed in Figure 4A. We furthermore performed rescue experiments and thoroughly characterize the different domains involved and interacting partners critical for its function.

Recent findings implicate mitochondrial dysfunction in neurodegenerative disease (ND), and more particularly in Parkinson's disease (PD) and AD. Although most reports show that a defect in mitophagy is deleterious for ND, and that TNIP1 negatively regulates mitophagy rates, one can hypothesize that loss of TNIP1's function in mitophagy regulation could be a factor leading to ND such as AD. For these reasons, efforts will be necessary to investigate whether and how TNIP1 could be involved in mitochondrial dysfunction. It will be particularly interesting to see if TNIP1's locus associated with AD is due to its loss of function in mitophagy or any of the other pathways it is involved in such as NF- κ B. On the other hand, for PD, efforts are being made to activate mitophagy. One strategy seen as amenable to pharmacologic manipulation is to inhibit the proteins that inhibit mitophagy such as USP30. One could consider pharmacologic inhibition of TNIP1 as an alternate approach.

3. 5 Methods

Cell lines

HEK293T and HeLa cells were purchased from ATCC. HEK293T and HeLa cells were cultured in Dulbecco's modified eagle medium (DMEM) with 10% (v/v) Fetal Bovine Serum (Sigma), 1 mM Sodium Pyruvate, 2 mM GlutaMAX. All media and supplements were from Thermo Fisher. All cells were tested for mycoplasma contamination every two weeks with Plasmotest kit (InvivoGen). Reagents used for transfections were, X-tremeGENE 9 (Roche) for sgRNA transfection, or Polyethylenimine (PEI) (PolySciences) for all other transfections.

Knockout line generation using CRISPR/Cas9 gene editing

CRISPR gRNAs were generated to target exon 3 of TNIP1, exon 2 of TNFAIP3 and exon 3 of TAX1BP1. gRNAs were cloned into pSpCas9(BB)-2A-Puro (PX459) V2.0 (Addgene plasmid #62988). To make KO, HeLa cells were transfected with the gRNA plasmid and treated with 1 µg/ml puromycin for 2 days to enrich transfected cells, which were then diluted and placed into 96-well plates for single colonies. Primer set (ggtggaccagcatggagttt and accagggagcttccaactca) were used for PCR screening of TNIP1 KO clones. Primer set (tcagtaccactctctgccttc and ctccaagcctcaatgtgctct) were used for PCR screening of TNFAIP3 KO clones. Primer set (ttatccttgagaaattggatagca and tagtacctaaaaagaaccactcttc) were used for PCR screening of TAX1BP1 KO clones.

Cloning, mutagenesis and stable cell line generation

For lentiviral constructs, inserts were either amplified by PCR and cloned into pHAGE vector, respectively by Gibson assembly (New England Labs) or Gateway cloning (Thermo Fisher). Deletion mutants were generated using Gibson Cloning. Point mutants were generated by site directed mutagenesis or Gibson cloning. All constructs used or generated in this study were validated by Sanger sequencing and complete plasmid sequences and maps are available upon request. Stable expression of lentiviral constructs in HeLa or HEK293T cells were achieved as follows: lentiviruses were packaged in HEK293T cells by transfecting constructs together with appropriate helper plasmids and PEI. The next day, media was exchanged with fresh media. Viruses were harvested 48 h and 72 h after transfection and

transduced in HeLa or HEK293T cells with 8 $\mu\text{g}/\text{mL}$ polybrene (Sigma). Cells were then directly used in experiments or optimized for expression by FACS.

Immunoblot analyses

Cells seeded into 12-well plates were washed with phosphate buffered saline (PBS) and lysed with RIPA buffer. The protein concentration was measured using a BCA kit. Samples were boiled at 99°C for 5 min 20–50 μg of protein lysate of each sample was loaded and separated on 4%–12% Bis-Tris gels (Thermo Fisher) according to manufacturer's protocol. Gels were transferred to polyvinyl difluoride membranes and immunostained using specific antibodies. For mitophagy measurements by immunoblotting, cells were treated with 10 μM Oligomycin (Calbiochem), 10 μM Antimycin A (Sigma) and 10 μM QVD (ApexBio) in growth medium at different timepoints indicated in figure legends, prior to western blot analysis. For starvation-induced autophagy, by immunoblotting, cells were washed 3 times with PBS and incubated for the indicated time with HBSS containing calcium and magnesium.

Recombinant protein/peptide production and protein purification

mATG8 proteins (LC3A, LC3B, LC3C, GABARAP, GABARAPL1, GABARAPL2) were first cloned into pENTR vector using GATEWAY cloning. They were cloned into pDEST60 GST vector using LR clonase. GST expression vector were expressed into DL21 (DE3) bacteria. 50mL LB broth was inoculated with 2mL pre-culture of the GST constructs. Bacteria were incubated for ~ 1 h at 37°C with agitation until an optical density of ~ 0.6 was reach. 400 μM IPTG was used to induce protein production for 4 Hrs. Bacteria were collected and the pellet was lysed with lysis buffer (20mM TRIS-HCl pH7.5, 10mM EDTA, 5mM EGTA, 150mM NaCl, 0.5% NP40, 1% Triton X-100, Benzonase, 1mM DTT, protease inhibitor, 2 mg/ml lysozyme). The lysate was shock-freezed with liquid nitrogen before thawing and sonication. The samples were centrifuged and cleared lysate was incubated with 100 μL of slurry GST beads, followed by an overnight incubation at 4°C on a rotating shaker. Beads were subsequently washed (20mM TRIS-HCl pH 7.5, 10mM EDTA, 5mM EGTA, 150mM NaCl, 1mM DTT) before exchanging the buffer for the storage buffer (20mM TRIS-

HCl pH 7.5, 10mM EDTA, 5mM EGTA, 150mM NaCl, 1mM DTT, 5% glycerol, proteinase inhibitor).

Production of recombinant His6-TEV-FIP200-CLAW domain was purified from *E. coli* BL21 (DE3) containing the plasmid was grown in TB medium containing 50 µg/L ampicillin, which was shaken at 37°C to an OD₆₀₀ of 0.5. The cell culture was cooled down to 20°C and induced with 1 mM isopropyl-beta-D-thiogalactopyranoside (IPTG) and harvested 16 h later by centrifugation. The cell pellet (≈6 g from 2 L) was suspended in the 30 mL lysis buffer [100 mM Tris (pH 7.4), 500 mM KCl, 5 mM MgCl₂, 20 mM imidazole, 5% glycerol, 2 mM β-mercaptoethanol, and protease inhibitor tablet (Roche)]. The cells (held in an ice bath) were lysed by six 30 s pulses of sonication, separated by 2 min intervals. The lysate was centrifuged at 20,000×g for 45 min at 4°C, and the resulting supernatant was loaded onto a Ni-NTA column [5 mL suspension, preequilibrated with wash buffer (50 mL, 50 mM HEPES [pH 7.4], 150 mM KCl, 5 mM MgCl₂, and 20 mM imidazole)] and incubated at 4°C with rotation for 30 min. The column was then flushed with wash buffer (100 mL), and His6-tagged FIP200-CLAW was eluted by an increased ration of imidazole elution buffer (500 mM imidazole in wash buffer) to wash buffer. Fractions containing the CLAW proteins were combined and concentrated with an Amicon Ultra-15 centrifugal filter unit (nominal molecular weight limit = 10 kDa). The mixture (0.5 mL of 20 mg/mL) was then fractionated with a gel filtration column (Tricorn Superdex 200; GE Healthcare), eluted with GF buffer [20 mM HEPES (pH 7.4), 150 mM KCl, and 1 mM MgCl₂] at 0.5 mL/min flow rate, and fractions corresponding to an apparent molecular weight of 15–30 kDa were collected and analyzed by 4%–12% SDS/PAGE to evaluate purity (Invitrogen). Fractions that contained FIP200 of ≥95% purity were concentrated to 4 mg/mL, exchanged into storage buffer [20 mM HEPES (pH 7.4), 150 mM KCl, 1 mM MgCl₂, 5% glycerol, and 1 mM TCEP], aliquoted, frozen in liquid nitrogen, and stored at –80°C.

Full-length TNIP1 cDNA was cloned into pFastbac-HTA vector with an N-terminal 6x His tag. Bac-to-Bac Baculovirus Expression System (Invitrogen) and pFastbac-HTA-6x His-TNIP1 were used to generate recombinant baculoviruses. To express TNIP1, 1L of Sf9 cells

(1.5×10^6 cells/ml) were infected with recombinant TNIP1 baculovirus and incubated in a 28°C orbital shaker at 100 rpm. After 72 h of incubation, insect cells were centrifuged at 1000xg for 20 min and cell pellets were flash frozen in liquid nitrogen and stored at -80°C. For protein purification, the insect cell pellets containing 6xHis-TNIP1 were re-suspended in 25 mL Buffer A (50 mM Tris-HCl pH 8.0, 300 mM NaCl, 10% glycerol, 0.1% Triton X-100, protease inhibitor cocktail). Cells were lysed using a microfluidizer at 15,000 psi. The lysate was centrifuged at 50,000xg at 4°C for 35 min to clear cell debris. The supernatant was incubated with 1 mL of Ni-NTA agarose (Qiagen) at 4°C with continuous rotation for 2h. Ni-NTA agarose beads were washed with Buffer A containing 20 mM imidazole and His-TNIP1 was eluted in buffer A with 250 mM imidazole. Subsequently, PD-10 Desalting Columns containing Sephadex G-25 resin was used to remove imidazole from the His-TNIP1 protein solution. His-TNIP1 was further purified by size exclusion chromatography using the Superdex 200 Increase 10/300 GL column. Purified His-TNIP1 was aliquoted, flash-frozen in liquid nitrogen, and stored at -80°C.

All TNIP1 and CCPG1 peptides used in this study were synthesized *in vitro* by Genescript.

Immunoprecipitation, GST-pull down, GFP-TRAP, and HA beads precipitation

For GFP-TRAP (Chromotek), HA-beads (Pierce) and GST precipitation experiments, HEK293T or HeLa cells seeded in 10cm plates were co-transfected with specific constructs to overexpress proteins of interest for 24 to 48 h, if indicated. IPs were performed following manufacturer's instructions.

Briefly, for HA-IP, cells were then lysed using ice-cold lysis buffer (25 mM Tris-HCl pH 7.4, 150 mM NaCl, 1% NP-40, 1 mM EDTA, 5% glycerol) supplemented with EDTA-free cOmplete protease inhibitor (Roche). Samples were incubated on ice with intermittent agitation by pipetting for 10 min. Beads were equilibrated using bead resuspension buffer (TBS containing 0.05% Tween-20 Detergent [TBS-T]). Protein lysates were precleared by centrifugation at 4°C for 10 min at 15,000 g. 1% INPUT was collected and clarified lysate was incubated with equilibrated beads for 1–2 h at 4°C. Beads were then washed with ice-

cold TBST Wash buffer 3 to 5 times. Bound proteins were eluted with 2x LDS lysis buffer (Thermo Fisher) in boiling conditions.

For GFP-Trap, cells were then lysed using ice-cold lysis buffer (10 mM Tris/Cl pH 7.5, 150 mM NaCl, 0.5 mM EDTA, 0.5% Nonidet™ P40 Substitute) supplemented with EDTA-free cOmplete protease inhibitor (Roche). Samples were incubated on ice with intermittent agitation by pipetting for 30 min. Beads were equilibrated using bead dilution buffer (10 mM Tris/Cl pH 7.5, 150 mM NaCl, 0.5 mM EDTA). Protein lysates were precleared by centrifugation at 4°C for 10 min at 15,000 g. Clarified lysates were diluted using dilution buffer, 1% INPUT was collected and lysate was incubated with equilibrated beads for 1–2 h at 4°C. Beads were then washed with ice-cold Wash buffer (10 mM Tris/Cl pH 7.5, 150 mM NaCl, 0.05% Nonidet™ P40 Substitute, 0.5 mM EDTA) 3 to 5 times. Bound proteins were eluted with 2x LDS lysis buffer (Thermo Fisher) in boiling conditions.

For GST pull down, cells were lysed (50mM TRIS-HCl 7.5, 150mM NaCl, 0.5% NP40, protease inhibitor). Samples were incubated at 4°C with constant agitation for 30 min. Protein lysates were precleared by centrifugation at 4°C for 10 min at 15,000 g. 1% INPUT was collected and clarified lysate was incubated with equilibrated beads overnight at 4°C with agitation. Beads were washed 5 times with wash buffer (20mM TRIS-HCl pH 7.5, 10mM EDTA, 5mM EGTA, 150mM NaCl, 1mM DTT). Bound proteins were eluted with 2x LDS lysis buffer (Thermo Fisher) in boiling conditions.

Live cell imaging

Cells seeded into a 96 well plate (MGB096-1-2-LG-L) were imaged in DMEM on a Nikon Ti2-E microscope with a CSU-W1 spinning disk, Hamamatsu ORCA-FLASH 4.0×sCMOS camera, and 20× objective (NA 0.75) at 37°C, 5% CO₂, and humidity. Twelve sites were imaged per well every hour for 24 h in triplicate wells.

Immunofluorescence microscopy

Cells seeded in 12 well plates with a 1.5mm pre-treated coverslip (neuVitro) were treated as indicated in figure legends. After treatment, cells were rinsed in PBS and fixed with 4% paraformaldehyde at room temperature (RT) for 10 min. Cells were washed with PBS. For immunostaining, cells were first permeabilized with 0.5% Triton X-100 for 10 min at RT and blocked with 3% goat serum in PBS for 1 h at RT. After, cells were incubated with 0.1% Triton X-100, 3% goat serum in PBS supplemented with antibodies (1:200) 1 h at RT or overnight at 4°C. Cells were then washed with PBST (PBS +0.1% Triton X-100) 3 times and incubated with Alexa 505, 488 or 594-conjugated secondary antibodies (Thermo Fisher). For cells expressing fluorescent tagged proteins, cells were seeded as above. After treatments, cells were fixed as above and washed 3 times with PBS prior to image analysis. Images were taken using 63x oil, DIC objective on an LSM 880 Airyscan microscope (Zeiss).

For quantitative measurement, cells were seeded in a 96 well plate, fixed, blocked and immunostained as described above and imaged on the Nikon spinning disk listed above using a 40-water objective (NA 1.15); For the ubiquitin puncta experiments, sixteen sites were imaged per well in triplicate wells. For recruitment experiments, nine sites were imaged per well in triplicate wells.

Mass spectrometry

After samples were bound to magnetic HA-beads as described above, samples were eluted with elution buffer (2 mg/ml HA peptide in TBS) according to manufacturer's instructions, followed by TCA precipitation. Briefly, 100% TCA was added to eluted peptides (f.c. 20% TCA), vortexed and incubated on ice for 30min before centrifugation. Precipitated peptides were washed with 10% ice-cold TCA, followed by 4 washes with ice-cold acetone. The tubes were left to air dry before trypsin digestion. Briefly, peptides were re-suspended with solubilizing buffer (5% SDS, 8M urea, 50mM TEAB, pH7.6). DTT was added for f.c. 5mM before incubating at 50°C for 30min. MMTS was added for 45min before adding an aqueous phosphoric acid solution. Meanwhile, S-Trap columns (Protifi) were conditioned with binding buffer (90% methanol, 100mM TEAB, pH7.1). 1µg of trypsin was added to the

acidified protein mixture and immediately added into the column containing binding buffer. Centrifugation and washing steps were performed before adding digestion buffer (Trypsin in 50mM TEAB) and incubation at 37°C overnight. Columns were rehydrated with 50mM TEAB before elution using 0.2% formic acid and another elution using 50% acetonitrile containing 0.2% formic acid.

Tryptic digests were analyzed using an orbitrap Fusion Lumos tribrid mass spectrometer interfaced to an UltiMate3000 RSLC nano HPLC system (Thermo Scientific) using data dependent acquisition. Initial protein identification was carried out using Proteome Discoverer (V2.4) software (Thermo Scientific). Search results from Proteome Discoverer were incorporated into Scaffold4 for relative quantification using spectral counting. Samples were compared to ~100 reference IPs using a Java script programmed according to the CompPASS software suite as previously described^{33,34} and also compared to the CRAPome.⁴⁷ For determination of the TNIP1 interaction network, thresholds for HCIPs were top 5% of interactors with highest Z score and lowest abundance in the CRAPome. Cytoscape was used to visualize the TNIP1 interaction network. To compare WT TNIP1 with TNIP1 Δ AHD3 and TNIP1 Δ AHD4, total spectral counts for each interactor were first normalized to 1000 and then expressed relative to WT/controls in fold-change (\log_2) and plotted as heatmap using GraphPad.

Mitophagy assay with mito-mKeima via fluorescence activated cytometer

Stable cell lines were generated to express mito-mKeima, HA-Parkin, FRB-Fis1 and FKBP-GFP-tagged target genes with lentivirus system. 200K cells were seeded in 12-well plates and treated with Rapalog for 24h or by O/A at various time points before FACS analysis. Quantification of mtKeima ratio (561/488) were performed as previously described.^{24,26} Briefly, Measurements of lysosomal mt-mKeima were made using dual-excitation ratiometric pH measurements at 488 (pH 7) and 561 (pH 4) nm lasers with 620/29 nm and 614/20 nm emission filters, respectively. For each sample, 50,000 events were collected and subsequently gated for YFP/mt-mKeima double-positive cells that were DAPI-negative. Data were analyzed using FlowJo.

Dynamic light scattering and nano Differential Scanning Fluorimetry/turbidity

Purified full-length TNIP1 and FIP200-CLAW domain at 1 mg/mL in GF buffer (150mM KCl, 20 mM HEPES pH 7.4, 1mM MgCl) were mixed at equal volumes with each other or more GF buffer, or together with the addition of 100uM CCPG1 pFIR peptides. Solutions were incubated at RT for 20 min before being measured for DLS and nanoDSF for turbidity using a Prometheus Panta (NanoTemper Technologies) in high-sensitivity mode. Experiments were performed from 25°C–95°C, in 3–4 independent replicates. Data was analyzed in Prometheus Panta analysis software v1.4.2 (Nanotemper Technologies).

Fluorescence polarization

For binding affinity measurements, purified FIP200-CLAW protein was diluted in series with FP-assay buffer (150mM KCl, 20 mM HEPES pH 7.4, 1mM MgCl, and 0.05% Tween 20). Next the protein was mixed 1:1 with FITC-tagged peptides at ~625nM. A set of solutions with each peptide alone (No FIP200-CLAW) was used to normalize FP measurements. For competition assays, FIP200-CLAW at 4uM and 625nM FITC-CCPG1-pFIR in FP-assay buffer were mixed with increasing concentrations of unlabeled TNIP1 peptides. The mixtures were allowed to incubate 20 min at RT before being measured in triplicate with a Synergy *Neo2* plate reader (BioTek) with FITC-Fluorescence Polarization filter set. Delta mP was calculated by subtracting each measurement from the appropriate peptide-alone control. Concentration vs Delta mP curves were fit for each experiment with a one-site binding model, with the mean \pm stand deviation for K_D calculated from 3–6 independent experiments. Competition experiments were fit with a one-site competition model.

Image analysis

Image analysis was performed using custom MATLAB scripts for each experiment. All images were background corrected then cells were segmented based on intensity and size. TNIP1 overexpressing cells were further segmented by BFP signal. For autophagy flux, the

average YFP and RFP signal was calculated within the cell area mask for each site. The ratio of YFP over RFP signal was calculated for each site then the median value of all sites assessed for each timepoint. Ubiquitin puncta were segmented by combining multiple masks generated from local background subtraction, high pass filtration, and high intensity then filtered by size. For recruitment experiments, to find only GFP-TNIP1 positive cells, single cells were segmented from each other with a water shedding algorithm, then cells with a total GFP intensity above a manual threshold selected for the cell mask, and finally a Pearson's Correlation Coefficient calculated between GFP-TNIP1 and either LC3B, GABARAP, or FIP200 within the cell mask.

Quantification and statistical analysis

All statistical analyses for FACS were calculated in GraphPad Prism 9. Error bars are expressed as mean \pm standard deviation. p values were obtained using a two-way ANOVA with multiple comparison. 0.12 (ns), 0.03 (*), 0.002 (**), <0.001 (***)

5.6 Acknowledgements

The authors would like to thank the laboratory of Michael Lazarou (Monash Biomedicine Discovery Institute) for sharing the LC3/GABARAP KO cells. We would also like to thank all other members of the Youle lab for sharing cell lines and reagents as well as discussions and advice. We further thank Dr Yan Wang from the National Institute of Dental and Craniofacial Research Mass Spectrometry Facility (ZIA DE00075) for performing mass spectrometry analysis. FACS data were acquired using the NINDS facility under the supervision of Dr. Dragan Maric. This work was supported by the Intramural Program of the NINDS and the NIDCR, NIH.

References

1. Mizushima, N. The ATG conjugation systems in autophagy. *Curr. Opin. Cell Biol.* **63**, 1–10 (2020).
2. Conway, O., Akpinar, H. A., Rogov, V. & Kirkin, V. Selective autophagy receptors in neuronal health and disease. *J. Mol. Biol.* (2019). doi:10.1016/J.JMB.2019.10.013
3. Gatica, D., Lahiri, V. & Klionsky, D. J. Cargo recognition and degradation by selective autophagy. *Nat. Cell Biol.* **20**, 233–242 (2018).
4. Khaminets, A., Behl, C. & Dikic, I. Ubiquitin-Dependent And Independent Signals In Selective Autophagy. *Trends Cell Biol.* **26**, 6–16 (2016).
5. Vargas, J. N. S., Hamasaki, M., Kawabata, T., Youle, R. J. & Yoshimori, T. The mechanisms and roles of selective autophagy in mammals. *Nat. Rev. Mol. Cell Biol.* 1–19 (2022). doi:10.1038/s41580-022-00542-2
6. Padman, B. S. *et al.* LC3/GABARAPs drive ubiquitin-independent recruitment of Optineurin and NDP52 to amplify mitophagy. *Nat. Commun.* **10**, 408 (2019).
7. Vargas, J. N. S. *et al.* Spatiotemporal Control of ULK1 Activation by NDP52 and TBK1 during Selective Autophagy. *Mol. Cell* (2019). doi:10.1016/J.MOLCEL.2019.02.010
8. Mauro, C. *et al.* ABIN-1 binds to NEMO/IKK γ and co-operates with A20 in inhibiting NF- κ B. *J. Biol. Chem.* **281**, 18482–8 (2006).
9. Cohen, S., Ciechanover, A., Kravtsova-Ivantsiv, Y., Lapid, D. & Lahav-Baratz, S. ABIN-1 negatively regulates NF- κ B by inhibiting processing of the p105 precursor. *Biochem. Biophys. Res. Commun.* **389**, 205–210 (2009).

10. G'Sell, R. T., Gaffney, P. M. & Powell, D. W. Review: A20-Binding Inhibitor of NF- κ B Activation 1 Is a Physiologic Inhibitor of NF- κ B: A Molecular Switch for Inflammation and Autoimmunity. *Arthritis Rheumatol.* **67**, 2292–2302 (2015).
11. Lee, Y. *et al.* Coordinate regulation of the senescent state by selective autophagy. *Dev. Cell* (2021). doi:10.1016/J.DEVCEL.2021.04.008
12. Gao, L. *et al.* ABIN1 Protein Cooperates with TAX1BP1 and A20 Proteins to Inhibit Antiviral Signaling *. *Publ. JBC Pap. Press* (2011). doi:10.1074/jbc.M111.283762
13. Ramirez, V. P., Gurevich, I. & Aneskievich, B. J. Emerging roles for TNIP1 in regulating post-receptor signaling. *Cytokine Growth Factor Rev.* **23**, 109–118 (2012).
14. Shamilov, R. & Aneskievich, B. J. TNIP1 in Autoimmune Diseases: Regulation of Toll-like Receptor Signaling. *J. Immunol. Res.* **2018**, 1–13 (2018).
15. Benyamin, B. *et al.* Cross-ethnic meta-analysis identifies association of the GPX3-TNIP1 locus with amyotrophic lateral sclerosis. *Nat. Commun.* **8**, 611 (2017).
16. van Rheenen, W. *et al.* Common and rare variant association analyses in amyotrophic lateral sclerosis identify 15 risk loci with distinct genetic architectures and neuron-specific biology. *Nat. Genet.* **53**, 1636–1648 (2021).
17. Wightman, D. P. *et al.* A genome-wide association study with 1,126,563 individuals identifies new risk loci for Alzheimer's disease. *Nat. Genet.* **53**, 1276–1282 (2021).
18. Herhaus, L. *et al.* Molecular Recognition of M1-Linked Ubiquitin Chains by Native and Phosphorylated UBAN Domains. *J. Mol. Biol.* (2019). doi:10.1016/J.JMB.2019.06.012
19. Wagner, S. *et al.* Ubiquitin binding mediates the NF- κ B inhibitory potential of ABIN proteins. *Oncogene* **27**, 3739–3745 (2008).

20. Zellner, S., Schifferer, M. & Behrends, C. Systematically defining selective autophagy receptor-specific cargo using autophagosome content profiling. *Mol. Cell* (2021). doi:10.1016/J.MOLCEL.2021.01.009
21. Johansen, T. & Lamark, T. Selective Autophagy: ATG8 Family Proteins, LIR Motifs and Cargo Receptors. *J. Mol. Biol.* (2019). doi:10.1016/J.JMB.2019.07.016
22. Kalvari, I. *et al.* iLIR: A web resource for prediction of Atg8-family interacting proteins. *Autophagy* **10**, 913–925 (2014).
23. Pankiv, S. *et al.* p62/SQSTM1 binds directly to Atg8/LC3 to facilitate degradation of ubiquitinated protein aggregates by autophagy. *J. Biol. Chem.* **282**, 24131–24145 (2007).
24. Goold, R. *et al.* The LIR motif – crucial for selective autophagy. *J Cell Sci* **126**, 3237–3247 (2013).
25. Lazarou, M. *et al.* The ubiquitin kinase PINK1 recruits autophagy receptors to induce mitophagy. **524**, 309–314 (2015).
26. Bayle, J. H. *et al.* Rapamycin Analogs with Differential Binding Specificity Permit Orthogonal Control of Protein Activity. *Chem. Biol.* **13**, 99–107 (2006).
27. Wang, C. A Sensitive and Quantitative mKeima Assay for Mitophagy via FACS. *Curr. Protoc. Cell Biol.* **86**, (2020).
28. Narendra, D., Kane, L. A., Hauser, D. N., Fearnley, I. M. & Youle, R. J. p62/SQSTM1 is required for Parkin-induced mitochondrial clustering but not mitophagy; VDAC1 is dispensable for both. *Autophagy* **6**, 1090–1106 (2010).
29. Kaizuka, T. *et al.* An Autophagic Flux Probe that Releases an Internal Control. *Mol. Cell* **64**, 835–849 (2016).

- 30.Sarraf, S. A. *et al.* Loss of TAX1BP1-Directed Autophagy Results in Protein Aggregate Accumulation in the Brain. *Mol. Cell* (2020). doi:10.1016/J.MOLCEL.2020.10.041
- 31.Allen, G. F. G., Toth, R., James, J. & Ganley, I. G. Loss of iron triggers PINK1/Parkin-independent mitophagy. *EMBO Rep.* **14**, 1127–35 (2013).
- 32.Werner, A. *et al.* Cell-fate determination by ubiquitin-dependent regulation of translation. *Nature* **525**, 523–527 (2015).
- 33.Sowa, M. E., Bennett, E. J., Gygi, S. P. & Harper, W. J. Defining the Human Deubiquitinating Enzyme Interaction Landscape. **138**, 389–403 (2009).
- 34.Turco, E. *et al.* FIP200 Claw Domain Binding to p62 Promotes Autophagosome Formation at Ubiquitin Condensates. *Mol. Cell* (2019). doi:10.1016/J.MOLCEL.2019.01.035
- 35.Ravenhill, B. J. *et al.* The Cargo Receptor NDP52 Initiates Selective Autophagy by Recruiting the ULK Complex to Cytosol-Invading Bacteria. *Mol. Cell* (2019). doi:10.1016/J.MOLCEL.2019.01.041
- 36.Zhou, Z. *et al.* Phosphorylation regulates the binding of autophagy receptors to FIP200 Claw domain for selective autophagy initiation. *Nat. Commun.* **12**, 1570 (2021).
- 37.Blom, N., Gammeltoft, S. & Brunak, S. Sequence and structure-based prediction of eukaryotic protein phosphorylation sites. *J. Mol. Biol.* **294**, 1351–1362 (1999).
- 38.Zhou, J. *et al.* TBK1 phosphorylation activates LIR-dependent degradation of the inflammation repressor TNIP1. *J. Cell Biol.* **222**, (2023).
- 39.Popelka, H. & Klionsky, D. J. When acidic residues do not mimic phosphorylation: high-affinity binding of the reticulophagy receptor TEX264 to LC3/GABARAP. *Autophagy* **18**, 2515–2518 (2022).

40. Wilhelm, L. P. *et al.* BNIP3L / NIX regulates both mitophagy and pexophagy. *EMBO J.* e111115 (2022). doi:10.15252/embj.2022111115
41. Oshima, S. *et al.* ABIN-1 is a ubiquitin sensor that restricts cell death and sustains embryonic development. *Nature* **457**, 906–909 (2009).
42. Bingol, B. *et al.* The mitochondrial deubiquitinase USP30 opposes parkin-mediated mitophagy. *Nature* **510**, 370–375 (2014).
43. Pattingre, S. *et al.* Bcl-2 Antiapoptotic Proteins Inhibit Beclin 1-Dependent Autophagy. *Cell* **122**, 927–939 (2005).
44. Vergne, I. *et al.* Control of autophagy initiation by phosphoinositide 3-phosphatase jumpy. *EMBO J.* **28**, 2244–2258 (2009).
45. Lee, J.-S. *et al.* FLIP-mediated autophagy regulation in cell death control. *Nat. Cell Biol.* **11**, 1355–1362 (2009).
46. Jia, R. & Bonifacino, J. S. Negative regulation of autophagy by UBA6-BIRC6-mediated ubiquitination of LC3. *Elife* **8**, (2019).
47. Zhong, Y. *et al.* Distinct regulation of autophagic activity by Atg14L and Rubicon associated with Beclin 1-phosphatidylinositol-3-kinase complex. *Nat. Cell Biol.* **11**, 468–476 (2009).
48. Matsunaga, K. *et al.* Two Beclin 1-binding proteins, Atg14L and Rubicon, reciprocally regulate autophagy at different stages. *Nat. Cell Biol.* **11**, 385–396 (2009).
49. Mejlvang, J. *et al.* Starvation induces rapid degradation of selective autophagy receptors by endosomal microautophagy. *J. Cell Biol.* **217**, 3640–3655 (2018).
50. Slowicka, K. *et al.* Physical and functional interaction between A20 and ATG16L1-WD40 domain in the control of intestinal homeostasis. *Nat. Commun.* **10**, 1834 (2019).

51.Shinkawa, Y. *et al.* ABIN1 is a signal-induced autophagy receptor that attenuates NF- κ B activation by recognizing linear ubiquitin chains. *FEBS Lett.* (2022). doi:10.1002/1873-3468.14323

52.Merline, R. *et al.* A20 binding and inhibitor of nuclear factor kappa B (NF- κ B)-1 (ABIN-1) - a novel modulator of mitochondrial autophagy. *Am. J. Physiol. Physiol.* (2022). doi:10.1152/ajpcell.00493.2022

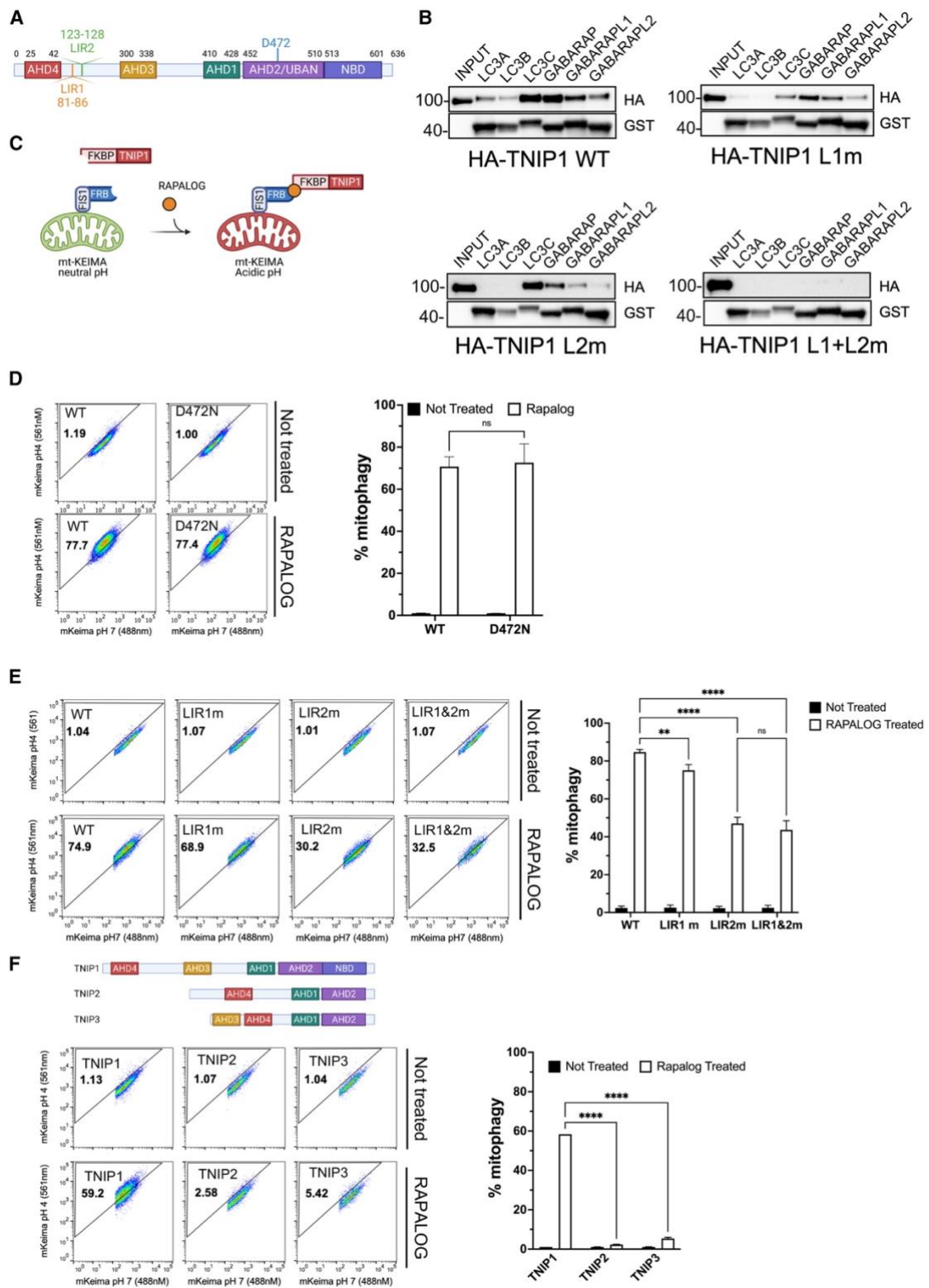


Figure 3.1: Ectopic localization of TNIP1 to the mitochondria induces mitophagy

(A) Schematic representation of TNIP1 and its 2 identified putative LIR motifs. **(B)** HeLa cells stably expressing HA-TNIP1 WT, LIR1 mutant, LIR2 mutant, or LIR1+LIR2 double mutant co-immunoprecipitated (coIP) with purified recombinant GST-tagged mATG8 proteins and subjected to immunoblot analysis (IB). **(C)** Schematization of [CID](#) experiment. **(D)** HeLa cells stably expressing mito-mKeima, FRB-FIS1, and FKBP-GFP-TNIP1 WT or UBAN mutant (D472N) were treated with Rapalog for 24 h and subjected to FACS analysis. Left, representative FACS plot. Right, bar graph representing data as mean \pm SEM obtained from 3 independent replicates. **(E)** HeLa cells stably expressing mito-mKeima, FRB-FIS1, and FKBP-GFP-TNIP1 WT, LIR1 mutant, LIR2 mutant, or LIR1+LIR2 double mutant were treated with Rapalog for 24 h and subjected to FACS acquisition. Left, representative FACS plot. Right, bar graph representing data as mean \pm SEM obtained from 3 independent replicates. **(F)** Top, schematic representation of the TNIP family TNIP1, TNIP2, and TNIP3. Bottom, HeLa cells stably expressing mito-Keima, FRB-FIS1, and FKBP-GFP-TNIP1, FKBP-GFP-TNIP2, or FKBP-GFP-TNIP3 were treated with Rapalog for 24 h and subjected to FACS acquisition. Left, representative FACS plot. Right, bar graph representing data as mean \pm SEM obtained from 3 independent replicates.

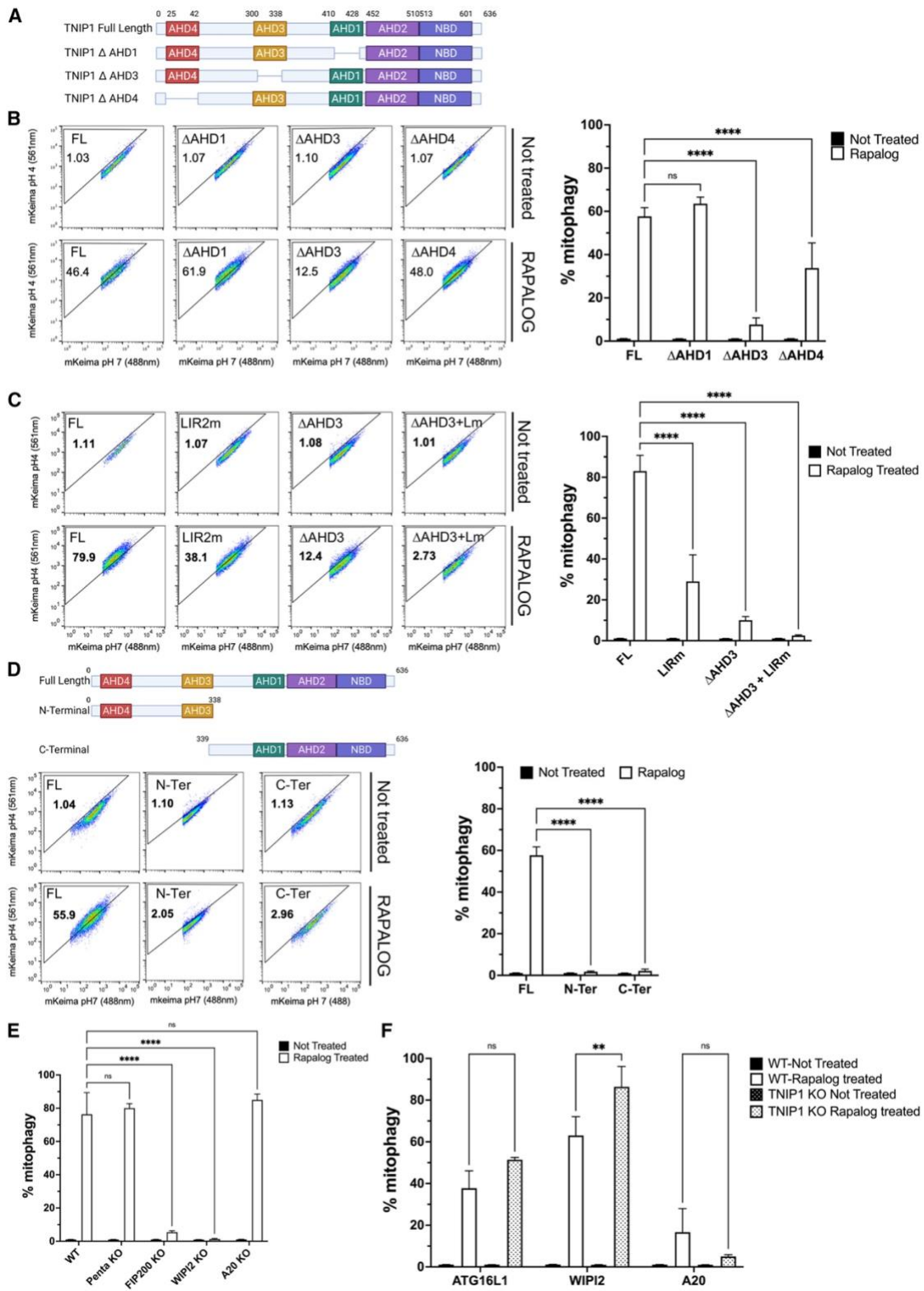


Figure 3.2: LIR2 and AHD3 domain of TNIP1 are essential for its role in mitophagy

(A) Schematic representation of TNIP1 and the AHD mutant constructs. **(B)** HeLa cells stably expressing mito-mKeima, FRB-FIS1, and FKBP-GFP-TNIP1 full-length (FL) or FKBP-GFP-TNIP1 mutants DAHD1, DAHD3, and DAHD4 were treated with Rapalog for 24 h and subjected to FACS analysis. Left, representative FACS plot. Right, bar graph representing data as mean \pm SEM obtained from 3 independent replicates. **(C)** HeLa cells stably expressing mito-mKeima, FRB-FIS1, and FKBP-GFP-TNIP1 FL, LIR2 mutant, DAHD3, or LIR2 mutant and DAHD3 were treated with Rapalog for 24 h and subjected to FACS acquisition. Left, representative FACS plot. Right, bar graph representing data as mean \pm SEM obtained from 3 independent replicates. **(D)** Top, schematic representation of FL TNIP1 or the C-terminal and N-terminal part of TNIP1. Bottom, HeLa cells stably expressing mito-Keima, FRB-FIS1, and FKBP-GFP-TNIP1 FL, FKBP-GFP-TNIP1 N-terminal, or FKBP-GFP-TNIP1 C-terminal were treated with Rapalog for 24 h and subjected to FACS acquisition. Left, representative FACS plot. Right, bar graph representing data as mean \pm SEM obtained from 3 independent replicates. **(E)** HeLa cells stably expressing mito-Keima, FRB-FIS1, and FKBP-GFP-TNIP1 in WT cells, PentaKO (SQSTM1, NBR1, NDP52, TAX1BP1, and TAX1BP1 KO cells), FIP200 KO, WIPI2KO, or A20 KO cells were treated with Rapalog for 24 h and subjected to FACS analysis. Bar graph representing data as mean \pm SEM obtained from 3 independent replicates. **(F)** HeLa cells stably expressing mito-Keima, FRB-FIS1, and FKBP-GFP-ATG16L1, FKBP-GFP-WIPI2, or FKBP-GFP-A20 in WT cells or TNIP1 KO cells were treated with Rapalog for 24 h and subjected to FACS analysis. Bar graph representing data as mean \pm SEM obtained from 3 independent replicates

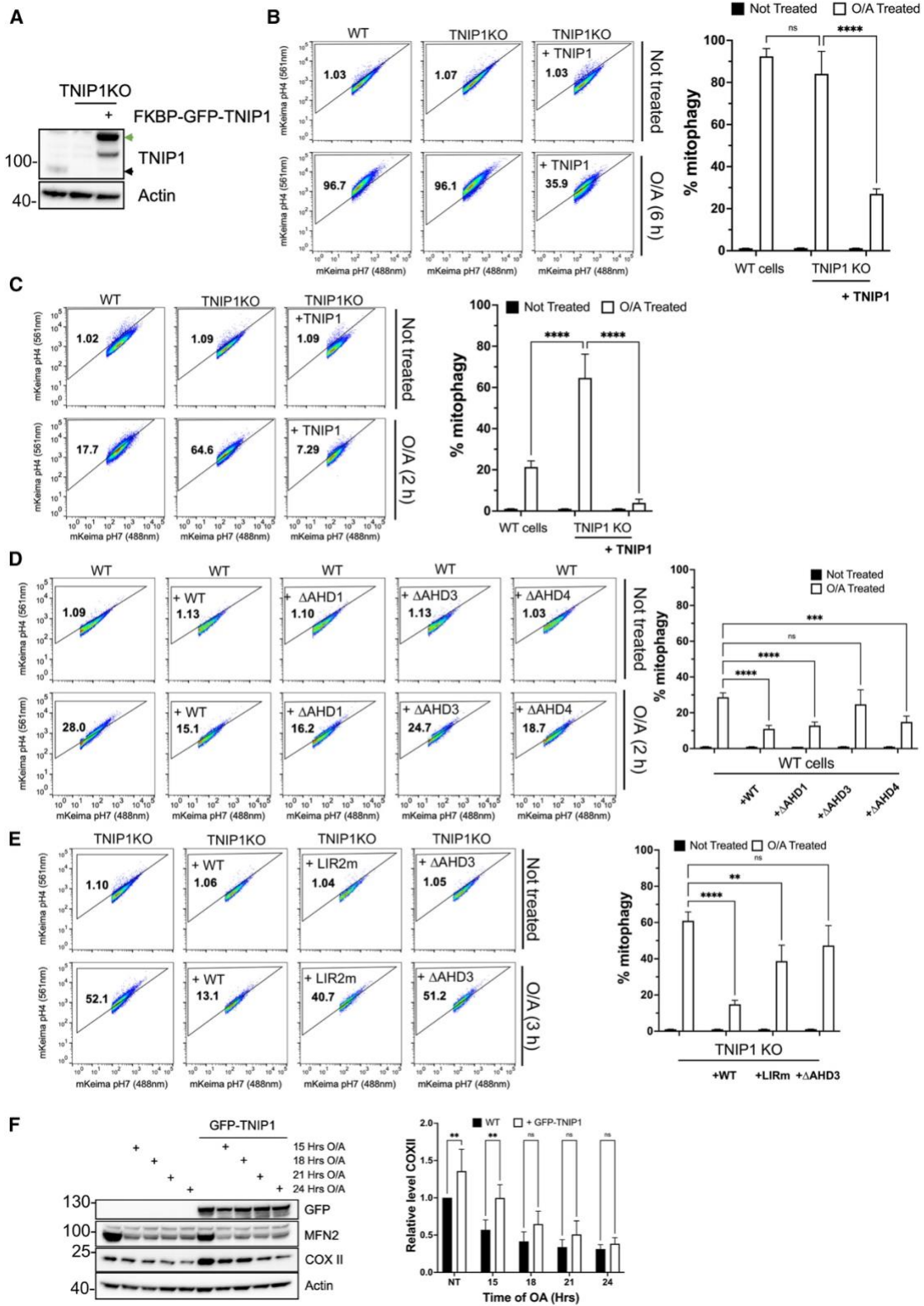


Figure 3.3: TNIP1 is a negative regulator of selective autophagy (A) IB of HeLa cells, HeLa TNIP1 KO cells, and HeLa TNIP1 KO rescued with FKBP-GFP-TNIP1. Green arrow, FKBP-GFP-TNIP1 construct. Black arrow, endogenous TNIP1. (B) HeLa cells stably expressing mito-mKeima and HA-Parkin in WT cells, TNIP1 KO cells, or TNIP1 KO cells rescued with FKBP-GFP-TNIP1 construct were treated with Oligomycin and Antimycin (O/A) for 6 h and subjected to FACS analysis. Left, representative FACS plot. Right, bar graph representing data as mean \pm SEM obtained from 3 independent replicates. (C) HeLa cells stably expressing mito-mKeima and HA-Parkin in WT cells, TNIP1 KO cells, or TNIP1 KO cells rescued with FKBP-GFP-TNIP1 construct were treated with O/A for 2 h and subjected to FACS analysis. Left, representative FACS plot. Right, bar graph representing data as mean \pm SEM obtained from 3 independent replicates. (D) HeLa cells stably expressing mito-mKeima and HA-Parkin and overexpressing FKBP-GFP-TNIP1 WT, DAHD1, DAHD3, or DAHD4 constructs were treated with O/A for 2 h and subjected to FACS analysis. Left, representative FACS plot. Right, bar graph representing data as mean \pm SEM obtained from 3 independent replicates. (E) HeLa TNIP1 KO cells stably expressing mito-mKeima and HA-Parkin and rescued with FKBP-GFP-TNIP1 WT, LIR2 mutant, or DAHD3 constructs were treated with O/A for 3 h and subjected to FACS analysis. Left, representative FACS plot. Right, bar graph representing data as mean \pm SEM obtained from 3 independent replicates. (F) IB of HeLa cells stably expressing BFP-Parkin and GFP-TNIP1 WT treated for 15 h, 18 h, 21 h, or 24 h with O/A. Right, bar graph representing data as mean \pm SEM obtained from 3 independent replicates.

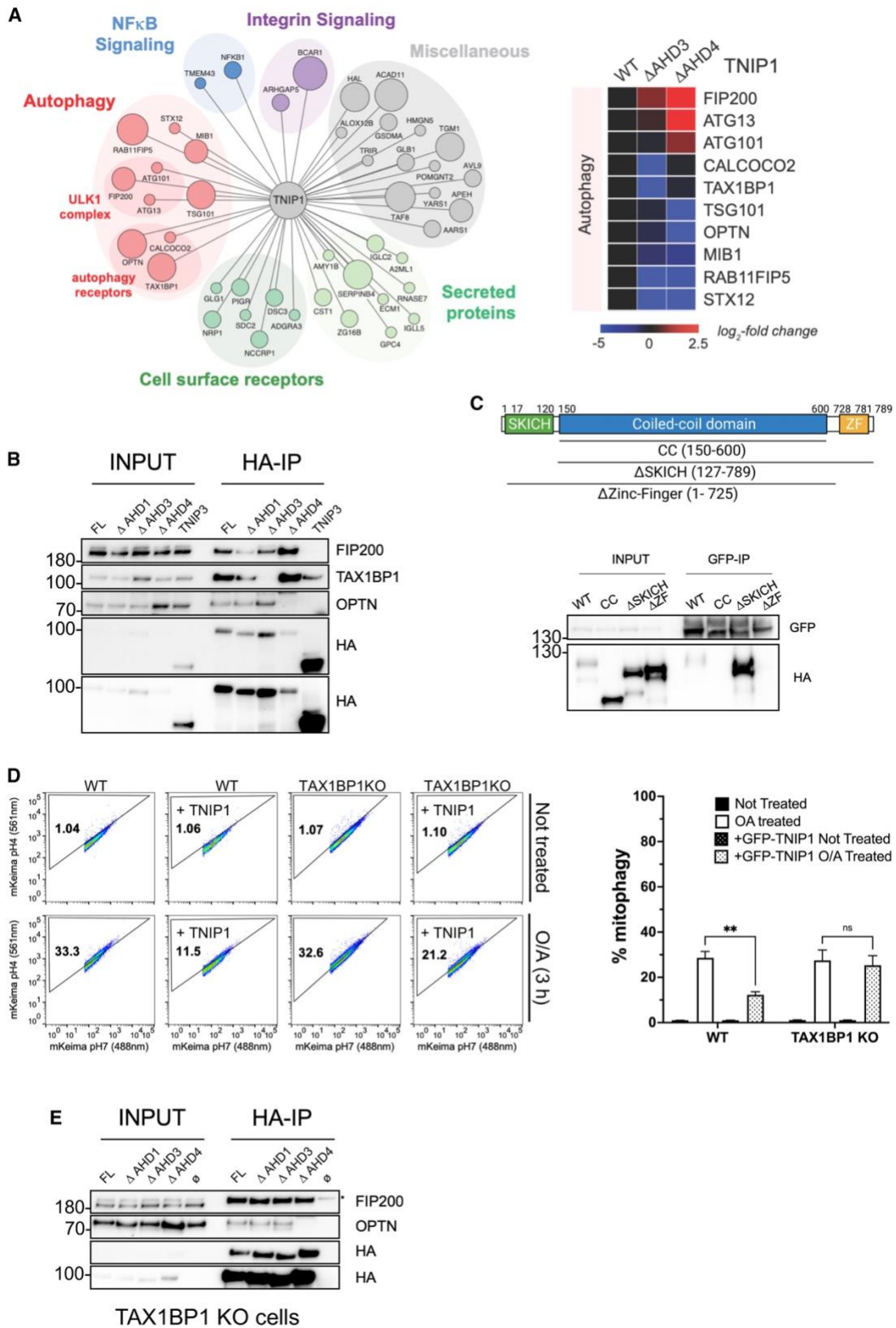


Figure 3.4: The interaction between the AHD3 domain of TNIP1 and the Zinc-Finger domain of TAX1BP1 is necessary for TNIP1's mitophagy inhibition (A) Left, high confidence candidate interaction proteins (HCIPs) network of HA-TNIP1 following an HA pull-down and MS analysis. The size of the bait represents higher Z score interaction. Right, heatmap of the interactors with WT TNIP1 or DAHD3 and DAHD4 mutants. (B) CoIP and IB of HEK293T cells stably expressing HA-TNIP1 FL, DAHD1, DAHD3, and DAHD4 constructs or HA-TNIP3 using magnetic HA beads. (C) Top, schematic representation of FL TAX1BP1 and the regions encompassing the CC domain (CC), SKICH truncation (DSKICH), and Zinc-Finger truncation (DZinc-Finger) constructs. Bottom, CoIP and IB of HEK293T cells stably expressing GFP-TNIP1 FL and transiently expressing HA-TAX1BP1 FL, CC, DSKICH, and DZinc-Finger constructs using magnetic GFP beads. (D) HeLa WT cells or TAX1BP1 KO stably expressing mito-mKeima and HA-Parkin and overexpressing FKBP-GFP-TNIP1 construct were treated with O/A for 3 h and subjected to FACS analysis. Left, representative FACS plot. Right, bar graph representing data as mean \pm SEM obtained from 3 independent replicates. (E) CoIP and IB of HeLa TAX1BP1 KO cells stably expressing HA-TNIP1 FL or the DAHD1, DAHD3, or DAHD4 constructs using magnetic HA beads. \emptyset , no overexpressed construct. * marks unspecific band.

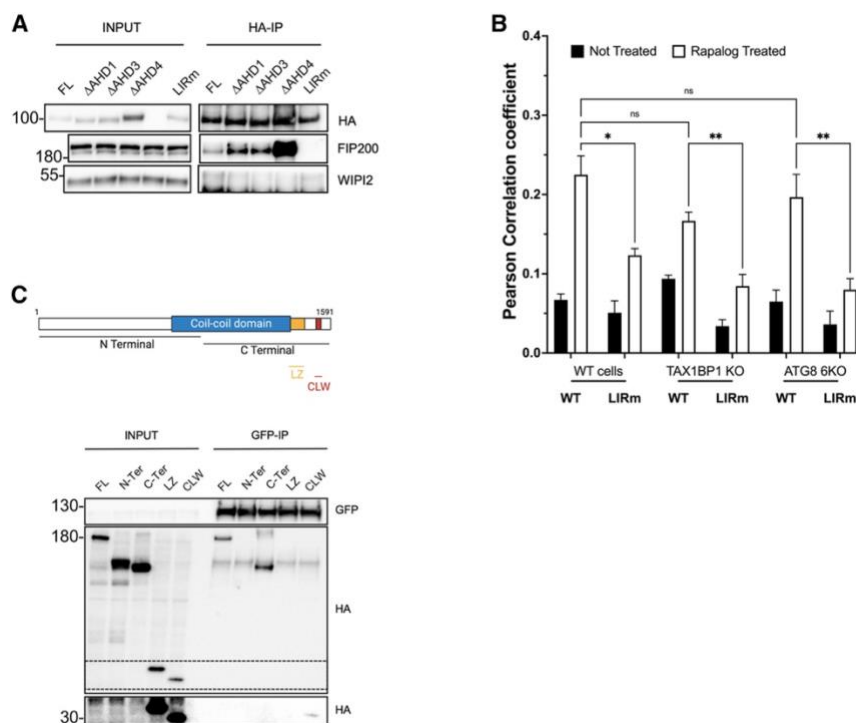


Figure 3.5: TNIP1 binds FIP200 via its LIR motif and to the CLAW domain of FIP200

(A) CoIP and IB of HEK293T cells stably expressing HA-TNIP1 FL or the DAHD1, DAHD3, DAHD4, and LIR2 mutant constructs using magnetic HA beads. (B) HeLa WT, TAX1BP1 KO, and LC3/GABARAP 6KO cells stably expressing FRB-FIS1 and FKBP-GFP-TNIP1 WT or LIR2m were treated for 24 h with Rapalog and stained for endogenous FIP200 before immunofluorescence acquisition on a confocal microscope. Quantifications as mean \pm SEM of Pearson correlation coefficient representing colocalization between FIP200 and GFP. See Figure S5B for representative images. (C) Top, schematic representation of FL FIP200 and the regions encompassing the N-terminal and C-terminal domains as well as the minimal leucine zipper (LZ) and Claw (CLW) domains. Bottom, CoIP and IB of HEK293T cells stably expressing GFP-TNIP1 FL and transiently expressing HAFIP200 FL, N-terminal, C-terminal, LZ, and CLW constructs using magnetic GFP beads. The zone in dotted lines was exposed longer to reveal the binding to the CLAW domain (lower part)

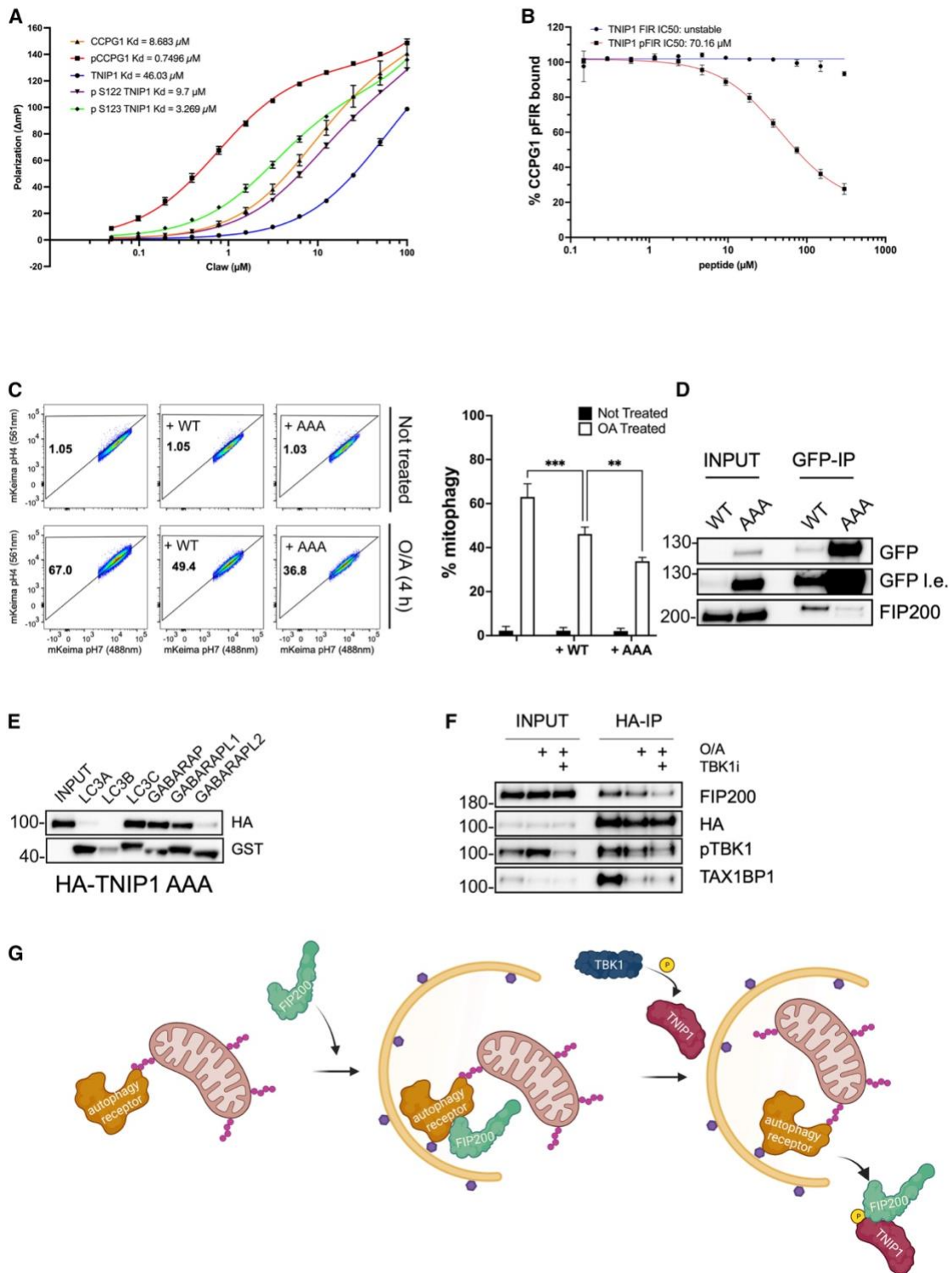


Figure 3.6: TNIP1 binds FIP200 via its FIR motif and is regulated by a phosphorylation upstream of FIR (A) FP of unmodified and phosphorylated FIR peptides of TNIP1 and

CCPG1 binding to the CLAW domain of FIP200 with increasing concentrations of CLAW. Error bars represent the standard deviation measured across 3–6 independent experiments for each condition. **(B)** Competition of the TNIP1 peptides for the displacement of CCPG1 peptides from binding with the CLAW domain of FIP200. Error bars represent the standard deviation measured across four independent experiments for each condition. **(C)** HeLa cells stably expressing mito-mKeima and HA-Parkin and overexpressing GFP-TNIP1 WT or AAA constructs were treated with O/A for 4 h and subjected to FACS analysis. Left, representative FACS plot. Right, bar graph representing data as mean \pm SEM obtained from 3 independent replicates. **(D)** CoIP and IB of HeLa cells stably expressing GFP-TNIP1 WT or AAA constructs using magnetic GFP beads. **(E)** CoIP and IB of HeLa cells stably expressing HA-TNIP1 AAA mutant with purified recombinant GST-tagged mATG8 proteins. **(F)** CoIP and IB of HEK293T cells stably expressing HA-TNIP1 treated for 6 h with the TBK1 inhibitor GSK8612 and/or O/A for 4 h using magnetic HA beads. **(G)** Schematic representation of the proposed model of the molecular function of TNIP1. Upon mitophagy stimulation, autophagy receptors are bound to the ubiquitinated mitochondria and subsequently recruit the ULK1 complex via FIP200 binding, starting the autophagosome formation. Before autophagosomal closure, TNIP1 is targeted to the autophagosome via LC3/GABARAP binding and later activated by TBK1, increasing its binding affinity for FIP200 and competing with the receptors for FIP200 binding, ultimately resulting in release of FIP200 from the autophagosome. Mitophagy can thus proceed, and FIP200 can be recycled at another location on the growing phagophore. In a parallel, separate event, an excess of TNIP1 inhibits mitophagy by binding TAX1BP1 via AHD3/ZF domains, and TAX1BP1 cannot bind ubiquitinated substrates as its UB-binding domain is occupied by TNIP1 as represented in the graphical abstract.

A

```

tr|E7FCP9|E7FCP9_DANBE      KLRRVVELVRDNEVLSSATSFASSLCMGTTPVQETTHGKRRKHGHTTERQ-----ES 114
sp|Q9WU08|TNIP1_MOUSE       RLQRKAELVKDSLELSPFTAPSLVSDG---LAELTGKDGKVPATTAATTATAT 114
tr|E2RCG3|E2RCG3_CANLF      RLQRKAELVKDSLELSPFTAPSLVSDG---LAELTGKDGKVPATTAATTATAT 103
sp|Q15025|TNIP1_HUMAN       RLQRKAELVKDNELLPPP--SPSLGSDP---LAELTGKDSNVTASPTAP----- 103
tr|AOA213SHK0|AOA213SHK0_PANTR  RLQRKAELVKDNELLPPP--SPSLGSDP---LAELTGKDSNVTASPTAP----- 103
                                     :*:::*****:  :  *  :
tr|E7FCP9|E7FCP9_DANBE      RDCLT---GNTLQQAETEGSSEFEVVMNEEKAPETQ-----AGVLHLPQENLELASQ 165
sp|Q9WU08|TNIP1_MOUSE       TGNSMEKPEPASKSPNGASDFEVVPTTEEQNSPET--GSHPTNMMDLGFPPEDSNLKLH 173
tr|E2RCG3|E2RCG3_CANLF      -AHPSDKSQPVKPPSSGTSSEFEVVTTEEKQSPVNGRTRNTEMLGFLPHEDSNLLH 162
sp|Q15025|TNIP1_HUMAN       -ACPSDKPAPVQKPPSSGTSSEFEVVTTEEKQSPVNGRTRNTEMLGFLPHEDSNLMLH 160
tr|AOA213SHK0|AOA213SHK0_PANTR  -ACPSDKPAPVQKPPSSGTSSEFEVVTTEEKQSPVNGRTRNTEMLGFLPHEDSNLMLH 160
                                     :  :  :  :  :  :  :  :  :  :  :  :  :  :  :  :  :  :  :  :  :  :  :  :  :

```

B

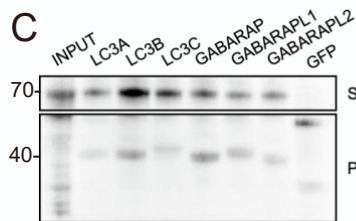
```

LIR1      GGCTCCTTCGACCCCTG
           G S F D P L
LIR1_mut  GGCTCCGCCACCCGCG
           G S A D P A

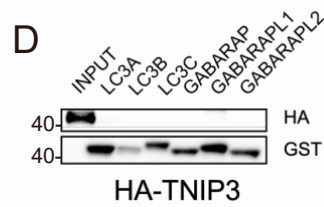
LIR2      TCTGAATTTGAAGTGTC
           S E F E V V
LIR2_mut  TCTGAAGCTGAAGTGCC
           S E A E V A

```

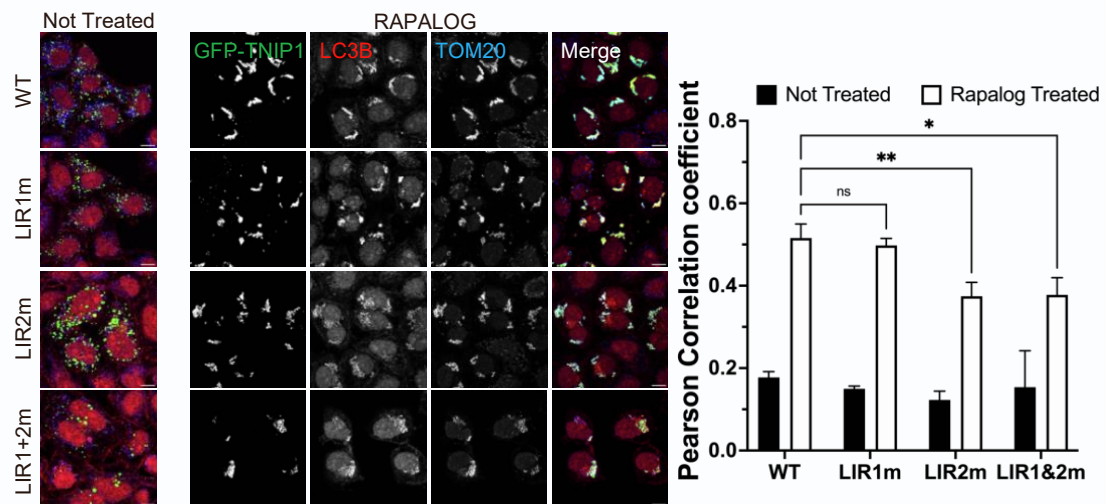
C



D



E



F

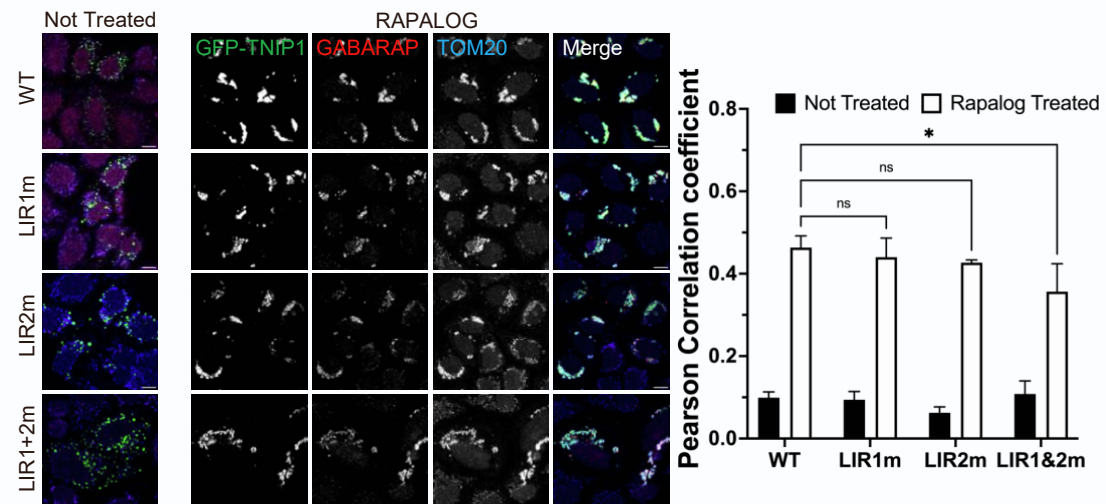


Figure S3.1: Characterization of the LIR motif of TNIP1. Related to Figure 1 (A)

Alignment of TNIP1 protein sequences from Human, Zebrafish (DANRE), Mouse, Dog (CANLF) and Chimpanzee(PANTR). Highlighted in red are the identified putative LIR motifs. **(B)** LIR1 mutant and LIR2 mutant showing the altered nucleotide and amino acid sequences in red. **(C)** Co-IP and IB of HeLa cells stably expressing HA-SQSTM1 with purified recombinant GST tagged mATG8 proteins or GFP. **(D)** Co-IP and IB of HeLa cells stably expressing HA-TNIP3 with purified recombinant GST tagged mATG8 proteins. **(E)** HeLa cells stably expressing FRB-FIS1 and FKBP-GFP-TNIP1 WT, FKBP-GFP-TNIP1 LIR1 mutant, FKBP-GFP-TNIP1 LIR2 mutant or FKBP-GFP-TNIP1 LIR1&LIR2 double mutant were left untreated or treated for 24 h with Rapallog and stained for the mitochondrial protein TOM20 and endogenous LC3B before immunofluorescence acquisition. Representative images. Scale bar: 10 μ m. Right, quantifications as mean \pm SEM of Pearson correlation coefficient representing colocalization between LC3B and GFP. **(F)** HeLa cells stably expressing FRB-FIS1 and FKBP-GFP-TNIP1 WT FKBP-GFP-TNIP1 LIR1 mutant, FKBP-GFP-TNIP1 LIR2 mutant or FKBP-GFP-TNIP1 LIR1&LIR2 double mutant were left untreated or treated for 24 h with Rapallog and stained for the mitochondrial protein TOM20 and endogenous GABARAP before immunofluorescence acquisition on a confocal microscope. Representative images. Scale bar: 10 μ m. Right, quantifications as mean \pm SEM of Pearson correlation coefficient representing colocalization between GABARAP and GFP.

2B. Representative gating FACS plots of HeLa cells stably expressing mito-mKeima, FRB-FIS1 and FKBP-GFP-TNIP1 Full Length or FKBP-GFP-TNIP1 mutants Δ AHD1, Δ AHD3 and Δ AHD4 treated with Rapalog for 24 h and subjected to FACS analysis. DP: double positive. **(B)** HeLa cells stably expressing FRB-FIS1 and FKBP-GFP-TNIP1 FL, FKBP-GFP-TNIP1 mutants Δ AHD1, Δ AHD3 and Δ AHD4 (Cyan) left untreated and stained for the mitochondrial protein TOM20 (magenta) and DAPI (Yellow) before immunofluorescence acquisition on a confocal microscope. Airyscan representative images. Scale bar: 10 μ m. **(C)** Related to 2E. Representative FACS plot. **(D)** Related to 2F. Representative FACS plot.

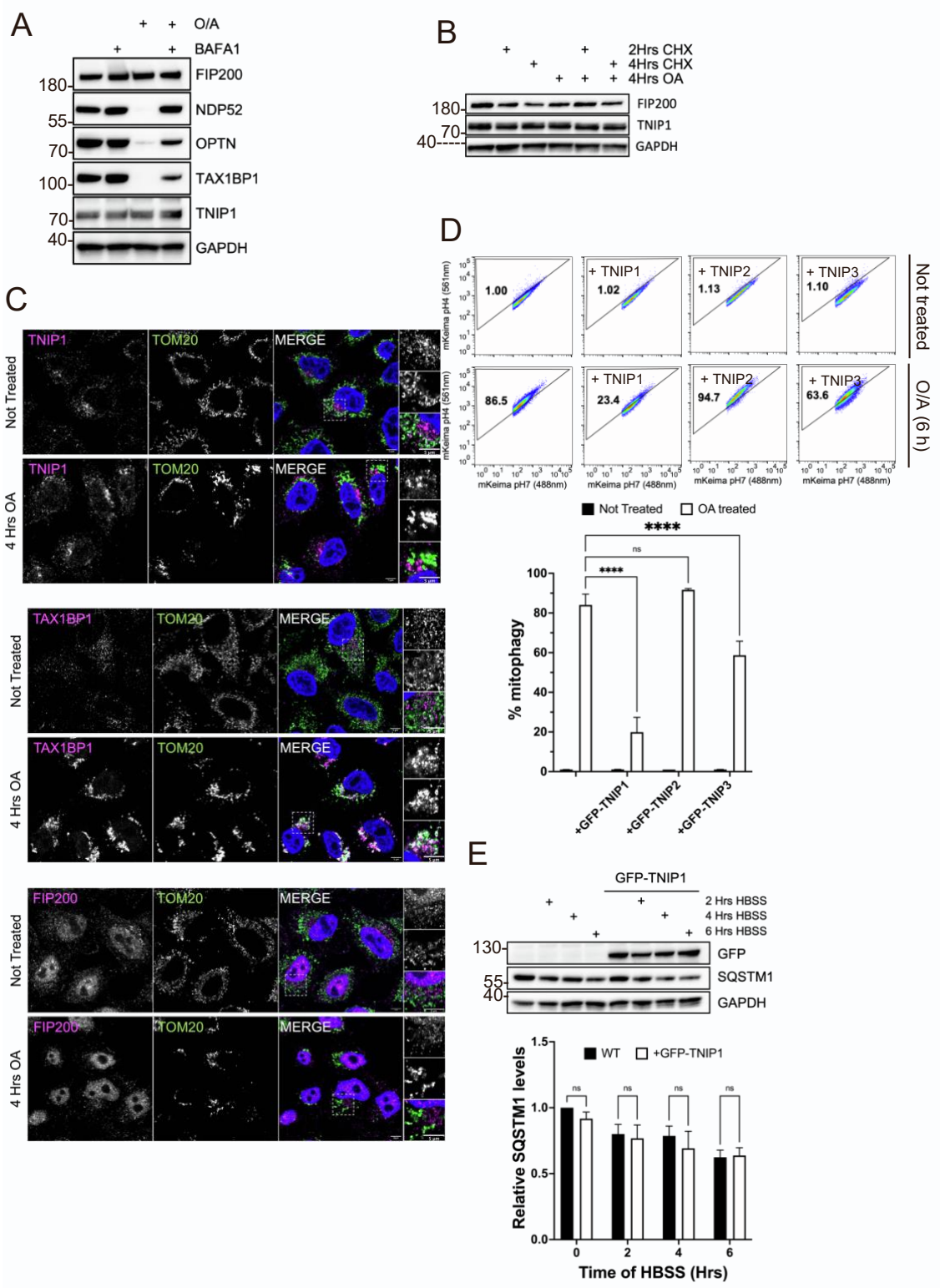


Figure S3.3: TNIP1 is not an autophagy receptor of mitophagy. Related to Figure 3

(A) IB of HeLa cells stably expressing HA-Parkin treated for 4 h with Oligomycin and Antimycin (O/A) and/or Bafilomycin A1 (BAFA1). **(B)** IB of HeLa cells stably expressing HA-Parkin treated for 4 h with O/A and/or 2 h and 4 h of cycloheximide (CHX). **(C)** HeLa cells stably expressing HA-Parkin were treated for 4 h with O/A and stained for the mitochondrial protein TOM20 (Green) and endogenous TNIP1 (Magenta), FIP200 (Magenta) or TAX1BP1 (Magenta) and DAPI (Blue) before immunofluorescence acquisition on a confocal microscope. Airyscan representative images. Scale bar: 5 μ m. **(D)** HeLa cells stably expressing mito-mKeima, HA-Parkin and overexpressing FKBP-GFP-TNIP1, FKBP-GFP-TNIP2 or FKBP-GFP-TNIP3 constructs were treated with O/A for 6 h and subjected to FACS acquisition. Top, representative FACS plot. Bottom, bar graph representing data as mean \pm SEM obtained from 3 independent replicates. **(E)** IB of HeLa cells stably expressing BFP-Parkin and GFP-TNIP1 WT starved for 2 h, 4 h or 6 h by incubation with HBSS. Right, bar graph representing data as mean \pm SEM obtained from 3 independent replicates.

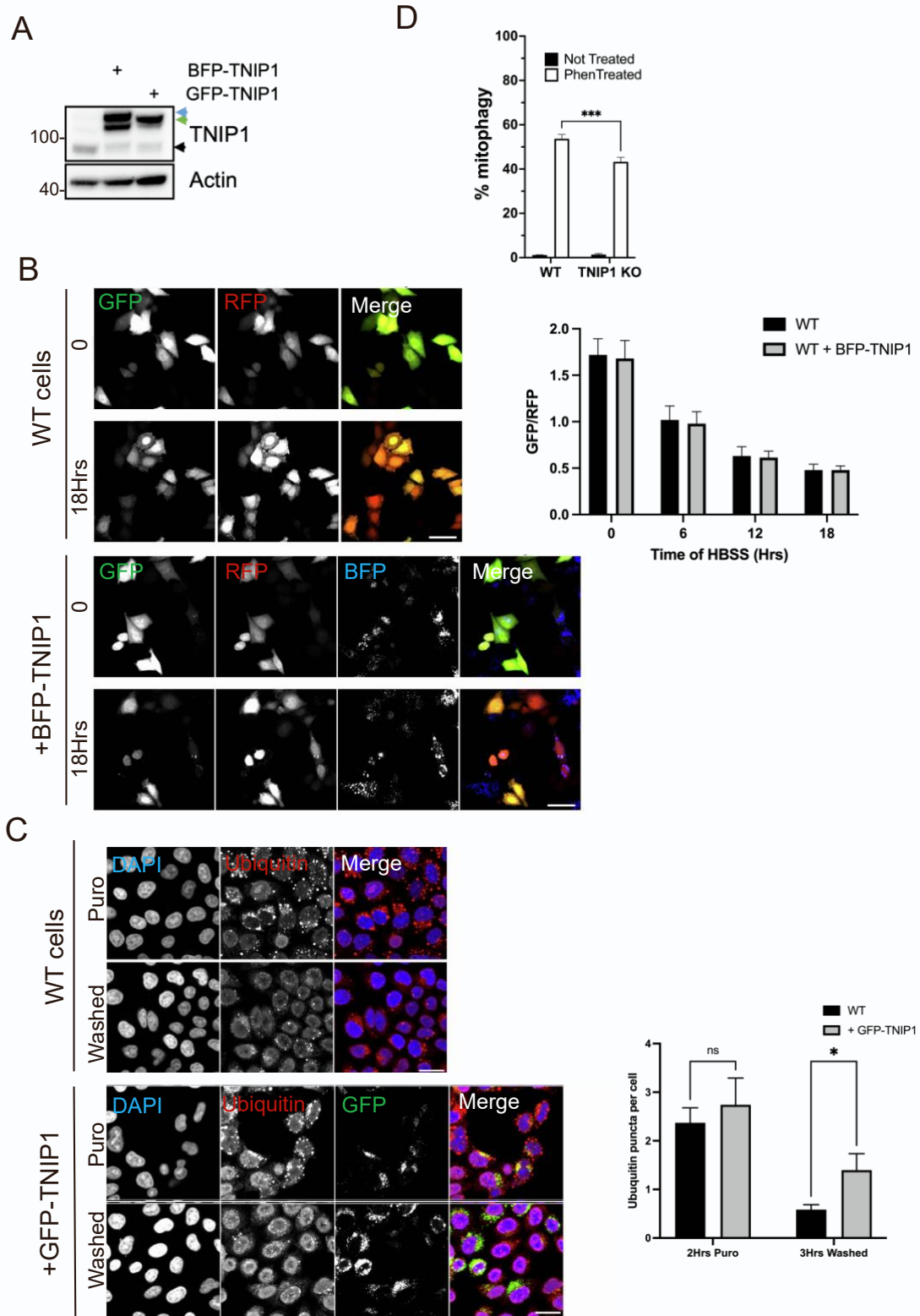


Figure S3.4: TNIP1 is specifically involved in selective autophagy. Related to Figure

3 (A) HeLa cells overexpressing BFP-TNIP1 or GFP-TNIP1 subjected to immunoblot analysis. Blue arrow, BFP-TNIP1 construct. Green arrow, GFP-TNIP1 construct. Black arrow, endogenous TNIP1. **(B)** HeLa cells stably expressing YFP-LC3B_RFP-LC3BΔG and BFP-TNIP1 were starved for 24 h by incubation with HBSS and monitored every hour under a confocal microscope. Left, representative images at the 0 h and 18 h time points. Scale bar: 50μm. Right, bar graph of the GFP/RFP ratio for time points 0, 6, 12 and 18 h are displayed representing data as mean ± SEM obtained from 3 independent replicates. **(C)** HeLa cells stably expressing or not GFP-TNIP1 were treated for 2 h with Puromycin and subsequently washed for 3 h or treated with Puromycin without washing and stained for Ubiquitin before immunofluorescence acquisition on a confocal microscope. Left, representative images of unwashed and washed cells. Scale bar: 50μm. Right, bar graph representing data as mean ± SEM obtained from 3 independent replicates. **(D)** HeLa WT cells and TNIP1 KO cells stably expressing mito-mKeima, were treated with Phenanthroline for 16 h and subjected to FACS analysis. Bar graph representing data as mean ± SEM obtained from 3 independent replicates.

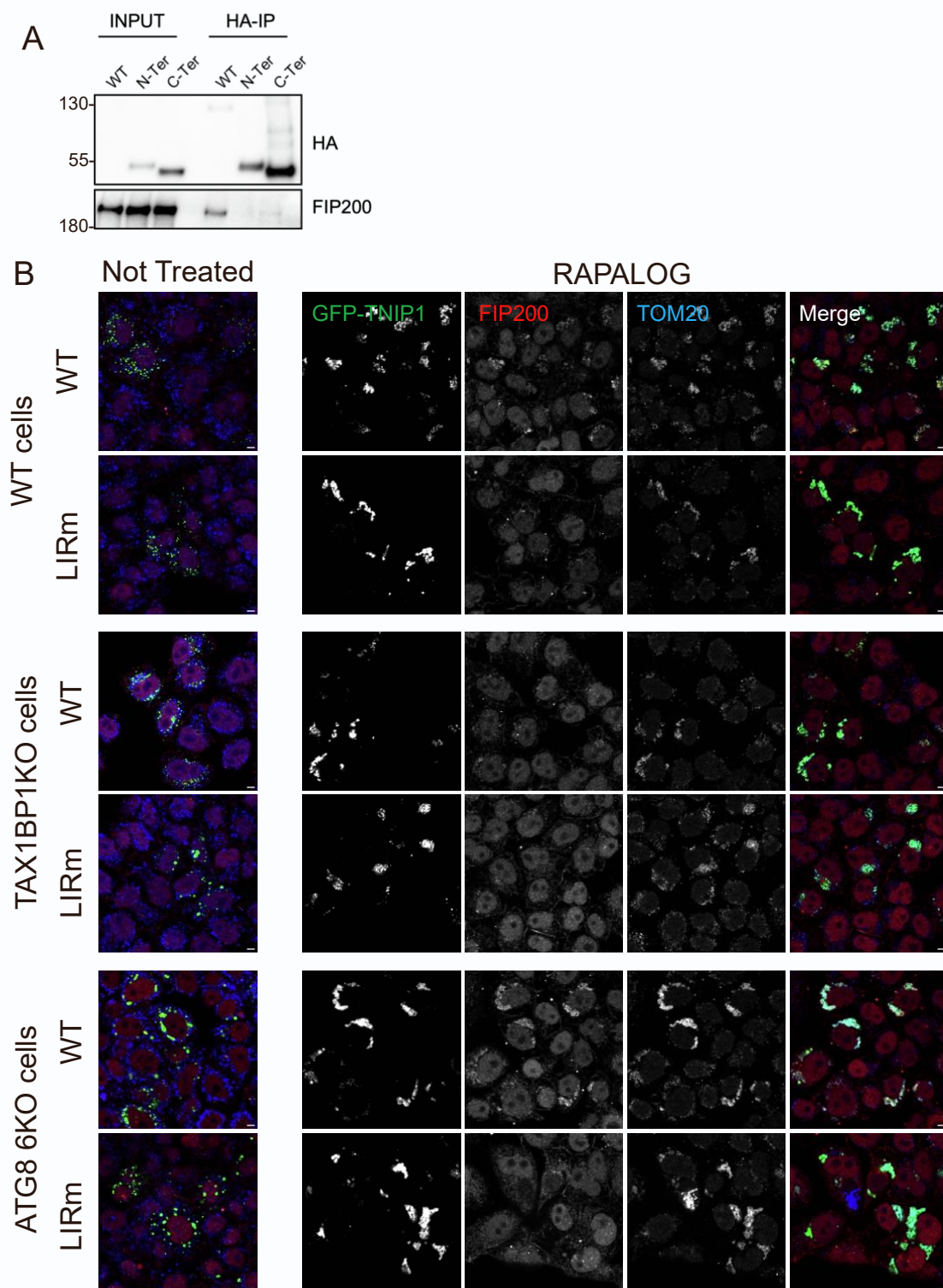


Figure S3.5: TNIP1 recruitment of FIP200 is independent of TAX1BP1 and mATG8 proteins. Related to Figure 5 (A) Co-IP and IB of HEK293T cells stably expressing HA-TNIP1 full length or the N-terminal and C-terminal constructs using magnetic HA beads. **(B)** Related to Fig 5B. HeLa wild type, TAX1BP1 KO and LC3/GABARAP 6KO cells stably expressing FRB-FIS1 and FKBP-GFP-TNIP1 WT or LIR2m were treated for 24 h with Rapalog and stained for the mitochondrial protein TOM20 and endogenous FIP200 before immunofluorescence acquisition on a confocal microscope. Representative images. Scale bar: 10 μ m.

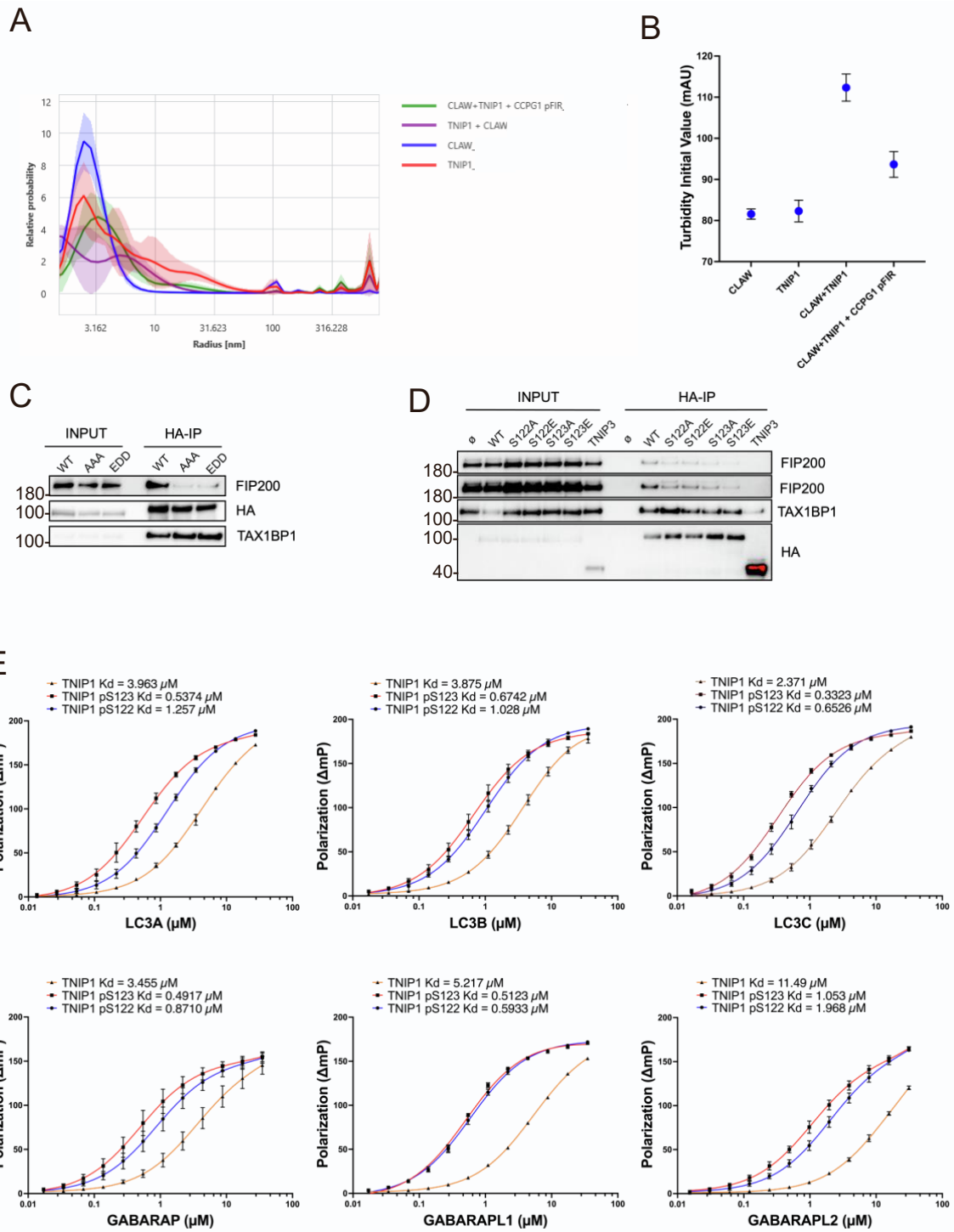


Figure S3.6: TNIP1 forms a complex with FIP200. Related to Figure 6 (A) Dynamic Light Scattering assay using purified recombinant full length TNIP1 in complex with CLAW domain of FIP200 and phosphorylated CCPG1 FIR peptides. The average relative probability distribution fit is shown as a solid line with the shaded region above and below representing the standard deviation in fits across four independent experiments. (B) Turbidity assay using purified recombinant full length TNIP1 in complex with CLAW domain of FIP200 and phosphorylated CCPG1 FIR peptides. Error bars represent the standard deviation from the mean for three independent experiments. (C) Co-IP and IB of HEK293T cells stably expressing HA-TNIP1 WT, AAA or EDD mutants using magnetic HA beads. (D) Co-IP and IB of HEK293T cells stably expressing HA-TNIP1 WT, S122A, S122E, S123A, S123E mutants or HATNIP3 using magnetic HA beads. Ø: no overexpressed construct. (E) Fluorescence polarization of unmodified and phosphorylated FIR peptides of TNIP1 and binding to the purified LC3A (top left), LC3B (top middle), LC3C (top right), GABARAP (bottom left), GABARAPL1 (bottom middle) or GABARAPL2 (bottom right) with increasing concentrations of recombinant proteins. Error bars represent the standard deviation measured across 3 independent experiments for each condition.

*Chapter 4***CONFORMATIONAL PLASTICITY OF MITOCHONDRIAL VDAC2
CONTROLS THE KINETICS OF ITS INTERACTION WITH CYTOSOLIC
PROTEINS**

The following chapter is adapted from Rosencrans et al., 2025 and modified according to the Caltech thesis format

William M. Rosencrans, Harisankar Khuntia, Motahareh Ghahari Larimi, Radhakrishnan Mahalakshmi, Tsyrr-Yan Dharma Yu, Sergey M. Bezrukov, Tatiana K. Rostovtseva
Conformational plasticity of mitochondrial VDAC2 controls the kinetics of its interaction with cytosolic proteins. *Sci. Adv.* 11, eadv4410(2025). DOI:10.1126/sciadv.adv4410

4.1 Abstract

The Voltage Dependent Anion Channel (VDAC) is a key conduit of the mitochondrial outer membrane for water-soluble metabolites and ions. Among the three mammalian isoforms, VDAC2 is unique due to its embryonic lethality upon knockout. Using single-molecule electrophysiology, we investigate the biophysical properties that distinguish VDAC2 from VDAC1 and VDAC3. Unlike the latter, VDAC2 exhibits dynamic switching between multiple high-conductance, anion-selective substates. Using α -synuclein (α Syn)—a known VDAC1 cytosolic regulator—we found that higher-conductance substates correlate with increased on-rates of α Syn-VDAC2 interaction but shorter blockage times, maintaining a consistent equilibrium constant across all substates. This suggests α Syn detects VDAC2's dynamic structural variations before final binding. We explored the dependence of VDAC2's unique N-terminal extension and cysteines on substate behavior, finding that both structural elements modulate substate occurrence. The discovered conformational flexibility enables VDAC2 recognition by diverse binding partners, explaining its critical physiological role via dynamical adaptation to mitochondrial metabolic conditions..

4.2 Introduction

The Voltage Dependent Anion Channel (VDAC) is the most abundant protein in the mitochondrial outer membrane (MOM) which represents a class of β -barrel channels originally derived from the endosymbiotic bacterial ancestors of modern mitochondria. It is the major pathway for water-soluble metabolites and small ions to cross the MOM. In mammals, there are three VDAC isoforms: VDAC1, VDAC2, and VDAC3. Despite ~70% sequence similarity between the isoforms and the ability of them all to form large conductive anionic channels (~4 nS in 1M KCl at room temperature), which gate in response to the applied voltage when reconstituted into a planar lipid membrane (PLM), each VDAC isoform has a distinct physiologic role. VDAC1 and VDAC2 are the most abundant isoforms, with VDAC3 expressed in low levels (~ 10 % of the total VDACs) in most tissues, except in the testis (Messina et al., 2012; Rahmani et al., 1998). VDAC2 is the most expressed isoform in brain tissue, as well as in placental endothelium (Piehowski et al., 2020). Studies in mice demonstrate that VDAC1 or VDAC3 knockouts are not lethal but result in metabolic impairment in the case of VDAC1 (Anflous-Pharayra et al., 2011) and male infertility in the case of VDAC3 knockouts (Sampson et al., 2001). VDAC2 knockout results in embryonic lethality or severely diseased neonatal pups (Cheng et al., 2003; Chin et al., 2018). VDAC2 alone has been shown to regulate the BAK/BAX-dependent apoptosis pathways, rationalizing the results of the murine studies (Cheng et al., 2003; Chin et al., 2018; Naghdi et al., 2015). In this paradigm, apart from its channel activity, VDAC2 acts as a membrane anchor for BAK/BAX within the MOM. In the case of BAK, binding to VDAC2 impairs its oligomerization in the MOM and subsequent apoptosis via cytochrome c release (Cheng et al., 2003; Lazarou et al., 2010). Studies on the biophysical basis of VDAC2's unique physiology have been complicated by the fact that, while multiple high-resolution structures of VDAC1 exist, human VDAC2 has eluded structural determination. VDAC2 differs from VDAC1 most obviously in an 11-residue N-terminal extension (NTE) and the presence of nine cysteines compared to two in VDAC1 (De Pinto, 2021). Mutagenesis studies by Naghdi et al. (Naghdi et al., 2015) showed that neither the NTE nor the extra cysteines were essential for the VDAC2-BAK interaction, instead finding that a cytosol-facing loop connecting two beta strands was the site of the interaction. Biophysical studies on VDAC2 have demonstrated that the NTE was important for maintaining the stability of the channel,

compensating for the increased number of cysteines (Maurya & Mahalakshmi, 2015).

VDAC2 channel properties are superficially identical to VDAC1 (Maurya & Mahalakshmi, 2013, 2015; Menzel et al., 2009; Xu et al., 1999), however studies on VDAC2 electrophysiology have identified subtle, yet unexplored, differences. The first study, systemically comparing the channel properties of each VDAC isoform (Xu et al., 1999), found that VDAC2 conductance deviated from a unimodal Gaussian distribution characteristic for VDAC1 or VDAC3. The authors speculated that VDAC2 existed in at least two states with different anionic selectivities, a finding recapitulated in more recent studies (Menzel et al., 2009). VDAC2 has been shown to be slightly more permeable to Ca^{2+} than VDAC1 (Rosencrans, Aguilera, et al., 2021). The structural features and physiologic role of these states remain unidentified.

VDACs are known to be regulated by cytosolic proteins, including α -Synuclein (α Syn), an intrinsically disordered neuronal protein intimately associated with Parkinson's disease (PD) (Goedert et al., 2017; Kim et al., 2014). The large aggregates and fibrils of α Syn found in Lewy bodies in the brains of PD patients are a hallmark of PD (Spillantini et al., 1997). α Syn aggregation and oligomerization are associated with its increased expression in dopaminergic neurons in PD and are generally considered to be pathological phenomena (Parres-Gold et al., 2020; Spillantini et al., 1997). However, the exact mechanism of α Syn-induced pathology remains mainly unknown. Especially the role of monomeric α Syn continues to be poorly understood. α Syn was found to be associated with both mitochondrial membranes, causing impairment of the mitochondrial respiratory complexes (Devi et al., 2008; Elkon et al., 2002) (Ludtmann et al., 2018), oxidative stress (Hsu et al., 2000), and fission (Chinta et al., 2010) (Nakamura et al., 2011). At the MOM, monomeric α Syn interacts with VDAC (reviewed in (Magri & Messina, 2017)) and translocates through VDAC1 into the mitochondrial intermembrane space, as was shown in neuroblastoma and HeLa cells (Rajendran et al., 2022; Rovini et al., 2020).

In vitro, monomeric α Syn at nanomolar concentrations induces voltage-dependent reversible blockages of reconstituted VDAC channel conductance, seen as rapid current fluctuations on the scale of 1-100 ms between the VDAC open and α Syn-blocked state with the residual

conductance of ~ 0.4 of the open state (Rostovtseva et al., 2015). aSyn is a 140-residue polypeptide that consists of three well-defined domains: an N-terminus amphipathic membrane binding domain, a central non-polar NAC domain, and a disordered highly negatively charged C-terminal domain (Ulmer & Bax, 2005). aSyn is essentially disordered in solutions, but upon binding to the anionic lipid membranes, its N-terminal domain adopts different α -helical conformations while leaving the C-terminus disordered above the membrane surface (Eliezer et al., 2001; Fusco et al., 2014; Ulmer & Bax, 2005). Based on these structural data and the results of extensive kinetic analysis of VDAC interaction with aSyn at the single-channel level, the current model is that the N-terminal domain of aSyn remains membrane-bound, and the anionic C-terminal domain is driven by the applied negative potential into the VDAC pore (Hoogerheide et al., 2021). At lower applied voltages, it retracts back to the same membrane surface after residing in the pore for some time which depends on the voltage magnitude (Hoogerheide et al., 2021). The increasing negative voltage keeps the anionic C-terminus inside the pore longer, which is seen as an exponential voltage dependence of the blockage time. The blocked state displays the reversal of selectivity, going to cationic versus anionic selectivity of the open state (Hoogerheide et al., 2018). At higher applied transmembrane voltages ($|V| > 35\text{-}45$ mV depending on experimental conditions), the blockage time starts to decrease with voltage, which is explained by aSyn translocation through the VDAC pore to the opposite side of the membrane (Rostovtseva et al., 2015). The translocation regime of aSyn was confirmed by direct experiments enabling real-time monitoring of a single aSyn molecule translocating through the VDAC pore (Hoogerheide et al., 2018).

In light of the proposed model, we can suggest a few immediate physiological implications of VDAC-aSyn interaction, driving regulation of ATP/ADP and Ca^{2+} fluxes across MOM. When the highly negatively charged C-terminal tail of aSyn is captured by the VDAC pore, it creates an electrostatic barrier for ATP/ADP (Gurnev et al., 2011) and, by inverting pore selectivity, promotes Ca^{2+} transport (Gurnev et al., 2014; Rosencrans, Aguilera, et al., 2021). The increased mitochondrial Ca^{2+} uptake in HeLa cells in response to aSyn overexpression (Cali et al., 2012) provides *in vivo* support to these predictions. Another anticipated implication of the proposed mechanism is the ability of aSyn to translocate through VDAC.

Translocation of aSyn into mitochondrial intermembrane space was recently confirmed in neuroblastoma and HeLa cells (Rajendran et al., 2022; Rovini et al., 2020). By entering mitochondria, aSyn could target electron transport chain (ETC) complexes in the inner membrane, thus inducing mitochondrial dysfunction and eventually leading to cell death (Ludtmann et al., 2018).

The structures of VDAC2 and VDAC3 are not available yet, but *in silico* reconstructions, based on a high sequence similarity between all three isoforms, predict their structures to be almost identical to VDAC1, which consists of 19 β -strands and an α -helical N-terminus lying in the middle of the pore (Maurya & Mahalakshmi, 2017). The position of NTE in VDAC2 remains unknown. Considering similar β -barrels formed by all three VDAC isoforms and the proposed model of aSyn-VDAC interaction, one would expect a similar interaction of aSyn with all isoforms. However, it was found that the rate of aSyn capture by VDAC1 (the on-rate) is 100 times higher than that by VDAC3 (Queralt-Martin et al., 2020) thus demonstrating, on a single-channel level, a clear quantitative difference between these two isoforms. Furthermore, the voltage required for aSyn to translocate through VDAC3 appeared to be 12 mV smaller than that for VDAC1 (Queralt-Martin et al., 2020). These data enabled us to speculate that the difference in interaction with known, such as aSyn and dimeric tubulin, and still unidentified VDAC regulators could constitute a general mechanism that distinguishes isoforms *in vivo* (Rosencrans, Rajendran, et al., 2021). Therefore, we reasoned that VDAC2 may differ from the other two isoforms by its interaction with cytosolic regulator proteins, thus providing a biophysical basis for its unique physiological role.

In this study, we examine VDAC2's properties at the single-channel level. We utilize recombinant human VDAC2 WT and its three mutants to understand the biophysical basis that distinguishes VDAC2 from the other two isoforms. We found that contrary to VDAC1 and VDAC3, which are characterized by a unique high conductive or "open" state, VDAC2 is a dynamic channel that spontaneously switches between multiple high-conducting open substates that vary by conductance and occurrence while remaining anion selective – a defining feature of the ATP-permeable open states of VDAC. Importantly, we show that

monomeric aSyn induces similar characteristic blockage events in all VDAC2 open substates but with up to ten-fold different on-rates and blockage times. The higher on-rate of the aSyn-VDAC2 interaction always corresponds to the substate with the higher conductance when measured for the same single channel. However, the equilibrium constant of the aSyn-VDAC interaction, which accounts for both the on-rates and the blockage times, remains the same for all substates, independent of their conductance. The finding that the pronounced difference is limited to the kinetic parameters only suggests that once the aSyn molecule is captured, its physical state and free energy in the pore are the same for all substates.

We propose that the appearance of distinct substates within the same channel and their different interaction kinetics with aSyn reveal the dynamic plasticity of VDAC2, which suggests a key for explanation of the exceptional role of this multifaceted channel in the cell. Indeed, the discovered conformational flexibility may allow VDAC2 to recognize a larger number of binding partners. This data could tentatively explain the physiological significance of VDAC2: its ability to dynamically adapt to metabolic cell conditions and change the rates of interaction with its multiple cytosolic protein partners.

4.3 Results

VDAC2 dynamically switches between multiple high-conductive open substates

When reconstituted into PLMs formed from a mixture of DOPG:DOPC:DOPE (2:1:1; wt/wt) (2PG/PC/PE) in a symmetrical 1M KCl solution, human recombinant VDAC2 WT forms channels of 3.0 – 4.0 nS conductance which gate, i.e., transition from the high conductance open state to the variety of low conductance “closed” states in response to the applied voltage (Figure 4.1A, B). This constitutes typical VDAC1 behavior (Eddy et al., 2012; Queralt-Martin et al., 2019). We examined VDAC2 gating in single-channel (Fig. 4.1A and Supplemental Fig. S4.1A) and in multichannel membranes (Fig. 4.1B) to find that the application of 50-60 mV was required to observe typical voltage gating (Fig. 4.1A and Supplemental Fig. S4.1A) (Queralt-Martin et al., 2019). The normalized conductance (G/G_{max}) plots for VDAC2 display the characteristic bell-shaped voltage dependence for all

VDACs with enhanced gating, i.e., lower G_{min} , in response to negative applied voltages (Fig. 4.1C).

The striking difference that we found between VDAC2 and VDAC1 was the appearance of multiple high-conducting open states. They were evident at any applied voltages starting at 10 mV (Supplemental Fig. S4.1B, C), in approximately 50% of single VDAC2 channels during an observation time of at least 20 min. The example of such spontaneous transitions between two high-conductance states can be seen in inset I in Fig. 1A of the single-channel record of the current through VDAC2. Conductance fluctuates between the long-lasting state O1 of 3.0 nS (indicated by blue dashed lines in Fig. 4.1, I) and the short-lived state of 3.5 nS (indicated by the orange dashed line). On different single channels (in different PLMs) such substates were observed either for relatively short times, less than 10% of the time spent in the initial state, as shown in the representative trace in Fig. 1A, or for substantially longer times. The existence of multiple substates in VDAC2 results in a relatively wide distribution of open states' conductances, spanning the range from 3.0 to 4.0 nS (Fig. 4.1D). Other channels showed a single stable open state throughout the observation time (Figure S4.1A). To determine if substate conductance distribution depends on the initial state in which the channel inserted in, the Empirical Cumulative Distribution Function (ECDF) plots for the initially observed conductance states (main state, blue) and for the substates (substates, orange) were generated (Fig. 4.1E). It shows that substate conductance distribution does not depend on the original state in which the channel inserts (main state in Fig. 4.1E). This suggests that a given VDAC2 channel can initially insert into PLM at any state and then subsequently spontaneously switch to a state of a different conductance.

VDAC2 high-conductance substates are anion-selective

VDAC1 is known to have multiple voltage-induced “closed” conducting states which are characterized by a wide range of conductances and low-anionic or cationic selectivity (Colombini, 1989). This is in contrast with the unique anion-selective open state of VDAC1. To determine whether the observed high-conductance substates of VDAC2 can be reliably attributed to open states and are not voltage-gated states, we examined their selectivity. For this purpose, single channels were reconstituted in a 5x salt gradient (1M

KCl *cis* and 0.2 M KCl), where they displayed the same substate behavior as observed in symmetrical salt conditions. A representative trace of VDAC2 obtained in the salt gradient (Fig. 4.2A) shows two conducting states: the initial long-lasting O1 (indicated by blue dashed lines) and the higher conductance short-lasting state O2 (indicated by orange dashed lines) (inset I in Fig. 4.2A). In the salt gradient, substates can be observed at 0 mV of applied voltage, indicating their presence is voltage independent. The corresponding I/V (current vs voltage) plots for two states O1 and O2 are given in Fig. 2B. The linear regressions determine the slope (conductance) and the reversal potential (Ψ_R , the voltage corresponding to zero current) for each substate. Under these salt gradient conditions, positive Ψ_R indicates anionic selectivity, and negative Ψ_R indicates cationic selectivity. Both conducting substates proved to be anion-selective. Moreover, the lower-conductance substate O1 has a higher reversal potential of 7.2 mV and, accordingly, higher anion selectivity than the higher-conductance substate O2 with $\Psi_R = 4.4$ mV (Fig. 4.2B).

The scatter plot of Ψ_R versus conductance for all observed conducting substates obtained in 19 individual VDAC2 WT channels is shown in Figure 2C. Ψ_R is plotted as a function of conductance for the initial or main states (shown as blue circles), which are also typically the most probable states observed for a given channel, and for substates (shown as orange stars). The main states and substates could be clustered in at least two groups: one with the higher conductance (>1.6 nS) and lower reversal potential, and another with the lower conductance (<1.6 nS, highlighted in haze blue) and higher Ψ_R (Fig. 4.2C). It could be seen that substates and main states of the channel occupy the same Ψ_R vs conductance clusters. To empirically determine the validity of such clustering, we performed K-means clustering analysis, with the cluster size determined by the maximum silhouette score. The analysis returned three clusters with the higher conducting states >1.6 nS clustering in two groups and most of the low conducting <1.6 nS states falling into a third cluster (Figure S4.1D).

These results suggest that the observed substates represent a set of VDAC2 open states characterized by anion selectivity. A comparison of VDAC2 selectivity with VDAC1 and VDAC3 confirms this conclusion. In Fig. 2D it can be seen that the high conductance state of VDAC2 (G_{high} , which corresponds to typical ~ 3.8 nS conductance in 1 M KCl

symmetrical solution) is similar in conductance and anion selectivity (with Cl^- to K^+ permeability ratio $P_{\text{Cl}^-}/P_{\text{K}^+} \sim 1.4$) to the open states of VDAC1 and VDAC3, while VDAC2 lower conductance state (G_{low} , corresponding to ~ 3.1 nS in 1 M KCl) is characterized by slightly higher anion selectivity with $P_{\text{Cl}^-}/P_{\text{K}^+} \sim 1.5$.

VDAC2 open substates vary in the kinetics of their interaction with cytosolic regulator aSyn

Previous work demonstrated that while the basic channel properties of VDAC1 and VDAC3 isoforms, such as conductance, ion selectivity, and voltage-gating, are similar, their interaction with VDAC cytosolic protein partners – dimeric tubulin and aSyn – is drastically different, thus reliably distinguishing each isoform (Queralt-Martin et al., 2020). Following these results, we tested the interaction between reconstituted human VDAC2 WT and aSyn at the single-channel level. According to the previously proposed model of aSyn-VDAC complexation (Hoogerheide et al., 2022), the first step of aSyn capture by the VDAC pore is binding of the aSyn N-terminal domain to the membrane surface (Hoogerheide et al., 2021; Jacobs et al., 2019) where aSyn preferentially binds to anionic lipids as have been shown in multiple studies (Eliezer et al., 2001; Fusco et al., 2014; Pfefferkorn et al., 2012; Ulmer & Bax, 2005; Ulmer et al., 2005). Therefore, to maximize aSyn-VDAC interaction, we used PLM formed from 2PG/PC/PE lipid mixture. The 50% content of anionic DOPG in the lipid mixture increases the on-rate of α Syn-VDAC interaction, allowing for the faster acquisition of statistically reliable data (Jacobs et al., 2019). In addition, another advantage of using PLM of this lipid composition is that VDAC stays mostly open at the applied voltages of up to 60 mV (Fig. 1 and (Queralt-Martin et al., 2019)), thus allowing the measurement of aSyn-VDAC interaction at the wide range of applied voltages. Figure 4.3A shows a representative trace of VDAC2 WT in the presence of aSyn. Initially, this channel showed two conductance levels, O1 of 3.0 nS and O2 of 3.6 nS, which were recorded at the applied voltages as low as 10 mV. Ten minutes after insertion, the channel spontaneously converted to a state with stable 3.8 nS conductance referred to as O3 (Fig. 4.3A, Insets I and II). In all three states, the channel is blocked by aSyn, which is manifested by fast current transitions between one of the open states (O1, O2, or O3) and the corresponding blocked states, B1, B2, or B3, of ~ 0.4 conductance of the corresponding open state (Fig. 4.1A and *Insets I and II*). Notably,

aSyn does not block VDAC2 voltage-induced low-conductance closed state (Supplemental Fig. S4.2), as was also reported for VDAC1 (Rostovtseva et al., 2015), due to its cationic selectivity. This is another piece of evidence indicating that VDAC2 high-conductance substates are substantially different from the voltage-induced “closed” states of the same single channel.

The important feature of VDAC2’s interaction with aSyn is that the frequency of blockage events varies dramatically between the high conductance substates, which can be clearly seen in insets I and II in Fig. 3A with a higher time resolution. Notably, at the same applied voltage, the state with a higher conductance, O3, for a channel shown in Fig. 3A, has a higher frequency of blockage events than the state with a lower conductance, O1. To quantify the aSyn-VDAC interaction, the open times, τ_{on} , the time between consequent aSyn blockage events, and blockage times, τ_b , (see cartoon in Fig. 4.3B) are plotted in log-binned histograms for each state at the applied voltage of +30 mV (Fig. 3C). State O1 has the longest intervals between aSyn blockage events, followed by O2 and finally O3, demonstrating that τ_{on} decreases with the state’s conductance increase (Fig. 4.3C, i). The blockage times follow the opposite sequence: state O1 has the longest $\tau_{off} = \langle \tau_b \rangle$ followed by O2 and O3 (Fig. 3C, ii). The comparison of the kinetic parameters of aSyn-VDAC binding for each state obtained in the experiment in Fig. 3A is shown in Fig. 4.3D. The on-rate constant of aSyn capture by the pore, $k_{on} = 1/(\langle \tau_{on} \rangle [C])$, where $[C]$ is α Syn bulk concentration, and the characteristic off-rate, τ_{off} , were calculated by averaging the rates determined via three separate fitting algorithms for the log-probability distribution (Fig. 4.3C) (see Methods). As conductance increases from state O1 to O2 to O3, k_{on} increases from 1.70 to 3.90 to 8.62 s⁻¹ nM⁻¹, respectively, and τ_{off} decreases from 5.79 ms in O1 to 2.59 ms in O2 to 1.63 ms in O3. Importantly, the equilibrium constant, $K_{eq} = k_{on} \tau_{off}$ (light blue bars in Fig. 4.3D), varies negligibly between the substates. To compare the trend in k_{on} values across multiple substates in individual VDAC2 channels, k_{on} values were plotted versus corresponding conductance (Supplemental Fig. S4.3A). In every case (7 independent experiments with different channels and a total of 12 analyzed substates), as substate conductance increased, k_{on} also increased (Supplemental Fig. S4.3C), confirming the results obtained on the same channel (Figure 4.3D). This trend is consistent across multiple observed single-channel measurements despite large variability in absolute

values of the kinetic parameters between individual channels and, correspondingly, a low coefficient of determination $R^2 = 0.33$.

For VDAC1 and VDAC3, the conductance of the aSyn blocked state is ~ 0.4 of the open state conductance (Queralto-Martin et al., 2020; Rostovtseva et al., 2015), giving $\Delta G/G \sim 0.6$. A comparison of the blocked state's relative conductance, $\Delta G/G$, for each state O1, O2, and O3 (as in Fig. 4.3A), is shown in Fig. 3E. State O1 has the highest $\Delta G/G$ with 0.70 of conductance blocked, followed by O2 with 0.61, and O3 with 0.55. A comparison of G/G values across different substates using the same set of individual VDAC2 channels as for k_{on} and τ_{off} analysis confirms the trend found for the same channel (Supplemental Fig. 4.S3D). Statistical analysis of the substates was performed using the nonparametric paired Wilcoxon signed rank test, comparing substates observed on the same channel, allowing comparison between data taken at different voltages (Supplemental Fig. S4.3A-B).

VDAC2 has a lower average k_{on} of aSyn blockage than VDAC1 but a larger variance (Supplemental Fig. S4.4A). At negative applied voltages, the ratio between the highest k_{on} and the lowest one is up to ~ 3 times. At positive applied voltages, there is an even larger variability between channels, namely, up to ~ 10 times difference in k_{on} between different channels, reflecting the intrinsic asymmetry of VDAC channel (Rostovtseva et al., 2006). Nevertheless, the range of k_{on} values for VDAC2 is below those for VDAC1 obtained under the same conditions (Jacobs et al., 2019).

VDAC2 N-terminal extension and extra cysteines affect the occurrence of conductance substates but do not eliminate them

VDAC2 differs most prominently from VDAC1 by the presence of an extra 11-amino acid NTE and seven extra cysteine residues, six of which face intermembrane space in mitochondria (De Pinto, 2021; Maurya & Mahalakshmi, 2017) (Fig. 4.4A). These features have been proposed to contribute to VDAC2's unique function (De Pinto et al., 2016; Maurya & Mahalakshmi, 2015) and have already been shown to alter the chemical-physical properties of the hVDAC2. Maurya et al showed that cysteine-less hVDAC2 protein has higher thermostability and, consequently, a more stable b-barrel than the WT (Maurya &

Mahalakshmi, 2014). They also showed that the 11-residue NTE plays a role in hVDAC2 refolding in micelles and lipids. However, neither cysteines nor NTE significantly affect VDAC2 basic properties such as single-channel conductance or voltage-gating. Based on these data, we decided to determine whether these sequence features are responsible for VDAC2's dynamic substate behavior. We utilized two previously characterized constructs: hVDAC2 with truncated Δ N-terminus 1-11 (Δ N-VDAC2) and a mutant lacking all cysteines (VDAC2- Δ Cys). Both Δ N-VDAC2 and VDAC2- Δ Cys mutants reconstituted into the same 2PG/PC/PE PLM display channels of 3.8-4.0 nS conductance. However, lower conductance states were still observed, prevalently in the Δ N-VDAC2 mutant and less so in the VDAC2- Δ Cys mutant.

To compare substate occurrence between two mutants and VDAC2 WT, the ECDF for two mutants and the WT VDAC2 was calculated (Fig. 4.4B). This allows to directly compare proportions of channels observed with substates. The analysis shows that \sim 93% of Δ N-VDAC2 channels have substates in comparison with \sim 54% of VDAC2 WT and \sim 19% of VDAC2- Δ Cys channels (Fig. 4.4C). Thus, the removal of the first 11-amino acids greatly enhances substate occurrence. In contrast, the removal of cysteines reduces, though less significantly, the occurrence of substates. Neither mutation abolishes the occurrence of substates; therefore, these structural features of VDAC2 are not the source of substate appearance. However, the NTE and cysteines can allosterically regulate the dynamics of this behavior. The Δ N-VDAC2 channel is less thermostable than VDAC2 WT (Maurya & Mahalakshmi, 2015), while the VDAC2- Δ Cys mutant had been shown to have a higher melting temperature (T_m) (Maurya & Mahalakshmi, 2013, 2014), thus suggesting that the presence of NTE and extra cysteines might influence the occurrence of the substates independently of their effect on b-barrel thermostability.

N-terminal extension and cysteines affect the VDAC2 interaction with aSyn

We showed previously that the removal of cysteines from hVDAC3 altered that channel's interaction with aSyn (Queralt-Martin et al., 2020). The on-rate of aSyn interaction with the VDAC3 cysteine-less mutant was \sim 10x higher than for the WT, but only at negative potentials (Queralt-Martin et al., 2020). Therefore, the next logical question was whether

cysteines and NTE could affect VDACC2's interaction with aSyn. Both Δ N-VDACC2 and VDACC2- Δ Cys mutants exhibited characteristic reversible blockages in the presence of aSyn (Fig. 4.5A, C, D). Δ N-VDACC2 displayed long-lasting substates with a visible difference in interaction kinetics with aSyn (Fig. 5A and Inset I). The representative trace of a single Δ N-VDACC2 channel in Fig. 4.5A shows three substates, O1, O2, and O3, at the applied voltages of ± 10 and ± 35 mV. The Δ N-VDACC2 mutant exhibited two predominant long-lasting substates of 3.2 and 4.0 nS in different channels, allowing the measurements of the kinetic interaction with aSyn for both substates at the wide range of applied voltages on different single channels (Fig. 4.5B). As observed for VDACC2 WT (Fig. 4.3D), the higher conductance substate of 4.0 nS has higher k_{on} than the lower conductance substate of 3.2 nS at all voltages of both polarities (Fig. 4.5B, i).

The mean blockage time t_{off} for VDACC2 mutants and the WT is also highly voltage-dependent and has a characteristic biphasic behavior (Fig. 4.5B, ii and Supplemental Fig. S4.4B) as it was shown for VDACC1 and VDACC3 (Queralt-Martin et al., 2020; Rostovtseva et al., 2015). At low applied voltages, t_{off} increases with voltage, which corresponds to the blockage/retraction regime when aSyn molecule is captured by the VDACC pore and then released back to the same side of the membrane (Hoogerheide et al., 2018, 2020; Hoogerheide et al., 2021). At higher applied voltages – usually $|V| > 40$ mV depending on the VDACC type and experimental conditions – t_{off} decreases with voltage, corresponding to the translocation regime. This happens because, under the high applied voltage, the N-terminus of aSyn detaches from the membrane, allowing the whole aSyn molecule to translocate to the opposite side of the membrane (Hoogerheide et al., 2018). The 4 nS substate of Δ N-VDACC2 has a shorter t_{off} than the 3.2 nS substate at all applied voltages (Fig. 4.5B, ii). This results in the unchanged equilibrium constant K_{eq} , calculated for the retraction regime only, which varies insignificantly between two substates across applied voltages (Fig 4.5B, iii), similar to the substates analyzed on the same VDACC2 WT channel (Figure 4.3D). These results indicate that while substate transitions can reliably affect the kinetics of the aSyn-VDACC2 interaction, the final energy change, or affinity between aSyn and the VDACC2 pore remains unaltered.

The VDAC2- Δ Cys mutant also exhibited conductance substates, but less frequently than Δ N-VDAC2 and the WT (Fig. 4.4C). An example of two substates in VDAC2- Δ Cys channel of 3.0 and 3.5 nS is shown in Fig. 5D. The on-rate of aSyn blockages was again higher in the higher-conductance substate than in the lower-conductance one. Notably, the conductance of this predominant state is typical for the open-state conductance of VDAC1.

E84A mutation increases b-barrel thermostability of VDAC2 but does not abolish the substates

One of the differences between mammalian VDAC isoforms is the charged glutamate in position 73 for VDAC1 and position 84 in VDAC2 and a non-charged glutamine in position 73 in VDAC3 (Rister et al., 2022). The E84 residue in VDAC2 corresponds to the notorious E73 of VDAC1 – a charged residue buried in the middle of the hydrophobic membrane and continuously under investigation to determine its physiological relevance (Colombini, 2009; Hiller et al., 2010; Israelson et al., 2007; Queralt-Martin et al., 2019). E73 was implicated in the stability of the VDAC1 b-barrel, whose dimeric channel interactions appear to be largely determined by this residue (Bayrhuber et al., 2008; Villinger et al., 2010). Previous work on VDAC gating has demonstrated that b-barrel dynamics are often the result of subtle allosteric network interactions across the channel (Ngo et al., 2022). E84 in VDAC2 is thought to be involved in biologically relevant interactions such as those with ceramide (Dadsena et al., 2019). We hypothesized that if conductance substates are due to the dynamic rearrangement of the salt bridge ensemble inside the pore leading to the set of pores of different selectivities and conductances, it is natural to expect a significant involvement of the E84 residue. Following this hypothesis, we tested the possible involvement of this residue in conductance substates formation in VDAC2 by using VDAC2 mutant E84A which replaces the membrane facing glutamate. E84A displayed enhanced thermostability, as measured by native tryptophan scanning fluorimetry (Fig. 4.6A). Its thermostability is significantly higher than that of VDAC1 and VDAC2, indicating the reduced flexibility of the b-barrel. Interestingly, the similar effect of VDAC1 E73 – the residue analogous to E84 in VDAC2 - on VDAC1 dynamics has been shown by using the combination of solid NMR spectroscopy and MD simulations by

Villinger et al. (Villinger et al., 2010). The removal of the charge on E73 by either mutation or chemical modification reduced the motions of VDAC1 N-terminal six b-strands underlying the key role of E73 in the elevated N-terminal protein dynamics.

However, notwithstanding the E84A mutant increased thermostability, the substates were still observed (Fig. 4.6B and Supplemental Fig. S4.5B). The VDAC2 E84A mutant gates similarly to the WT in single and multichannel experiments (Supplemental Fig. S4.5B). Thus, the E84 residue does not affect VDAC2 voltage gating, consistent with observations in the E73A VDAC1 mutant voltage gating experiments (Queralt-Martin et al., 2019). The VDAC2 E84A mutant displayed more stable and long-lasting substates than the WT, similarly to the substate stabilization observed in Δ N-VDAC2. An example of the E84A mutant displaying two long-lasting stable substates of 3.0 and 3.6 nS is shown in Fig. 6B in the presence of 10 nM aSyn. Similar to VDAC2 WT and the Δ N-VDAC2 and VDAC2- Δ Cys mutants, the substate with higher conductance of 3.6 nS in the E84A mutant has higher k_{on} and shorter t_{off} than the lower conductance substates of 3 nS, resulting in unchanged K_{eq} (Fig. 4.6C). These findings indicate that, similarly to NTE and extra cysteines, E84 mutation affects b-barrel flexibility but does not eliminate substate appearance.

4.4 Discussion

VDACs have been implicated in diverse mitochondrial signaling pathways, with VDAC2 being crucially important in development (Cheng et al., 2003; Lazarou et al., 2010). Yet, the biophysical underpinnings of its special role in regulating functions remain unexplored. In this study, we revisited the basic biophysical properties of recombinant human VDAC2 using single-molecule electrophysiology to demonstrate the unique plasticity of this channel's properties and its interaction with cytosolic proteins. Our data show that VDAC2 stochastically switches between multiple high-conductance states, which results in a wide conductance distribution of the “open” state uncommon for other VDACs. The existence of VDAC2 multiple open states (but not the spontaneous transitions between them) was reported previously (Xu et al., 1999), with an average conductance of \sim 3.5 nS in 1 M KCl at room temperature, which is lower than the typical open state conductance of VDAC1

and VDAC3 at these conditions. We verified that these states are not the conventional VDAC's voltage-gated states because they are even more anion selective than typical ~ 4 nS open states of VDAC1 or VDAC3 (Fig. 4.2C) (Queralt-Martin et al., 2020) as opposed to the more cationic voltage-gated states. Besides, they are observed at all applied voltages starting from as low as 10 mV with the frequency of their appearance independent of the applied voltage (Fig. 4.1, 2), suggesting that membrane potential, including in vivo conditions, is not required to induce substate behavior. Under sufficiently high applied voltage, VDAC2 characteristically gates similarly to its other two isoforms (Queralt-Martin et al., 2019; Queralt-Martin et al., 2020) and to VDACs isolated from their native mitochondria of different species - fungus, yeast, or plant (Colombini, 1989; Guardiani et al., 2018; Mlayeh et al., 2010; Mlayeh et al., 2017). This is manifested by a bell-shaped conductance vs voltage (G/V) dependence (Fig. 4.1C) and single-channel current transitions from the open state to the variety of closed states under the applied voltages of $|V| \geq 60$ mV (Fig. 4.1A). Therefore, the distinctiveness of VDAC2 among the three isoforms is that instead of the unique high-conductance anion-selective state, VDAC2 possesses a variety of such states. Notably, the characteristic duration and probability of each conductance state varies significantly between individual channels. The selectivity of the states with high conductances, which appeared to be in the range of open state conductances of VDAC1 and VDAC3 (1.8 – 2.1 nS in 1.0 M /0.2 M KCl salt gradient), fits into the range of VDAC1 and VDAC3 selectivity with permeability ratio $P_{Cl^-}/P_{K^+} = 1.35 \pm 0.15$, while the VDAC2 substates with lower conductance of 1.5 ± 0.05 nS have, on average, even higher anionic selectivity with $P_{Cl^-}/P_{K^+} = 1.5 \pm 0.05$ (Fig. 4.2 D).

Using aSyn, a known potent cytosolic regulator of VDAC1 and VDAC3 (Queralt-Martin et al., 2020; Rosencrans, Aguilera, et al., 2021; Rovini et al., 2020), as a sensitive molecular probe of the VDAC pore, we explored different substates of VDAC2. We found that aSyn characteristically blocks all registered high-conductance VDAC2 substates. Notably, aSyn does not block conventional voltage-gated low-conductance states either in VDAC2 or other VDACs (Rostovtseva et al., 2015). This, together with anionic selectivity and high conductance, proves that these VDAC2 substates differ from the voltage-induced,

more cation-selective lower-conductance states. Our results also show that aSyn quantitatively discriminates between different high conductance states: the on-rate of aSyn capture by the VDAC2 pore rises with the substate conductance while the blockage time decreases (Fig. 4.3D). This correlation is especially clear if the on- and off-rates for different substates are compared on the same VDAC2 WT channel. Across multiple individual channels of VDAC2, considerable variability in kinetic parameters exists, especially in k_{on} values, suggesting that channel structure is highly dynamic. The enhanced conformational heterogeneity of VDAC2 in comparison with VDAC1 was suggested by Gattin et al. based on a broad solid-state NMR spectra obtained with VDAC2 in liposomes, indicating a large structural ensemble (Gattin et al., 2015). The following solid-NMR study of VDAC2 reconstituted in 2D lipid bilayer crystals by Eddy et al. (Eddy et al., 2019) showed that line shapes and peak dispersion exhibited by VDAC1 and VDAC2 are very similar and mostly depend on protein sample preparation. However, they also found that the extended N-terminal residues of VDAC2 were not sufficiently mobile on very fast timescales to be detectable in ^{13}C INEPT-type experiments (Insensitive Nuclei Enhancement by Polarization Transfer). In addition, these residues were not observable in their cross-polarization experiments, suggesting the N-terminal tail is dynamic, possibly indicating conformational heterogeneity. These two structural studies testify to the difficulties of studying an enigmatic VDAC2 protein, emphasizing the urgent need to determine its structure.

Considering that VDAC permeability to mitochondrial metabolites, such as ATP, ADP, and Ca^{2+} , depends on VDAC pore anion/cation selectivity, we can speculate that by switching between substates, VDAC2 is capable of fine-tuning the regulation of metabolite and Ca^{2+} transport in and out of mitochondria (Rosencrans, Rajendran, et al., 2021). If such a physiologically meaningful mechanism exists, the immediate questions to answer concern the structural features of the substates' appearance and the physiological factors that regulate these substates in VDAC2 in live cells.

Possible conformational changes in VDAC2 leading to substate appearance

In an attempt to answer the first question, we studied the effect of the apparent sequence differences between VDAC2 and VDAC1 – the 11-amino acid NTE and the seven extra cysteines – on the formation of substates. We found that both NTE and cysteines quantitatively affect substates' appearance frequencies (Fig. 4.4) with their substantial decrease in VDAC2- Δ Cys down to ~19% and increase up to ~92% in Δ N-VDAC2, compared with ~54% of substates occurrence for the WT. The absence or presence of NTE and extra cysteines influences substates' appearance but does not eliminate them, thus suggesting that neither is the structural basis for substates' formation. Furthermore, the deletion of NTE, in fact, stabilizes two predominant conductance substates in different Δ N-VDAC2 channels.

The VDAC2 E84A mutant is more thermostable than the VDAC2 WT and VDAC1 (Fig. 4.6A). Still, the reduced flexibility of its b-barrel does not eliminate conductance substates. Like in Δ N-VDAC2, E84A mutation results in the stabilization of two predominant substates of 3 and 3.6 nS. The kinetic analysis of aSyn interaction with Δ N-VDAC2 and E84A mutants confirms the results obtained in VDAC2 WT. They also exhibit a positive correlation between conductance and k_{on} and a negative correlation between conductance and t_{off} , resulting in the same K_{eq} for both conductance levels. The results show that VDAC2's NTE, cysteines, and E84 residue all contribute to, but are insufficient, to determine VDAC2's dynamic behavior. Based on the available structural and computational studies on VDAC1 (Bayrhuber et al., 2008; Ngo et al., 2022; Ujwal et al., 2009; Villinger et al., 2010; Zachariae et al., 2012) and the predicted structural similarity between VDAC1 and VDAC2 (Maurya & Mahalakshmi, 2017) shown experimentally for VDAC2 zebrafish (Schredelseker et al., 2014), we can only speculate that the variety of conductance substates in VDAC2 may arise from dynamic rearrangements in the network of charged residues and salt bridges inside the pore in the proximity to the restriction zone and the tentative selectivity filter formed by two N-terminus α -helices as in VDAC1 (Ngo et al., 2022; Song et al., 1998a, 1998b; Thomas et al., 1993). VDAC2 b-barrel enhanced flexibility in comparison with VDAC1, manifested in its reduced thermostability (Fig. 4.6A), should also contribute to the proposed dynamicity of the salt bridges. Importantly,

the conductance substates were also observed for zebrafish VDAC2 (Supplemental Fig. S4.6).

Furthermore, aSyn recognizes these substates by interacting from both sides of the bilayer, implying that the structural changes underlying the states' appearance most likely occur close to the center of the channel rather than in the asymmetric loops on either cytosolic or mitochondrial-facing sides. The long-awaited atomic structure of mammalian VDAC2 will help to test these speculations.

One of the important results is that despite the significantly different on-rates of aSyn capture by different VDAC2 substates, the equilibrium constants K_{eq} remain virtually unaltered. This can be explained by the transition path energy landscapes shown in Fig. 7 for two VDAC2 substates. K_{eq} is an exponential function of the change in the free energy ΔU between the minima for the membrane-bound “free” aSyn molecule (potential well on the left) and for the pore-trapped one (potential well on the right). Because the experiment does not show any differences in the equilibrium constant in different substates, this means that ΔU is conserved, suggesting that the physical state of the aSyn molecule trapped within the VDAC pore is the same for all the substates. However, the profound changes in the on- and off-rates indicate that the region of the highest energy (the transition state) that the synuclein molecules must cross before reaching their final state in the pore differs for different substates. We can estimate the change in the transition state energy for substates 1 and 2, $\Delta\Delta U^{(1,2)}$, from k_{on} values as

$$\Delta\Delta U^{(1,2)} = k_B T \ln \left(\frac{k_{on}^{(1)}}{k_{on}^{(2)}} \right), \quad \text{Eq. (1)}$$

where $k_{on}^{(1)}$ and $k_{on}^{(2)}$ are the on-rates in substate (1) and (2), respectively. For example, applying Eq. (1) to the WT channel data presented in Fig. 3, we find that the change in the transition state energy between the open substate of the highest conductance, O3, and that of the lowest conductance, O1, is $1.6k_B T$.

On the one hand, empirical observations on aSyn-VDAC interaction (Jacobs et al., 2019; Rostovtseva et al., 2015) show that the on-rate is a strong exponential function of the

applied voltage. On the other hand, in the case of open VDAC2 substates studied here, it turns out that the on-rate is very sensitive to the ionic current through the channel, even at the same applied voltage. Specifically, it increases up to an order of magnitude for the higher currents, corresponding to the substates of higher conductance. In both scenarios – increasing applied voltage and increasing current at the same voltage – the fraction of the applied voltage that projects into the bulk solution in the vicinity of channel entrances increases. This is especially important in the case of VDAC because of the quite substantial access resistance of this channel, as was shown in experiments with water-soluble polymers that change the specific conductivity of the bulk solution (Aksoyoglu et al., 2016; Vodyanoy & Bezrukov, 1992) and confirmed within a mean-field approach by solving three-dimensional Poisson and Nernst-Planck equations (Aguilella-Arzo & Aguilera, 2020). The fraction of the applied potential extending into the bulk changes the local concentration of charged molecules in the vicinity of the channel entrance and thus is able to change their capture rates. A similar phenomenon was described for DNA capture into nanofabricated solid-state nanopores (Gershow & Golovchenko, 2007) using the notions of “electrostatic focusing” and “effective capture radius” (Wanunu et al., 2010). A natural question is whether the field at the channel entrance is strong enough to account for the observed effects and contribute significantly to the free energy profile in Fig. 4.7.

Let us first analyze the on-rate voltage dependence presented in Figs. 4.5B and 4.6C. The total channel resistance, R , is the sum of access resistances at both entrances of the channel, $2R_{acc}$, and the resistance of the channel proper, R_{ch_p} (Hille, 2001)

$$R = 2R_{acc} + R_{ch_p}. \quad \text{Eq. (2)}$$

Both experimental work and the mean-field calculations performed for VDAC in 1 M KCl give the value of $2R_{acc}$ as 19 to 20 % of the total channel resistance, that is $2R_{acc} \simeq 0.2R$, which means that the access resistance at each channel entrance is close to $0.1R$. Therefore, $\sim 10\%$ of the applied voltage drops at the channel entrance. The data in Figs. 5B and 6C

show that upon a 10 mV increase in the (modulus of) applied voltage, the k_{on} increases by a factor of ~ 8 . Using Eq. (1) for $\Delta\Delta U^{(1,2)}$, where indices (1) and (2) now refer to the heights of the barriers for aSyn capture, ΔU_C , at the two voltages differing by 10 mV, we arrive to $1.7 k_B T$. If we now assign the on-rate increase to the access resistance effect, then recalling that the change in the fraction of potential extending from the channel is 10% only, that is, $\Delta V_{acc} \simeq 1$ mV, and using

$$\Delta\Delta U^{(1,2)} = \Delta V_{acc} Q_{trap} \quad \text{Eq. (3)}$$

we arrive at ~ 50 elementary charges for the effective “trapping charge”, Q_{trap} . This charge significantly exceeds the total charge of the aSyn C-terminus, meaning that the applied voltage effect on the height of the transition state in Fig. 7 is more complex.

Let us now look at the change in the on-rates between the open substates using the same line of reasoning. As explained above, at 30 mV of applied potential, the transition of the VDACC2 channel from the open substate O1 of conductance $G^{(O1)} = 3.0$ nS to substate O3 of conductance $G^{(O3)} = 3.8$ nS decreases the barrier by $1.6 k_B T$. The change in the V_{acc} can be estimated through the change in the channel current, $\Delta I = (G^{O3} - G^{O1})V$ as $\Delta V_{acc} = R_{acc}\Delta I = 0.65$ mV. Using Eq. (3), we arrive at Q_{trap} of ~ 60 elementary charges. Again, this number is too large for the access resistance effects to explain the on-rate change between the states. However, the closeness of the two charge estimates, namely 50 vs 60, strongly suggests a similar physical mechanism of on-rate regulation in both cases. The capture is governed by the voltage distribution along the channel and within its access areas, which defines the physics of the observed phenomena. The exponential dependence of the on-rate on voltage and a factor of four overestimation of Q_{trap} , compared to the actual charge of the aSyn C-terminus, means that the capture of a disordered protein molecule by the channel is a complex process dominated by an entropic barrier (Muthukumar, 2010) and that the transition state in Fig. 7 corresponds to the C-terminus

being partially captured by the pore. This way, the potential drop over the terminus is much larger than the potential drop over the VDAC access resistance.

The significant differences in $\Delta G/G$ found for different substates (Fig. 4.3D) also suggest that the substates should vary by structural rearrangements inside the pore. Indeed, one may expect that the trapped polypeptide will influence the narrower, less conducting channel to a greater degree than the wider, more conducting one.

It is worth noting here that a similar correlation between the channel conductance and the on-rate of aSyn molecule capture was previously demonstrated when comparing three different β -barrels formed by α -Hemolysin, MspA, and VDAC (Hoogerheide et al., 2022). At the applied voltage of 35 mV, VDAC1, the channel of the highest conductance of 4 nS in 1M KCl has about three orders of magnitude higher on-rate than that for α -Hemolysin, the channel of the lowest conductance of 0.73 nS in the same salt. However, remarkably, the equilibrium constant was not conserved for these three channels, which is opposite to what is reported here for the VDAC2 substates. We conclude that the regulation of all substates of the open conformation of VDAC2 by aSyn is described by the same affinity, suggesting that once the aSyn molecule is captured, its physical state and interactions in the pore are the same for all substates, but differs significantly by its kinetic parameters

Physiological implications of VDAC2 unique plasticity

It has been recognized that the physiological roles of all three VDAC isoforms, and particularly VDAC2, exceed their function as “simple” pores (Maurya & Mahalakshmi, 2016; Summers et al., 2012). β -barrel pores are unique to the outer membrane of gram-negative bacteria, mitochondria, and plastids, suggesting a common evolutionary origin (Diederichs et al., 2021). While the bacterial ancestor of VDAC is still unknown and controversial, VDAC is believed to share a common evolutionary origin with other 19 stranded β -barrel channels in the MOM such as TOM40 and Mdm10 (Bay et al., 2012). One characteristic that distinguishes VDAC2 from the other isoforms is the N-terminal extension. In the TOM40, the N-terminal extension, which is exposed to the mitochondrial intermembrane space (IMS), physically interacts with other TOM complex members

(Araiso & Endo, 2022). It is likely that VDAC2's N-terminal extension also interacts in a similar fashion with other MOM and IMS proteins, thus defining VDAC2's physiological uniqueness among three isoforms (Maurya & Mahalakshmi, 2016). It would be of great importance to identify VDAC2-specific interactors using proximity labeling or immune precipitation mass spectrometry experiments. We can further speculate that by interacting with VDAC2 partner proteins, the N-terminus could also, in turn, affect the state of VDAC2 conductance and, consequently, its selectivity, which defines VDAC's permeability for calcium (Rosencrans, Aguilera, et al., 2021; Tan & Colombini, 2007) and ATP/ADP (Rostovtseva & Colombini, 1996; Rostovtseva et al., 2002).

VDAC2 has two cysteines on the N-terminus extension along with the 6 cysteines on the loops facing IMS that may have a role in sensing oxidative stress in the IMS. Many studies and reviews have pointed to the 9 cysteines of VDAC2 as being critical for its function (De Pinto et al., 2016; Karachitos et al., 2021; Maurya & Mahalakshmi, 2013, 2014, 2015; Pittala et al., 2024). The strongest suppression of substate behavior was observed in the cysteine-null mutant VDAC2- Δ Cys (Fig. 4.4C), suggesting that the redox state of mitochondria and oxidation states of the cysteines in VDAC2 could strongly affect the conformational state of the channel. While extensive studies highlight the important role of VDAC3, the isoform that has 4 cysteines facing the IMS, in redox signaling (Reina et al., 2022), there is a lack of studies on such a role of VDAC2. Our finding that VDAC2's cysteines modulate substate occurrence suggests that mitochondrial reactive oxygen species (ROS) production could change the redox state of VDAC2, thereby transmitting the mitochondrial redox state to the cytoplasm.

The unexpected finding that substates vary by the kinetics of α Syn's interaction with VDAC2 but not its affinity implies that substates do not tune α Syn regulation of channel fluxes. However, the altered kinetics demonstrate that the capture of the synuclein molecule is indeed affected by the structural changes in the channel. It is natural to expect that such conformational changes in VDAC2 will affect its interactions with other proteins. Potential interactors may include cytosolic pro-apoptotic proteins such as BAK and BAX, kinases such as hexokinase 1 and 2, cytoskeletal proteins such as tubulin and actin, etc.

While Naghdi et al. (Naghdi et al., 2015) didn't see an effect of N-terminal or cysteine deletion on BAK binding to VDAC2, these proteins could selectively recognize and bind a particular substate of VDAC2. Experimental validation of the BAX/BAK interaction at the single molecule level remains challenging due to the pore-forming nature of these molecules. Nevertheless, the dynamic conformational flexibility identified in the present study may allow VDAC2 to recognize many such binding partners. Furthermore, our results demonstrate that aSyn-VDAC2 complexation could be a promising experimental approach to detect the subtle conformational changes of the single membrane nanopore beyond that of VDACS. Together, VDAC2's role in apoptosis and redox sensing suggests that the N-terminal extension and cysteine residues alter VDAC2 channel properties for performing new non-redundant roles in eukaryotes, thus confirming phylogenetic analysis of VDAC gene duplication in vertebrates (Saccone et al., 2003).

The question as to why VDAC2 knockout is lethal or partially lethal, but knockouts of the other two isoforms are not, remains open. We speculate that VDAC2's unique plasticity, manifested by spontaneous transitions between high conductance substates revealed in our in vitro single-channel experiments, could be a key to understanding its physiological significance. These data could tentatively explain the unique functional role of VDAC2 through its ability to dynamically adapt to rapidly changing metabolic cell conditions and to alter the rate of interaction with its presumably multiple protein partners. By elucidating how VDAC2's basic biophysical characteristics, such as its ability to stochastically switch between high-conductive substates, contribute to its physiological functions, we provide a deeper understanding of its unique role in cellular homeostasis.

Limitations to this Study: This work focused on the biophysical study and mechanistic modeling of specifics and peculiarities of the VDAC2 channel. Therefore, translation of these observations to physiological implications in the native mitochondrial environment remains speculative. For these hypotheses about VDAC2 conformation to be tested in cells, the mutants described here can be reintroduced into VDAC2 KO cell lines. We would expect mitochondrial functions to be altered and for the interactome (via an immunoprecipitation or proximity labeling strategy) to be shifted. Moreover, a more

detailed understanding of the structural basis of VDAC2 substates would be enabled by a high resolution crystal structure of human VDAC2.

4.5 Materials and Methods

Cloning, recombinant protein production, and purification. Recombinant VDAC2 WT and VDAC2 E84A were purified and isolated as described in *Supplemental Methods* and stored in the buffer containing 25 mM HEPES pH 7.4, 100 mM NaCl, 0.1% LDAO, 1mM TCEP, and 1mM EDTA. The cysteine-less VDAC2 mutant (VDAC2-DCys) and VDAC2 mutant without N-terminal extension residues 1-11 (VDAC2-DN) were purified and isolated as previously describes (Maurya & Mahalakshmi, 2015). Recombinant zebrafish VDAC2 (zfVDAC2) was the generous gift of Dr. Johann Schredelseker (Walther Straub Institute of Pharmacology and Toxicology, Munich, Germany). Recombinant aSyn WT was the generous gift of Dr. Jennifer Lee (NHLBI, NIH). aSyn was purified and characterized as described previously (Pfefferkorn & Lee, 2010) and stored at -80°C.

VDAC reconstitution and conductance measurements. The procedure of VDAC reconstitution into lipid bilayers was described previously (Rostovtseva et al., 2015; Rostovtseva et al., 2006) and in *Supplemental methods*. Planar lipid membranes (PLMs) were formed from lipid mixtures of dioleoyl-phosphatidylglycerol (DOPG), dioleoyl-phosphatidylcholine (DOPC), and dioleoyl-phosphatidylethanolamine (DOPE) in a ratio of 2:1:1 (wt/wt) in single-channel experiments or from soybean polar lipid extract (PLE) in multichannel gating experiments. All lipids were purchased from Avanti Polar Lipids. Typically, channel insertion was achieved 2–20 min after the addition of 0.2–0.5 µl of VDAC2 diluted in 2.5% Triton X-100 buffer (50 mM KCl, 100 mM Tris at pH 3.35, 1 mM EDTA, 15% (vol/vol) DMSO, 2.5 % Triton X-100) on the Teflon partition facing the *cis* compartment. The potential is defined as positive when it is greater at the side of VDAC addition (*cis* side). Current recordings were performed as described previously (Rostovtseva et al., 2015) using an Axopatch 200B amplifier (Axon Instruments) in the voltage-clamp mode. Data were filtered by a low-pass 8-pole Butterworth filter (Model 900 Frequency

Active Filter, Frequency Devices) at 15 kHz, digitized with a sampling frequency of 50 kHz, and analyzed using pClamp 10.7 software (Axon Instruments).

When a single VDAC channel was reconstituted into PLM and recorded, α Syn was added to both compartments of the experimental chamber to 10 nM final concentration. For data analysis by Clampfit version 10.7, a digital filtering using a 5 kHz low-pass Bessel (8-pole) filter was applied. Individual events of current blockages were discriminated, and kinetic parameters were acquired by fitting logarithmic single exponentials to logarithmically binned histograms as (Sigworth & Sine, 1987) described previously (Weinrich et al., 2017). All lifetime histograms used 10 bins/decade. The number of blockage events for each analyzed current fragment was in the range from 250 to 2500. Three different logarithmic probability fits were generated using different fitting algorithms, and the mean and S.D. of the fitted time constants were used as mean and S.D. for the characteristic open and blockage times. Each channel experiment was repeated at least three times on different membranes. Records for analysis were obtained no less than 30 min after α Syn addition to ensure a steady state. Fits to histograms such as those in Figs. 3C used the maximum likelihood estimator with the simplex algorithm in Clampfit version 10.7.

VDAC ion selectivity was measured in a 1.0 M (*cis*) versus 0.2 M KCl (*trans*) gradient, buffered with 5 mM HEPES at pH 7.4, as described previously (Rosencrans, Aguilera, et al., 2021; Tejjido et al., 2014). The reversal potential – the potential corresponding to the zero-current level – was measured only for single channels under application of either 5 mHz triangular voltage wave of ± 50 mV amplitude or by measuring current acquired at different applied voltages typically at 5 mV intervals. Cl^-/K^+ permeability ratio was calculated using the Goldman-Hodgkin-Katz equation as previously described (Tejjido et al., 2014). VDAC voltage-gating was measured on multichannel membranes using a previously described protocol (Colombini, 1989; Rappaport et al., 2015; Rostovtseva et al., 2006) and in *Supplemental Methods*.

Thermal fluorescent protein stability assay. The melting temperatures (T_m) of recombinant VDAC were determined by native tryptophan fluorescence using a Tycho Differential Scanning Fluorometer (Nanotemper). VDAC samples were diluted to 1mg/ml

in 25 mM HEPES at pH 7.4, 100 mM NaCl, 0.1% LDAO, 1mM TCEP, and 1mM EDTA buffer. The ratio of native tryptophan 350 nm to 330 nm fluorescence increases at higher temperatures due to exposure of unfolded tryptophan to the solution. The T_m was determined from the inflection point of the curve.

Purification of VDAC2 mutants

Cells were resuspended in lysis buffer (50 mM Tris-HCl, 250 mM NaCl, 10 mM 2-mercaptoethanol (Bioshop, Burlington), protease inhibitors tablets (Roche, Basel), pH 7.0 and lysed by a French press (Genizer, Irvine). The VDAC2 containing inclusion bodies were isolated using sucrose cushion centrifugation (50 mM Tris-HCl, 500 mM NaCl, 50 % sucrose, pH 7.0). The inclusion bodies were dissolved in denaturing buffer (6 M GdnHCl, 50 mM Tris-HCl, 100 mM NaCl, 20 mM imidazole, pH 7.5), applied to Ni-NTA agarose resin (Cytiva, Uppsala) and then VDAC2 was eluted with elution buffer (6 M GdnHCl, 50 mM Tris-HCl, 100 mM NaCl, 250 mM imidazole, 1mM TCEP, pH 7.5). Purified VDAC2 in elution buffer was precipitated by dialysis against 4 liters of dialysis buffer (50 mM Tris-HCl, 50 mM NaCl, 1 mM EDTA, 1 mM TCEP, pH 7.5) in a 12,000-14,000 molecular weight cutoff (MWCO) dialysis membrane. Precipitated VDAC2 was isolated by centrifugation at 12,000 g.

Refolding and purification of VDAC2 mutants in LDAO detergent

Purified precipitated VDAC2 was dissolved in guanidine hydrochloride buffer (100 mM NaPi, 100 mM NaCl, 6 M GdnHCl, 2 mM TCEP, 1 mM EDTA, pH 6.8) at a concentration of 2.5-3 mg/ml. VDAC2 was refolded at 4°C by dropwise dilution of one volume of VDAC2 solution into ten volumes of refolding buffer (100 mM NaPi, pH 7.0, 100 mM NaCl, 1 mM EDTA, 2 mM TCEP, 1.5% (64.5 mM) LDAO (Anatrace, Maumee) with stirring. The final ratio of VDAC2 protein to LDAO micelles is about 1:90, assuming the aggregation number of LDAO micelle is 76. After overnight stirring at 4°C the refolded VDAC2 sample was dialyzed against 4 liters of buffer (25 mM NaPi, 1 mM EDTA, 1 mM TCEP, pH 7.0) for 12 to 16 hours. Precipitated VDAC2 was removed using centrifugation at 12,000 g, followed by filtration with a 0.2- μ m membrane.

Cation exchange chromatography was employed to isolate properly folded VDAC2 protein in LDAO detergent micelles. The sample was loaded onto a 20 mL SP Sepharose HP column equilibrated with buffer A (25 mM NaPi, 1 mM EDTA, 1 mM TCEP, 0.1% LDAO, pH 7.0). VDAC2 was eluted during a 5%-55% gradient with buffer B (25 mM NaPi, 1 mM EDTA, 1 mM TCEP, 0.1% LDAO, 1M NaCl, pH 5.9) at about 35% buffer B. Pure VDAC-2 fractions were pooled and concentrated to the desired concentration using 30 kDa molecular weight cutoff (MWCO) concentrators. VDAC2 was further purified by gel filtration chromatography using a Superdex 200 prep grade column (Cytiva, Wilmington DE), pre-equilibrated with NMR buffer (25 mM NaPi, 50 mM NaCl, 0.08% LDAO, 2 mM EDTA, pH 6.5).

Channel reconstitution and conductance measurements

Planar lipid membranes were formed on a ~70-100-mm diameter orifice in a 15-mm thick Teflon partition that separated two compartments filled with 1 M KCl buffered with 5 mM HEPES at pH 7.4, as described previously (48). Lipid monolayers for membrane formation were made from 5 mg/mL solution of lipid in pentane. Single-channel data were filtered by a low-pass eight-pole Butterworth filter (Model 900 Frequency Active Filter; Frequency Devices, Ottawa, IL) at 15 kHz and saved with a sampling frequency of 50 kHz and analyzed using pClamp 10.7 Software (Molecular Devices, San Jose, CA). All data were collected at room temperature of 21.0 ± 1.0 °C.

Measuring of voltage-gating on multichannel membrane

VDAC voltage-dependent gating was measured using a previously described protocol (93), in which gating is inferred from the response of multiple channels to a slow symmetrical 5 mHz triangular voltage wave of ± 60 mV amplitude applied with a 33220A arbitrary waveform generator (Agilent Technologies, Santa Clara, CA). VDAC multichannel recordings were filtered by a low-pass eight-pole Bessel filter at 1 kHz, digitized at a sampling frequency of 2 Hz, and analyzed, as described previously (93), using pClamp 10.7 Software and an algorithm developed in-house (93).

Statistical analysis. Empirical Cumulative Distribution Functions (ECDFs) were calculated based on observed conductances using the Python package *iqplot*. To determine the confidence interval for the ECDF, 1,000 bootstrap replicates were utilized. The shaded region on the ECDF plots represents the 95% confidence interval derived from the bootstrap analysis. To evaluate the change in substate occurrences for a given mutant or the probability that a channel will display substates for a given number of observations, we modeled the process as being generated by the binomial equation and calculated the maximum likelihood estimation (MLE) for the binomial coefficient. The MLE for Binomial Coefficient to estimate the proportion of channels with substates for each mutant was computed based on 25, 27, and 16 observations for the VDAC2 WT, VDAC2-DN, and VDAC2-DCys channels, respectively. 10,000 bootstrapped replicates were generated. Significance was determined using a chi-squared test.

4.6 Acknowledgments

We thank David Hoogerheide and Megha Rajendran for discussions and for reading our manuscript. W.M.R, M.G.L, T.K.R. and S.M.B. were supported by the Intramural Research Program of the *Eunice Kennedy Shriver* National Institute of Child Health and Human Development of the National Institutes of Health. This research was funded in part by a generous gift from the J. Yang and Family Foundation.

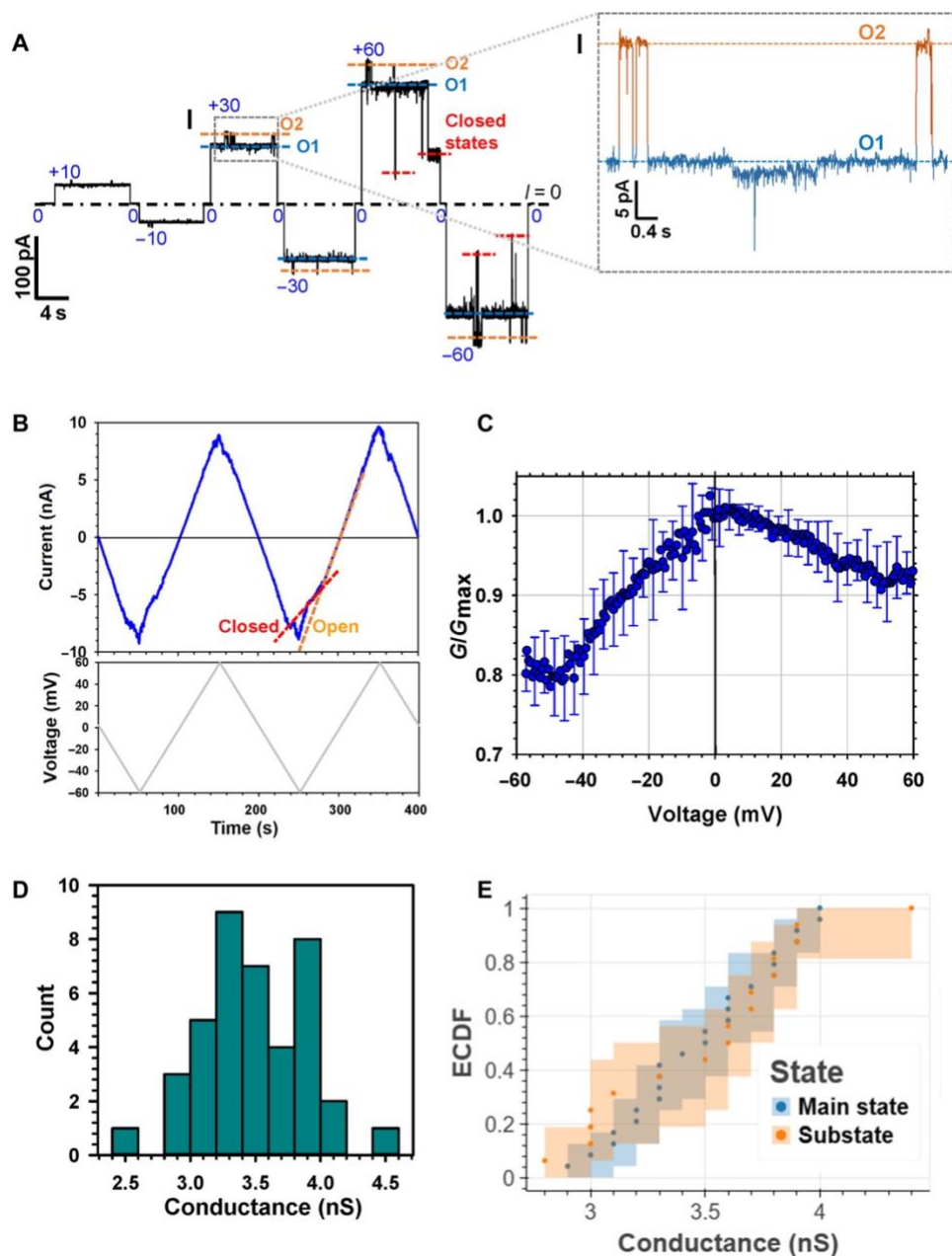


Figure 4.1: VDAC2 stochastically switches between different “open” conductance substates. (A) Representative record of the current through a single VDAC2 WT channel reconstituted into the PLM formed from 2PG/PC/PE lipid mixture in 1M KCl, pH 7.4 at the increasing applied voltages as specified. Two distinct substates of the open state (“O” state) indicated as O1 of 3.0 nS (blue dashed line) and O2 of 3.5 nS (orange dashed line) were observed at all voltages. Here and elsewhere the dash-dotted line represents zero

current level; dashed lines indicate conductance substates. The current record was digitally filtered at 500 Hz using a low-pass Bessel (8-pole) filter. Inset **(I)**: Transitions between two conducting states are shown in a finer timescale using a digital 1 kHz Bessel filter. **(B)** Representative current trace obtained on a multichannel (~ 40 channels) membrane (upper panel) in response to the applied triangular voltage wave of ± 60 mV, 5 mHz (bottom panel). High conductance of open states (orange dashed line) at low potentials and lower conductance of “closed” states (red dashed line) at higher potentials are indicated. PLM were made of Polar Lipid Extract (PLE) in 1 M KCl buffered with 5 mM KCl. **(C)** Typical bell-shaped voltage dependence of VDAC2 WT normalized conductance, G/G_{max} , obtained in multichannel experiments as in (B). G is a conductance at given voltage and G_{max} is the maximum conductance at $|V| \leq 10$ mV. Data points are means of three experiments \pm SD. **(D)** VDAC2 WT single channel conductance histogram. The main state conductance was measured for 24 independent molecules. **(E)** The Empirical Cumulative Distribution Function (ECDF) calculated for all main states (blue) and substates (orange) conductances observed in all experiments (N=24 channels). Solid dots denote raw data points. The shaded region represents the 95% confidence interval from 10,000 bootstrap replicates.

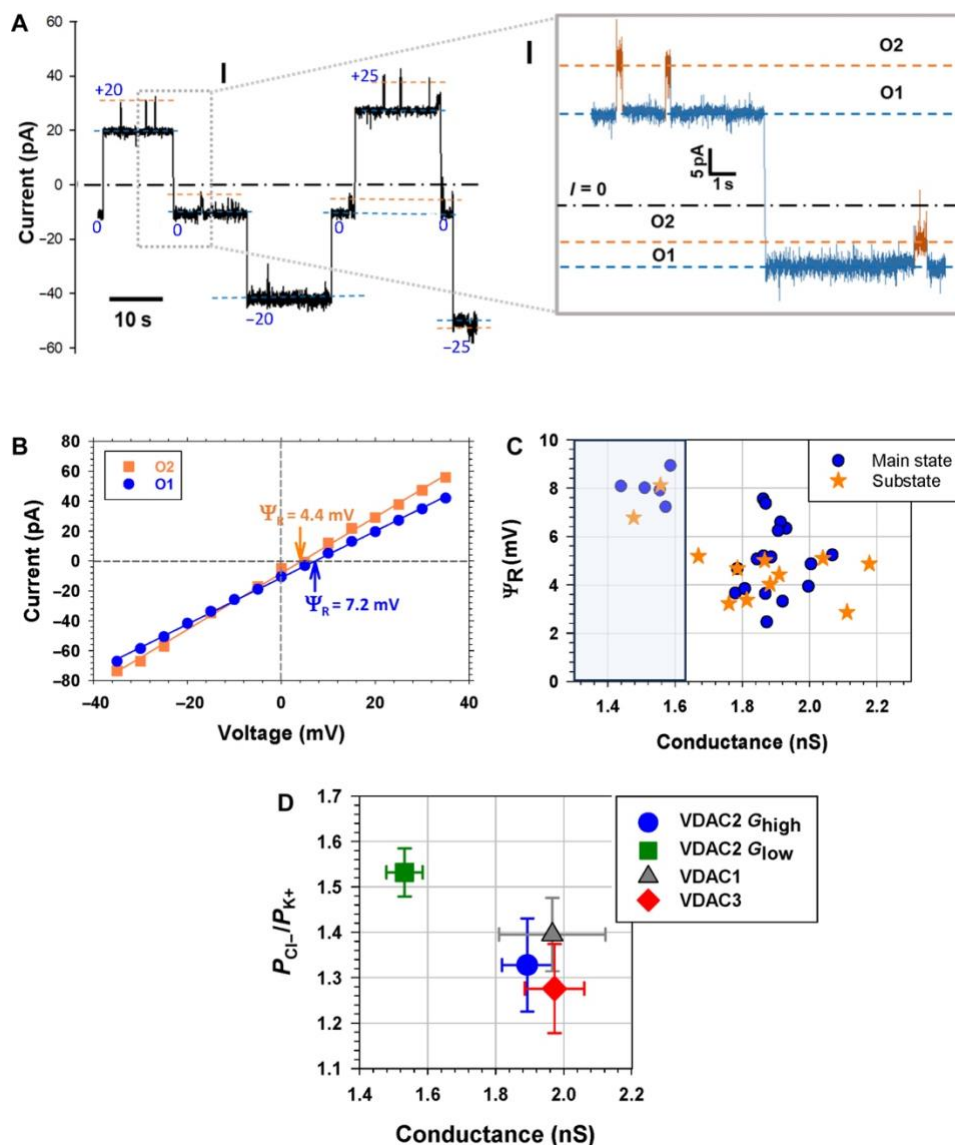


Figure 4.2: VDAC2 substates are anion-selective open states. (A) Representative single-channel trace of the current through VDAC2 WT was obtained using a 1.0 M (cis) / 0.2 M (trans) KCl gradient at different applied voltages, as specified. Blue and orange dashed lines indicate two open substates. Inset (I) shows a fragment of ion current (accentuated by a gray box) at a finer time scale, demonstrating two open states, O1 and O2, at +20 mV and 0 mV of the applied voltage. The current record was digitally filtered using a 500 Hz (1 kHz in (I)) low-pass Bessel (8-pole) filter. Other experimental conditions were as in Fig. 1. (B). Current-voltage (I/V) curves were obtained for the two

states O1 (blue circles) and O2 (orange squares) for the experiment shown in (A). Linear regressions allow for the calculation of the reversal potential (Y_R) indicated by arrows for each state. Positive Y_R corresponds to anion selectivity. (C) Reversal potential (Y_R) versus conductance scatter plot for all observed conductance substates: main or long-lasting (blue circles) and short-lasting (orange stars) substates for 19 individual VDAC2 WT channels. (D) Comparison of the mean open state conductance and Cl^-/K^+ permeability ratio ($P_{\text{Cl}^-} / P_{\text{K}^+}$) for each VDAC isoform. The full set of the analyzed VDAC2 conductances was divided into a high conductance state of $> 1.6 \text{ nS}$ (G_{high}) and $P_{\text{Cl}^-}/P_{\text{K}^+} \sim 1.3$ similar to those of VDAC1 and VDAC3, and a state with conductance lower than 1.6 nS (G_{low}) (highlighted by blue in (C)) and high anion selectivity with $P_{\text{Cl}^-}/P_{\text{K}^+} \sim 1.5$. Error bars are $\pm \text{SD}$ from at least 5 independent channel measurements for each VDAC isoform.

the time when the channel is open between each blockage event (t_{on}) and the blockage time (t_b). **(C)** Representative log-binned histograms of t_{on} (i) and t_b (ii) of each state at 30mV obtained from the experiment in (A). Solid lines are fits to a single-exponential function with $\langle t_{on} \rangle$ equal to 19.7, 8.62, and 3.87 ms for state O1, O2, and O3, respectively (i); and $t_{off} = \langle \tau_b \rangle$ equal to 5.79, 2.59, and 1.63 ms for state B1, B2, and B3, respectively(ii). **(D)** The kinetic parameters: $k_{on} = 1/(\langle \tau_{on} \rangle [C])$, where $[C]$ is α Syn bulk concentration, τ_{off} , and the equilibrium constant, $K_{eq} = k_{on} \tau_{off}$, of α Syn-VDAC binding for each state at 30 mV. Error bars are $t \pm SD$. of three fitting algorithms for the exponential fits. **(E)** Comparison of the α Syn-blocked conductance of each state B1, B2, B3 as shown in panel (A) in I and II. DG/G is the relative conductance drop, where DG is the difference between open (G) and blocked state conductances of each state O1, O2, and O3. Error bars $\pm SD$ between measurements of DG/G .

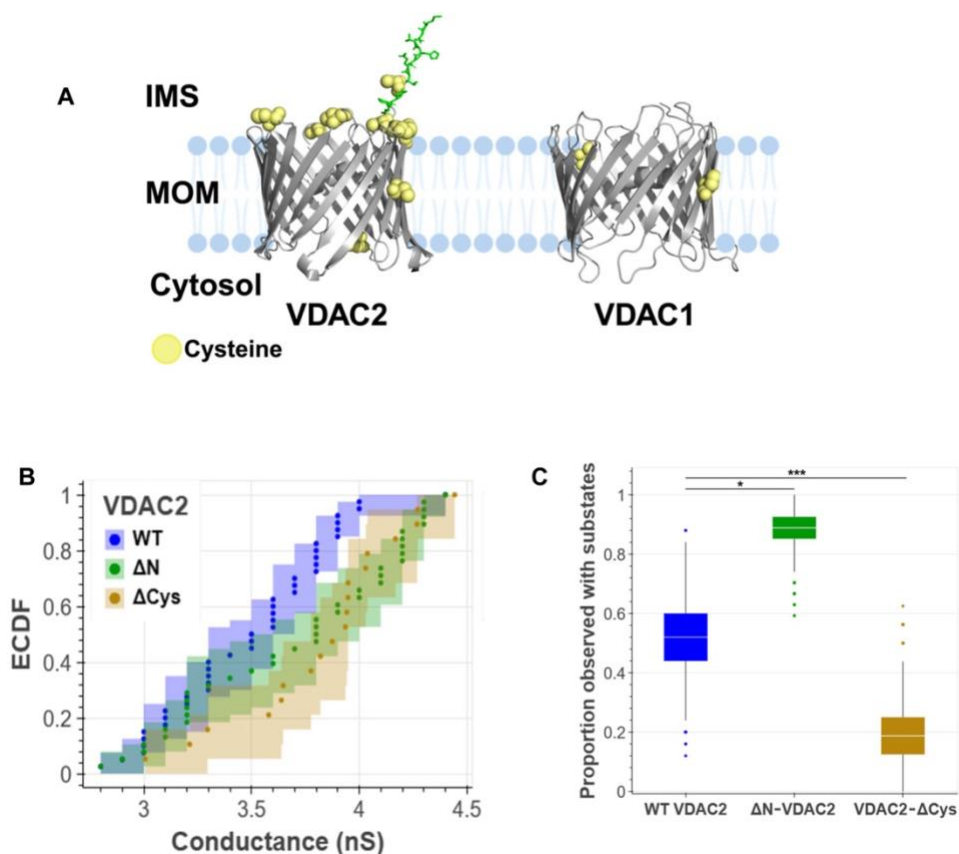


Figure 4.4: N-terminal extension and cysteine mutations influence but do not abolish VDAC2 substates. (A) Structure of human VDAC2 (Alphafold2 prediction) and VDAC1 (hVDAC1: PDB ID: 2JK4). Cysteines are shown as yellow balls. NTE of VDAC2 is shown in green. (B) ECDF was calculated using conductance values of the measured substates for all conductances observed for WT (blue), ΔN (green), and ΔCys (goldenrod) VDAC2 channels. Occurrence was liberally defined as whether a state transition had been observed during the entire recording period for a given channel. Out of 24 single-channel recordings of VDAC2 WT, 13 channels displayed substate behavior, compared to 25 channels out of a total of 27 for ΔN -VDAC2 channels and 3 out of 16 channels of VDAC2- ΔCys . Solid dots represent raw data points. The shaded region represents the 95% confidence interval from 1000 bootstrap replicates. (C) Box and Whisker plots for MLE probability of the binomial coefficient; substate behavior being observed in WT (blue), ΔN (green), and ΔCys (goldenrod) VDAC2 channels. 10,000 bootstrapped replicates were simulated from a maximum likelihood estimation of

the binomial coefficient originally calculated from 25, 27, and 16 observations of WT, ΔN , and ΔCys VDAC2, respectively. The top and bottom of the box are, respectively, the 75th and 25th percentiles of the data. The line in the middle of the box is the median. The top whisker extends to the maximum of the set of data points that are less than 1.5 times the interquartile regions beyond the top of the box, with an analogous definition for the lower whisker. Data points not between the ends of the whiskers are plotted as individual points. Substate occurrence between mutants was compared with a chi-squared test. “*” indicates p-value < 0.05, “****” indicates a p-value < 0.001.

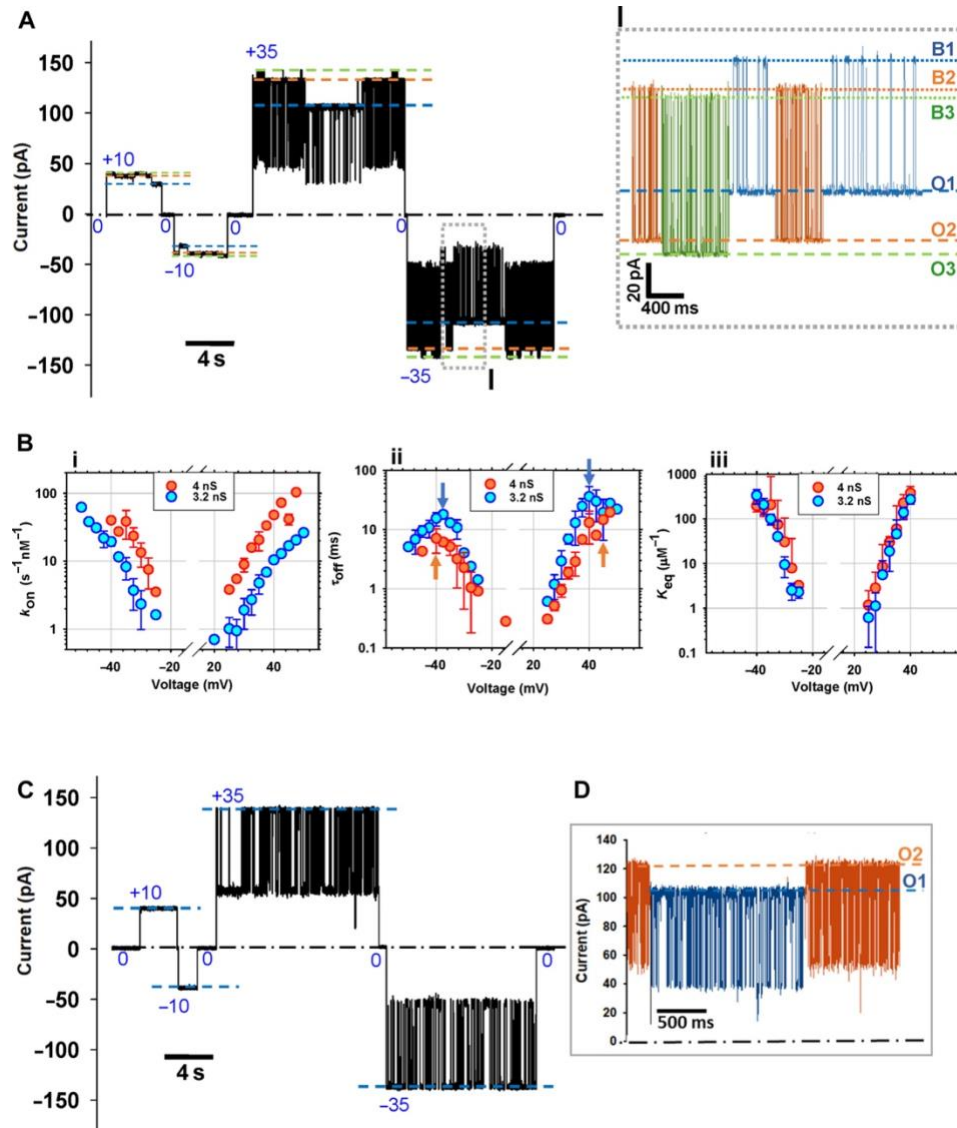


Figure 4.5: aSyn blocks the higher-conductance substates with a higher on-rate than the lower-conductance states across VDAC2 mutants. (A) Representative single-channel current trace obtained with the reconstituted ΔN -VDAC2 mutant with 10 nM αSyn added to both sides of the membrane. Three distinct substates, O1, O2, and O3 are observed at ± 10 and ± 35 mV of the applied voltage. Inset (I) shows αSyn -induced blockage events at a finer time scale for each of the three observed substates at -35 mV (accentuated by the gray box in the left trace). Open states O1, O2, and O3 can be observed along with their corresponding αSyn blocked states B1, B2, and B3. The current

record was digitally filtered using a 1 kHz low-pass Bessel (8-pole) filter. **(B)** Voltage dependences of the on-rate constant k_{on} (i), the mean blockage time t_{off} (ii), and the equilibrium constant K_{eq} (iii) (calculated for the retraction regime only) of aSyn binding to two Δ N-VDAC2 substates with conductances of 4 and 3.2 nS. Arrows in (ii) indicate the transitions between blockage/retraction and translocation regimes. Data are means of three independent experiments \pm SD. **(C)** A representative current record of VDACC2- Δ Cys single channel in the presence of 10 nM α Syn on both sides of the membrane showing one open state of 4 nS. **(D)** Example of the current record of VDACC2- Δ Cys with two substates of 3.5 and 3 nS obtained at +35 mV of the applied voltage. Current records were digitally filtered using 500 Hz (C) and 1 kHz (D) low-pass Bessel (8-pole) filters.

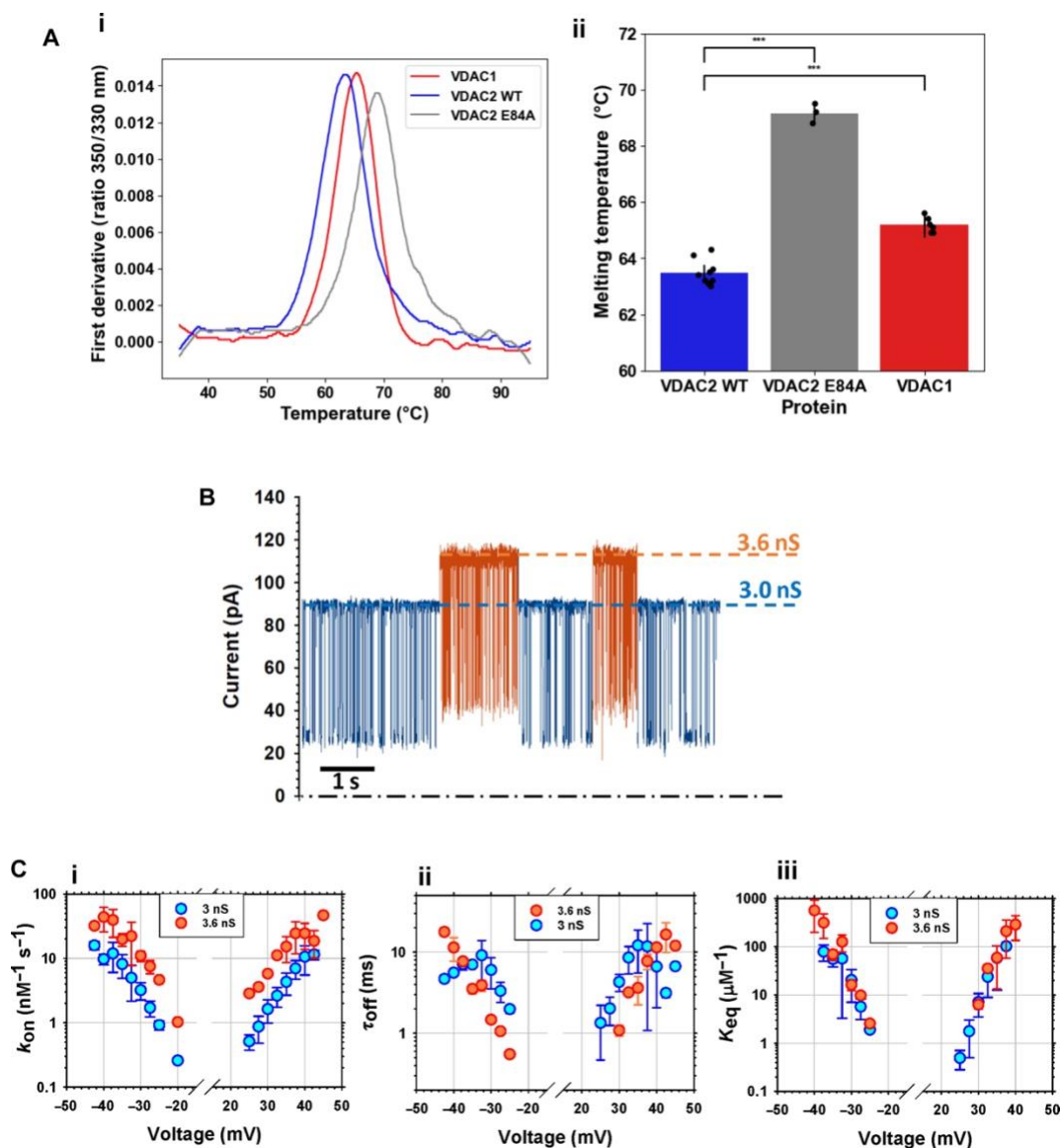


Figure 4.6: E84 residue of VDAC2 contributes to b-barrel stability but does not affect substates appearance. (A) (i) The first derivative of the ratio of 350 nm / 330 nm tryptophan fluorescence vs temperature demonstrates the inflection melting point (T_m) for VDAC1 (red), VDAC2 WT (blue), and VDAC2 E84A (gray). **(ii)** Box and scatter plot demonstrating average T_m for VDAC1 (red), VDAC2 WT (blue), and VDAC2 E84A (gray). Melting temperatures were compared with Student's T-Test; “****” indicates a p-value < 0.000001. **(B)** The representative current record of the VDAC2 E84A mutant showing two equally long-lasting conducting states of 3.0 and 3.6 nS in the presence of 10 nM aSyn on both sides of the membrane at the applied voltage of 30 mV.

The current record was digitally filtered using a 1 kHz low-pass Bessel (8-pole) filter.

(C) Voltage dependences of the on-rate constant k_{on} (i), the mean blockage time t_{off} (ii), and the equilibrium constant K_{eq} (iii) of aSyn binding to two VDAC2 E84A states with conductances of 3.6 and 3.0 nS. Data are means of three independent experiments \pm SD.

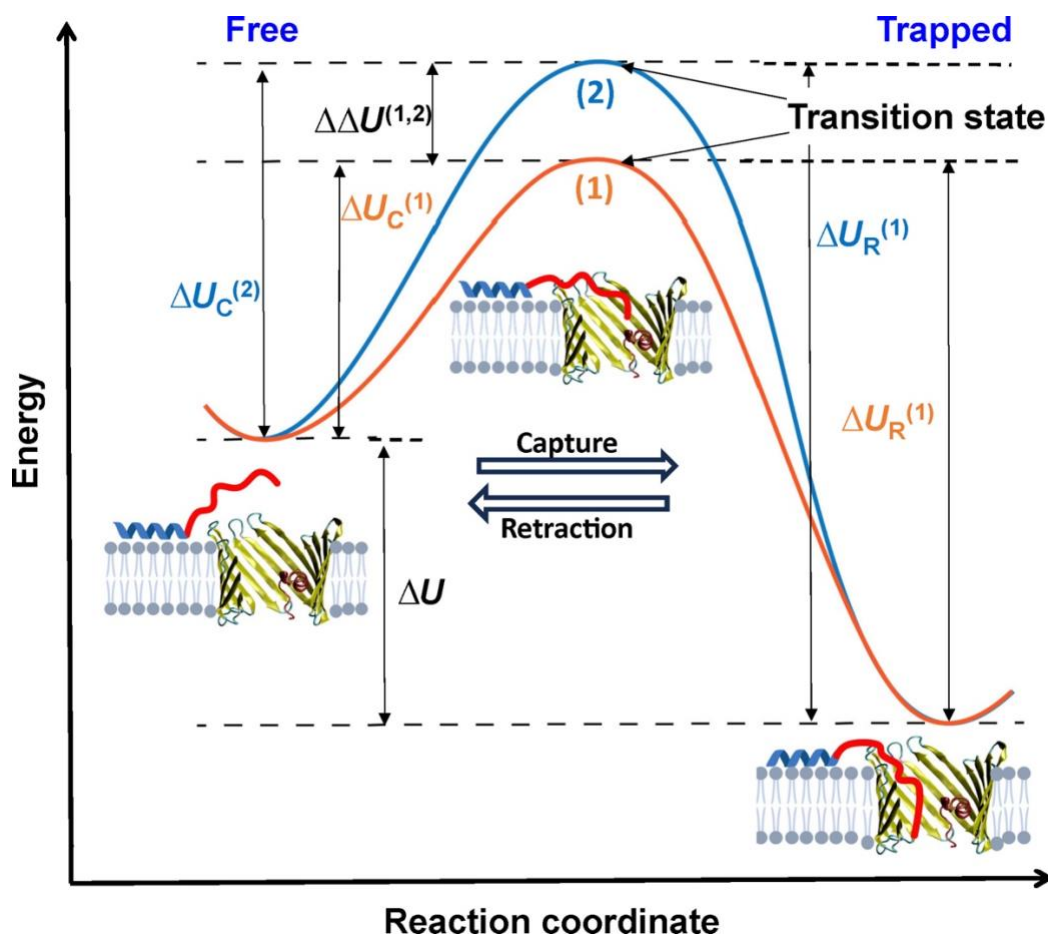


Figure 4.7: Changes in the transition state energy barrier underlie the kinetic differences in the aSyn-VDAC interaction between substates. Free energy landscape diagram representing a model of the aSyn-VDAC interaction as a function of the reaction coordinate. The potential well of the initial state of free aSyn bound to the membrane is shown on the left. The potential well of the final state, whereupon the aSyn molecule is captured by the VDAC pore, is shown on the right. The energy landscape experienced by the aSyn molecule as it complexes with the higher conductance VDAC2 substate (1) is represented in orange, whereas the landscape for the lower conductance substate (2) is represented in blue.

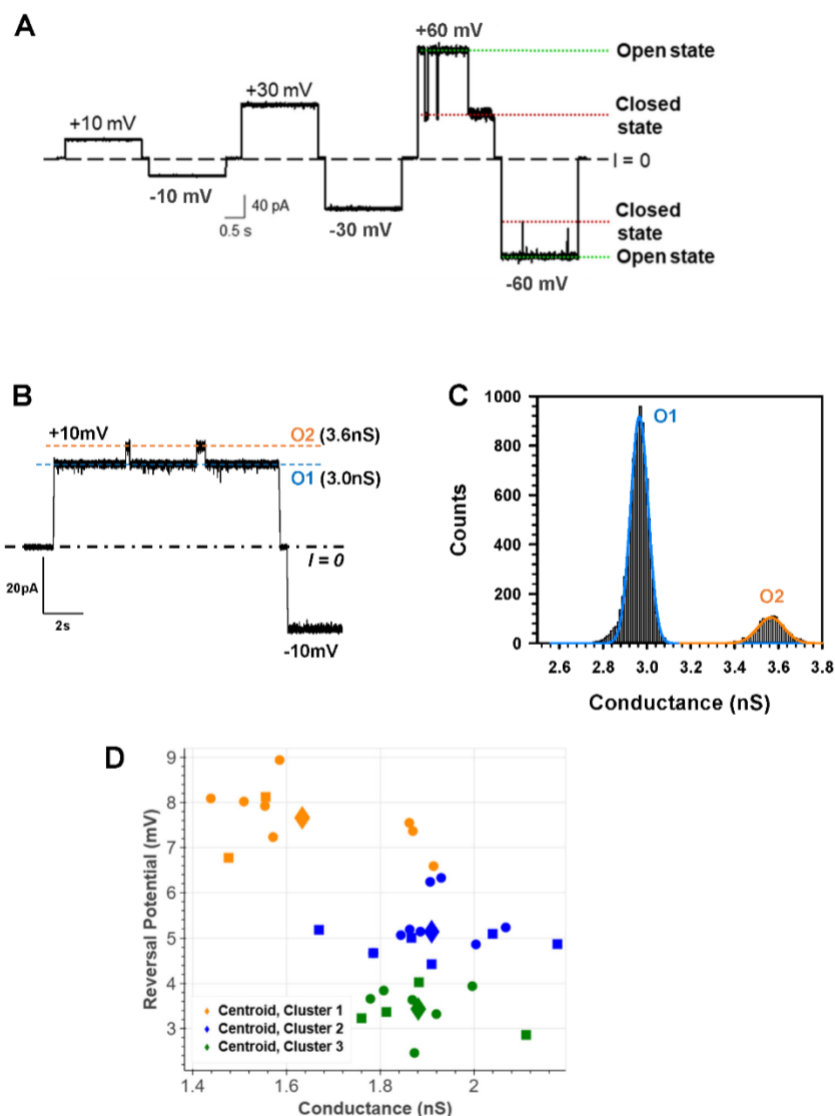


Figure S4.1: Conductance substates in VDAC2 WT are observed at low voltages. (A) A current record of VDAC2 single channel characteristic gating at ± 60 mV. The dashed line represents zero current; dotted lines indicate open (green) and voltage-induced closed state (orange). This record is an example displaying no substates across multiple applied voltages. (B) A representative current record of single VDAC2 at ± 10 mV of applied voltage. Two substates O1 of 3.0 nS and O2 of 3.6 nS are indicated by blue and orange lines, respectively. The current record was digitally filtered at 500 Hz using a low-pass Bessel (8-pole) filter. (C) The conductance histogram corresponding to the current trace in (B) at +10 mV shows two well-separated conductance levels. (D) K-means clustering plot of Conductance vs

Reversal Potential for VDAC2 WT obtained in a 5:1 KCl salt gradient. Each individual measurement is colored to the cluster in which it lies. Each of the three larger diamonds represents the mean of one of the calculated clusters. Planar lipid membranes were formed from 2PG/PC/PE lipid mixture in 1M KCl, pH 7.4.

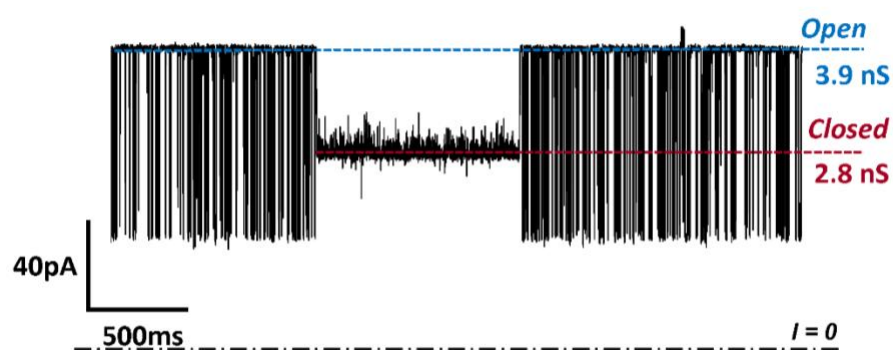


Figure S4.2: The voltage-induced low conducting, closed state of VDAC2 is not blocked by α Syn. The applied voltage was +32.5 mV. 10 nM α Syn on both sides of the membrane. The current record was digitally filtered using a 1 kHz low-pass Bessel (8-poles) filter. The planar membrane was formed from 2PG/PC/PE in 1 M KCl at pH 7.

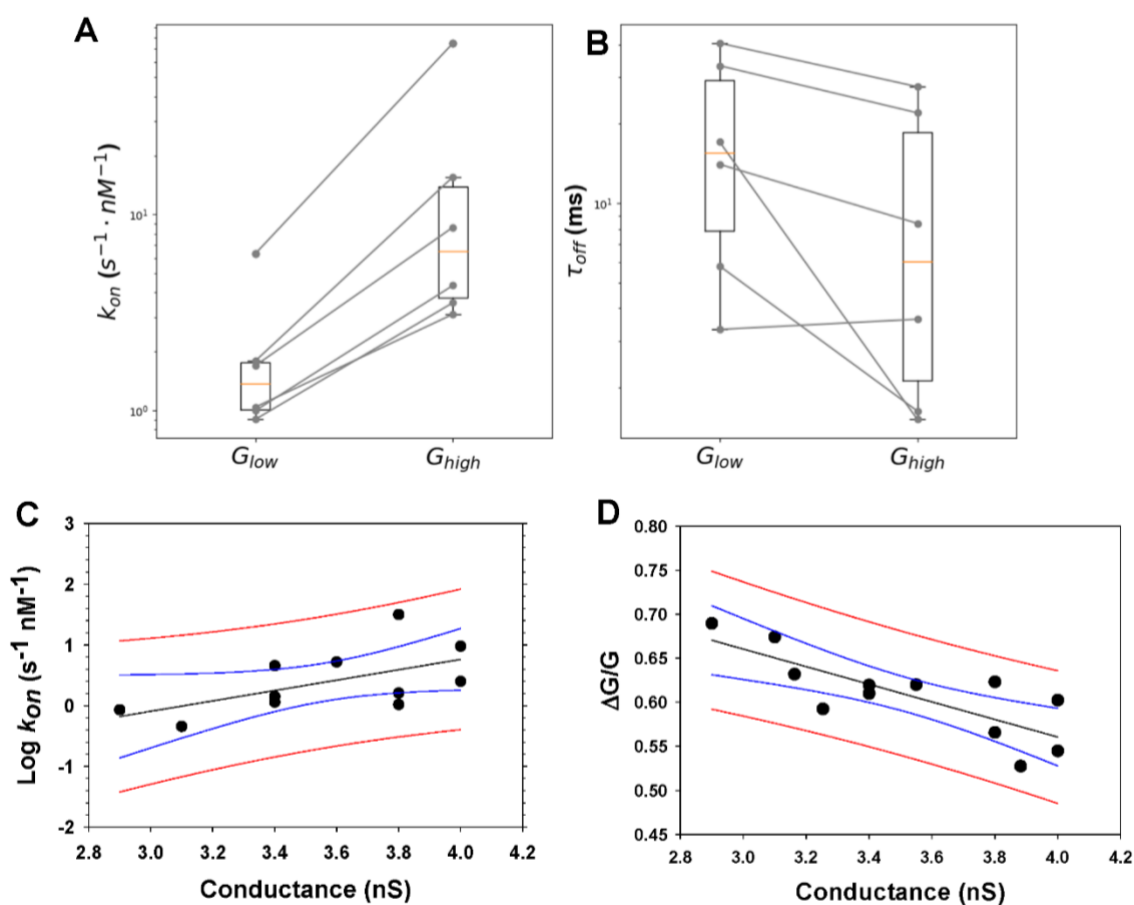


Figure S4.3: Statistical analysis of the kinetic parameters of α Syn interaction with different VDAC2 conductance states. Box and Whisker plot for k_{on} (A) and τ_{off} (B) of higher conducting G_{High} and lower conducting substates G_{Low} observed in independent single-channel experiments with VDAC2 WT. (C, D) Lines represent the statistical analysis of the linear correlation between the on-rate (k_{on}) of α Syn-VDAC2 WT interaction (C) and the conductance of α Syn-blocked state ($\Delta G/G$) (D) with the conductance of different substates (N=12) in 7 individual channels recorded in different a different formed membrane. $\Delta G/G$ is a relative conductance, where ΔG is the difference between open (G) and blocked state conductances for each substate. Black lines are linear regressions with $R^2 = 0.33$ (A) and 0.62 (B). Blue lines represent 95% of the confidence band, and red lines represent 95% of the prediction band. Data are obtained at 32.5 mV. All experimental conditions are as in Fig. S2. Statistical analysis of the substates was performed using the nonparametric paired

Wilcoxon signed rank test, comparing substates observed on the same channel, allowing comparison between data taken at different voltages.

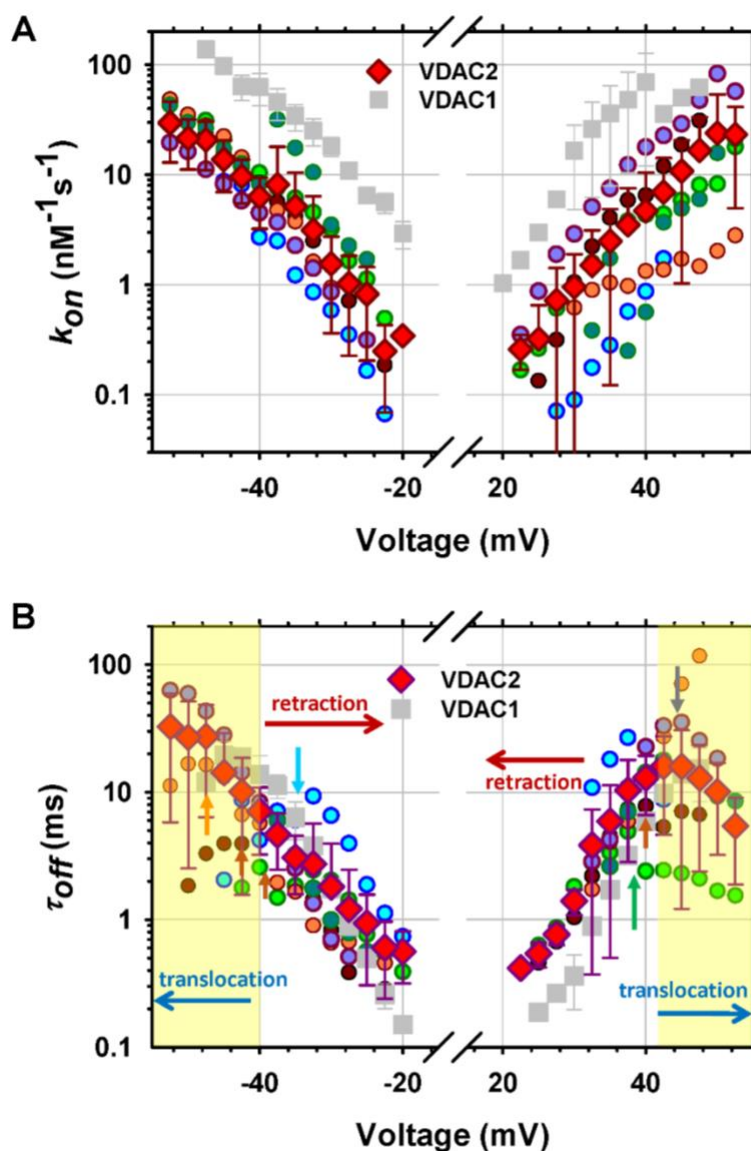


Figure S4.4: Voltage dependences of the kinetic parameters of α Syn-VDAC2 interactions.

Voltage dependences of k_{on} (A) and blockage time, τ_{off} , (B) obtained in 7 individual VDAC2 WT

channels in the presence of 10 nM α Syn in both compartments (circular symbols). Each color of the circular symbol represents a separate experiment. The analyzed conductances vary from 2.9 to 4.1 nS with an average of 3.5 ± 0.4 nS. Red diamond symbols are means \pm SD of 7 experiments. Grey squares are mean data for VDAC1 WT \pm SD (N=4) shown for comparison. (A) - Despite high variability in k_{on} between channels and substates, all k_{on} for VDAC2 WT are below k_{on} values for VDAC1. (B) - The increase of τ_{off} with voltage amplitude corresponds to the α Syn blockage/retraction regime, which is similar for individual VDAC2 channels and for VDAC1. The decrease of τ_{off} corresponds to the translocation regime indicated by yellow highlights. The voltages at which the blockage/retraction regime becomes translocation vary from -32.5 to -52.5 mV at negative polarities and from 37.5 to 45 mV at positive and indicated by arrows. In some experiments, the translocation regime starts at $V > |55|$ mV. Other experimental conditions, as in Fig. S2.

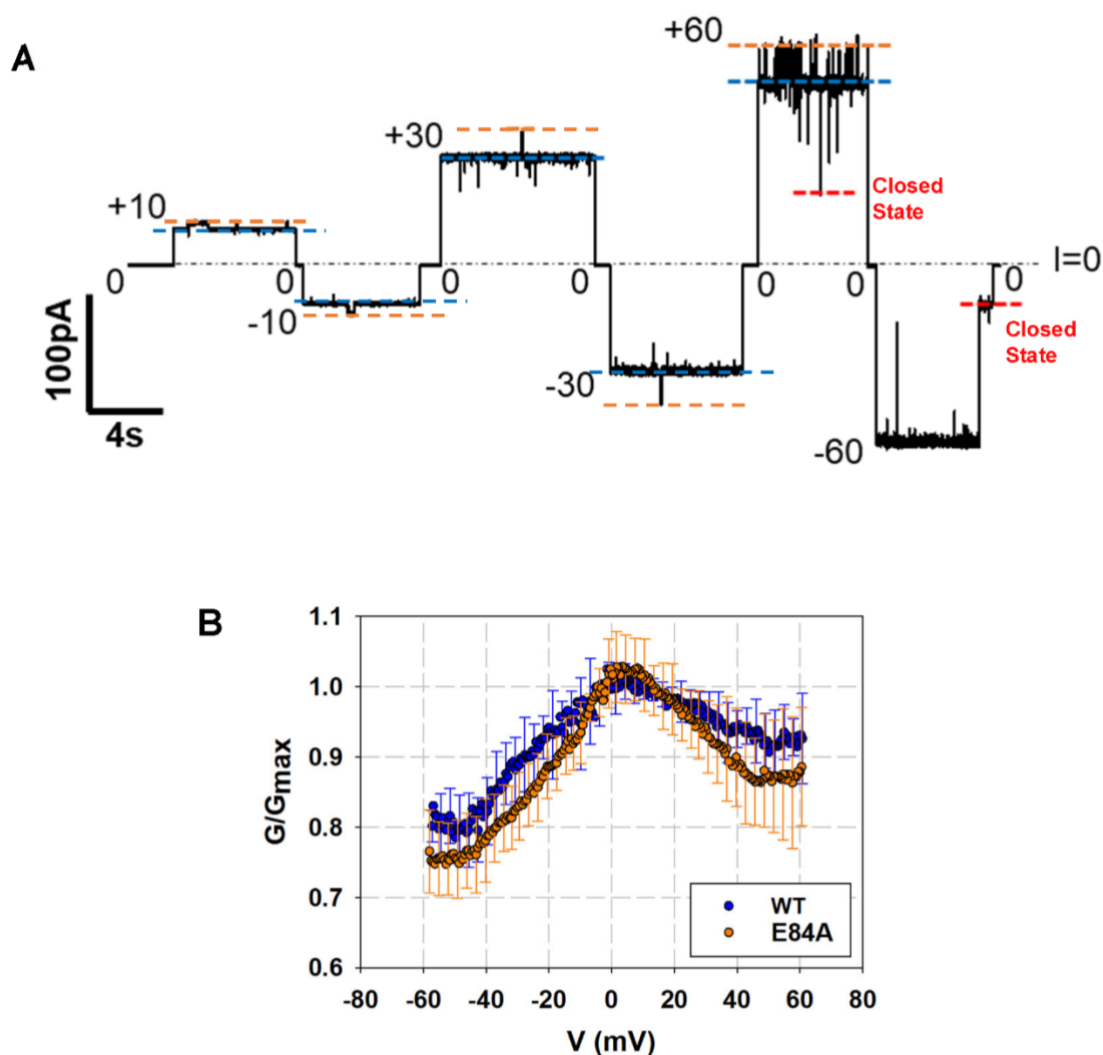


Figure S4.5: VDAC2 E84A mutant forms a functional voltage-gating channel with multistate behavior. (A) -Representative single-channel current traces obtained with reconstituted VDAC2 E84A inserted into 2PG/PC/PE membrane in 1M KCl at pH 7.4 demonstrates one main conducting state of 3 ± 0.1 nS (blue dashed lines) and higher conducting substate of 3.5 ± 0.1 nS (orange dashed lines) at all applied voltages starting from ± 10 mV. The dash-dotted line represents zero current level; dashed lines indicate conductance substates. Channel is characteristically voltage-gated – transition to the lower conducting state of (red dashed line) at -60 mV. The current record was digitally filtered at 500 Hz using a digital low-pass Bessel (8-pole) filter. (B) - Characteristic bell-shaped plots of normalized average conductance as functions of the applied voltage for WT and E84A

VDAC2. G/G_{\max} is the normalized conductance, where G_{\max} is the maximum conductance at voltages closest to 0 mV. Data are means of 3-4 independent experiments \pm S.D.

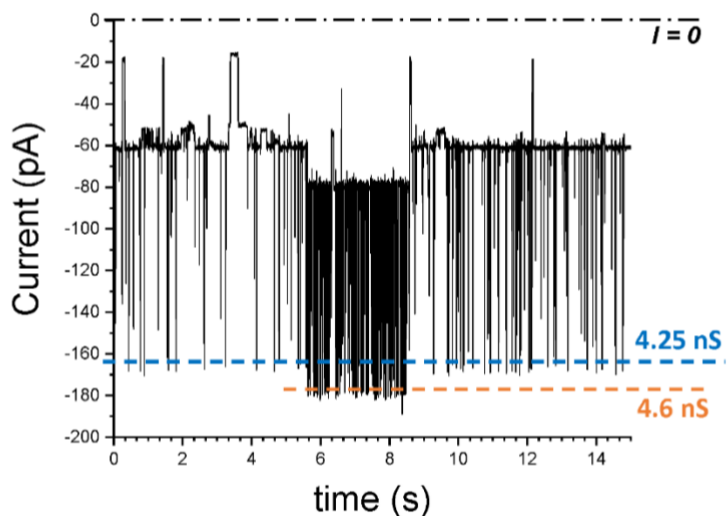


Figure S4.6: Zebrafish VDAC2 (zfVDAC2) has conductance substates that interact differently with α Syn. The representative current record of single zfVDAC2 channel reconstitute to the PLM formed from DPhPC in 1M KCL, 5mM HEPES, pH 7.4 in the presence of 10 nM of α Syn added to both sides of the membrane at -40 mV of applied voltage. Channel conductance transitions between two levels of 4.25 and 4.6 nS. The intensity of blockage events is higher for the higher conductance level. The trace was digitally filtered at 1 kHz.

Works cited

- Aguilella-Arzo, M., & Aguilella, V. M. (2020). Access resistance in protein nanopores. A structure-based computational approach. *Bioelectrochemistry*, *131*.
[https://doi.org/ARTN 107371](https://doi.org/ARTN%20107371)
 10.1016/j.bioelechem.2019.107371
- Aksoyoglu, M. A., Podgornik, R., Bezrukov, S. M., Gurnev, P. A., Muthukumar, M., & Parsegian, V. A. (2016). Size-dependent forced PEG partitioning into channels: VDAC, OmpC, and alpha-hemolysin. *Proc Natl Acad Sci U S A*, *113*(32), 9003-9008. <https://doi.org/10.1073/pnas.1602716113>
- Anflous-Pharayra, K., Lee, N., Armstrong, D. L., & Craigen, W. J. (2011). VDAC3 has differing mitochondrial functions in two types of striated muscles. *Biochim Biophys Acta*, *1807*(1), 150-156. <https://doi.org/10.1016/j.bbabi.2010.09.007>
- Araiso, Y., & Endo, T. (2022). Structural overview of the translocase of the mitochondrial outer membrane complex. *Biophys Physicobiol*, *19*, e190022.
<https://doi.org/10.2142/biophysico.bppb-v19.0022>
- Bay, D. C., Hafez, M., Young, M. J., & Court, D. A. (2012). Phylogenetic and coevolutionary analysis of the beta-barrel protein family comprised of mitochondrial porin (VDAC) and Tom40. *Biochim Biophys Acta*, *1818*(6), 1502-1519. <https://doi.org/10.1016/j.bbame.2011.11.027>
- Bayrhuber, M., Meins, T., Habeck, M., Becker, S., Giller, K., Villinger, S., Vorrhein, C., Griesinger, C., Zweckstetter, M., & Zeth, K. (2008). Structure of the human voltage-dependent anion channel. *Proc Natl Acad Sci U S A*, *105*(40), 15370-15375. <https://doi.org/10.1073/pnas.0808115105>
- Cali, T., Ottolini, D., Negro, A., & Brini, M. (2012). alpha-Synuclein controls mitochondrial calcium homeostasis by enhancing endoplasmic reticulum-mitochondria interactions. *J Biol Chem*, *287*(22), 17914-17929.
<https://doi.org/10.1074/jbc.M111.302794>
- Cheng, E. H., Sheiko, T. V., Fisher, J. K., Craigen, W. J., & Korsmeyer, S. J. (2003). VDAC2 inhibits BAK activation and mitochondrial apoptosis. *Science*, *301*(5632), 513-517. <https://doi.org/10.1126/science.1083995>
- Chin, H. S., Li, M. X., Tan, I. K. L., Ninnis, R. L., Reljic, B., Scieluna, K., Dagley, L. F., Sandow, J. J., Kelly, G. L., Samson, A. L., Chappaz, S., Khaw, S. L., Chang, C., Morokoff, A., Brinkmann, K., Webb, A., Hockings, C., Hall, C. M., Kueh, A. J., . . . Dewson, G. (2018). VDAC2 enables BAX to mediate apoptosis and limit tumor development. *Nat Commun*, *9*(1), 4976. <https://doi.org/10.1038/s41467-018-07309-4>
- Chinta, S. J., Mallajosyula, J. K., Rane, A., & Andersen, J. K. (2010). Mitochondrial alpha-synuclein accumulation impairs complex I function in dopaminergic neurons and results in increased mitophagy in vivo. *Neurosci Lett*, *486*(3), 235-239. <https://doi.org/10.1016/j.neulet.2010.09.061>
- Colombini, M. (1989). Voltage gating in the mitochondrial channel, VDAC. *J Membr Biol*, *111*(2), 103-111. <https://doi.org/10.1007/BF01871775>

- Colombini, M. (2009). The published 3D structure of the VDAC channel: native or not? *Trends Biochem Sci*, 34(8), 382-389. <https://doi.org/10.1016/j.tibs.2009.05.001>
- Dadsena, S., Bockelmann, S., Mina, J. G. M., Hassan, D. G., Korneev, S., Razzera, G., Jahn, H., Niekamp, P., Muller, D., Schneider, M., Tafesse, F. G., Marrink, S. J., Melo, M. N., & Holthuis, J. C. M. (2019). Ceramides bind VDAC2 to trigger mitochondrial apoptosis. *Nat Commun*, 10(1), 1832. <https://doi.org/10.1038/s41467-019-09654-4>
- De Pinto, V. (2021). Renaissance of VDAC: New Insights on a Protein Family at the Interface between Mitochondria and Cytosol. *Biomolecules*, 11(1). <https://doi.org/10.3390/biom11010107>
- De Pinto, V., Reina, S., Gupta, A., Messina, A., & Mahalakshmi, R. (2016). Role of cysteines in mammalian VDAC isoforms' function. *Biochim Biophys Acta*, 1857(8), 1219-1227. <https://doi.org/10.1016/j.bbabi.2016.02.020>
- Devi, L., Raghavendran, V., Prabhu, B. M., Avadhani, N. G., & Anandatheerthavarada, H. K. (2008). Mitochondrial import and accumulation of alpha-synuclein impair complex I in human dopaminergic neuronal cultures and Parkinson disease brain. *J Biol Chem*, 283(14), 9089-9100. <https://doi.org/10.1074/jbc.M710012200>
- Diederichs, K. A., Buchanan, S. K., & Botos, I. (2021). Building Better Barrels - beta-barrel Biogenesis and Insertion in Bacteria and Mitochondria. *J Mol Biol*, 433(16), 166894. <https://doi.org/10.1016/j.jmb.2021.166894>
- Eddy, M. T., Ong, T. C., Clark, L., Tejjido, O., van der Wel, P. C., Garces, R., Wagner, G., Rostovtseva, T. K., & Griffin, R. G. (2012). Lipid dynamics and protein-lipid interactions in 2D crystals formed with the beta-barrel integral membrane protein VDAC1. *J Am Chem Soc*, 134(14), 6375-6387. <https://doi.org/10.1021/ja300347v>
- Eddy, M. T., Yu, T. Y., Wagner, G., & Griffin, R. G. (2019). Structural characterization of the human membrane protein VDAC2 in lipid bilayers by MAS NMR. *J Biomol NMR*, 73(8-9), 451-460. <https://doi.org/10.1007/s10858-019-00242-8>
- Eliezer, D., Kutluay, E., Bussell, R., Jr., & Browne, G. (2001). Conformational properties of alpha-synuclein in its free and lipid-associated states. *J Mol Biol*, 307(4), 1061-1073. <https://doi.org/10.1006/jmbi.2001.4538>
- Elkon, H., Don, J., Melamed, E., Ziv, I., Shirvan, A., & Offen, D. (2002). Mutant and wild-type alpha-synuclein interact with mitochondrial cytochrome C oxidase. *J Mol Neurosci*, 18(3), 229-238. <https://doi.org/10.1385/JMN:18:3:229>
- Fusco, G., De Simone, A., Gopinath, T., Vostrikov, V., Vendruscolo, M., Dobson, C. M., & Veglia, G. (2014). Direct observation of the three regions in alpha-synuclein that determine its membrane-bound behaviour. *Nat Commun*, 5, 3827. <https://doi.org/10.1038/ncomms4827>
- Gattin, Z., Schneider, R., Laukat, Y., Giller, K., Maier, E., Zweckstetter, M., Griesinger, C., Benz, R., Becker, S., & Lange, A. (2015). Solid-state NMR, electrophysiology and molecular dynamics characterization of human VDAC2. *J Biomol NMR*, 61(3-4), 311-320. <https://doi.org/10.1007/s10858-014-9876-5>
- Gershow, M., & Golovchenko, J. A. (2007). Recapturing and trapping single molecules with a solid-state nanopore. *Nat Nanotechnol*, 2(12), 775-779. <https://doi.org/10.1038/nnano.2007.381>

- Goedert, M., Jakes, R., & Spillantini, M. G. (2017). The Synucleinopathies: Twenty Years On. *J Parkinsons Dis*, 7(s1), S51-S69. <https://doi.org/10.3233/JPD-179005>
- Guardiani, C., Magri, A., Karachitos, A., Di Rosa, M. C., Reina, S., Bodrenko, I., Messina, A., Kmita, H., Ceccarelli, M., & De Pinto, V. (2018). yVDAC2, the second mitochondrial porin isoform of *Saccharomyces cerevisiae*. *Biochim Biophys Acta Bioenerg*, 1859(4), 270-279. <https://doi.org/10.1016/j.bbabi.2018.01.008>
- Gurnev, P. A., Rostovtseva, T. K., & Bezrukov, S. M. (2011). Tubulin-blocked state of VDAC studied by polymer and ATP partitioning. *FEBS Lett*, 585(14), 2363-2366. <https://doi.org/10.1016/j.febslet.2011.06.008>
- Gurnev, P. A., Yap, T. L., Pfefferkorn, C. M., Rostovtseva, T. K., Berezhkovskii, A. M., Lee, J. C., Parsegian, V. A., & Bezrukov, S. M. (2014). Alpha-synuclein lipid-dependent membrane binding and translocation through the alpha-hemolysin channel. *Biophys J*, 106(3), 556-565. <https://doi.org/10.1016/j.bpj.2013.12.028>
- Hille, B. (2001). *Ion Channels of Excitable Membranes* (third ed., Vol. third ed.). Sinauer Associates Inc. <Go to ISI>://WOS:A1994PT48400010
- Hiller, S., Abramson, J., Mannella, C., Wagner, G., & Zeth, K. (2010). The 3D structures of VDAC represent a native conformation. *Trends Biochem Sci*, 35(9), 514-521. <https://doi.org/10.1016/j.tibs.2010.03.005>
- Hoogerheide, D. P., Gurnev, P. A., Rostovtseva, T. K., & Bezrukov, S. M. (2018). Real-Time Nanopore-Based Recognition of Protein Translocation Success. *Biophys J*, 114(4), 772-776. <https://doi.org/10.1016/j.bpj.2017.12.019>
- Hoogerheide, D. P., Gurnev, P. A., Rostovtseva, T. K., & Bezrukov, S. M. (2020). Effect of a post-translational modification mimic on protein translocation through a nanopore. *Nanoscale*, 12(20), 11070-11078. <https://doi.org/10.1039/d0nr01577f>
- Hoogerheide, D. P., Gurnev, P. A., Rostovtseva, T. K., & Bezrukov, S. M. (2022). Voltage-activated complexation of alpha-synuclein with three diverse beta-barrel channels: VDAC, MspA, and alpha-hemolysin. *Proteomics*, 22(5-6), e2100060. <https://doi.org/10.1002/pmic.202100060>
- Hoogerheide, D. P., Rostovtseva, T. K., & Bezrukov, S. M. (2021). Exploring lipid-dependent conformations of membrane-bound alpha-synuclein with the VDAC nanopore. *Biochim Biophys Acta Biomembr*, 1863(9), 183643. <https://doi.org/10.1016/j.bbamem.2021.183643>
- Hsu, L. J., Sagara, Y., Arroyo, A., Rockenstein, E., Sisk, A., Mallory, M., Wong, J., Takenouchi, T., Hashimoto, M., & Masliah, E. (2000). alpha-synuclein promotes mitochondrial deficit and oxidative stress. *Am J Pathol*, 157(2), 401-410. [https://doi.org/10.1016/s0002-9440\(10\)64553-1](https://doi.org/10.1016/s0002-9440(10)64553-1)
- Israelson, A., Abu-Hamad, S., Zaid, H., Nahon, E., & Shoshan-Barmatz, V. (2007). Localization of the voltage-dependent anion channel-1 Ca²⁺-binding sites. *Cell Calcium*, 41(3), 235-244. <https://doi.org/10.1016/j.ceca.2006.06.005>
- Jacobs, D., Hoogerheide, D. P., Rovini, A., Jiang, Z., Lee, J. C., Rostovtseva, T. K., & Bezrukov, S. M. (2019). Probing Membrane Association of alpha-Synuclein Domains with VDAC Nanopore Reveals Unexpected Binding Pattern. *Sci Rep*, 9(1), 4580. <https://doi.org/10.1038/s41598-019-40979-8>

- Karachitos, A., Grabinski, W., Baranek, M., & Kmita, H. (2021). Redox-Sensitive VDAC: A Possible Function as an Environmental Stress Sensor Revealed by Bioinformatic Analysis. *Front Physiol*, 12, 750627. <https://doi.org/10.3389/fphys.2021.750627>
- Kim, W. S., Kagedal, K., & Halliday, G. M. (2014). Alpha-synuclein biology in Lewy body diseases. *Alzheimers Res Ther*, 6(5), 73. <https://doi.org/10.1186/s13195-014-0073-2>
- Lazarou, M., Stojanovski, D., Frazier, A. E., Kotevski, A., Dewson, G., Craigen, W. J., Kluck, R. M., Vaux, D. L., & Ryan, M. T. (2010). Inhibition of Bak activation by VDAC2 is dependent on the Bak transmembrane anchor. *J Biol Chem*, 285(47), 36876-36883. <https://doi.org/10.1074/jbc.M110.159301>
- Ludtmann, M. H. R., Angelova, P. R., Horrocks, M. H., Choi, M. L., Rodrigues, M., Baev, A. Y., Berezhnov, A. V., Yao, Z., Little, D., Banushi, B., Al-Menhali, A. S., Ranasinghe, R. T., Whiten, D. R., Yapom, R., Dolt, K. S., Devine, M. J., Gissen, P., Kunath, T., Jaganjac, M., . . . Gandhi, S. (2018). alpha-synuclein oligomers interact with ATP synthase and open the permeability transition pore in Parkinson's disease. *Nat Commun*, 9(1), 2293. <https://doi.org/10.1038/s41467-018-04422-2>
- Magri, A., & Messina, A. (2017). Interactions of VDAC with Proteins Involved in Neurodegenerative Aggregation: An Opportunity for Advancement on Therapeutic Molecules. *Curr Med Chem*, 24(40), 4470-4487. <https://doi.org/10.2174/0929867324666170601073920>
- Maurya, S. R., & Mahalakshmi, R. (2013). Modulation of human mitochondrial voltage-dependent anion channel 2 (hVDAC-2) structural stability by cysteine-assisted barrel-lipid interactions. *J Biol Chem*, 288(35), 25584-25592. <https://doi.org/10.1074/jbc.M113.493692>
- Maurya, S. R., & Mahalakshmi, R. (2014). Influence of protein-micelle ratios and cysteine residues on the kinetic stability and unfolding rates of human mitochondrial VDAC-2. *PLoS One*, 9(1), e87701. <https://doi.org/10.1371/journal.pone.0087701>
- Maurya, S. R., & Mahalakshmi, R. (2015). N-helix and Cysteines Inter-regulate Human Mitochondrial VDAC-2 Function and Biochemistry. *J Biol Chem*, 290(51), 30240-30252. <https://doi.org/10.1074/jbc.M115.693978>
- Maurya, S. R., & Mahalakshmi, R. (2016). VDAC-2: Mitochondrial outer membrane regulator masquerading as a channel? *FEBS J*, 283(10), 1831-1836. <https://doi.org/10.1111/febs.13637>
- Maurya, S. R., & Mahalakshmi, R. (2017). Mitochondrial VDAC2 and cell homeostasis: highlighting hidden structural features and unique functionalities. *Biol Rev Camb Philos Soc*, 92(4), 1843-1858. <https://doi.org/10.1111/brv.12311>
- Menzel, V. A., Cassara, M. C., Benz, R., de Pinto, V., Messina, A., Cunsolo, V., Saletti, R., Hinsch, K. D., & Hinsch, E. (2009). Molecular and functional characterization of VDAC2 purified from mammal spermatozoa. *Biosci Rep*, 29(6), 351-362. <https://doi.org/10.1042/BSR20080123>

- Messina, A., Reina, S., Guarino, F., & De Pinto, V. (2012). VDAC isoforms in mammals. *Biochim Biophys Acta*, *1818*(6), 1466-1476.
<https://doi.org/10.1016/j.bbamem.2011.10.005>
- Mlayeh, L., Chatkaew, S., Leonetti, M., & Homble, F. (2010). Modulation of plant mitochondrial VDAC by phytosterols. *Biophys J*, *99*(7), 2097-2106.
<https://doi.org/10.1016/j.bpj.2010.07.067>
- Mlayeh, L., Krammer, E. M., Leonetti, M., Prevost, M., & Homble, F. (2017). The mitochondrial VDAC of bean seeds recruits phosphatidylethanolamine lipids for its proper functioning. *Biochim Biophys Acta Bioenerg*, *1858*(9), 786-794.
<https://doi.org/10.1016/j.bbabi.2017.06.005>
- Muthukumar, M. (2010). Theory of capture rate in polymer translocation. *J Chem Phys*, *132*(19), 195101. <https://doi.org/10.1063/1.3429882>
- Naghdi, S., Varnai, P., & Hajnoczky, G. (2015). Motifs of VDAC2 required for mitochondrial Bak import and tBid-induced apoptosis. *Proc Natl Acad Sci U S A*, *112*(41), E5590-5599. <https://doi.org/10.1073/pnas.1510574112>
- Nakamura, K., Nemani, V. M., Azarbal, F., Skibinski, G., Levy, J. M., Egami, K., Munishkina, L., Zhang, J., Gardner, B., Wakabayashi, J., Sesaki, H., Cheng, Y., Finkbeiner, S., Nussbaum, R. L., Masliah, E., & Edwards, R. H. (2011). Direct membrane association drives mitochondrial fission by the Parkinson disease-associated protein alpha-synuclein. *J Biol Chem*, *286*(23), 20710-20726.
<https://doi.org/10.1074/jbc.M110.213538>
- Ngo, V. A., Queralt-Martin, M., Khan, F., Bergdoll, L., Abramson, J., Bezrukov, S. M., Rostovtseva, T. K., Hoogerheide, D. P., & Noskov, S. Y. (2022). The Single Residue K12 Governs the Exceptional Voltage Sensitivity of Mitochondrial Voltage-Dependent Anion Channel Gating. *J Am Chem Soc*, *144*(32), 14564-14577. <https://doi.org/10.1021/jacs.2c03316>
- Parres-Gold, J., Chieng, A., Wong Su, S., & Wang, Y. (2020). Real-Time Characterization of Cell Membrane Disruption by alpha-Synuclein Oligomers in Live SH-SY5Y Neuroblastoma Cells. *ACS Chem Neurosci*, *11*(17), 2528-2534.
<https://doi.org/10.1021/acscchemneuro.0c00309>
- Pfefferkorn, C. M., Jiang, Z., & Lee, J. C. (2012). Biophysics of alpha-synuclein membrane interactions. *Biochim Biophys Acta*, *1818*(2), 162-171.
<https://doi.org/10.1016/j.bbamem.2011.07.032>
- Pfefferkorn, C. M., & Lee, J. C. (2010). Tryptophan probes at the alpha-synuclein and membrane interface. *J Phys Chem B*, *114*(13), 4615-4622.
<https://doi.org/10.1021/jp908092e>
- Piehowski, P. D., Zhu, Y., Bramer, L. M., Stratton, K. G., Zhao, R., Orton, D. J., Moore, R. J., Yuan, J., Mitchell, H. D., Gao, Y., Webb-Robertson, B. M., Dey, S. K., Kelly, R. T., & Burnum-Johnson, K. E. (2020). Automated mass spectrometry imaging of over 2000 proteins from tissue sections at 100-mum spatial resolution. *Nat Commun*, *11*(1), 8. <https://doi.org/10.1038/s41467-019-13858-z>
- Pittala, M. G. G., Reina, S., Cucina, A., Cunsolo, V., Guarino, F., Di Francesco, A., Foti, S., De Pinto, V., & Saletti, R. (2024). Intramolecular Disulfide Bridges in Voltage-Dependent Anion Channel 2 (VDAC2) Protein from *Rattus norvegicus* Revealed

- by High-Resolution Mass Spectrometry. *J Am Soc Mass Spectrom*, 35(7), 1422-1433. <https://doi.org/10.1021/jasms.4c00033>
- Queralt-Martin, M., Bergdoll, L., Jacobs, D., Bezrukov, S. M., Abramson, J., & Rostovtseva, T. K. (2019). Assessing the role of residue E73 and lipid headgroup charge in VDAC1 voltage gating. *Biochim Biophys Acta Bioenerg*, 1860(1), 22-29. <https://doi.org/10.1016/j.bbabi.2018.11.001>
- Queralt-Martin, M., Bergdoll, L., Teijido, O., Munshi, N., Jacobs, D., Kuszak, A. J., Protchenko, O., Reina, S., Magri, A., De Pinto, V., Bezrukov, S. M., Abramson, J., & Rostovtseva, T. K. (2020). A lower affinity to cytosolic proteins reveals VDAC3 isoform-specific role in mitochondrial biology. *J Gen Physiol*, 152(2). <https://doi.org/10.1085/jgp.201912501>
- Rahmani, Z., Maunoury, C., & Siddiqui, A. (1998). Isolation of a novel human voltage-dependent anion channel gene. *Eur J Hum Genet*, 6(4), 337-340. <https://doi.org/10.1038/sj.ejhg.5200198>
- Rajendran, M., Queralt-Martin, M., Gurnev, P. A., Rosencrans, W. M., Rovini, A., Jacobs, D., Abrantes, K., Hoogerheide, D. P., Bezrukov, S. M., & Rostovtseva, T. K. (2022). Restricting alpha-synuclein transport into mitochondria by inhibition of alpha-synuclein-VDAC complexation as a potential therapeutic target for Parkinson's disease treatment. *Cell Mol Life Sci*, 79(7), 368. <https://doi.org/10.1007/s00018-022-04389-w>
- Rappaport, S. M., Teijido, O., Hoogerheide, D. P., Rostovtseva, T. K., Berezhkovskii, A. M., & Bezrukov, S. M. (2015). Conductance hysteresis in the voltage-dependent anion channel. *Eur Biophys J*, 44(6), 465-472. <https://doi.org/10.1007/s00249-015-1049-2>
- Reina, S., Nibali, S. C., Tomasello, M. F., Magri, A., Messina, A., & De Pinto, V. (2022). Voltage Dependent Anion Channel 3 (VDAC3) protects mitochondria from oxidative stress. *Redox Biol*, 51, 102264. <https://doi.org/10.1016/j.redox.2022.102264>
- Rister, A. B., Gudermann, T., & Schredelseker, J. (2022). E as in Enigma: The Mysterious Role of the Voltage-Dependent Anion Channel Glutamate E73. *Int J Mol Sci*, 24(1). <https://doi.org/10.3390/ijms24010269>
- Rosencrans, W. M., Aguilera, V. M., Rostovtseva, T. K., & Bezrukov, S. M. (2021). alpha-Synuclein emerges as a potent regulator of VDAC-facilitated calcium transport. *Cell Calcium*, 95, 102355. <https://doi.org/10.1016/j.ceca.2021.102355>
- Rosencrans, W. M., Rajendran, M., Bezrukov, S. M., & Rostovtseva, T. K. (2021). VDAC regulation of mitochondrial calcium flux: From channel biophysics to disease. *Cell Calcium*, 94, 102356. <https://doi.org/10.1016/j.ceca.2021.102356>
- Rostovtseva, T., & Colombini, M. (1996). ATP flux is controlled by a voltage-gated channel from the mitochondrial outer membrane. *J Biol Chem*, 271(45), 28006-28008. <https://doi.org/10.1074/jbc.271.45.28006>
- Rostovtseva, T. K., Gurnev, P. A., Protchenko, O., Hoogerheide, D. P., Yap, T. L., Philpott, C. C., Lee, J. C., & Bezrukov, S. M. (2015). alpha-Synuclein Shows High Affinity Interaction with Voltage-dependent Anion Channel, Suggesting Mechanisms of Mitochondrial Regulation and Toxicity in Parkinson Disease. *J Biol Chem*, 290(30), 18467-18477. <https://doi.org/10.1074/jbc.M115.641746>

- Rostovtseva, T. K., Kazemi, N., Weinrich, M., & Bezrukov, S. M. (2006). Voltage gating of VDAC is regulated by nonlamellar lipids of mitochondrial membranes. *J Biol Chem*, 281(49), 37496-37506. <https://doi.org/10.1074/jbc.M602548200>
- Rostovtseva, T. K., Komarov, A., Bezrukov, S. M., & Colombini, M. (2002). Dynamics of nucleotides in VDAC channels: structure-specific noise generation. *Biophys J*, 82(1 Pt 1), 193-205. [https://doi.org/10.1016/S0006-3495\(02\)75386-1](https://doi.org/10.1016/S0006-3495(02)75386-1)
- Rovini, A., Gurnev, P. A., Beilina, A., Queralt-Martin, M., Rosencrans, W., Cookson, M. R., Bezrukov, S. M., & Rostovtseva, T. K. (2020). Molecular mechanism of olesoxime-mediated neuroprotection through targeting alpha-synuclein interaction with mitochondrial VDAC. *Cell Mol Life Sci*, 77(18), 3611-3626. <https://doi.org/10.1007/s00018-019-03386-w>
- Saccone, C., Caggese, C., D'Erchia, A. M., Lanave, C., Oliva, M., & Pesole, G. (2003). Molecular clock and gene function. *J Mol Evol*, 57 Suppl 1, S277-285. <https://doi.org/10.1007/s00239-003-0037-9>
- Sampson, M. J., Decker, W. K., Beaudet, A. L., Ruitenbeek, W., Armstrong, D., Hicks, M. J., & Craigen, W. J. (2001). Immobile sperm and infertility in mice lacking mitochondrial voltage-dependent anion channel type 3. *J Biol Chem*, 276(42), 39206-39212. <https://doi.org/10.1074/jbc.M104724200>
- Schredelseker, J., Paz, A., Lopez, C. J., Altenbach, C., Leung, C. S., Drexler, M. K., Chen, J. N., Hubbell, W. L., & Abramson, J. (2014). High resolution structure and double electron-electron resonance of the zebrafish voltage-dependent anion channel 2 reveal an oligomeric population. *J Biol Chem*, 289(18), 12566-12577. <https://doi.org/10.1074/jbc.M113.497438>
- Sigworth, F. J., & Sine, S. M. (1987). Data Transformations for Improved Display and Fitting of Single-Channel Dwell Time Histograms. *Biophys. J.*, 52(6), 1047-1054. <Go to ISI>://A1987L184900014
- Song, J., Midson, C., Blachly-Dyson, E., Forte, M., & Colombini, M. (1998a). The sensor regions of VDAC are translocated from within the membrane to the surface during the gating processes. *Biophys J*, 74(6), 2926-2944. [https://doi.org/10.1016/S0006-3495\(98\)78000-2](https://doi.org/10.1016/S0006-3495(98)78000-2)
- Song, J., Midson, C., Blachly-Dyson, E., Forte, M., & Colombini, M. (1998b). The topology of VDAC as probed by biotin modification. *J Biol Chem*, 273(38), 24406-24413. <https://doi.org/10.1074/jbc.273.38.24406>
- Spillantini, M. G., Schmidt, M. L., Lee, V. M., Trojanowski, J. Q., Jakes, R., & Goedert, M. (1997). Alpha-synuclein in Lewy bodies. *Nature*, 388(6645), 839-840. <https://doi.org/10.1038/42166>
- Summers, W. A., Wilkins, J. A., Dwivedi, R. C., Ezzati, P., & Court, D. A. (2012). Mitochondrial dysfunction resulting from the absence of mitochondrial porin in *Neurospora crassa*. *Mitochondrion*, 12(2), 220-229. <https://doi.org/10.1016/j.mito.2011.09.002>
- Tan, W., & Colombini, M. (2007). VDAC closure increases calcium ion flux. *Biochim Biophys Acta*, 1768(10), 2510-2515. <https://doi.org/10.1016/j.bbamem.2007.06.002>
- Teijido, O., Rappaport, S. M., Chamberlin, A., Noskov, S. Y., Aguilera, V. M., Rostovtseva, T. K., & Bezrukov, S. M. (2014). Acidification asymmetrically

- affects voltage-dependent anion channel implicating the involvement of salt bridges [Research Support, N.I.H., Intramural Research Support, Non-U.S. Gov't]. *J Biol Chem*, 289(34), 23670-23682. <https://doi.org/10.1074/jbc.M114.576314>
- Thomas, L., Blachly-Dyson, E., Colombini, M., & Forte, M. (1993). Mapping of residues forming the voltage sensor of the voltage-dependent anion-selective channel. *Proc Natl Acad Sci U S A*, 90(12), 5446-5449. <https://doi.org/10.1073/pnas.90.12.5446>
- Ujwal, R., Cascio, D., Chaptal, V., Ping, P., & Abramson, J. (2009). Crystal packing analysis of murine VDAC1 crystals in a lipidic environment reveals novel insights on oligomerization and orientation. *Channels (Austin)*, 3(3), 167-170. <https://doi.org/10.4161/chan.3.3.9196>
- Ulmer, T. S., & Bax, A. (2005). Comparison of structure and dynamics of micelle-bound human alpha-synuclein and Parkinson disease variants. *J Biol Chem*, 280(52), 43179-43187. <https://doi.org/10.1074/jbc.M507624200>
- Ulmer, T. S., Bax, A., Cole, N. B., & Nussbaum, R. L. (2005). Structure and dynamics of micelle-bound human alpha-synuclein. *J Biol Chem*, 280(10), 9595-9603. <https://doi.org/10.1074/jbc.M411805200>
- Villinger, S., Briones, R., Giller, K., Zachariae, U., Lange, A., de Groot, B. L., Griesinger, C., Becker, S., & Zweckstetter, M. (2010). Functional dynamics in the voltage-dependent anion channel. *Proc Natl Acad Sci U S A*, 107(52), 22546-22551. <https://doi.org/10.1073/pnas.1012310108>
- Vodyanoy, I., & Bezrukov, S. M. (1992). Sizing of an ion pore by access resistance measurements. *Biophys J*, 62(1), 10-11. [https://doi.org/10.1016/S0006-3495\(92\)81762-9](https://doi.org/10.1016/S0006-3495(92)81762-9)
- Wanunu, M., Morrison, W., Rabin, Y., Grosberg, A. Y., & Meller, A. (2010). Electrostatic focusing of unlabelled DNA into nanoscale pores using a salt gradient. *Nat Nanotechnol*, 5(2), 160-165. <https://doi.org/10.1038/nnano.2009.379>
- Weinrich, M., Worcester, D. L., & Bezrukov, S. M. (2017). Lipid nanodomains change ion channel function. *Nanoscale*, 9(35), 13291-13297. <https://doi.org/10.1039/c7nr03926c>
- Xu, X., Decker, W., Sampson, M. J., Craigen, W. J., & Colombini, M. (1999). Mouse VDAC isoforms expressed in yeast: channel properties and their roles in mitochondrial outer membrane permeability. *J Membr Biol*, 170(2), 89-102. <https://doi.org/10.1007/s002329900540>
- Zachariae, U., Schneider, R., Briones, R., Gattin, Z., Demers, J. P., Giller, K., Maier, E., Zweckstetter, M., Griesinger, C., Becker, S., Benz, R., de Groot, B. L., & Lange, A. (2012). beta-Barrel mobility underlies closure of the voltage-dependent anion channel. *Structure*, 20(9), 1540-1549. <https://doi.org/10.1016/j.str.2012.06.015>

VDAC ISOFORMS PLAY DISTINCT ROLES IN MODULATING METABOLISM AND MAINTAINING MITOCHONDRIAL FUNCTION

The following chapter is adapted from Rajendran and Rosencrans et al 2025 to adhere to Caltech's thesis guidelines

Megha Rajendran*, William M. Rosencrans*, Wendy Fitzgerald, Diana Huynh, Bethel G. Beyene, Baiyi Quan, Julie Hwang, Nina A. Bautista, Tsui-Fen Chou, Sergey M. Bezrukov, Tatiana K. Rostovtseva. bioRxiv 2025.02.20.639106; doi: <https://doi.org/10.1101/2025.02.20.639106>

*Denotes equal contribution

5.1 Abstract

The Voltage Dependent Anion Channel (VDAC) is the most ubiquitous protein on the mitochondrial outer membrane that facilitates the flux of water-soluble metabolites and ions. VDAC has been implicated in several cellular processes, such as apoptosis, calcium signaling, and lipid metabolism. There are three VDAC isoforms in mammalian cells, VDAC 1, 2, and 3, with varying tissue-specific expression profiles. The isoforms conduct metabolites and ions with similar efficiency. However, isoform knockouts (KOs) in mice lead to distinct phenotypes. To understand the functional role of each VDAC isoform, we created CRISPR-Cas9 KOs of each isoform in HeLa cells to compare their metabolic activity and proteomics. We found that each isoform KO alters the proteome and respiration differently, with VDAC3 KO downregulating the electron transport chain (ETC) subunits while increasing glutamine metabolism. In contrast, VDAC2 KO did not affect respiration but upregulated ETC components. VDAC1 KO reduced glycolytic activity. These results reveal non-redundant roles of VDAC isoforms in cancer cell metabolic adaptability.

5.2 Introduction

Voltage-dependent anion channel (VDAC), an outer mitochondrial membrane (MOM) protein, is crucial for the exchange of small ions such as calcium and water-soluble metabolites such as ATP, ADP, and NADH between cytosol and mitochondria. VDAC, a monomeric weakly anion-selective β -barrel channel, not only conducts but also effectively regulates their fluxes across MOM. *In vitro* studies with VDAC reconstituted into the planar lipid membranes showed that one of the mechanisms of such regulation is VDAC's characteristic and evolutionarily conserved voltage-dependent gating when under applied voltage, the channel moves from high-conducting unique "open state" passable for ATP, to low-conducting so-called "closed states" that are impermeable to ATP (Rostovtseva & Colombini, 1996) but more permeable for calcium (Tan & Colombini, 2007). Recent studies *in vitro* have revealed that metabolite and calcium fluxes through VDAC can also be regulated by VDAC complexation with various cytosolic proteins such as dimeric tubulin and α -synuclein (Gurnev et al., 2011; Rostovtseva et al., 2015; Rostovtseva et al., 2008). Furthermore, VDAC is known to be involved in the regulation of calcium signaling through the formation of complexes with calcium transporters on the endoplasmic reticulum (ER) (Lock & Parker, 2020), sarcoplasmic reticulum (SR) (Min et al., 2012; Subedi et al., 2011), and lysosomes (Peng et al., 2020). In addition, VDAC is implicated in apoptosis through its interaction with several pro-and anti-apoptotic proteins (Arbel et al., 2012; Huang et al., 2013; Huang et al., 2014; Liu et al., 2015; Shimizu et al., 2000; Shimizu et al., 2001; Vander Heiden et al., 2001). This highlights the intricate role of VDAC in regulating metabolism, calcium signaling, and cell death, which is further complicated by the isoform-specific differences in VDAC interactome and function.

There are three VDAC isoforms in mammals: VDAC1, 2, and 3. VDAC1 and 2 diverged from VDAC3, which is considered the oldest isoform (Saccone et al., 2003; Young et al., 2007). All three isoforms show high sequence similarity (~ 70%) and form similar anion-selective voltage-gating channels *in vitro* based on single-channel electrophysiology experiments (Queralt-Martin et al., 2020; Xu et al., 1999). However, mice knockout (KO) studies suggest distinct roles for each VDAC isoform, with VDAC2 KO resulting in development delays and embryonic lethality (Cheng et al., 2003; Chin et al., 2018). VDAC1

KO mice exhibit mild bioenergetic defects (Weeber et al., 2002) and VDAC3 KO results in male infertility (Sampson et al., 2001). The latter was attributed to each isoform's tissue-specific role and expression level since VDAC3 is the highest expressed isoform in testis. However, VDAC3 KO also results in mitochondrial dysfunction in heart muscles, where it is the least expressed isoform. VDAC1 and 3 demonstrate different affinities for interaction with two identified VDAC cytosolic regulators - tubulin and α -synuclein (Queralt-Martin et al., 2020). Dimeric α/β -tubulin is the building block of microtubules, and α -synuclein is a neuronal protein implicated in Parkinson's disease (PD). These two abundant cytosolic proteins have no structural, functional, or genetic similarity but possess a common feature—disordered and negatively charged C-terminal tails that act as effective VDAC blocking domains by being reversibly captured by the VDAC pore and reversing its selectivity to cationic by a similar mechanism (Rostovtseva et al., 2021). VDAC1 binds tubulin and α -synuclein with a 10-100 times higher affinity than VDAC3 (Queralt-Martin et al., 2020). In addition, reconstituted VDAC isoforms differ in calcium selectivity, with VDAC3 having a higher calcium preference than VDAC1 (Rosencrans, Aguilera, et al., 2021). De Stefani et al. showed similar results in cells with VDAC3 overexpression, resulting in increased mitochondrial calcium uptake, while VDAC1 may play a role in apoptotic calcium signaling (De Stefani et al., 2012). VDAC2 has recently emerged as an important regulator of mitochondrial calcium uptake, especially in cardiomyocytes (Rosenberg, 2022; Rosencrans, Rajendran, et al., 2021). Interestingly, although both VDAC1 and VDAC2 are implicated in apoptosis, each of them interacts with a different set of Bcl-2 family proteins: VDAC1 preferably interacts with anti-apoptotic Bcl2, Bcl-xL (Huang et al., 2013; Shimizu et al., 1999), and VDAC2 with pro-apoptotic Bak and Bax proteins (Cheng et al., 2003; Chin et al., 2018; van Delft et al., 2019).

VDAC1 and 2 are the most abundant isoforms in most human tissues, and VDAC1 is the only one whose crystal structure has been solved (Bayrhuber et al., 2008; Hiller et al., 2008; Ujwal et al., 2009). Therefore, rather naturally, VDAC1 isoform is the most studied *in vitro* and *in vivo*, followed by VDAC2. VDAC3 isoform, in contrast, is the least expressed *in vivo* (except for testis) and the least biophysically and biochemically studied *in vitro* isoform.

Despite the initial publication by Colombini's and Craigen's labs in 1999 (Xu et al., 1999), where VDAC3's ability to form typical voltage-gated ion channels has been demonstrated, the following publications often reported that VDAC3 does not form voltage-gated channels (Checchetto et al., 2014) or even that it cannot form channels at all (Sampson et al., 1997). Only recently, the record was straightened out in Queralt-Martin et al. work (Queralt-Martin et al., 2020), where it was unambiguously demonstrated that reconstituted VDAC3, similar to VDAC1 and 2, forms typical anion-selective voltage-gated channels. One of the differences between isoforms is the number of cysteines, with VDAC2 and VDAC3 having seven and nine cysteines, respectively, and VDAC1 having only two cysteines (Maurya & Mahalakshmi, 2017; Messina et al., 2012). Such a drastic difference focused the studies of VDAC3 on its role in oxidative stress (Reina et al., 2022), where it was shown that VDAC3 KO in HAP1 cells promoted the accumulation of free radicals dependent on the cysteines, thus suggesting a role for VDAC3 cysteines in countering ROS-induced oxidative stress.

Early studies using mice knockout models demonstrated VDAC isoform-specific differences in mitochondrial functions. VDAC1 KO resulted in a universal decrease in the activity of electron transport chain (ETC) complexes, but VDAC3 KO specifically affected mitochondrial function in the heart and sperm (Anflous-Pharayra et al., 2011). VDAC1 KO in MEF cells showed decreased respiration and glycolytic capacity (Brahimi-Horn et al., 2015). However, until recently, VDAC was mostly ignored in mitochondrial bioenergetics studies as it was historically considered a "molecular sieve" in MOM, except for the studies focused on VDAC1's role in MOM permeabilization at the earlier stages of apoptosis (Baines et al., 2007; McCommis & Baines, 2012) and its tentative involvement in the mitochondrial Permeability Transition Pore (PTP) (Crompton, 1999; Vyssokikh & Brdiczka, 2004). Recently, Magri et al. showed that VDAC1 KO diminished complex I-linked respiration in HAP1 cells due to decreased respiratory reserves (Magri et al., 2023). However, Yang et al. reported no change in respiration but showed increased glycolysis due to VDAC1 KO in H9c2 cells (Yang et al., 2020). Beyond the mentioned discrepancies, a comprehensive systematic study comparing the role of each VDAC isoform in mitochondrial respiration and metabolism in the same cell type is lacking.

To understand the mechanism of differences in isoform function in metabolism, we systematically investigated the role of each VDAC isoform knockout using CRISPR-Cas9 mediated gene editing in HeLa cells. We found that VDAC1 KO affected glycolysis, while VDAC2 KO did not measurably affect glycolysis or mitochondrial respiration. Surprisingly, it was VDAC3 KO that decreased mitochondrial respiration. Proteomic studies revealed increased expression of mitochondrial proteins upon VDAC2 KO in contrast to extensive downregulation of mitochondrial proteins in VDAC3 KO cells. Overexpression of glutaminases in VDAC3 KO cells, necessary for mitochondrial glutamine metabolism, results in a dependence of these cells on glutamine. We demonstrate that VDAC3, the least expressed isoform, is crucial for mitochondrial function to fuel high-energy demand. Overall, the data reveals non-redundant roles of VDAC isoforms in cancer cell metabolic adaptability.

5.3 Results

Characterization of HeLa VDAC isoform knockout cells.

Functional Knockouts (KOs) of each VDAC isoform were generated using CRISPR-Cas9 in HeLa cells. The indels were confirmed by sequencing (Supplementary Figure S5.1), and the KO was confirmed by western blot (Supplementary Figure S5.2A). HeLa cells were chosen as they express characteristic levels of VDAC isoforms found in most human cell types. Although different proteins may respond differently to mass spectrometry (MS) quantitation, considering the sequence similarity amongst the VDAC isoforms, we postulated that the relative abundances for VDAC isoforms are proportional to their copy numbers. Through MS observation, VDAC1 is the most expressed isoform (~50%), followed by VDAC2 (~30%), and VDAC3 (~18%) is the least expressed isoform in HeLa cells (Supplementary Figure S5.2B). The metabolic activity for all VDAC KO clones was investigated by measuring NADH (Supplementary Figure S3A), FAD (Supplementary Figure S5.3B) fluorescence using flow cytometry, and ATP production rates (Supplementary Figure S5.4) using Seahorse XF Pro Analyzer. While VDAC2 KO clones do not affect NADH and FAD levels, VDAC1 and VDAC3 KO showed some variability. VDAC1 KO consistently decreased glycolytic ATP production, but mitochondrial ATP production rate was variable (Supplementary Figure S5.4A).

VDAC3 KO results in different glycolytic and mitochondrial ATP production rates (Supplementary Figure S5.4C). Such variability between clones is intriguing and suggests a compensatory mechanism. We chose to focus on the representative clones with altered mitochondrial function VDAC1 (G8), VDAC2 (C9), and VDAC3 (E5) to understand the isoform-specific role of this mitochondrial outer membrane (MOM) protein in metabolism in HeLa cells.

Conventional thinking would assume that the overexpression of other VDAC isoforms might compensate for the loss of one isoform. Using the MS results, the expression level of each VDAC isoform in each of the KOs could be directly compared. We found only mild changes in VDAC isoform expression in response to specific KO. VDAC1 KO cells show a ~20% decrease in VDAC2 expression, and VDAC2 KO increases VDAC3 expression (~40%), but these changes do not compensate for the KO of each isoform (Figure 5.1A). The KO cells do not show appreciable difference in cell morphology (Supplementary Figure S5A), but VDAC2 and VDAC3 KOs decrease the growth rate of HeLa cells by 30-40% in 72 hours (Supplementary Figure S5.5 B and C). Cell proliferation was also measured using the CellTiter 96® AQueous One Solution Cell Proliferation Assay. The assay contains an MTS tetrazolium compound that is reduced by NADPH or NADH in metabolically active cells into a colored formazan product with absorbance at 490 nm. While this assay is widely used to measure the number of viable cells, the absorbance depends on the metabolic activity of cells. Interestingly, only VDAC3 KO significantly decreases the absorbance (~40-55%) (Figure 5.1B), which suggests that VDAC3 KO specifically affects the metabolic activity in HeLa cells.

To decipher the role of each VDAC isoform in metabolism, we compared the metabolic activity using a Seahorse XF analyzer.

VDAC1 KO affects basal glycolysis in HeLa cells.

To examine the role of each isoform in glycolysis, we performed a glycolysis stress test, which measures the changes in Extracellular Acidification Rate (ECAR) due to increased

glycolytic activity in cells. Figure 5.2A shows the ECAR trace in WT and KO cells upon the addition of glucose, oligomycin, and 2-deoxyglucose (2-DG). Basal glycolysis is calculated by subtracting non-glycolytic acidification after adding 2-DG (red box) from the increase in ECAR upon adding glucose (blue box). Only VDAC1 KO decreases basal glycolysis (Figure 5.2B). Surprisingly, VDAC3 KO resulted in the complete loss of glycolytic capacity in HeLa cells, even though basal glycolysis was unaffected (Figure 5.2C). Glycolytic capacity (Figure 5.2A green box) measures the ability of cells to increase glycolysis upon the inhibition of OXPHOS with oligomycin, which may be linked to mitochondrial dysfunction in VDAC3 KO cells.

VDAC3 KO decreases mitochondrial respiration in HeLa cells.

The mitochondrial stress test was performed to determine the effect of VDAC isoform KOs on mitochondrial respiration. The Oxygen Consumption Rate (OCR) was measured under basal conditions and after adding oligomycin, FCCP, and rotenone/antimycin-A (Figure 5.3A). VDAC1 KO and VDAC2 KO showed no significant change in respiration compared to WT HeLa WT cells (Figure 5.3B). However, VDAC3 KO significantly decreased basal and maximal respiration (Figure 5.3B). Interestingly, VDAC3 KO results in a complete loss of spare respiratory capacity (SRC) (Figure 5.3C), which suggests that HeLa cells with VDAC3 KO are unable to meet increased energy demand during acute cellular stress. SRC depends on the availability of mitochondrial substrates, suggesting a role for VDAC3, the least expressed isoform, in the uptake of mitochondrial substrates in HeLa cells.

VDAC shows isoform-specific changes in cellular proteome.

To understand the molecular basis of these striking phenotypes of VDAC isoforms KOs at the level of protein expression, label-free proteomics was performed on each of the KO cell lines. Using liquid chromatography coupled with tandem MS, we identified and quantified over 9,500 unique proteins across all four cell lines: WT, VDAC1 KO, VDAC2 KO, and VDAC3 KO.

Most proteins (9,168) were identified in all studied cell lines, enabling direct comparison without the need for excessive imputation (Figure 5.4A). Expression data were subjected to a median normalization (Jones et al., 2023). The principal component analysis (PCA) demonstrated tight clustering of each of the sample replicates within each cell type compared to different genetic backgrounds (Figure 5.4B). Each cell line is separated into distinct regions of the principal component plot of the PC1/PC2 plot, with the WT cells remaining directly between each VDAC KO. These data indicate that each VDAC isoform KO generally leads to a unique change in the cellular proteome.

To determine the proteins that were most altered in each KO compared to the WT, differential protein expression analysis was performed. Focusing on those proteins with the most significant and largest magnitude of change between the different KOs, we observed alteration in several proteins hitherto not connected to VDAC in the existing literature. In the VDAC1 KO cells, the highest magnitude loss was of the transcription factor LZTS3 (Figure 5.4C). Among the most expressed proteins upon VDAC1 KO was the fatty-acid transporter CD36. In the VDAC2 KO cells, the highest magnitude loss was in the protein PLA2G6, a phospholipase, a gene for which loss of function results in a series of infantile neurodevelopmental disorders and Parkinson's disease. PLA2G6 mutations are known to cause mitochondrial deficits, putatively from alterations in lipid homeostasis (Kinghorn et al., 2015). We also observed the loss of the metallo-reductase STEAP4, which is associated with mitochondrial dysfunction (Xue et al., 2017). VDAC2 KO led to overexpression of the apoptosis and inflammasome-related protein PYCARD and the upregulation of the E3 ubiquitin ligase FBOX2 protein. Notably, VDAC2 KO led to a downregulation of Bak. VDAC2 is known to be essential for the import of the pro-apoptotic Bak into the MOM (Cheng et al., 2003). The downregulation of Bak may indicate a response to the reduced mitochondrial import of Bak in the absence of VDAC2. Naghdi et al also showed the importance of VDAC2 in the mitochondrial recruitment of Bak in HepG2 cells and hepatocytes (Naghdi et al., 2025). Interestingly, autophagy receptor p62 was downregulated in HeLa cells with VDAC3 KO. The western blot further confirmed that VDAC3 KO decreases p62 expression (Supplementary Figure S5.6). This result suggests either an

alteration to autophagy pathways or oxidative stress pathways via KEAP1-Nrf2 due to the loss of VDAC3 (Sun et al., 2016). VDAC3 KO resulted in the loss of cell death and mitochondrial-related protein CASP9, as well as the metabolic protein PDK4. In VDAC3 KO, we observed upregulation of the spermatogenesis protein SPOCK1, consistent with VDAC3's unique role in this developmental process (Sampson et al., 2001). These data indicate that the majority of pathways altered by each VDAC KO are unique.

To investigate the pathways uniquely perturbed by each isoform, we performed unbiased gene ontology analysis of VDAC KO proteomics data to identify groups of pathways both conserved and altered uniquely by different isoform KOs (Figure 5.4D). Among pathways downregulated in all VDAC isoform KOs, the loss of glycolysis and gluconeogenesis-related proteins was observed. Proteins associated with these terms include hexokinase 1 (HK1) (Figure 5.4E). Two HK isoforms, HK1 and HK2, are suggested to regulate glycolysis through their interaction with mitochondria. We imaged the colocalization of HK1-GFP (Figure 5.5A) and HK2-GFP (Supplementary Figure S5.7A) with mitochondria labeled with Omp25-mCherry in HeLa WT and KO cells. Though all VDAC isoform KOs downregulate the expression level of HK1, only VDAC1 KO significantly decreases the localization of HK1 (Figure 5.5B) and HK2 (Supplementary Figure S7B) to the mitochondria. Other lowered proteins in the glycolytic pathway included aldolases A and C, transaldolase, and GAPDH. We also observed a downregulation in proteins related to exocytosis in all KO cells (Figure 5.4D). Of pathways altered uniquely in each isoform, VDAC1 KO showed a reduction in proteasome regulation and ER protein trafficking. VDAC2 KO resulted in a minor downregulation of proteins related to the actin cytoskeleton, which is upregulated in the VDAC3 KO cells compared to WT, along with focal adhesion (Figure 5.4D). VDAC3 KO cells show the strongest effects on mitochondrially annotated proteins with significant losses of proteins involved in the ETC and oxidative respiration. Following these links to the modulation of mitochondrial pathways, we focused on the alterations to the mitoproteome.

VDAC isoform KOs rewire the mitoproteome.

To focus on the mitoproteome, we segmented those proteins annotated as mitochondrial in the Mitocarta3 database. All VDAC isoform KOs showed some alteration to mitochondrial proteins, with 26 proteins found downregulated in all VDAC KOs (Figure 5.6A). VDAC3 KO cells have 116 unique downregulated mitochondrial proteins, consistent with the GO term analysis. In contrast, VDAC3 KO cells had the least number of unique mitochondrial proteins upregulated at 32, compared to VDAC1 with 84 and VDAC2 with 96. Only 14 proteins were found upregulated across all VDAC KOs. These data support the notion that VDAC3 KO shows severe loss of mitochondrial proteins, whereas VDAC1 and VDAC2 KO appear to show milder alterations in mitochondrial proteins. The STRING analysis of mitochondrial proteins uniquely altered in each VDAC KO shows that VDAC3 KO cells have a large, downregulated cluster of proteins involved in the ETC (Figure 6B, red box), as described in the GO Term analysis. In contrast, VDAC2 KO cells show an upregulation of a cluster of ETC-related proteins. These results show that VDAC1 KO causes the least defined alteration to the mitochondrial proteome in HeLa cells despite VDAC1 being one of the most ubiquitous mitochondrial proteins.

VDAC3 KO leads to defects in the ETC.

Figure 5.7A shows that VDAC3 KO causes a substantial loss in expression across most ETC components, whereas VDAC2 KO shows mostly upregulation in the mass-spectrometry results. In contrast, VDAC1 KO cells demonstrate the least perturbation in the ETC proteome. The proteomic results are further validated by a select number of these hits by western blot (Figure 5.7B, C). The proteins in complex I (NDUFA9), complex IV (MT-CO1), and complex V (ATP5A) are found to be consistently downregulated in the VDAC3 KO cells. In contrast, VDAC2 KO showed significant upregulation of ATP5A but downregulation of NDUFA9 and MT-CO1. In addition, the VDAC3 KO causes a slight, but not significant, defect in the expression of TCA enzyme citrate synthase, whereas VDAC2 KO upregulated citrate synthase. The western blots show similar expression trends. VDAC3 KO causes the most severe defects, consistent with decreased mitochondrial respiration (Figure 5.3).

VDAC3 KO leads to an increased dependence on glutamine metabolism.

The STRING analysis of the mitochondrial proteome (Figure 5.6B) across VDAC KO lines shows an upregulation of glutamine pathway proteins in VDAC3 KO cells and a downregulation in VDAC2 KO (Figure 6B, blue box). To get insight into these surprising results, we investigated the expression of other proteins in the glutamine metabolic pathway across the VDAC KO cells.

We found that VDAC3 KO upregulates glutaminases (GLS1/2) and GLUD1/GPT2 (Figure 5.8A). GLS1 is a key mitochondrial enzyme that converts glutamine into glutamate, which GLUD1/GPT2 then converts into α -ketoglutarate to feed the TCA cycle. Western blotting further confirms the upregulation of GLS1 in VDAC3 KO cells (Figure 5.8B). These data indicate that VDAC3 KO cells rewire the metabolic program pathways, increasing reliance on glutamine for mitochondrial respiration. Notably, the upregulation of glutaminase is a hallmark of certain cancers, such as ovarian, breast, and colorectal cancer, resulting in their dependence on glutamine (Cluntun et al., 2017). Targeting glutaminase in these cancers has been a popular target of therapeutic intervention (Jin et al., 2023). To determine whether these alterations have functional effects on the metabolic state of the VDAC KO cells, we performed a mitochondrial fuel flex test using a Seahorse XF analyzer to determine their dependencies on glucose, glutamine, and fatty acid to fuel mitochondrial respiration. In this assay, a series of metabolic inhibitors is used to separate the contribution of each fuel source to respiration. UK5099 blocks the mitochondrial pyruvate carrier (MPC) to inhibit the glucose oxidation pathway; etomoxir inhibits carnitine palmitoyltransferase 1A (CPT1A), which transports long chain fatty acid into mitochondria inhibiting long chain fatty acid oxidation pathway; and BPTES inhibits GLS1, which converts glutamine to glutamate inhibiting glutamine oxidation pathway (Figure 5.8C). The relative fuel dependence can be estimated by measuring the oxygen consumption rate in the presence or absence of the fuel pathway inhibitors. WT HeLa cells have equal dependence on glucose and glutamine with a small contribution from fatty acid oxidation (Figure 5.8D). We found that VDAC3 KO has a significantly increased (~30%) dependence on glutamine metabolism, demonstrating that the overexpression of GLS and other glutamine pathway proteins leads to a functional change in metabolic phenotype (Figure 5.8D). There is also an increased dependence on fatty acid

metabolism in the VDAC3 KO cells. VDAC1 KO cells show a 37% decrease in glucose dependence compared to WT, while VDAC2 KO cells show no significant changes in fuel oxidation compared to the WT cells (Figure 5.8D).

5.4 Discussion

We characterized stable KOs of the three VDAC isoforms in HeLa cells. Knocking out both alleles of each VDAC isoform in an identical cellular background enabled us to compare isoform-specific effects across a battery of different assays.

VDAC1 KO decreased basal glycolysis and decreased mitochondria-bound HK1 and HK2. This is consistent with mice KO studies where VDAC1 KO impaired glucose tolerance and reduced mitochondria-bound HK activity (Anflous-Pharayra et al., 2007). VDAC1 KO in H9C2 cells also decreased HKII bound to mitochondria even though it did not affect basal glycolysis (Yang et al., 2020). The different effects on glycolysis could be due to increased glycolysis in HeLa cells compared to H9C2 cells, which prefer oxidative phosphorylation similar to primary cardiomyocytes (Kuznetsov et al., 2015). HeLa cells also express a 10-fold increase in HKII compared to HEK-293 cells (Woldetsadik et al., 2017), which has been implicated in the increased glycolysis (Warburg effect) characteristic of cancer cells. In our experiment, VDAC1 KO did not affect mitochondrial respiration in HeLa cells in contrast to VDAC1 KO in HAP1 cells, which decreased mitochondrial respiration and reserve capacity by increasing complex-I-linked respiration (Magri et al., 2023). This discrepancy may be due to distinct responses to VDAC1 KO in different cell types. Comparing the effect of VDAC1 KO in two oxidative muscles (ventricle and soleus) and a glycolytic muscle (gastrocnemius) showed opposite effects on MOM permeability, which is dependent on VDAC, measured as apparent $K_m[\text{ADP}]$ in different muscle types (Anflous et al., 2001). The ventricle and gastrocnemius muscles showed an increase in $K_m[\text{ADP}]$ compared to the soleus, which had decreased $K_m[\text{ADP}]$. Only the soleus muscle showed a decreased rate of respiration in the presence of maximum ADP (V_{max}). This suggests that while VDAC1 KO only affects the MOM permeability in the ventricle and gastrocnemius muscles, both mitochondrial membranes are affected by VDAC1 KO in the soleus. More studies are needed to understand the basis for these differences.

Interestingly, VDAC2 KO does not strongly affect metabolism in our assays despite decreasing cell growth and altered mitochondrial proteome. This may be due to a compensatory upregulation of certain ETC complexes in proteomics studies. The decreased cell growth in VDAC2 KO may be due to changes in apoptosis. Proteomics data show changes in apoptosis-related proteins, such as down-regulation of Bak and upregulation of PYCARD in VDAC2 KO cells. This is consistent with past studies highlighting VDAC2's role in apoptosis through complexation with Bak and BAX (Cheng et al., 2003; Chin et al., 2018; Naghdi et al., 2025; Naghdi et al., 2015; Roy et al., 2009; van Delft et al., 2019). Further studies are needed to confirm that the decreased cell growth in VDAC2 KO cells is related to changes in apoptosis pathways in HeLa cells.

Finally, to our surprise, VDAC3 KO decreased cell growth and showed a significant decrease in metabolic activity measured using MTS assay, confirming the decrease in reducing agents such as NADH and FAD measured by flow cytometry. VDAC3 KO decreases mitochondrial ATP and shows severe defects in mitochondrial respiration. Proteomic studies further confirmed the large-scale downregulation of mitochondrial proteins, such as ETC complexes involved in respiration for VDAC3 KO. We also found the upregulation of glutamine metabolism pathway enzymes in accord with increased glutamine dependence in VDAC3 KO cells.

Our results suggest an evolutionarily conserved metabolite transport function for the oldest VDAC3 isoform, given the decrease in mitochondrial respiration, increased glutamine metabolism, and the complete loss of spare respiratory capacity in VDAC3 KO cells. Spare respiratory capacity corresponds to cells' ability to increase mitochondrial respiration during high energy demand. VDAC3 KO in mice results in mitochondrial dysfunction in sperm and heart, two of the most energy-demanding cells. VDAC3 KO-induced male infertility could be expected, given the high expression of VDAC3 in the testis (Sampson et al., 2001). However, VDAC3 is only a minor isoform in the heart, and the expression profile of VDAC isoforms is similar to that of HeLa cells (Zinghirino et al., 2021). Notably, VDAC3 KO mouse heart muscles showed an increased apparent affinity for mitochondria to ADP ($K_m[ADP]$). In contrast, gastrocnemius, a mixed glycolytic/oxidative muscle, did not show

significant changes in $K_m[\text{ADP}]$ (Anflous-Pharayra et al., 2011). This suggests cell type-specific changes in MOM permeability in VDAC3 KO mice.

One of the possible explanations for the different roles of VDAC isoforms in cell metabolism could be their different regulation by cytosolic protein partners such as hexokinase, tubulin, α -synuclein, and Bcl2 family proteins. Seminal work by Valdur Saks' group showed that isolated mitochondria have lower $K_m[\text{ADP}]$ than permeabilized cells (Saks et al., 1995). This effect was initially linked to cytoskeletal proteins and subsequently shown to be due to free tubulin blocking VDAC (Rostovtseva et al., 2008). The addition of free tubulin to isolated mitochondria increased the $K_m[\text{ADP}]$ of mitochondria, suggesting decreased permeability of MOM to ADP due to VDAC reversible blockage by dimeric tubulin. A second component with unchanged $K_m[\text{ADP}]$ was identified, possibly due to a fraction of VDAC remaining open to ADP. This led to the hypothesis that two rates of ADP uptake could be due to differences in the binding affinity to free tubulin of the three VDAC isoforms. Later, Queralt-Martin et al. confirmed in experiments with VDAC reconstituted into planar membranes that tubulin (and α -synuclein) blocks VDAC1 with ~ 100 times higher affinity than VDAC3 (Queralt-Martin et al., 2020). This suggests that VDAC3 may always be open for metabolite transport in and out of mitochondria, while VDAC1 and VDAC2 are mostly blocked by one of their cytosolic partners, such as tubulin or α -synuclein. This is consistent with calculations by Marko Vendelin's group suggesting that only 2% of VDAC channels are open (accessible for cytosolic ADP) in cardiomyocytes (Simson et al., 2016). Finally, VDAC3 knock-down in HepG2 cancer cells also resulted in the largest decreased ATP, ADP, and NAD(P)H compared with knock-down of the other two VDAC isoforms (Maldonado et al., 2013). These results obtained in HepG2 cells were also interpreted as VDAC1 and VDAC2 being mostly closed by free tubulin and VDAC3 being less sensitive to tubulin. Interestingly, theoretical calculations predicted that VDAC3 may prevent electrical suppression of MOM permeability at elevated MOM potential (Lemeshko, 2017). Overall, these results allow us to speculate that the least expressed VDAC3 isoform is constitutively open in cancer cells for essential metabolite transport function.

Alternatively, VDAC3 expression may constitute part of a signaling axis that promotes oxidative phosphorylation similar to VDAC2's functions in apoptosis, not through

direct channel properties but through the recruitment of Bak. VDAC3 may be a critical signaling intermediate via protein-protein interactions that ultimately promote nuclear expression of pro-OXPHOS gene expression through PGC1- α or an alternative pathway (Mootha et al., 2004). To test this hypothesis, future studies are needed to determine the interacting partners unique to VDAC3 using immunoprecipitation-mass spectrometry. Additionally, following the approach performed for VDAC2's binding to Bak (Naghdi et al., 2015), VDAC2/VDAC3 chimeras can be synthesized to determine which regions of the channel are critical for maintaining the respiration phenotype.

In conclusion, comparing the role of each VDAC isoform in a single cell type allowed us to reveal the distinct roles of each VDAC isoform to be revealed. Consistent with previous studies, we show that VDAC1 and VDAC2 are involved in glycolysis and apoptosis, respectively. To our surprise, VDAC3, the oldest but minor VDAC isoform, which was initially assumed not to form a channel, plays the most crucial role in regulating mitochondrial function and metabolic pathways in HeLa cells. We propose that VDAC3 uniquely enables cells to sustain higher energy demands, explaining its role in energy-demanding cell types such as the heart and sperm. Determining whether VDAC3's effect on metabolism is direct or happens via a yet undescribed cellular signaling pathway represents the next avenue for interrogation. Future studies are needed to understand clonal variability in CRISPR-Cas9 KO cell lines and the role of the VDAC3 isoform in cancer metabolism.

5.5 Materials and methods

Cell culture

HeLa cells (CCL-2) were purchased from ATCC (American Type Culture Collection). HeLa cells with CRISPR-Cas9 knockout cell lines of VDAC1, VDAC2, and VDAC3 were generated by Synthego. The cells were grown in DMEM (Gibco, 15607) supplemented with 10% fetal bovine serum (Gibco, 10437) at 37 °C and 5% CO₂.

Cell proliferation assay

Cells were seeded at 2,500 cells per well in 96-well plates (ThermoFisher Scientific, 165305), and cell count was measured every 24 hours. Cells were washed with PBS and

fixed with 4% PFA (Electron Microscopy Sciences, 15710) containing 25 μ M Hoechst 33342 (ThermoFisher Scientific, 62249) for 15 mins. Cells were washed with PBS and imaged using a DAPI filter in BioTek Lionheart FX automated microscope.

CellTiter 96® AQueous One Solution Cell Proliferation Assay (MTS) (Promega, G3582) was performed based on manufacturer protocol. Cells were seeded at 2,500 cells in a 96-well plate and incubated at 37 °C in a 5% CO₂ incubator for 72 hours. 20 μ L CellTiter 96® AQueous One Solution Reagent was added to 100 μ L media per well and incubated for 1 hour at 37 C in a 5% CO₂ incubator. The absorbance was measured at 490 nm using a CLARIOstar plate reader.

Seahorse metabolic flux assay

Cells were seeded at 10,000-15,000 cells/well in Seahorse XFp PDL miniplates (Agilent, 103721) or XFe96/XF Pro PDL cell culture microplates (Agilent, 103798). They were incubated overnight at 37 °C and 5% CO₂. The following day, the media was replaced with Seahorse XF DMEM assay media (Agilent, 103575) supplemented with glucose, pyruvate, and glutamine based on the manufacturer's protocol for cell mitochondrial stress (Agilent, 103010), glycolysis stress (Agilent, 103020), and mitochondria fuel flex (Agilent, 103260) assays. The assays were performed on Seahorse XF HS mini or XF Pro analyzers (Agilent) according to the manufacturer's protocol. Hoechst 33342 (ThermoFisher Scientific, 62249) was added to the last port to stain nuclei for cell count and imaged using Lionheart FX or Cytation5 (BioTek).

Colocalization of hexokinase to mitochondria

Cells were seeded at 25,000 cells/well in μ -Slide 8 well chambered coverslip (Ibidi, 80807) and grown at 37 °C and 5% CO₂ overnight. Cells were transfected with HK1-GFP (Addgene, 21917) or HK2-GFP (Addgene, 21920) along with Omp25-mCherry (Addgene, 157758) using Lipofectamine™ Stem transfection reagent (ThermoFisher Scientific, STEM00008) according to the manufacturer's protocol. The cells were washed and imaged in Fluorobrite DMEM (Gibco, A18967) with a 20x/0.75 N.A. objective in Leica TCS SP8 microscope.

GFP was excited with a 488 nm laser, and emission was captured using a 500–582 nm filter, and mCherry was excited with a 587 nm laser and emission was captured using a 592–784 nm filter. Images were optimized for contrast and brightness, and Pearson's correlation coefficient was measured using the BIOP JACoP plugin in ImageJ (NIH).

Western blot of mitochondrial proteins

After harvesting, cell pellets were resuspended in 150 μ L lysis buffer (50 mM Tris-HCl pH 8.0, 150 mM NaCl, 1% Triton X-100 with protease inhibitor tablet (Pierce), and incubated on ice for 10 min with occasional vortex. Samples were centrifuged at 15,000 rpm at 4 °C for 10 min, and 120 μ L of the supernatant was transferred into a new 1.5 mL tube. Total soluble protein concentrations were measured using the Bradford reagent (Bio-Rad, 5000006). After that, 40 μ L of 4x Laemmli sample buffer (Bio-Rad, 161–0774) containing 0.1 M DTT (Cytiva, 17-1318-02) was mixed with the samples and heated for 5 min at 95 °C. Equal amounts of protein samples were loaded and separated using 4–20% Mini-PROTEAN TGX precast gels (Bio-Rad, 456–1096) and transferred to nitrocellulose membranes using Trans-Blot Turbo Transfer System (Bio-Rad, 170–4155). Membranes were blocked with 5% w/v nonfat milk prepared in TBST buffer, incubated with primary antibodies overnight at 4 °C, washed with 5% milk (three times for 10 min each), incubated with proper secondary antibodies for two h at room temperature, and washed with TBST buffer (three times for 5 min each). The blots were imaged using an ECL reagent (MilliporeSigma, WBKLS0500) and the ChemiDoc MP Imaging System (Bio-Rad). Blot densities were analyzed using Image Lab 6.0.1 software (Bio-Rad).

ANTIBODIES	SOURCE	IDENTIFIER
Mouse Anti-MT-CO1	Abcam	ab14705
Mouse Anti-NDUFA9	Abcam	ab14713
Mouse Anti-NDUFB7	Santa Cruz	Sc-365552
Rabbit Anti-GLS1	Proteintech	29519-1-AP
Rabbit Anti-CS	Proteintech	16131-1-AP
Rabbit Anti-ATP5 α	Abcam	ab176569

P62	Santa Cruz	sc-28359
-----	------------	----------

Label-free proteomics

1.2 million cells were harvested with trypsin, quenched with PBS, spun down to remove the trypsin, and resuspended and spun down in ice-cold PBS. The supernatant was removed, and LC-MS samples were prepared using the Thermo EasyPep Mini MS Sample Prep Kit (ThermoFisher Scientific, A4006) according to the manufacturer's instructions. Samples were then resuspended in 0.1% formic acid (ThermoFisher Scientific, 85178) solution, and peptide concentration was tested using the Pierce Quantitative Fluorometric Peptide Assay (ThermoFisher Scientific, 23290). LC-MS/MS experiments were performed by loading a 500 µg sample onto an EASY-nLC 1000 (ThermoFisher Scientific) connected to an Orbitrap Eclipse Tribrid mass spectrometer (ThermoFisher Scientific). Peptides were separated on an Aurora UHPLC Column (25 cm x 75 µm, 1.6 µm C18, AUR2-25075C18A, Ion Opticks) with a flow rate of 0.4 mL/min and for a total duration of 131 min. The gradient was composed of 3% Solvent B for 1 min, 3–19% B for 72 min, 19–29% B for 28 min, 29–41% B for 20 min, 41–95% B for 3 min, and 95–98% B for 7 min. Solvent A consists of 97.8% H₂O, 2% acetonitrile, and 0.2% formic acid, and solvent B of 19.8% H₂O, 80% ACN, and 0.2% formic acid. MS1 scans were acquired with a range of 400–1600 m/z in the Orbitrap at 120 k resolution. The maximum injection time was 50 ms, and the AGC target was 2 3 105. MS2 scans were acquired using quadrupole isolation mode and higher-energy collisional dissociation (HCD) activation type in the Iontrap. The isolation window was 1.4 m/z, collision energy was 35%, maximum injection time was 35 ms, and the AGC target was 1 3 104. Other global settings were set to the following: ion source type, NSI; spray voltage, 2500 V; ion transfer tube temperature, 300 °C. Method modification and data collection were performed using Xcalibur software (ThermoFisher Scientific).

Quantification and statistical analysis

Proteomic analysis was performed using Proteome Discoverer 2.4 (PD 2.4, ThermoFisher Scientific) software, the Uniprot human database, and SequestHT with Percolator validation. Percolator FDRs were set at 0.001 (strict) and 0.01 (relaxed). Peptide FDRs was set at 0.001

(strict) and 0.01 (relaxed), with medium confidence and a minimum peptide length of 6. Carbamidomethyl (C) was set as a static modification; oxidation (M) was set as a dynamic modification; acetyl (protein N-term), Met-loss (Protein N-term M) and Met-loss + acetyl (Protein N-term M) were set as dynamic N-Terminal modifications. Protein abundance normalization was performed relative to the total peptide amount. Differential Expression analysis was performed with media using a custom Python module following the user guide 7 or one-tailed Student's t-test with PD 2.4. Principal Component Analysis (PCA) analyses were conducted with custom Python code. Volcano plots were generated in R using the Tidy Proteomics and Enhanced Volcano plot packages. Venn diagram was plotted using Python3. Gene ontology analysis was performed using g:Profiler (website (<https://biit.cs.ut.ee/gprofiler/gost>)). Other statistical analyses were carried out by one-tailed Student's t-test or one-way ANOVA using Prism 7.0. Three independent biological replicates were used. p values < 0.05 are reported as statistically significant and are depicted as follows throughout the manuscript: * p < 0.05, ** p < 0.01, **** p < 0.0001.

Supplemental Material

Supplemental Methods describing western blot, flow cytometry, Seahorse ATP rate assay, and *Supplemental Figures S1-S7* are available.

Data Availability

The raw and processed proteomics data underlying Figures 1A, 4, 6, 7A and 8A are available in the MassIVE database under the identifier [MSV000097150](#) (Reviewer_account: **MSV000097150_reviewer**; Password: QFyuFW9Z51Wzd6U4). The data underlying Figures 1B,2,3,5, 7B-C, and 8B-D are available in the main text. The authors can provide any additional information required to reanalyze the data reported in this paper upon request.

5.6 Acknowledgments

M.R., W.F., B.G.B., N.A.B., T.K.R. and S.M.B. were supported by the Intramural Research Program of the *Eunice Kennedy Shriver* National Institute of Child Health and Human

Development of the National Institutes of Health. W.M.R. was supported by the National Institute of Neurological Disorders and Stroke, NIH, and a generous grant from the J. Yang and Family Foundation, Caltech.

References

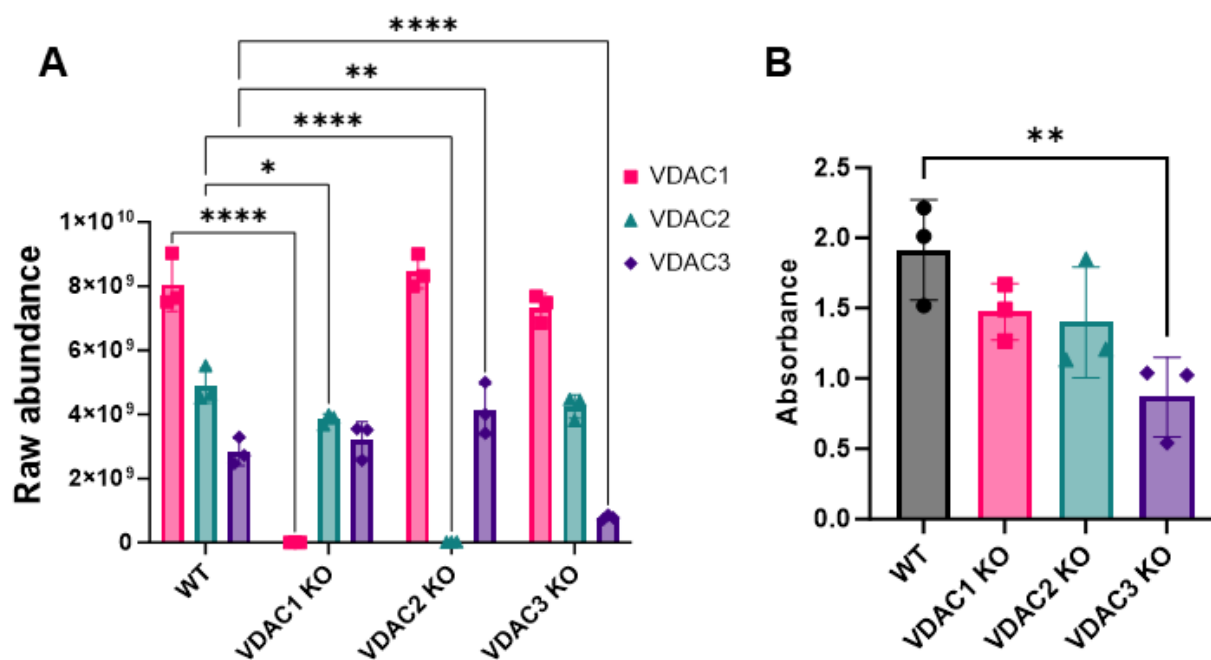


Figure 5.1: VDAC3 KO decreases metabolic activity in HeLa cells. A) The bar graph represents the raw abundance of VDAC1 (pink), VDAC2 (teal), and VDAC3 (purple) in WT, VDAC1 KO, VDAC2 KO, and VDAC3 KO HeLa cell lines measured using mass spectrometry (MS). The ~30% expression of VDAC3 in VDAC3 KO despite western blot confirmation complete KO (Supplementary Figure S2B) may correspond to the expression of a shorter transcript since the two VDAC3 peptides detected by MS correspond to the C-terminal of VDAC3 (Supplementary MS table). B) The bar graph shows the metabolic activity of WT, VDAC1 KO, VDAC2 KO, and VDAC3 KO cells 72 hours post seeding measured using CellTiter 96® AQueous one solution cell proliferation assay. The symbols represent data from 3 independent experiments, and error bars indicate the standard deviation

from the mean. Significance was tested using one-way ANOVA followed by the Dunnett post hoc test (* $p < 0.05$, ** $p < 0.01$, **** $p < 0.0001$)

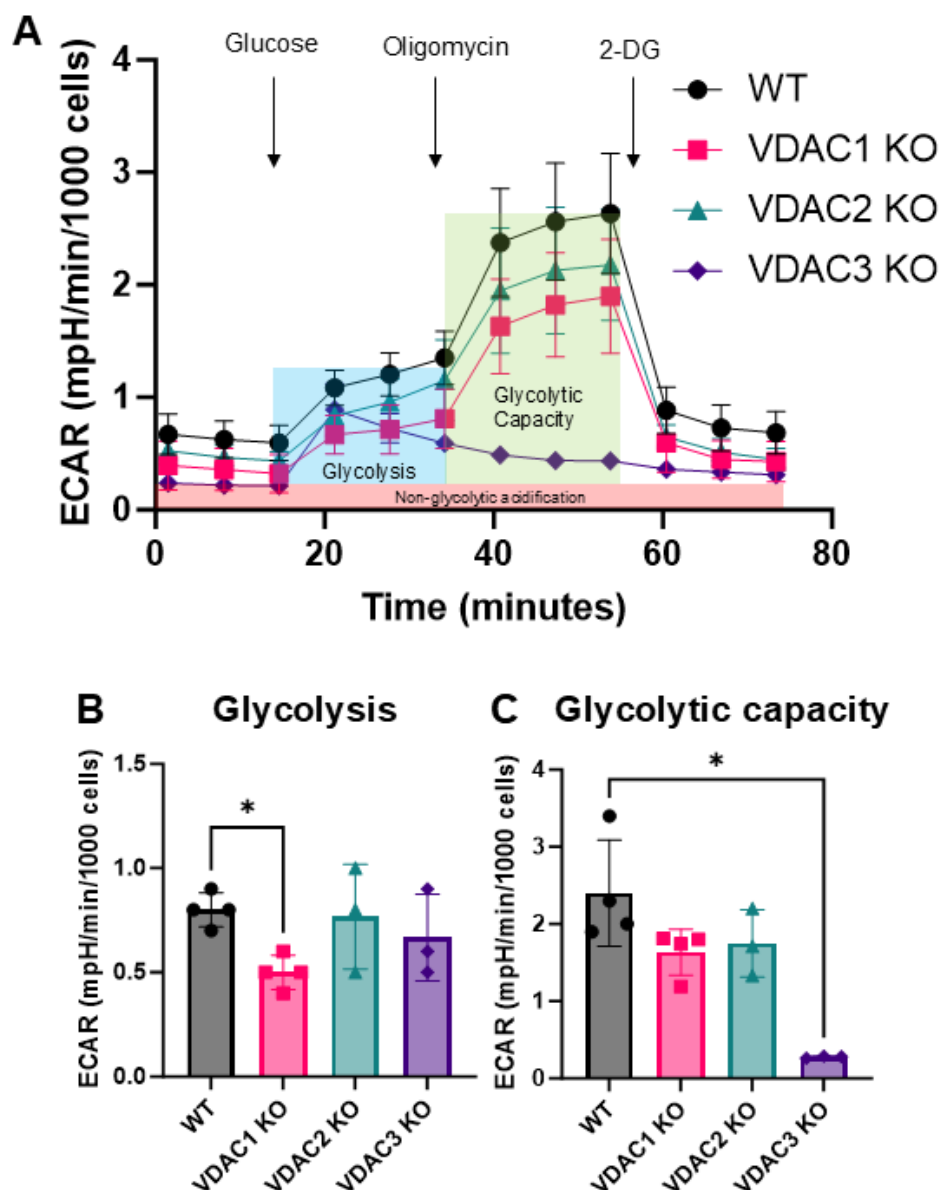


Figure 5.2: VDAC1 KO decreases glycolysis in HeLa cells. A) Traces of extracellular acidification rate (ECAR) upon the addition of glucose, oligomycin, and 2-deoxyglucose for WT (black circle), VDAC1 KO (pink square), VDAC2 KO (teal triangle), and VDAC3 KO (purple diamond) cells. Glycolysis (blue box) and glycolytic capacity (green box) are calculated after subtraction from non-glycolytic acidification (red box). Bar graphs

comparing glycolysis (B) and the glycolytic capacity (C) between WT (gray), VDAC1 KO (pink), VDAC2 KO (teal), and VDAC3 KO (purple) HeLa cells. Data from 3-4 independent experiments are represented in the bar graph, and the error bars indicate the standard deviation from the mean. The symbols represent data from independent experiments. Significance was tested using one-way ANOVA followed by the Dunnett post hoc test (* $p < 0.05$).

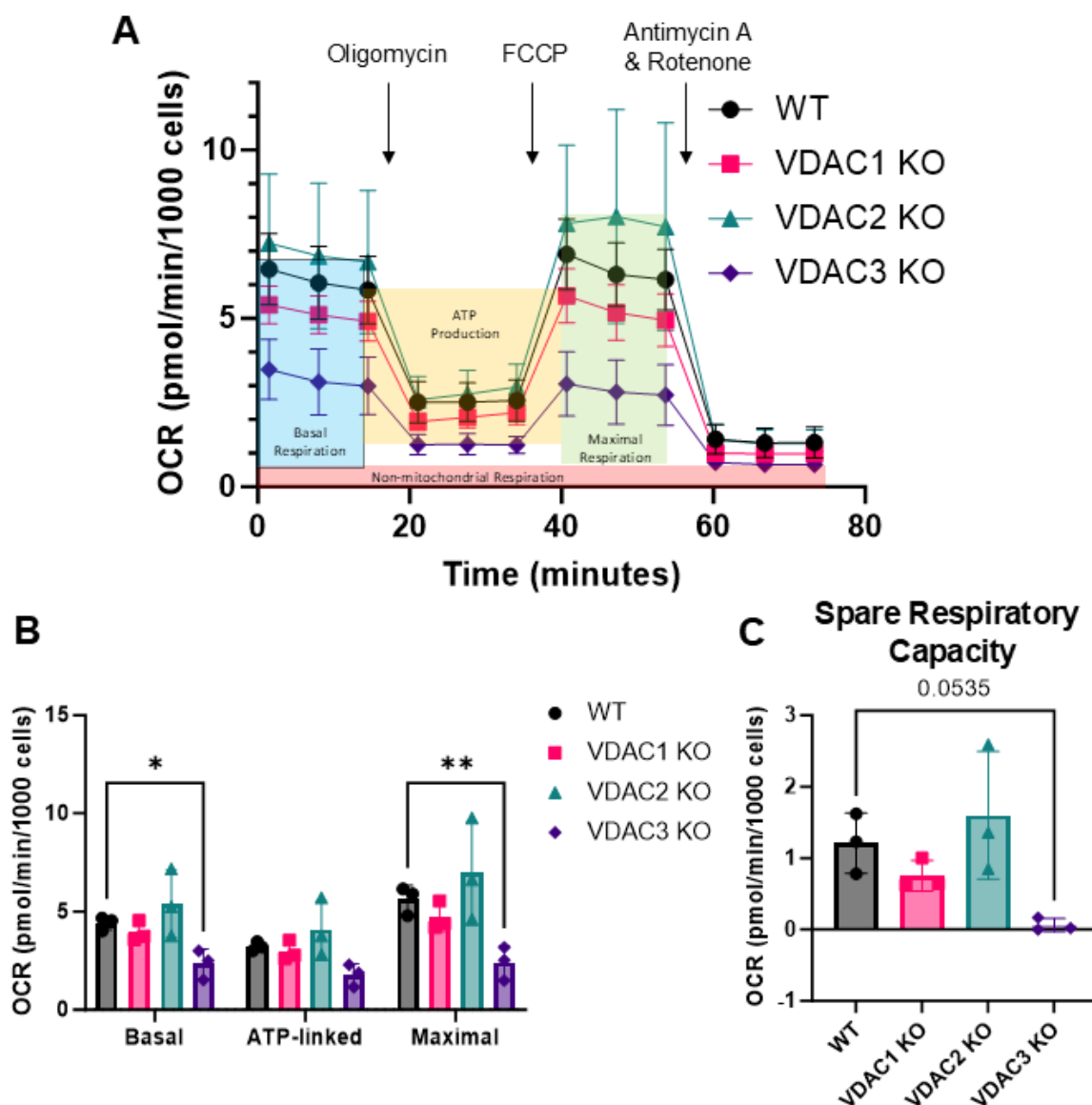


Figure 5.3: VDAC3 KO decreases mitochondrial respiration in HeLa cells, resulting in the complete loss of spare respiratory capacity. A) Trace of oxygen consumption rate (OCR) upon the addition of oligomycin, FCCP, and Antimycin A/Rotenone for WT (black circle), VDAC1 KO (pink square), VDAC2 KO (teal triangle), and VDAC3 KO (purple diamond) cells. Non-mitochondrial respiration (red box) is subtracted from basal (blue box), ATP-linked (yellow box), and maximal (green box) respiration for analysis. B) Bar graphs comparing basal, ATP-linked, maximal respiration, and SRC (C) in WT (gray), VDAC1 KO (pink), VDAC2 KO (teal), and VDAC3 KO (purple) HeLa cells. Data from three

independent experiments (symbols) are averaged, and the error bar indicates the standard deviation from the mean. Significance was tested using one-way ANOVA followed by the Dunnett post hoc test (* $p < 0.05$, ** $p < 0.01$).

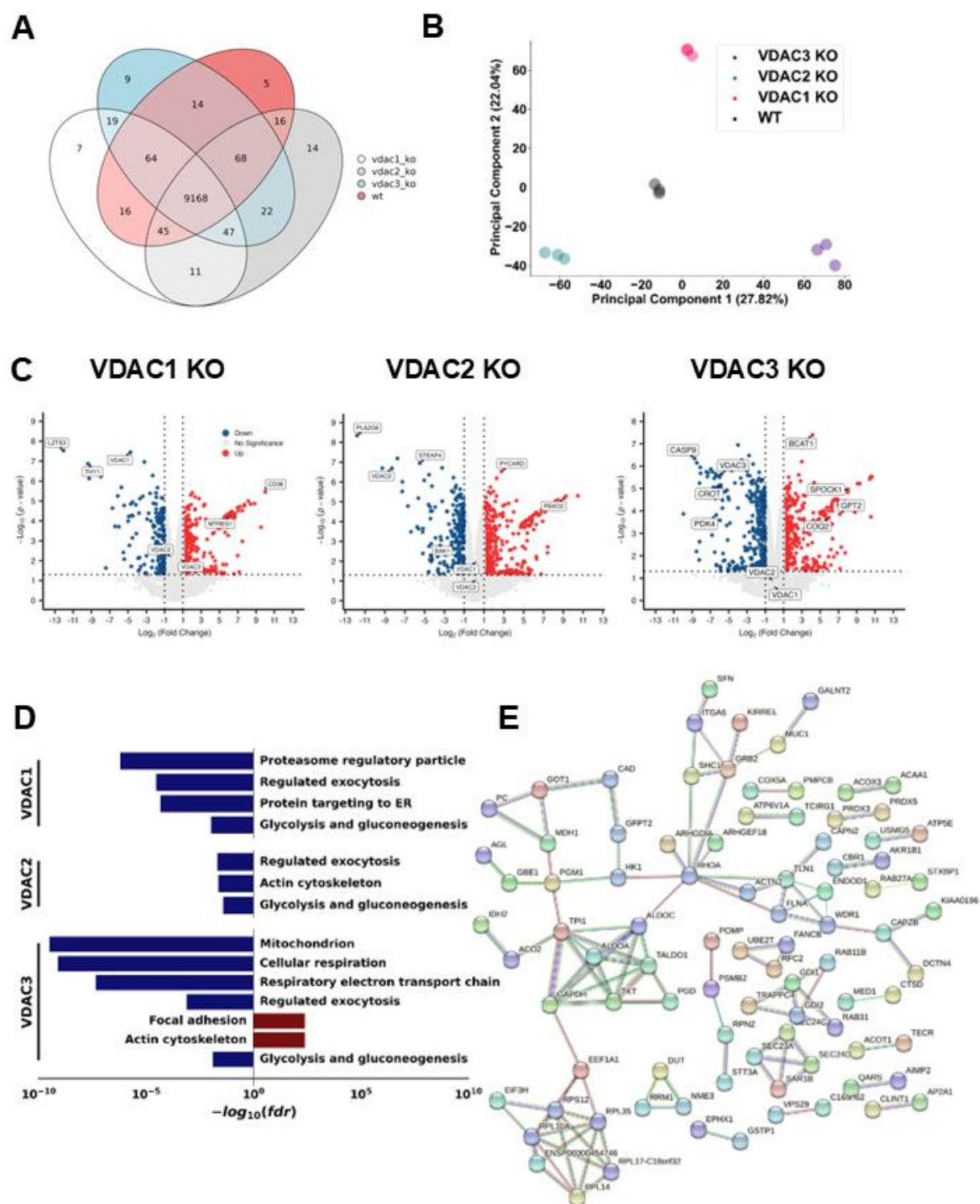


Figure 5.4: Total proteomics reveals isoform-specific proteome remodeling in HeLa cells. A) Venn diagram detailing the number of unique proteins identified in each sample

group. B) PCA plot demonstrating the stratification of each VDAC isoform KO sample compared to WT cells along PC1 and PC2. C) Volcano plots of each VDAC isoform KO compared to WT cells. Proteins with > 1 -fold absolute change and p -value < 0.05 are colored blue for downregulation and red for upregulation compared to the WT. Proteins of interest are labeled. D) Representative GO Term analysis showing pathways significantly downregulated upon each VDAC isoform (blue) or upregulated (red) compared to the WT. E) STRING analysis of glycolysis and gluconeogenesis proteins downregulated in all VDAC isoform KOs compared to WT.

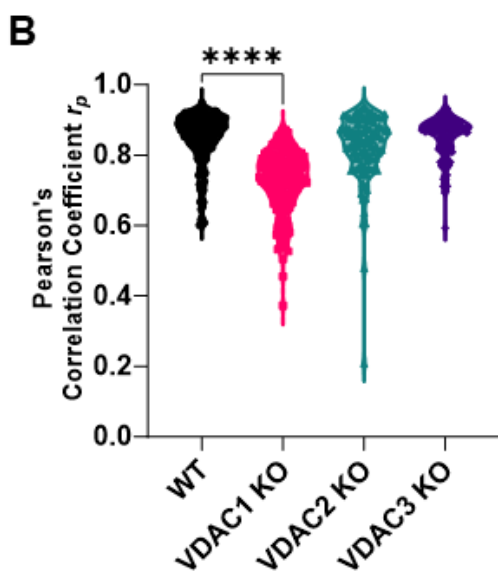
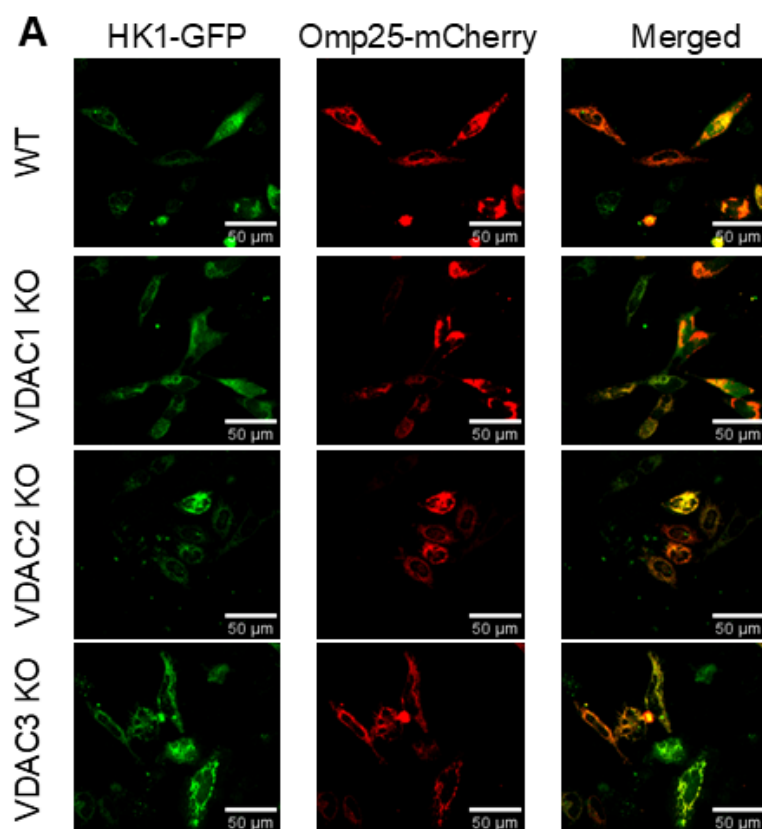


Figure 5.5: Mitochondrial localization of HK1 is dependent on VDAC1 isoform. A) Representative images of HK1-GFP (green) colocalization with Omp25-mCherry (red) shown in the merged image (yellow) for WT, VDAC1 KO, VDAC2 KO, and VDAC3 KO

HeLa cells. B) Colocalization analysis of HK1 with Omp25 measured by Pearson's correlation coefficient (PCC) shows a significant decrease in HK1 mitochondrial localization in VDAC1 KO. The symbols represent PCC for each cell. Significance was tested using one-way ANOVA followed by the Dunnett post hoc test (**** $p < 0.0001$).

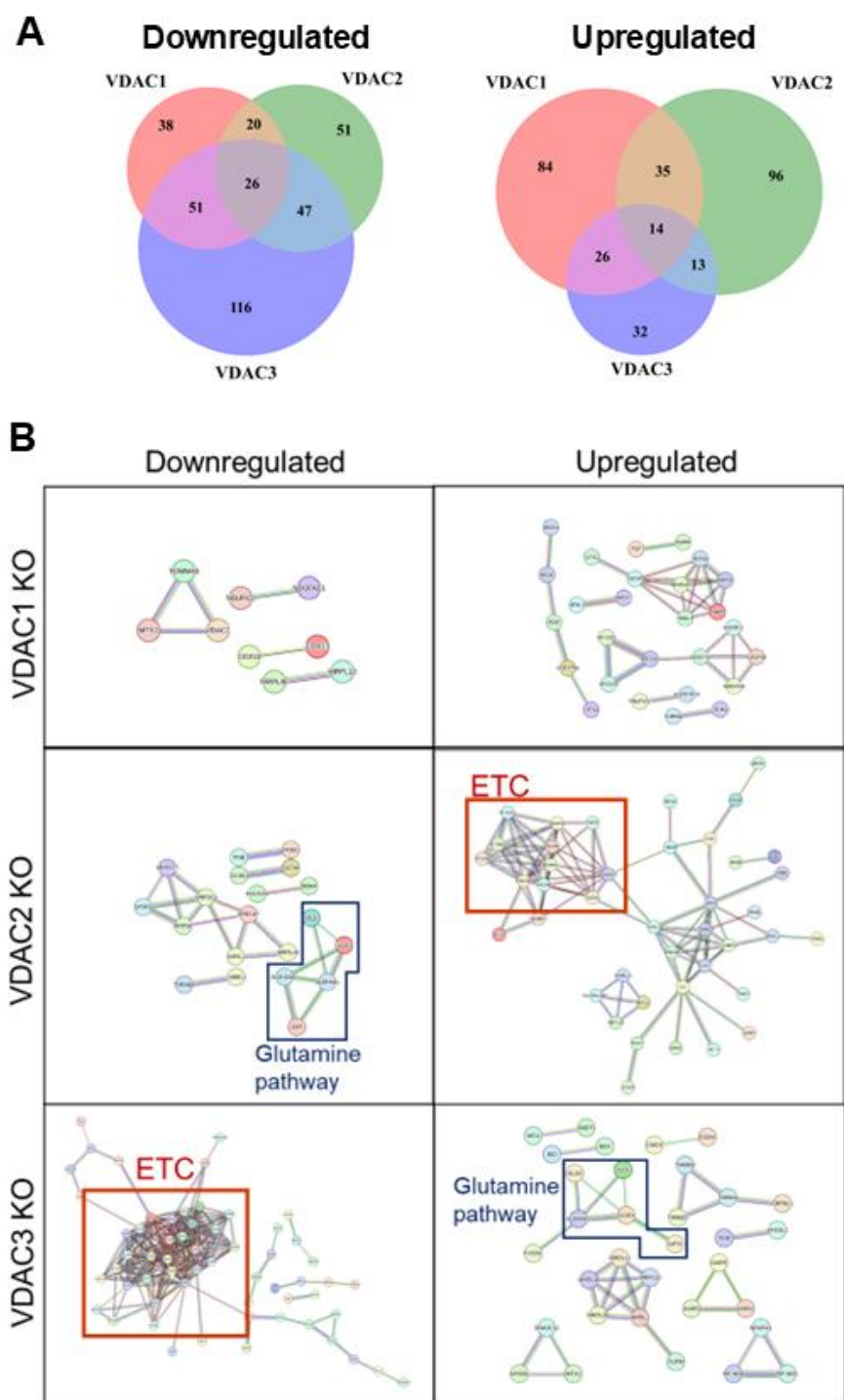


Figure 5.6: VDAC isoform KO leads to distinct mitochondrial proteome remodeling.
 A) Venn diagram showing mitochondrially annotated proteins found to be downregulated or upregulated in each of the three VDAC isoform KOs compared to WT. B) STRING analysis

of mitochondrial pathways uniquely downregulated or upregulated in each VDAC isoform KO cell lines. Proteins involved in the electron transport chain (ETC) (red box) and glutamine pathway (blue box) are highlighted.

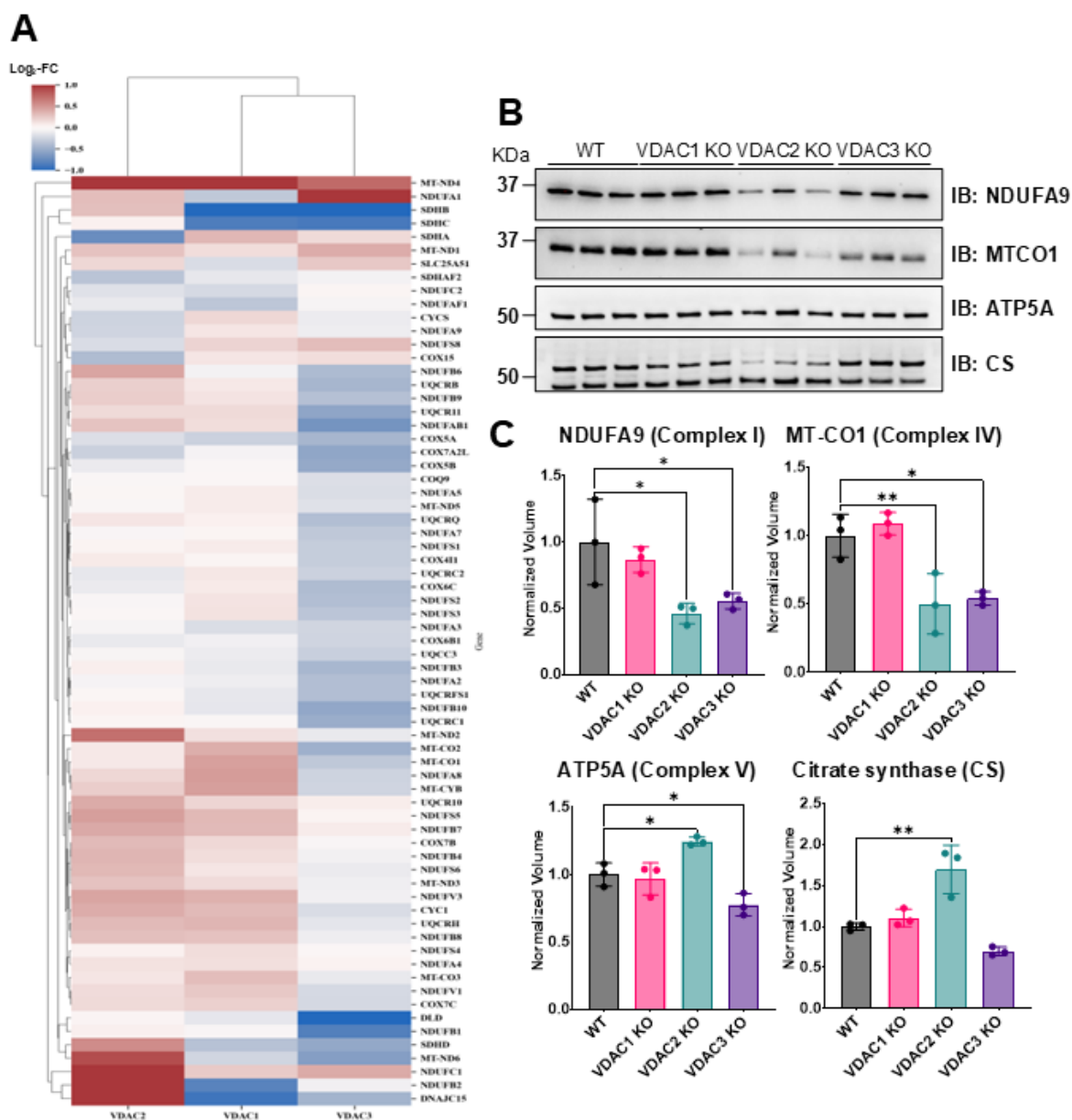


Figure 5.7: VDAC2 KO and VDAC3 KO result in widespread upregulation and downregulation of ETC components. A) Heatmap of altered proteins associated with the mitochondrial ETC. B) Western blot of selected ETC components across VDAC isoform KO cell lines and (C) the corresponding densitometry quantification. Data for three repeats are averaged in the bar graphs, and error bars indicate the standard deviation from the mean. The symbols represent data from each repeat. Significance was tested using one-way ANOVA followed by the Dunnett post hoc test (* $p < 0.05$, ** $p < 0.01$).

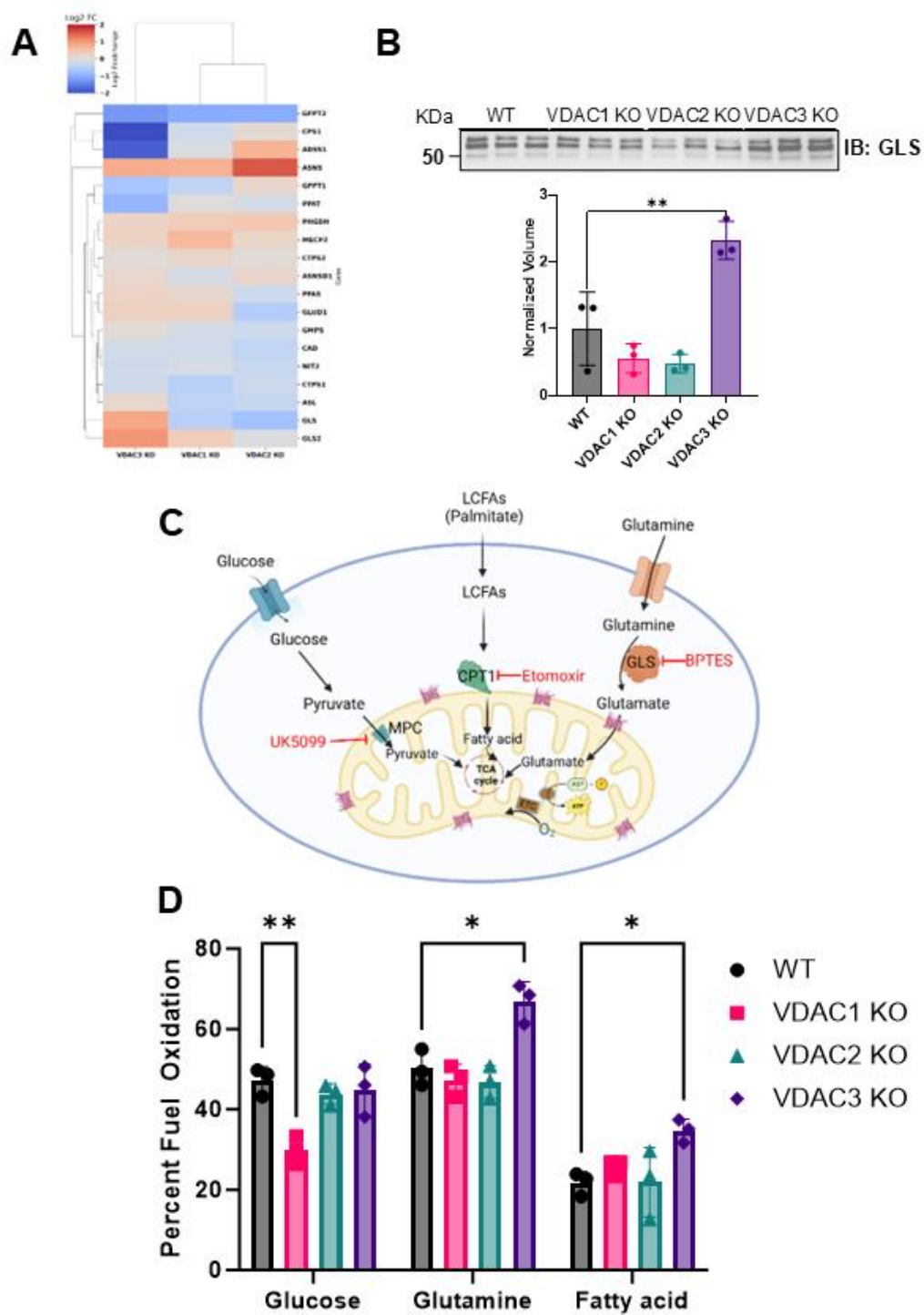
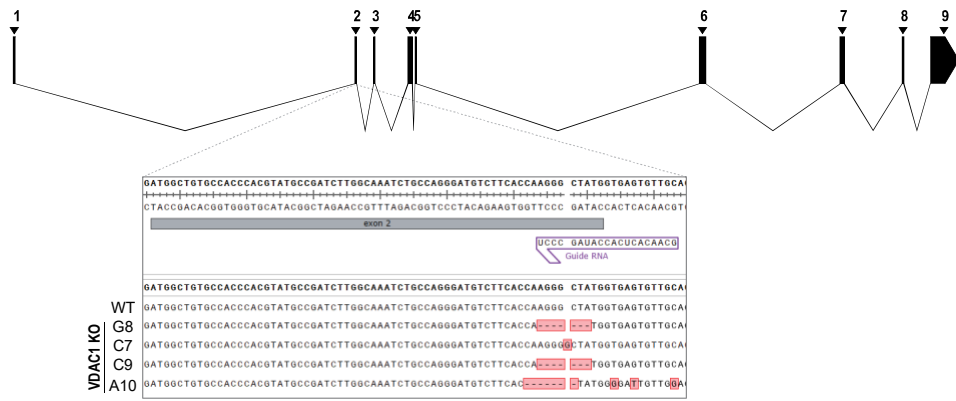
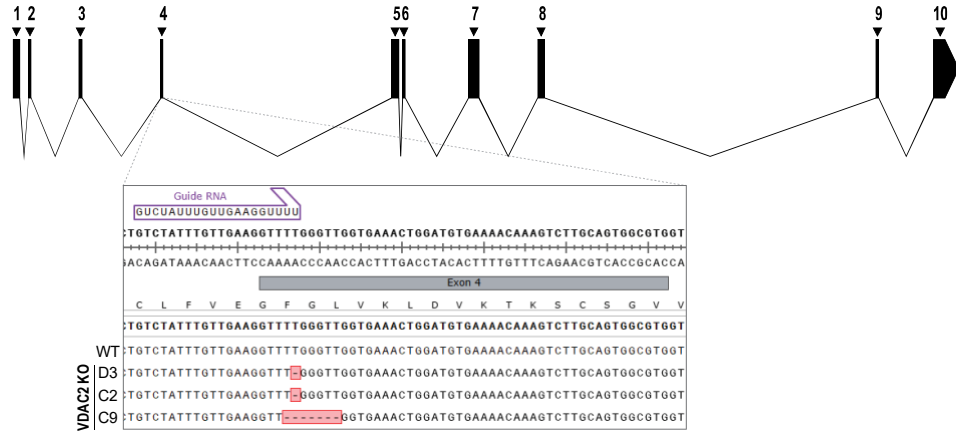


Figure 5.8: VDAC3 KO leads to increased reliance on glutamine metabolism. A) Heatmap of altered proteins associated with glutamine metabolism in VDAC1, VDAC2 and VDAC3 KO cells. B) Western blot of GLS expression in WT HeLa cells and VDAC isoform KO cell lines and the corresponding densitometry quantification. The bar graph represents the average of 3 repeats. C) Simplified metabolic map of mitochondrial fuel pathways and inhibitors used in Agilent Seahorse XF mitochondria fuel flex test (created on BioRender). D) Bar graph comparing the glucose, glutamine, and fatty acid dependency for WT (gray), VDAC1 KO (pink), VDAC2 KO (teal), and VDAC3 KO (purple). Data from 3 independent experiments are represented. The symbols represent data from independent experiments, and error bars indicate the standard deviation from the mean. Significance was tested using one-way ANOVA followed by the Dunnett post hoc test (* $p < 0.05$, ** $p < 0.01$).

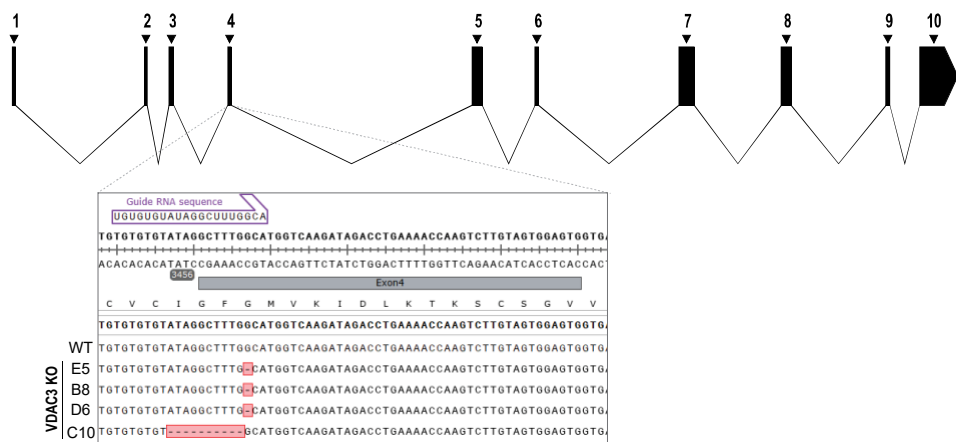
VDAC1



VDAC2



VDAC3



S5.1: Location and sequencing confirmation of VDAC isoform CRISPR target sequences.

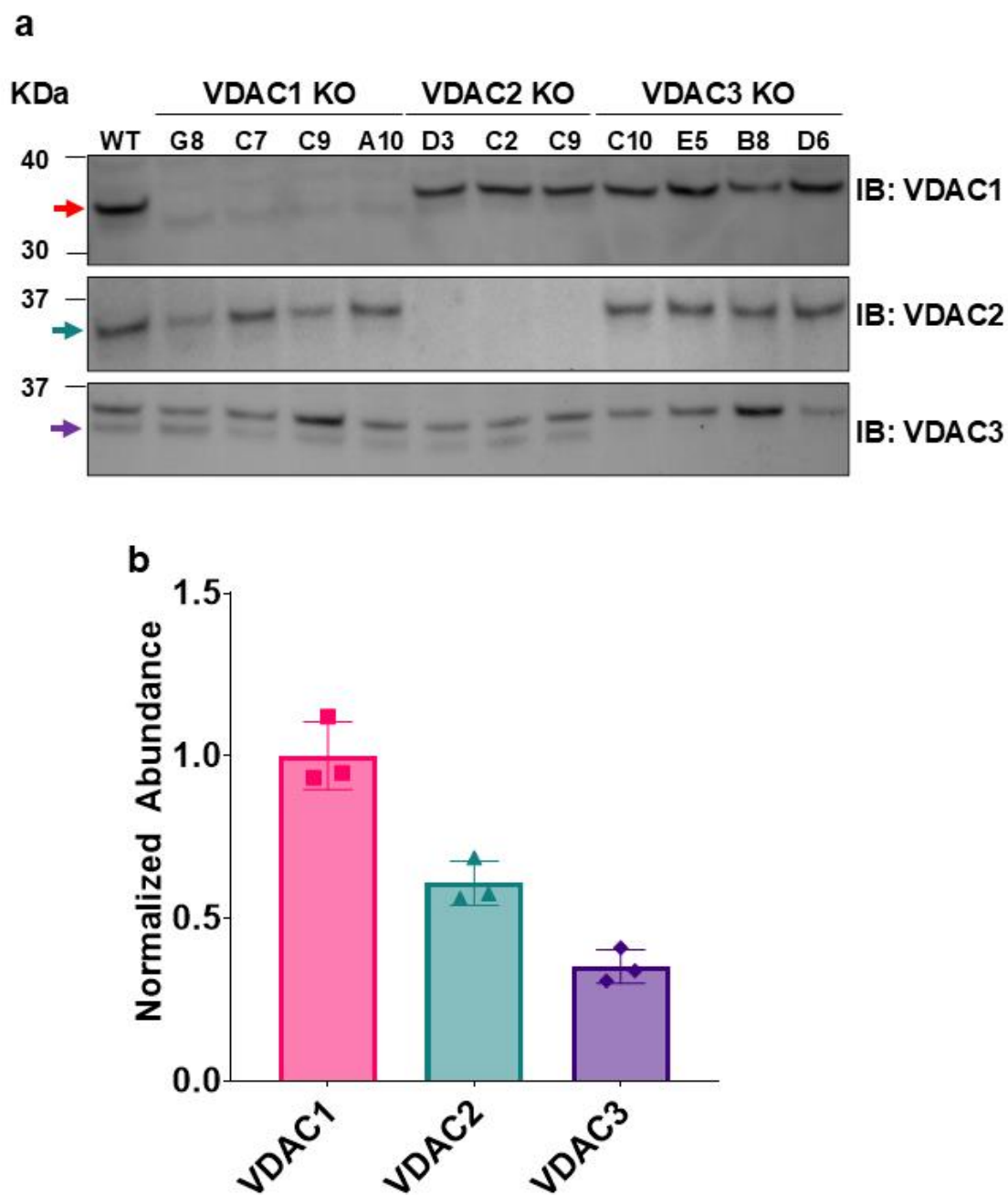


Figure S5.2: VDAC1, 2, and 3 expression in HeLa cells A) Western blot VDAC1, VDAC2, and VDAC3 expression levels in HeLa WT and KO clones. The top band (pink arrow) corresponds to VDAC1 expression in VDAC1 immunoblot (IB), and the bottom band (purple arrow) corresponds to VDAC3 expression in VDAC3 IB. B) VDAC isoform

expression ratio measured by mass spectrometry in WT HeLa cells normalized to VDAC1 expression level.

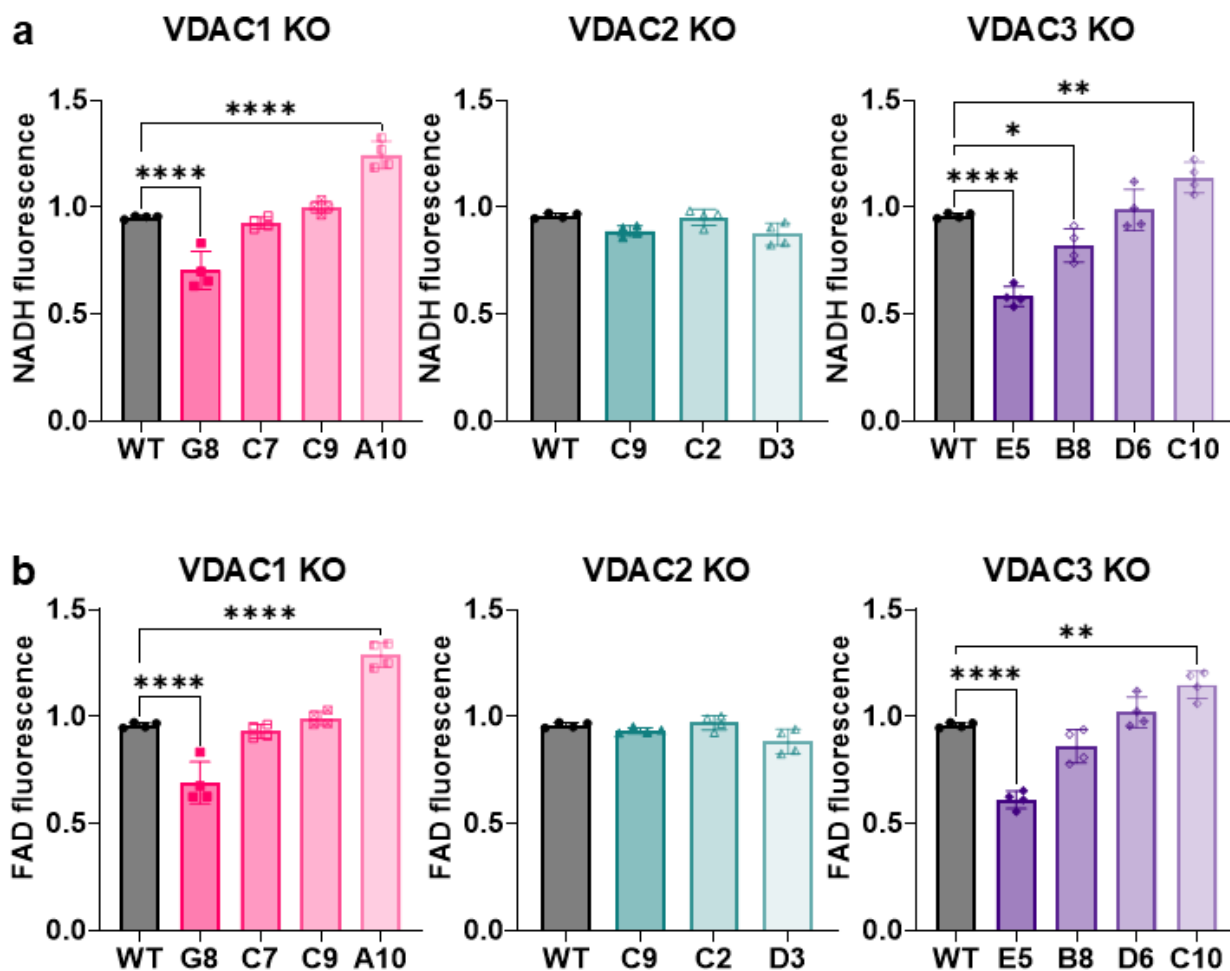


Figure S5.3: NADH and FAD autofluorescence in HeLa WT and VDAC isoform KO cells. Normalized NADH fluorescence (A) and FAD fluorescence (B) in VDAC1, VDAC2, and VDAC3 KO clones compared to HeLa WT (gray) were measured using flow cytometry (see Supplemental Methods). While VDAC2 KO clones do not affect NADH and FAD fluorescence, VDAC1 and VDAC3 KOs show clonal variability in NADH and FAD fluorescence. Clones VDAC1 KO G8 and VDAC3 KO E5 show the most significant decrease in NADH and FAD. The symbols represent data from four independent experiments. Error bars indicate the standard deviation from the mean. Significance was tested using one-way ANOVA followed by the Dunnett post hoc test (* $p < 0.05$, ** $p < 0.01$, **** $p < 0.0001$).

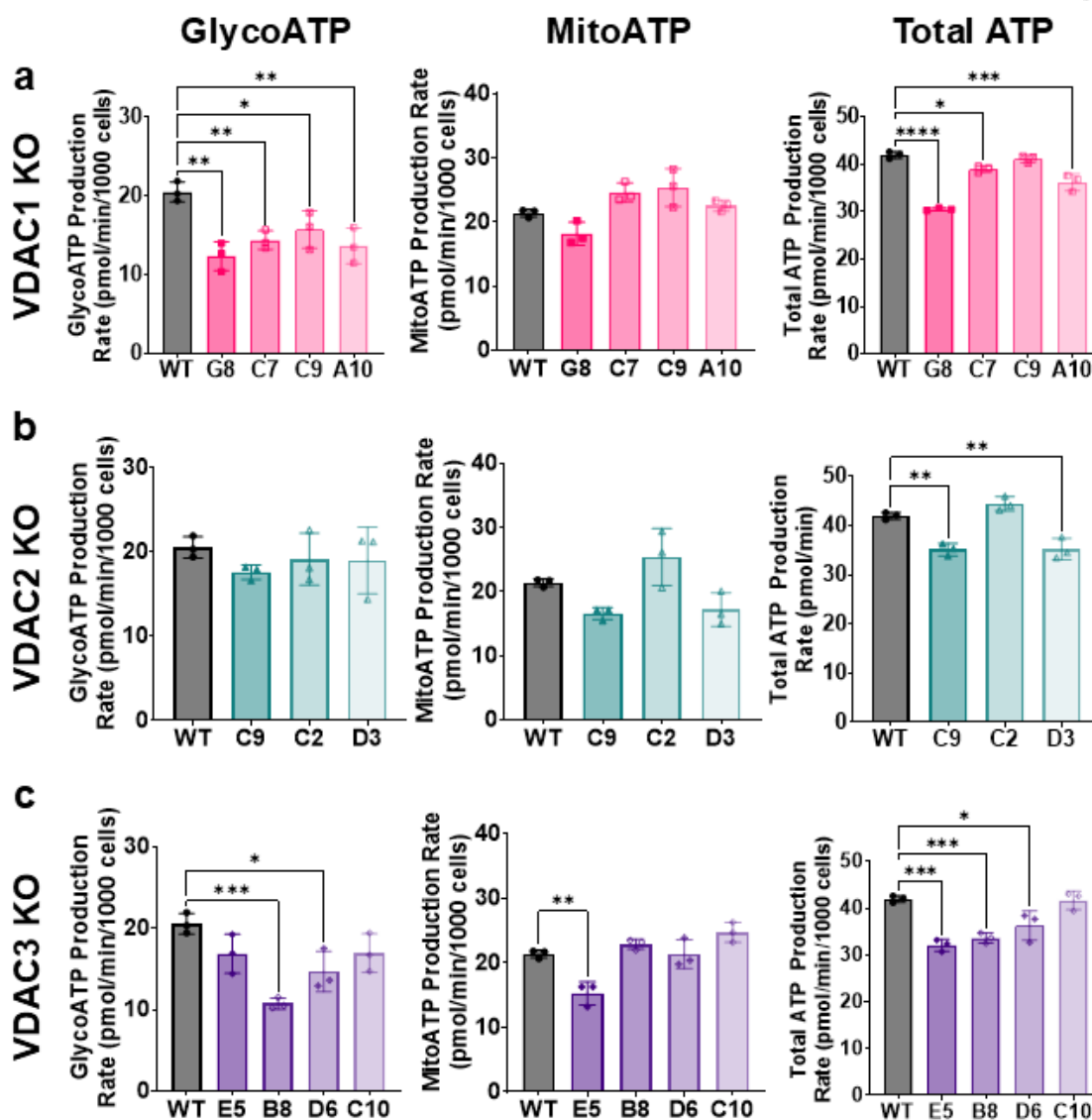
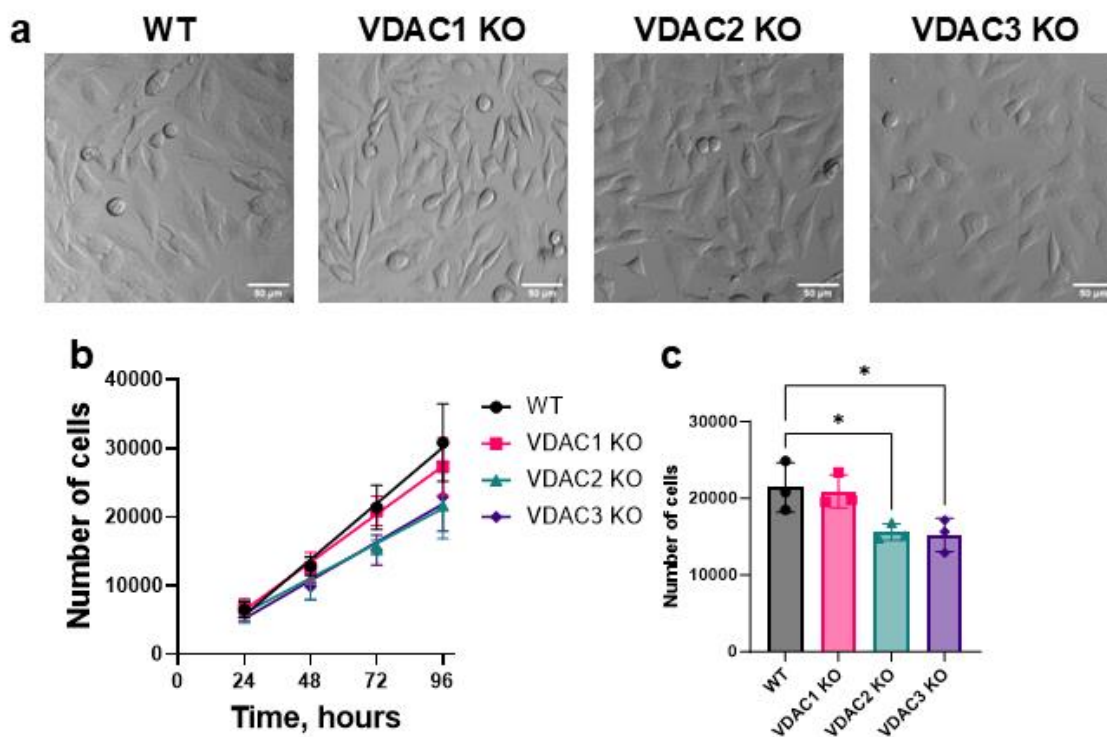


Figure S5.4: ATP production rate in HeLa WT and VDAC isoform KO cells. The total, glycolytic (GlycoATP), and mitochondrial (MitoATP) ATP production rate in HeLa cells with VDAC1 KO (A), VDAC2 KO (B), and VDAC3 KO (C) clones. A) All VDAC1 KO clones show a significant decrease in glycoATP production rate compared to the WT. There is no significant difference in mitoATP production rate, but the minor differences result in a variable total ATP production rate. VDAC1 KO G8 clone has the largest decrease in total ATP production rate. B) GlycoATP and mitoATP are not significantly affected in VDAC2 KO clones, while the total ATP production rate is decreased by ~16% for VDAC2 KO C9 and D3 clones. C) VDAC3 KO results in variable glycoATP and mitoATP production rates

for each clone. GlycoATP production rate is significantly decreased for VDAC3 KO clones B8 (~48%) and D6 (~29%). Only VDAC3KO E5 shows a significant decrease in mitoATP production rate. This results in some variability of the total ATP production rate, with the VDAC3 KO E5 clone having the largest effect on the total ATP production rate. The symbols represent data from three independent experiments. Error bars indicate the standard deviation from the mean. Significance was tested using one-way ANOVA followed by the Dunnett post hoc test (* $p < 0.05$, ** $p < 0.01$, *** $p < 0.001$, **** $p < 0.0001$).



Supplementary Figure S5.5: Cell morphology and growth of HeLa WT and VDAC isoform KO cells A) Brightfield images of HeLa cells WT, VDAC1 KO, VDAC2 KO, and VDAC3 KO. B) Number of cells measured using Hoechst 33342 staining every 24 hours and C) bar graph represents the number of cells after 72 hours for WT (gray circle), VDAC1 KO (pink square), VDAC2 KO (teal triangle), and VDAC3 KO cells (purple diamond). The symbols represent data from three independent experiments, and error bars indicate the standard deviation from the mean. Significance was tested using one-way ANOVA followed by the Dunnett post hoc test (* $p < 0.05$).

Works cited

- Anflous, K., Armstrong, D. D., & Craigen, W. J. (2001). Altered mitochondrial sensitivity for ADP and maintenance of creatine-stimulated respiration in oxidative striated muscles from VDAC1-deficient mice. *J Biol Chem*, 276(3), 1954-1960. <https://doi.org/10.1074/jbc.M006587200>
- Anflous-Pharayra, K., Cai, Z. J., & Craigen, W. J. (2007). VDAC1 serves as a mitochondrial binding site for hexokinase in oxidative muscles. *Biochim Biophys Acta*, 1767(2), 136-142. <https://doi.org/10.1016/j.bbabi.2006.11.013>
- Anflous-Pharayra, K., Lee, N., Armstrong, D. L., & Craigen, W. J. (2011). VDAC3 has differing mitochondrial functions in two types of striated muscles. *Biochim Biophys Acta*, 1807(1), 150-156. <https://doi.org/10.1016/j.bbabi.2010.09.007>
- Arbel, N., Ben-Hail, D., & Shoshan-Barmatz, V. (2012). Mediation of the antiapoptotic activity of Bcl-xL protein upon interaction with VDAC1 protein. *J Biol Chem*, 287(27), 23152-23161. <https://doi.org/10.1074/jbc.M112.345918>
- Baines, C. P., Kaiser, R. A., Sheiko, T., Craigen, W. J., & Molkentin, J. D. (2007). Voltage-dependent anion channels are dispensable for mitochondrial-dependent cell death. *Nat Cell Biol*, 9(5), 550-555. <https://doi.org/10.1038/ncb1575>
- Bayrhuber, M., Meins, T., Habeck, M., Becker, S., Giller, K., Villinger, S., Vonnrhein, C., Griesinger, C., Zweckstetter, M., & Zeth, K. (2008). Structure of the human voltage-dependent anion channel. *Proc Natl Acad Sci U S A*, 105(40), 15370-15375. <https://doi.org/10.1073/pnas.0808115105>
- Brahimi-Horn, M. C., Giuliano, S., Saland, E., Lacas-Gervais, S., Sheiko, T., Pelletier, J., Bourget, I., Bost, F., Feral, C., Boulter, E., Tauc, M., Ivan, M., Garmy-Susini, B., Popa, A., Mari, B., Sarry, J. E., Craigen, W. J., Pouyssegur, J., & Mazure, N. M. (2015). Knockout of Vdac1 activates hypoxia-inducible factor through reactive oxygen species generation and induces tumor growth by promoting metabolic reprogramming and inflammation. *Cancer Metab*, 3, 8. <https://doi.org/10.1186/s40170-015-0133-5>
- Checchetto, V., Reina, S., Magri, A., Szabo, I., & De Pinto, V. (2014). Recombinant human voltage dependent anion selective channel isoform 3 (hVDAC3) forms pores with a very small conductance. *Cell Physiol Biochem*, 34(3), 842-853. <https://doi.org/10.1159/000363047>
- Cheng, E. H., Sheiko, T. V., Fisher, J. K., Craigen, W. J., & Korsmeyer, S. J. (2003). VDAC2 inhibits BAK activation and mitochondrial apoptosis. *Science*, 301(5632), 513-517. <https://doi.org/10.1126/science.1083995>
- Chin, H. S., Li, M. X., Tan, I. K. L., Ninnis, R. L., Reljic, B., Scicluna, K., Dagley, L. F., Sandow, J. J., Kelly, G. L., Samson, A. L., Chappaz, S., Khaw, S. L., Chang, C., Morokoff, A., Brinkmann, K., Webb, A., Hockings, C., Hall, C. M., Kueh, A. J., . . . Dewson, G. (2018). VDAC2 enables BAX to mediate apoptosis and limit tumor development. *Nat Commun*, 9(1), 4976. <https://doi.org/10.1038/s41467-018-07309-4>

- Cluntun, A. A., Lukey, M. J., Cerione, R. A., & Locasale, J. W. (2017). Glutamine Metabolism in Cancer: Understanding the Heterogeneity. *Trends Cancer*, 3(3), 169-180. <https://doi.org/10.1016/j.trecan.2017.01.005>
- Crompton, M. (1999). The mitochondrial permeability transition pore and its role in cell death. *Biochem J*, 341 (Pt 2)(Pt 2), 233-249. <https://www.ncbi.nlm.nih.gov/pubmed/10393078>
- De Stefani, D., Bononi, A., Romagnoli, A., Messina, A., De Pinto, V., Pinton, P., & Rizzuto, R. (2012). VDAC1 selectively transfers apoptotic Ca²⁺ signals to mitochondria. *Cell Death Differ*, 19(2), 267-273. <https://doi.org/10.1038/cdd.2011.92>
- Gurnev, P. A., Rostovtseva, T. K., & Bezrukov, S. M. (2011). Tubulin-blocked state of VDAC studied by polymer and ATP partitioning. *FEBS Lett*, 585(14), 2363-2366. <https://doi.org/10.1016/j.febslet.2011.06.008>
- Hiller, S., Garces, R. G., Malia, T. J., Orekhov, V. Y., Colombini, M., & Wagner, G. (2008). Solution structure of the integral human membrane protein VDAC-1 in detergent micelles. *Science*, 321(5893), 1206-1210. <https://doi.org/10.1126/science.1161302>
- Huang, H., Hu, X., Eno, C. O., Zhao, G., Li, C., & White, C. (2013). An interaction between Bcl-xL and the voltage-dependent anion channel (VDAC) promotes mitochondrial Ca²⁺ uptake. *J Biol Chem*, 288(27), 19870-19881. <https://doi.org/10.1074/jbc.M112.448290>
- Huang, H., Shah, K., Bradbury, N. A., Li, C., & White, C. (2014). Mcl-1 promotes lung cancer cell migration by directly interacting with VDAC to increase mitochondrial Ca²⁺ uptake and reactive oxygen species generation. *Cell Death Dis*, 5(10), e1482. <https://doi.org/10.1038/cddis.2014.419>
- Jin, J., Byun, J. K., Choi, Y. K., & Park, K. G. (2023). Targeting glutamine metabolism as a therapeutic strategy for cancer. *Exp Mol Med*, 55(4), 706-715. <https://doi.org/10.1038/s12276-023-00971-9>
- Jones, J., MacKrell, E. J., Wang, T. Y., Lomenick, B., Roukes, M. L., & Chou, T. F. (2023). Tidyproteomics: an open-source R package and data object for quantitative proteomics post analysis and visualization. *BMC Bioinformatics*, 24(1), 239. <https://doi.org/10.1186/s12859-023-05360-7>
- Kinghorn, K. J., Castillo-Quan, J. I., Bartolome, F., Angelova, P. R., Li, L., Pope, S., Cocheme, H. M., Khan, S., Asghari, S., Bhatia, K. P., Hardy, J., Abramov, A. Y., & Partridge, L. (2015). Loss of PLA2G6 leads to elevated mitochondrial lipid peroxidation and mitochondrial dysfunction. *Brain*, 138(Pt 7), 1801-1816. <https://doi.org/10.1093/brain/awv132>
- Kuznetsov, A. V., Javadov, S., Sickinger, S., Frotschnig, S., & Grimm, M. (2015). H9c2 and HL-1 cells demonstrate distinct features of energy metabolism, mitochondrial function and sensitivity to hypoxia-reoxygenation. *Biochim Biophys Acta*, 1853(2), 276-284. <https://doi.org/10.1016/j.bbamcr.2014.11.015>
- Lemeshko, V. V. (2017). The Mitochondrial Outer Membrane Potential as an Electrical Feedback Control of Cell Energy Metabolism. In *Molecular Basis for Mitochondrial Signaling* (pp. 217-250). https://doi.org/10.1007/978-3-319-55539-3_9

- Liu, Z., Luo, Q., & Guo, C. (2015). Bim and VDAC1 are hierarchically essential for mitochondrial ATF2 mediated cell death. *Cancer Cell Int*, 15, 34. <https://doi.org/10.1186/s12935-015-0188-y>
- Lock, J. T., & Parker, I. (2020). IP₃ mediated global Ca²⁺ signals arise through two temporally and spatially distinct modes of Ca²⁺ release. *Elife*, 9. <https://doi.org/10.7554/eLife.55008>
- Magri, A., Cubisino, S. A. M., Battiato, G., Lipari, C. L. R., Conti Nibali, S., Saab, M. W., Pittala, A., Amorini, A. M., De Pinto, V., & Messina, A. (2023). VDAC1 Knockout Affects Mitochondrial Oxygen Consumption Triggering a Rearrangement of ETC by Impacting on Complex I Activity. *Int J Mol Sci*, 24(4). <https://doi.org/10.3390/ijms24043687>
- Maldonado, E. N., Sheldon, K. L., DeHart, D. N., Patnaik, J., Manevich, Y., Townsend, D. M., Bezrukov, S. M., Rostovtseva, T. K., & Lemasters, J. J. (2013). Voltage-dependent anion channels modulate mitochondrial metabolism in cancer cells: regulation by free tubulin and erastin. *J Biol Chem*, 288(17), 11920-11929. <https://doi.org/10.1074/jbc.M112.433847>
- Maurya, S. R., & Mahalakshmi, R. (2017). Mitochondrial VDAC2 and cell homeostasis: highlighting hidden structural features and unique functionalities. *Biol Rev Camb Philos Soc*, 92(4), 1843-1858. <https://doi.org/10.1111/brv.12311>
- McCommis, K. S., & Baines, C. P. (2012). The role of VDAC in cell death: friend or foe? *Biochim Biophys Acta*, 1818(6), 1444-1450. <https://doi.org/10.1016/j.bbamem.2011.10.025>
- Messina, A., Reina, S., Guarino, F., & De Pinto, V. (2012). VDAC isoforms in mammals. *Biochim Biophys Acta*, 1818(6), 1466-1476. <https://doi.org/10.1016/j.bbamem.2011.10.005>
- Min, C. K., Yeom, D. R., Lee, K. E., Kwon, H. K., Kang, M., Kim, Y. S., Park, Z. Y., Jeon, H., & Kim, D. H. (2012). Coupling of ryanodine receptor 2 and voltage-dependent anion channel 2 is essential for Ca²⁺ transfer from the sarcoplasmic reticulum to the mitochondria in the heart. *Biochem J*, 447(3), 371-379. <https://doi.org/10.1042/BJ20120705>
- Mootha, V. K., Handschin, C., Arlow, D., Xie, X., St Pierre, J., Sihag, S., Yang, W., Altshuler, D., Puigserver, P., Patterson, N., Willy, P. J., Schulman, I. G., Heyman, R. A., Lander, E. S., & Spiegelman, B. M. (2004). Errα and Gabpa/b specify PGC-1α-dependent oxidative phosphorylation gene expression that is altered in diabetic muscle. *Proc Natl Acad Sci U S A*, 101(17), 6570-6575. <https://doi.org/10.1073/pnas.0401401101>
- Naghdi, S., Mishra, P., Roy, S. S., Weaver, D., Walter, L., Davies, E., Antony, A. N., Lin, X., Moehren, G., Feitelson, M. A., Reed, C. A., Lindsten, T., Thompson, C. B., Dang, H. T., Hoek, J. B., Knudsen, E. S., & Hajnoczky, G. (2025). VDAC2 and Bak scarcity in liver mitochondria enables targeting hepatocarcinoma while sparing hepatocytes. *Nat Commun*, 16(1), 2416. <https://doi.org/10.1038/s41467-025-56898-4>
- Naghdi, S., Varnai, P., & Hajnoczky, G. (2015). Motifs of VDAC2 required for mitochondrial Bak import and tBid-induced apoptosis. *Proc Natl Acad Sci U S A*, 112(41), E5590-5599. <https://doi.org/10.1073/pnas.1510574112>

- Peng, W., Wong, Y. C., & Krainc, D. (2020). Mitochondria-lysosome contacts regulate mitochondrial Ca^{2+} dynamics via lysosomal TRPML1. *Proc Natl Acad Sci U S A*, *117*(32), 19266-19275. <https://doi.org/10.1073/pnas.2003236117>
- Queralt-Martin, M., Bergdoll, L., Teijido, O., Munshi, N., Jacobs, D., Kuszak, A. J., Protchenko, O., Reina, S., Magri, A., De Pinto, V., Bezrukov, S. M., Abramson, J., & Rostovtseva, T. K. (2020). A lower affinity to cytosolic proteins reveals VDAC3 isoform-specific role in mitochondrial biology. *J Gen Physiol*, *152*(2). <https://doi.org/10.1085/jgp.201912501>
- Reina, S., Nibali, S. C., Tomasello, M. F., Magri, A., Messina, A., & De Pinto, V. (2022). Voltage Dependent Anion Channel 3 (VDAC3) protects mitochondria from oxidative stress. *Redox Biol*, *51*, 102264. <https://doi.org/10.1016/j.redox.2022.102264>
- Rosenberg, P. (2022). VDAC2 as a novel target for heart failure: Ca^{2+} at the sarcomere, mitochondria and SR. *Cell Calcium*, *104*, 102586. <https://doi.org/10.1016/j.ceca.2022.102586>
- Rosencrans, W. M., Aguilera, V. M., Rostovtseva, T. K., & Bezrukov, S. M. (2021). alpha-Synuclein emerges as a potent regulator of VDAC-facilitated calcium transport. *Cell Calcium*, *95*, 102355. <https://doi.org/10.1016/j.ceca.2021.102355>
- Rosencrans, W. M., Rajendran, M., Bezrukov, S. M., & Rostovtseva, T. K. (2021). VDAC regulation of mitochondrial calcium flux: From channel biophysics to disease. *Cell Calcium*, *94*, 102356. <https://doi.org/10.1016/j.ceca.2021.102356>
- Rostovtseva, T., & Colombini, M. (1996). ATP flux is controlled by a voltage-gated channel from the mitochondrial outer membrane. *J Biol Chem*, *271*(45), 28006-28008. <https://doi.org/10.1074/jbc.271.45.28006>
- Rostovtseva, T. K., Bezrukov, S. M., & Hoogerheide, D. P. (2021). Regulation of Mitochondrial Respiration by VDAC Is Enhanced by Membrane-Bound Inhibitors with Disordered Polyanionic C-Terminal Domains. *Int J Mol Sci*, *22*(14). <https://doi.org/10.3390/ijms22147358>
- Rostovtseva, T. K., Gurnev, P. A., Protchenko, O., Hoogerheide, D. P., Yap, T. L., Philpott, C. C., Lee, J. C., & Bezrukov, S. M. (2015). alpha-Synuclein Shows High Affinity Interaction with Voltage-dependent Anion Channel, Suggesting Mechanisms of Mitochondrial Regulation and Toxicity in Parkinson Disease. *J Biol Chem*, *290*(30), 18467-18477. <https://doi.org/10.1074/jbc.M115.641746>
- Rostovtseva, T. K., Sheldon, K. L., Hassanzadeh, E., Monge, C., Saks, V., Bezrukov, S. M., & Sackett, D. L. (2008). Tubulin binding blocks mitochondrial voltage-dependent anion channel and regulates respiration. *Proc Natl Acad Sci U S A*, *105*(48), 18746-18751. <https://doi.org/10.1073/pnas.0806303105>
- Roy, S. S., Ehrlich, A. M., Craigen, W. J., & Hajnoczky, G. (2009). VDAC2 is required for truncated BID-induced mitochondrial apoptosis by recruiting BAK to the mitochondria. *EMBO Rep*, *10*(12), 1341-1347. <https://doi.org/10.1038/embor.2009.219>
- Saccone, C., Caggese, C., D'Erchia, A. M., Lanave, C., Oliva, M., & Pesole, G. (2003). Molecular clock and gene function. *J Mol Evol*, *57 Suppl 1*, S277-285. <https://doi.org/10.1007/s00239-003-0037-9>

- Saks, V. A., Kuznetsov, A. V., Khuchua, Z. A., Vasilyeva, E. V., Belikova, J. O., Kesvatera, T., & Tiivel, T. (1995). Control of cellular respiration in vivo by mitochondrial outer membrane and by creatine kinase. A new speculative hypothesis: possible involvement of mitochondrial-cytoskeleton interactions. *J Mol Cell Cardiol*, 27(1), 625-645. [https://doi.org/10.1016/s0022-2828\(08\)80056-9](https://doi.org/10.1016/s0022-2828(08)80056-9)
- Sampson, M. J., Decker, W. K., Beaudet, A. L., Ruitenbeek, W., Armstrong, D., Hicks, M. J., & Craigen, W. J. (2001). Immotile sperm and infertility in mice lacking mitochondrial voltage-dependent anion channel type 3. *J Biol Chem*, 276(42), 39206-39212. <https://doi.org/10.1074/jbc.M104724200>
- Sampson, M. J., Lovell, R. S., & Craigen, W. J. (1997). The murine voltage-dependent anion channel gene family. Conserved structure and function. *J Biol Chem*, 272(30), 18966-18973. <https://doi.org/10.1074/jbc.272.30.18966>
- Shimizu, S., Ide, T., Yanagida, T., & Tsujimoto, Y. (2000). Electrophysiological study of a novel large pore formed by Bax and the voltage-dependent anion channel that is permeable to cytochrome c. *J Biol Chem*, 275(16), 12321-12325. <https://doi.org/10.1074/jbc.275.16.12321>
- Shimizu, S., Matsuoka, Y., Shinohara, Y., Yoneda, Y., & Tsujimoto, Y. (2001). Essential role of voltage-dependent anion channel in various forms of apoptosis in mammalian cells. *Journal of Cell Biology*, 152(2), 237-250. <https://doi.org/10.1083/jcb.152.2.237>
- Shimizu, S., Narita, M., & Tsujimoto, Y. (1999). Bcl-2 family proteins regulate the release of apoptogenic cytochrome c by the mitochondrial channel VDAC. *Nature*, 399(6735), 483-487. <https://doi.org/10.1038/20959>
- Simson, P., Jepihhina, N., Laasmaa, M., Peterson, P., Birkedal, R., & Vendelin, M. (2016). Restricted ADP movement in cardiomyocytes: Cytosolic diffusion obstacles are complemented with a small number of open mitochondrial voltage-dependent anion channels. *J Mol Cell Cardiol*, 97, 197-203. <https://doi.org/10.1016/j.yjmcc.2016.04.012>
- Subedi, K. P., Kim, J. C., Kang, M., Son, M. J., Kim, Y. S., & Woo, S. H. (2011). Voltage-dependent anion channel 2 modulates resting Ca²⁺ sparks, but not action potential-induced Ca²⁺ signaling in cardiac myocytes. *Cell Calcium*, 49(2), 136-143. <https://doi.org/10.1016/j.ceca.2010.12.004>
- Sun, X., Ou, Z., Chen, R., Niu, X., Chen, D., Kang, R., & Tang, D. (2016). Activation of the p62-Keap1-NRF2 pathway protects against ferroptosis in hepatocellular carcinoma cells. *Hepatology*, 63(1), 173-184. <https://doi.org/10.1002/hep.28251>
- Tan, W., & Colombini, M. (2007). VDAC closure increases calcium ion flux. *Biochim Biophys Acta*, 1768(10), 2510-2515. <https://doi.org/10.1016/j.bbamem.2007.06.002>
- Ujwal, R., Cascio, D., Chaptal, V., Ping, P., & Abramson, J. (2009). Crystal packing analysis of murine VDAC1 crystals in a lipidic environment reveals novel insights on oligomerization and orientation. *Channels (Austin)*, 3(3), 167-170. <https://doi.org/10.4161/chan.3.3.9196>
- van Delft, M. F., Chappaz, S., Khakham, Y., Bui, C. T., Debrincat, M. A., Lowes, K. N., Brouwer, J. M., Grohmann, C., Sharp, P. P., Dagley, L. F., Li, L., McArthur, K., Luo, M. X., Chin, H. S., Fairlie, W. D., Lee, E. F., Segal, D., Duflocq, S., Lessene,

- R., . . . Kile, B. T. (2019). A small molecule interacts with VDAC2 to block mouse BAK-driven apoptosis. *Nat Chem Biol*, *15*(11), 1057-1066. <https://doi.org/10.1038/s41589-019-0365-8>
- Vander Heiden, M. G., Li, X. X., Gottlieb, E., Hill, R. B., Thompson, C. B., & Colombini, M. (2001). Bcl-xL promotes the open configuration of the voltage-dependent anion channel and metabolite passage through the outer mitochondrial membrane. *J Biol Chem*, *276*(22), 19414-19419. <https://doi.org/10.1074/jbc.M101590200>
- Vyssokikh, M., & Brdiczka, D. (2004). VDAC and peripheral channelling complexes in health and disease. *Molecular and Cellular Biochemistry*, *256-257*(1-2), 117-126. <https://doi.org/10.1023/b:mcbi.0000009863.69249.d9>
- Weeber, E. J., Levy, M., Sampson, M. J., Anfous, K., Armstrong, D. L., Brown, S. E., Sweatt, J. D., & Craigen, W. J. (2002). The role of mitochondrial porins and the permeability transition pore in learning and synaptic plasticity. *J Biol Chem*, *277*(21), 18891-18897. <https://doi.org/10.1074/jbc.M201649200>
- Woldetsadik, A. D., Vogel, M. C., Rabeh, W. M., & Magzoub, M. (2017). Hexokinase II-derived cell-penetrating peptide targets mitochondria and triggers apoptosis in cancer cells. *FASEB J*, *31*(5), 2168-2184. <https://doi.org/10.1096/fj.201601173R>
- Xu, X., Decker, W., Sampson, M. J., Craigen, W. J., & Colombini, M. (1999). Mouse VDAC isoforms expressed in yeast: channel properties and their roles in mitochondrial outer membrane permeability. *J Membr Biol*, *170*(2), 89-102. <https://doi.org/10.1007/s002329900540>
- Xue, X., Bredell, B. X., Anderson, E. R., Martin, A., Mays, C., Nagao-Kitamoto, H., Huang, S., Gyorffy, B., Greenson, J. K., Hardiman, K., Spence, J. R., Kamada, N., & Shah, Y. M. (2017). Quantitative proteomics identifies STEAP4 as a critical regulator of mitochondrial dysfunction linking inflammation and colon cancer. *Proc Natl Acad Sci U S A*, *114*(45), E9608-E9617. <https://doi.org/10.1073/pnas.1712946114>
- Yang, M., Sun, J., Stowe, D. F., Tajkhorshid, E., Kwok, W. M., & Camara, A. K. S. (2020). Knockout of VDAC1 in H9c2 Cells Promotes Oxidative Stress-Induced Cell Apoptosis through Decreased Mitochondrial Hexokinase II Binding and Enhanced Glycolytic Stress. *Cell Physiol Biochem*, *54*(5), 853-874. <https://doi.org/10.33594/000000274>
- Young, M. J., Bay, D. C., Hausner, G., & Court, D. A. (2007). The evolutionary history of mitochondrial porins. *BMC Evol Biol*, *7*, 31. <https://doi.org/10.1186/1471-2148-7-31>
- Zinghirino, F., Pappalardo, X. G., Messina, A., Nicosia, G., De Pinto, V., & Guarino, F. (2021). VDAC Genes Expression and Regulation in Mammals. *Front Physiol*, *12*, 708695. <https://doi.org/10.3389/fphys.2021.708695>

CONCLUSION

“The first principle is you must not fool yourself, and you are the easiest person to fool.” –

Richard Feynman

In this thesis, I have explored the regulation of mitophagy and mitochondrial function by pharmacological and endogenous cellular effectors. Interest in both drugs and novel biological pathways that regulate these processes has grown with the increasing realization of their roles in disease pathogenesis. Autophagy remains a difficult pathway to study given the incredible redundancy of its effectors and its susceptibility to perturbation by secondary stresses. An example of this redundancy is in the autophagy step for PINK1/Parkin mitophagy. To block the recruitment of the autophagosome to damaged mitochondria in the PINK/Parkin pathway, simultaneous knockout (KO) of five autophagy adaptor proteins—OPTN, NDP52, TAX1BP1, p62, and NBR1 (the so-called Penta-KO) was required (Lazarou et al., 2015). In another impressive feat, a six-protein KO was required to dissect the role of the ubiquitous ATG8/GABARAP family of proteins. Yet, it was only after these rigorous studies that the conventional theory, that the ATG8 family was required for recruitment of the autophagosome to cargo, was overturned. Instead it was realized that ATG8 proteins are essential for growth of the autophagosome, closure, and fusion to the lysosome (Nguyen et al., 2016). These case studies highlight the difficulty of using traditional CRISPR/siRNA-based screens, which silence one gene at a time, to discover regulators of these highly redundant processes.

In this thesis, I highlight proteomics as a tool to uncover novel regulators of these convoluted pathways. For example, TNIP1 was initially discovered as an interactor of the LC3 machinery and likely autophagic cargo. A more focused analysis of this protein led to the discovery that it was a unique negative regulator of mitophagy. Here, subtle experimental conditions could have changed the entire course of the study; TNIP1 only appreciably slowed mitophagy at earlier stages, and its rate recovered at longer time points (Le Guerroue et al., 2023). Proteomics also helped elucidate the mechanism of action of the TNIP1 mitophagy

block. TNIP1 was found to bind multiple autophagy effectors, including FIP200, TAX1BP1, and ATG8 proteins. Alteration of these binding interactions one by one only led to partial blocks in TNIP1's inhibitory function. Immuno-pulldown coupled with mass spectrometry also revealed potentially novel functions of TNIP1. One of TNIP1's top hits, not explored in this study, was Tumor Suppressor Gene 101 (TSG101). The spuriously named TSG101 is a core member of the ESCRT machinery that drives endosomal sorting and degradation (Ferraiuolo et al., 2020). This interaction could indicate that TNIP1 may also function as an ESCRT adapter targeting substrates for endosomal degradation or trafficking. Given TNIP1's intimate role in regulating immune-related pathways, it may degrade immune machinery to regulate those pathways (Yin et al., 2022). TNIP1 deficiency has been associated with both autoimmune disorders and, more recently, Alzheimer's Disease and Related Dementias (AD/RD) (Medhavy et al., 2024; Panyard et al., 2024).

A separate challenge in autophagy research is the potential for secondary stresses to induce the process independently of direct autophagic alteration. Inherent in studying a "stress response" is that many manipulations we perform in the lab, whether drug screening or gene silencing, make cells very "unhappy." There is no simple assay to determine whether a perturbation induces autophagy via a direct or secondary effect. This thesis highlights the especially difficult task of identifying pharmacological activators of the PINK1/Parkin pathway. It is often more difficult to activate a protein than to inhibit it; easier to break a complex machine than improve it. PINK1/Parkin presents many formidable challenges to drug discovery. Firstly, PINK1 is constitutively degraded, and Parkin remains inactive until triggered by PINK1 phosphorylation and phosphorylated ubiquitin (pUb). Groups have attempted to overcome this limitation by adding low levels of mitochondrial toxins to boost the cellular PINK1 pool capable of activation by a drug. However, this approach is foiled by the exquisitely sensitive, switch-like nature of the PINK1/Parkin system. As shown in this thesis, priming the PINK1/Parkin pathway just below the threshold of PINK1 accumulation needed for mitophagy makes the pathway prone to activation by any weak mitochondrial toxin. It is increasingly understood that many drugs have some off-target inhibition of mitochondrial function. This is likely because the electron transport chain (ETC) is an

enormous, finely tuned machine with numerous hydrophobic sites amenable to small molecule binding. In isolation, these molecules have little effect, but together with strong toxins, they appear as potent mitophagy activators. The reason drugs like MTK458 have advanced is that the weak toxicity was assumed to be an off-target effect incapable of explaining potent mitophagy induction. However, I show that even the weak mitochondrial inhibition, which should have been originally noted in the glucose/galactose counter-screen, is sufficient to activate the PINK1/Parkin pathway under mitochondrial stress. At the end of Chapter 2, I demonstrate that a “toy model” of sequential, rate-limited biochemical reactions with a threshold step can recapitulate the surprising dynamics of drug combination-induced mitophagy. More rigorous mathematical work has already introduced a realistic set of differential equations for modeling the PINK1-Parkin input threshold (Waters et al., 2023). Future work applying these models could determine the real physical parameters dictating the PINK1-Parkin pathway and the inhibitory effects of each drug. Such a model could predict a novel drug’s effect on mitophagy in combination with other drugs and under different mitochondrial conditions.

The future of drugging mitophagy is not entirely gloomy! Although this thesis casts doubt on promising clinical candidates for Parkinson’s disease (PD), it also offers solutions. Leveraging the power of proteomics, I discovered that, in addition to activating PINK1, these compounds also initiate the parallel DELE1-HRI integrated stress response. The evolutionarily convergent DELE1/PINK1 mitochondrial-to-cytosol relay system makes an excellent proxy for distinguishing general mitochondrial stress from unique direct PINK1 activation. ATF4 reporters could provide a secondary counter-screen for any PINK1 activator campaign to exclude stress-sensitization as the mechanism of action (MOA). Furthermore, I unexpectedly discovered that HRI inhibition activates PINK1-Parkin. Although partially conflicting with contemporaneous reports regarding whether HRI inhibition enhances mitophagy under basal conditions or only with the addition of toxins, both this thesis and other groups report enhanced mitophagy following HRI knockdown. Other groups have suggested chemical inhibition of HRI as a potential approach for mitophagy enhancement (Singh et al., 2025). Notably, silencing the integrated stress response

(ISR) could inadvertently suppress transcriptional upregulation of proteins important for mitochondrial recovery, such as KLF4, which we found to be enhanced by the ISR (Rosencrans et al., 2020).

Concurrent structural studies of active PINK1 at the TOMM/VDAC channels provide opportunities to improve drug screening for PINK1 activators (Callegari et al., 2025). Virtual screens could identify molecular glues that promote PINK1 dimerization, stabilize the TOMM40-PINK1 interaction, or stabilize VDAC2 dimers. VDAC2 is a particularly compelling target. This thesis demonstrates that the seemingly simple beta-barrel pore exhibits impressive conformational plasticity, regulating its interactions with partner proteins. Critically, I showed that the nine cysteine residues of VDAC2 significantly influence these dynamics. In the PINK1-VDAC2 structure, bridging cysteines on the intermembrane space (IMS) side of VDAC2 tether the complex together. Cysteine-reactive chemistry may thus provide a feasible approach for drugging VDAC2 to either promote or inhibit its dimerization.

In total, this thesis has uncovered mechanisms by which pharmacological agents and endogenous effectors regulate mitophagy and mitochondrial function. I have shown how a hitherto underappreciated PINK1 sensitization effect can explain the action of multiple clinical-stage Parkinson's disease-targeting drugs. This work suggests potential strategies to avoid such artifacts in future screening campaigns and novel targets for mitophagy enhancement. Additionally, I uncovered a role for the immune-related protein TNIP1 in the regulation of mitophagy and demonstrated that the mitophagy-related protein VDAC2 is uniquely characterized by biophysical plasticity, helping rationalize its role in orthogonal signaling pathways.

Works Cited

Callegari, S., Kirk, N. S., Gan, Z. Y., Dite, T., Cobbold, S. A., Leis, A., Dagley, L. F., Glukhova, A., & Komander, D. (2025). Structure of human PINK1 at a mitochondrial TOM-VDAC array. *Science*, 388(6744), 303-310. <https://doi.org/10.1126/science.adu6445>

Ferraiuolo, R. M., Manthey, K. C., Stanton, M. J., Triplett, A. A., & Wagner, K. U. (2020). The Multifaceted Roles of the Tumor Susceptibility Gene 101 (TSG101) in Normal Development and Disease. *Cancers (Basel)*, 12(2). <https://doi.org/10.3390/cancers12020450>

Lazarou, M., Sliter, D. A., Kane, L. A., Sarraf, S. A., Wang, C., Burman, J. L., Sideris, D. P., Fogel, A. I., & Youle, R. J. (2015). The ubiquitin kinase PINK1 recruits autophagy receptors to induce mitophagy. *Nature*, 524(7565), 309-314. <https://doi.org/10.1038/nature14893>

Le Guerroue, F., Bunker, E. N., Rosencrans, W. M., Nguyen, J. T., Basar, M. A., Werner, A., Chou, T. F., Wang, C., & Youle, R. J. (2023). TNIP1 inhibits selective autophagy via bipartite interaction with LC3/GABARAP and TAX1BP1. *Mol Cell*, 83(6), 927-941 e928. <https://doi.org/10.1016/j.molcel.2023.02.023>

Medhavy, A., Athanasopoulos, V., Bassett, K., He, Y., Stanley, M., Enosi Tuipulotu, D., Cappello, J., Brown, G. J., Gonzalez-Figueroa, P., Turnbull, C., Shanmuganandam, S., Tummala, P., Hart, G., Lea-Henry, T., Wang, H., Nambadan, S., Shen, Q., Roco, J. A., Burgio, G., . . . Vinuesa, C. G. (2024). A TNIP1-driven systemic autoimmune disorder with elevated IgG4. *Nat Immunol*, 25(9), 1678-1691. <https://doi.org/10.1038/s41590-024-01902-0>

Nguyen, T. N., Padman, B. S., Usher, J., Oorschot, V., Ramm, G., & Lazarou, M. (2016). Atg8 family LC3/GABARAP proteins are crucial for autophagosome-lysosome fusion but not autophagosome formation during PINK1/Parkin mitophagy and starvation. *J Cell Biol*, 215(6), 857-874. <https://doi.org/10.1083/jcb.201607039>

Panyard, D. J., Reus, L. M., Ali, M., Liu, J., Deming, Y. K., Lu, Q., Kollmorgen, G., Carboni, M., Wild, N., Visser, P. J., Bertram, L., Zetterberg, H., Blennow, K., Gobom, J., Western, D., Sung, Y. J., Carlsson, C. M., Johnson, S. C., Asthana, S., . . . Snyder, M. P. (2024). Post-GWAS multiomic functional investigation of the TNIP1 locus in Alzheimer's disease highlights a potential role for GPX3. *Alzheimers Dement*, 20(7), 5044-5053. <https://doi.org/10.1002/alz.13848>

Rosencrans, W. M., Walsh, Z. H., Huerbi, N., Blum, A., Belew, M., Liu, C., Chernak, B., Brauer, P. R., Trazo, A., Olson, A., & Hagos, E. (2020). Cells deficient for Kruppel-like factor 4 exhibit mitochondrial dysfunction and impaired mitophagy. *Eur J Cell Biol*, 99(1), 151061. <https://doi.org/10.1016/j.ejcb.2019.151061>

Singh, P. K., Agarwal, S., Volpi, I., Wilhelm, L. P., Becchi, G., Keenlyside, A., Macartney, T., Toth, R., Rousseau, A., Masson, G. R., Ganley, I. G., & Muqit, M. M. K. (2025). Kinome screening identifies integrated stress response kinase EIF2AK1/HRI as a negative regulator of PINK1 mitophagy signaling. *Sci Adv*, 11(19), eadn2528. <https://doi.org/10.1126/sciadv.adn2528>

Waters, C. S., Angenent, S. B., Altschuler, S. J., & Wu, L. F. (2023). A PINK1 input threshold arises from positive feedback in the PINK1/Parkin mitophagy decision circuit. *Cell Rep*, 42(10), 113260. <https://doi.org/10.1016/j.celrep.2023.113260>

Yin, H., Karayel, O., Chao, Y. Y., Seeholzer, T., Hamp, I., Plettenburg, O., Gehring, T., Zielinski, C., Mann, M., & Krappmann, D. (2022). A20 and ABIN-1 cooperate in balancing CBM complex-triggered NF-kappaB signaling in activated T cells. *Cell Mol Life Sci*, 79(2), 112. <https://doi.org/10.1007/s00018-022-04154-z>

INDEX

A

Aristotle, 3

F

From a Galaxy, 2

G

Geocentric theory, 2

H

Heliocentric theory, 3

M

Mariner space mission, 2

Mercury, 3

Milky Way, 2

O

Orbit

Mercury, 3

P

Planets and Moons, 2

R

Rotation

Mercury, 3

S

Solar system

creation, 2

geocentric theory, 2

heliocentric theory, 3

Mariner mission, 2

Voyager mission, 2

T

The Solar System, 2

V

Voyager space mission,

2

